Development and application of functional MRI methods to investigate brainstem haemodynamics in the context of systemic hypertension

Owen Bleddyn Woodward

A Thesis submitted to Cardiff University in partial fulfilment of the requirements for the degree Doctor of Philosophy

November 2023

Acknowledgments

Thank you to the Medical Research Council for funding this research, and for the GW4 BioMed MRC Doctoral Training Programme for the training opportunities and support they provided.

I would like to especially thank both my main supervisor, Richard Wise, and co-supervisor, Ian Driver, for all their support and guidance. Thank you both for giving up so much of your time to guide and advise me, for always being approachable, and for your invaluable expertise.

Thank you also to Emma Hart, my co-supervisor at the University of Bristol, for her invaluable input throughout.

Thank you to Kevin Murphy, Emre Kopanoglu, and everyone else at CUBRIC who contributed in any way, especially those who gave up their time to be participants in my research.

Diolch yn fawr i fy rhieni am eu holl gefnogaeth dros y blynyddoedd (ac am fod yn Nain a Taid rhagorol!).

Thank you to my in-laws for all their support and for being great grandparents.

A special thank you to my wife Yasmeen. Thank you for being so patient and supportive while I worked on this thesis alongside my clinical training, and for doing such a great job raising our two boys.

Yn olaf, diolch i Idris ac Afan am fod yn hogiau da rhan fwyaf o'r amser.

Contributors

Thank you to everyone who has contributed in any way to the work presented in this thesis. A big thank you to the following people from outside the main supervisory team.

Esther Warnert, whose data was used in Chapter 3.

Mike Germuska, who provided invaluable feedback on Chapter 4.

Neeraj Saxena and Sharmila Khot, who worked on the study design and data collection in Chapter 7 and provided invaluable clinical expertise when planning other aspects of this thesis.

James Coulson, who worked on the proposed study of hypertensives outlined in Chapter 8.

Thesis summary

The selfish brain mechanism proposes that in some cases hypertension could develop as a compensatory mechanism that aims to maintain cerebral blood flow (CBF) by increasing systemic blood pressure through an increase in cardiovascular sympathetic tone. The mechanism that might trigger this hypothesised initial reduction in CBF is uncertain, but the brainstem is an important component of the central autonomic nervous system and may therefore play an important role in the development of hypertension via the selfish brain mechanism.

Various techniques have been used to investigate the selfish brain mechanism in humans, including magnetic resonance imaging (MRI) methods to measure CBF and cerebrovascular reactivity (CVR). CVR quantifies the change in CBF in response to a vascular stimulus, and is related to the responsiveness, tone and functional reserve of the cerebrovascular system.

This thesis aims to validate, optimise and apply a variety of MRI-based methods of quantifying human cerebrovascular function, which may then be used in future studies to further investigate the selfish brain mechanism. Firstly, methods of measuring CBF and CVR using MRI are tailored towards their application in the brainstem and the feasibility of measuring regional brainstem CBF and CVR is demonstrated. Next, existing data is explored to study the association between vertebral artery hypoplasia (VAH) and brainstem CBF in hypertensives but no statistically significant association between regional CBF, VAH and hypertension is found. Brainstem co-registration is then optimised using machine learning. The UK biobank dataset is explored to study the amplitude of low-frequency fluctuations (ALFF) in the BOLD signal, a potential surrogate index of CVR, in hypertensives. There is no statistically significant difference in the regional variation in ALFF between hypertensives and normotensives. Following this, the relationship between ALFF and CVR is investigated to validate ALFF as a surrogate marker of CVR, but no evidence to support the use of ALFF as a specific metric of CVR is demonstrated. Finally, a pilot study of functional MRI in the locus coeruleus, an important noradrenergic brainstem nucleus that is integral to the central autonomic network, is undertaken. The feasibility of mapping functional connectivity of the LC using an anatomical localiser tailored to each participant is demonstrated.

Publication and abstracts resulting from this thesis

Publications

Woodward OB, Driver I, Hart E, Wise R. “In search of a marker of altered cerebrovascular function in hypertension: Analysis of the fractional amplitude of low-frequency fluctuations in UK Biobank resting state fMRI data”. Cerebral Circulation – Cognition & Behavior 2024.

Woodward OB, Driver I, Schwarz ST, Hart E, Wise R. “Assessment of brainstem function and haemodynamics by MRI: challenges and clinical prospects.” British Journal of Radiology 2023.

Abstracts

Poster presentation: Woodward OB, Driver I, Hart E, Wise R. “Fractional amplitude of low-frequency fluctuations in hypertensives – retrospective analysis of UK Biobank resting-state functional MRI data.” Abstracts of the Europhysiology Conference 2022. p790-791.

Oral communication: Woodward OB, Germuska M, Driver I, Wise R. “Implementation of a convolutional neural network for brainstem landmark detection and co-registration.” International Society for Magnetic Resonance in Medicine – British and Irish Chapter 2022. P75-80.

Oral communication: Woodward OB, Warnert E, Driver I, Hart E, Wise R. “Vertebral artery hypoplasia and brainstem blood flow in patients with hypertension.” Physiology 2021. P166-168.

Abbreviations

ALFF	Amplitude of low-frequency fluctuations
ASL	Arterial spin labelling
ATT	Arterial transit time
BOLD	Blood oxygen level dependent
BP	Blood pressure
CBF	Cerebral blood flow
CBV	Cerebral blood volume
$CMRO_2$	Cerebral metabolic rate of oxygen
CNN	Convolutional neural network
CNR	Contrast-to-noise ratio
CO	Cardiac output
CVLM	Caudal ventrolateral medulla
CVR	Cerebrovascular reactivity
$ETCO_2$	End-tidal carbon dioxide
FID	Free induction decay
fALFF	Fractional amplitude of low-frequency fluctuations
fMRI	Functional magnetic resonance imaging
GLM	General linear model
Hb	Haemoglobin
HR	Heart rate
HTN	Hypertension
LC	Locus coeruleus
MAP	Mean arterial pressure
MRI	Magnetic resonance imaging
MT	Magnetisation transfer
NTN	Normotension
NTS	Nucleus tractus solitarius
OEF	Oxygen extraction fraction
$PaO_2/PaCO_2$	Arterial partial pressure of oxygen/carbon dioxide
PCASL	Pseudo-continuous arterial spin labelling
PLD	Post-label delay
R2*	Decay rate of transverse magnetisation
RVLM	Rostral ventrolateral medulla
SAR	Specific absorption rate
SNA	Sympathetic nerve activity
SNR	Signal-to-noise ratio
SV	Stroke volume

TE	Echo time
TR	Repetition time
VAH	Vertebral artery hypoplasia

Contents

1. Introduction

A persistent elevation in systemic arterial blood pressure is referred to as hypertension. Despite the high prevalence and high morbidity associated with hypertension, its aetiology is poorly understood (Hart 2016). The selfish brain mechanism proposes that in some cases hypertension could develop as a compensatory mechanism that aims to maintain cerebral blood flow (CBF) by increasing systemic blood pressure through an increase in cardiovascular sympathetic tone (Hart 2016). According to the selfish brain mechanism, if CBF is compromised, increased neuronal activity in regions of the brain which modulate sympathetic nerve activity leads to an elevation in cardiovascular sympathetic tone and subsequently an increase in systemic blood pressure. This helps to maintain adequate cerebral perfusion. The mechanism that triggers this hypothesised initial reduction in CBF is uncertain. The brainstem, and specifically the medulla, is an important component of the central autonomic nervous system that governs sympathetic and parasympathetic efferent outflow to the cardiovascular system. It may therefore play an important role in the development of hypertension via the selfish brain mechanism.

Various techniques have been used to investigate the selfish brain mechanism and cerebral haemodynamics in humans (Hart 2016), (Warnert 2016). These include, among others, non-invasive methods that use magnetic resonance imaging (MRI) to measure CBF and cerebrovascular reactivity (CVR). CVR quantifies the change in CBF in response to a given vascular stimulus. It is related to the responsiveness, tone and functional reserve of the vascular system and is often regarded as an important marker of the health of the cerebrovascular system.

This thesis aims to validate, optimise, and apply a variety of MRI-based methods of quantifying human cerebrovascular function, which may then be used in future studies to investigate the selfish brain mechanism. There is a particular focus on the brainstem because of its importance to autonomic control of blood pressure. The brainstem is also an especially challenging structure to study, and it is therefore necessary to carefully tailor and optimise MRI techniques if valid functional MRI measurements in the brainstem are to be acquired.

Chapter 1 is an introductory chapter. Firstly, the physical principles of MRI are discussed. Functional MRI methods of assessing neuronal activity (blood oxygen level dependent or BOLD MRI) and cerebral blood flow (arterial spin labelling or ASL) are described, and the concept of cerebrovascular reactivity is introduced. The challenges associated with applying MRI to study the brainstem are discussed. The physiological mechanisms that govern systemic blood pressure are introduced, including the role of the sympathetic nervous system, and the central autonomic network. Finally, the selfish brain mechanism as a cause of hypertension is introduced.

Arterial spin labelling (ASL) is a non-invasive method of measuring cerebral blood flow using magnetic resonance imaging. It can also be used in conjunction with a vasoactive stimulus to measure cerebrovascular reactivity. In chapter 2, an ASL pulse sequence is tailored to optimise measurement of brainstem CBF and CVR. The feasibility of measuring regional brainstem CBF and CVR is demonstrated.

In chapter 3, existing data from a previous study was revisited to investigate whether there is an association between structural variations in brainstem arterial supply (via the vertebral arteries) and brainstem blood flow, and whether this association (if any) varies according to blood pressure status. If there is an association between vertebral artery hypoplasia (VAH), impaired brainstem blood flow, and hypertension, this would raise the possibility that VAH could be causative of hypertension via the selfish brain mechanism. Contrary to our main hypothesise that hypertensives with VAH have lower CBF to the posterior circulation and brainstem compared to the anterior circulation, no statistically significant association between regional CBF, VAH and hypertension was found.

Accurate brainstem co-registration is paramount to obtaining accurate measurements of brainstem CBF and CVR, as well as probing functional neuronal activity within brainstem nuclei that are of the order of millimetres in diameter. In chapter 4, machine learning is used to develop a semi-automatic method of facilitating optimal brainstem co-registration. An improvement over conventional methods in the accuracy of brainstem co-registration is demonstrated.

Chapter 5 investigates the amplitude of low-frequency fluctuations (ALFF) in resting state functional MRI in the brainstem and other parts of the central autonomic network. ALFF

is a non-specific marker of neurovascular function in the brain and has been proposed as a possible surrogate index of CVR. Data from the UK Biobank repository are analysed to investigate for variations in ALFF that would raise the possibility of regional differences in CVR between hypertensives and normotensives. There is no statistically significant difference in the regional variation in ALFF between hypertensives and normotensives. This led to an investigation of the validity of ALFF as an index of CVR in chapter 6. ALFF at various bandpass frequencies is correlated with conventional MRI methods of measuring CVR (ASL CVR and BOLD CVR). The within-subject distribution of ALFF is also investigated to determine whether ALFF maps accurately represent the spatial distribution of CVR, an important consideration if ALFF is to be useful as a clinical tool within individual patients. No statistically significant correlation between ALFF and ASL or BOLD CVR was found, and therefore no evidence to support the use of ALFF as a specific metric of CVR was demonstrated.

Chapter 7 involves the development of methods to probe the structure and function of the locus coeruleus, a pontine nucleus that has many functions, and that has extensive projections throughout the CNS including to parasympathetic and sympathetic centres in the brainstem and spinal cord, as well as throughout the cerebral hemispheres (Sara 2009). The feasibility of using a magnetisation transfer (MT) weighted sequence to generate individual LC localisers for each participant and their application to generate functional connectivity maps of the LC is successfully demonstrated. Efforts are made to determine whether accurate and reproducible measurements of LC contrast and volume are possible at an individual level. This was not possible using the MT-weighted acquisition used in this study. The feasibility of eliciting a measurable change in various functional parameters in the LC, in response to the application of a noradrenergic antagonist sedative, dexmedetomidine, is also studied, but no significant difference in functional connectivity pre- and post-sedation was demonstrated in this small pilot study population.

Finally, chapter 8 is an overview of the main results and outcomes of the thesis. The potential future applications of the methods developed here are discussed, including a proposed study of CVR in a hypertensive cohort.

1.1. MRI physics

1.1.1. Nuclear magnetic resonance (NMR)

Magnetic resonance imaging (MRI) exploits the fundamental electromagnetic properties of atomic nuclei within biological tissues to form images. Elementary particles possess a fundamental physical property known as spin, which is analogous to the angular momentum of macroscopic objects, although the elementary particle is not actually rotating. Rather, spin is an intrinsic property of the particle (Buxton 2013). Spin is quantised into integer and half-integer values. Particles with non-zero spin undergo nuclear magnetic resonance and can be studied using MRI. Protons, neutrons, and electrons all have spin ½. The nucleus of the most common isotope of hydrogen (hydrogen-1 or ^{1}H) contains a single proton, and therefore has spin ½. Hydrogen is the most abundant element in the human body and is therefore the nucleus that is of principal interest in MRI.

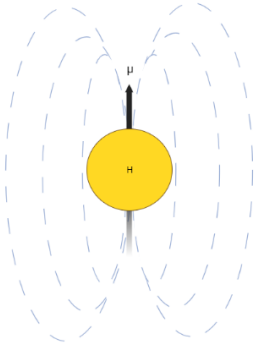

Figure 1.1: Representation of a hydrogen nucleus as a magnetic dipole with magnetic dipole moment μ, together with its corresponding magnetic field.

From the perspective of the classical view of physics the hydrogen nucleus behaves like a spinning ball of uniformly distributed charge. It therefore possesses a magnetic dipole moment (see figure 1.1). The dipole moment μ is directly proportional to the spin angular momentum S:

$$\mu = \gamma S \qquad (1.1)$$

where γ is the gyromagnetic ratio, a constant that varies according to the nucleus.

In the absence of a magnetic field a population of spins will all point in different directions, with a spherical distribution and no overall net magnetisation (Buxton 2013). If a magnetic field, B_0, is applied, the overall distribution of the orientation of the spins remains spherical due to their thermal energy, but the spins will now demonstrate a slight tendency to point in the same direction as B_0 (Hanson 2008). A net magnetisation vector, M_0, is therefore established, aligned parallel to B_0.

B_0 also exerts a torque on the spins, causing them to precess in a circular motion around the axis of B_0. The precession frequency is defined by the Larmor frequency:

$$\omega_0 = \gamma B_0. \qquad (1.2)$$

The precessing nuclei exchange energy via emission and absorption of radiofrequency waves at the Larmor frequency. In MRI, a transmission coil is used to apply energy to the system causing M_0 to rotate away from its alignment with B_0. M_0 is rotated (or 'flipped') by applying an oscillating magnetic field, B_1, in the form of a radiofrequency pulse at the Larmor frequency. According to Faraday's law of induction, a time-varying magnetic field induces a current in a loop of wire placed within it. 'Receive' coils are positioned near the object that is being imaged, and the rotating magnetisation M_0 induces a current in these coils. This is the MRI signal which is processed to ultimately form an image (Chappell 2017).

M_0 is proportional to both B_0 and to the number of spins in the system. In the presence of the Earth's relatively weak magnetic field, M_0 is small. Most MRI scanners use a superconducting coil to generate a magnetic field, B_0, that is thousands of times stronger than the Earth's magnetic field. M_0 is commensurately increased and can subsequently be exploited to form an image using the processes discussed below (Chappell 2017).

1.1.2. Relaxation

After a B_1 field has been applied and M_0 has rotated away from alignment with B_0, the nuclear spins will immediately begin to return to their equilibrium states via a process known as relaxation. There are two main relaxation time constants, T1 and T2, which are pertinent to this process.

T1 describes the return to equilibrium of the longitudinal component of M_0 (along the z-axis, in the direction of B_0) and T2 describes the decay of the transverse component of M_0 (in the transverse x-y plane, perpendicular to B_0). T1 relaxation is driven by thermal collisions and electromagnetic interactions between nearby atoms. The main mechanism which underlies T1 relaxation is dipole-dipole interactions (interactions between the magnetic fields of two adjacent spins). T2 relaxation describes the dephasing of groups of spins in the transverse plane as they experience different time-varying magnetic fields. In an idealised system, T2 relaxation is also driven by the same processes as T1 relaxation. In the real world, magnetic field inhomogeneities also contribute to the decay of the transverse component of M_0. Magnetically susceptible substances such as haemosiderin induce local magnetic field inhomogeneities which modulate the precession frequency of nearby nuclear spins. This leads to a loss of phase coherence between nuclear spins, which accelerates the decay of the transverse component of M_0. Relaxation via these additional extrinsic mechanisms is known as T2* relaxation (Buxton 2013), (Chappell 2017).

The Bloch equations are a set of differential equations that model the ensemble behaviour of the magnetization of a group of magnetic dipoles. These equations describe the precession and relaxation properties of the nuclei when they are placed in a magnetic field. They can be simplified by moving into a frame of reference that is rotating at the frequency of the oscillating B_1 magnetic field (ω). The Bloch equations (equations 1.3-1.5) describe the movement of M_0 as it spirals up from the transverse plane back to its equilibrium alignment with B_0 (Buxton 2013).

$$\frac{dM_x}{dt} = \gamma B_0 M_y - \frac{M_x}{T_2} \quad (1.3)$$

$$\frac{dM_y}{dt} = -\gamma B_0 M_x - \frac{M_y}{T_2} \quad (1.4)$$

$$\frac{dM_z}{dt} = -\frac{M_z - M_0}{T_1} \quad (1.5)$$

1.1.3. Spatial encoding

Information about the spatial origin of the signal can be imparted through the application of spatially varying magnetic fields or *gradients*. Traditionally, cartesian coordinates are used in MRI scanning. A traditional 2D pulse sequence acquires one slice of the image at a time. Prior to application of the B_1 radiofrequency pulse a magnetic field gradient is applied parallel to B_0. Only the spins that are precessing at a frequency that is resonant with B_1will be rotated. In this way it is possible to image one slice at a time. The imaging volume can therefore be acquired one slice at a time (figure 1.2) by applying a frequency encoding magnetic field gradient along the z-axis (Chappell 2017).

The in-plane spatial location of the signal is normally determined by using frequency and phase encoding. After slice selection has been performed, each spin within that slice precesses at its local Larmor frequency ω_0 given by equation 1.2. In-plane spatial encoding involves applying additional magnetic field gradients, ΔB, along each of the in-plane imaging axes to modulate the precession frequency of the nuclear spins. The Larmor frequency of each spin is then a function of its spatial position:

$$\omega_x = \gamma(B_0 + \frac{dB_z}{dx}.x). \qquad (1.6)$$

where x is the position of each spin on the x-axis. This process, known as frequency encoding, enables the spatial location of each spin along one of the in-plane axes to be determined (Buxton 2013).

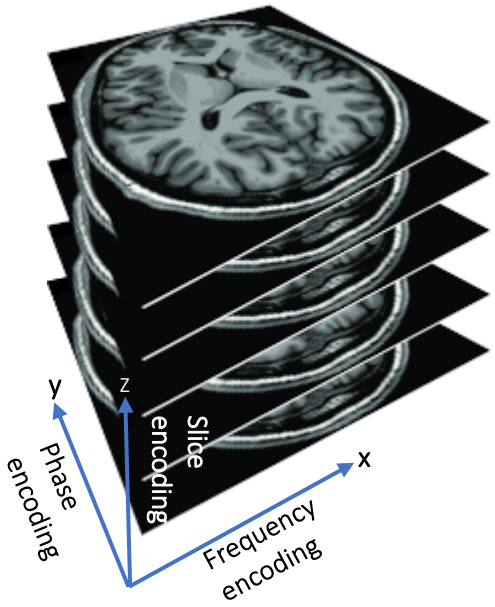

Figure 1.2: In 2D-MRI, a field gradient is applied along the z-axis, the resonant frequency of the spins then varies as a function of z, and the spins are excited one slice at a time. Within each slice, the spatial location of the spins is subsequently encoded by applying frequency and phase encoding gradients.

It is not possible to assign a unique precession frequency to every pixel in the x-y imaging plane using frequency encoding alone. In the presence of a single in-plane field gradient, there will always be more than one pixel that possesses the same frequency, and therefore their spatial locations cannot be separated. To overcome this, the third spatial axis is encoded via phase encoding. This involves the application of a brief magnetic field gradient which induces a temporary change in the precession frequency of each spin. The change in precession frequency is a function of the spin's spatial location along the gradient direction. After the field gradient is removed, the spins will return to precessing at the Larmor frequency. However, they will have acquired a phase shift, the magnitude of which is proportional to their position along the phase encoding axis. Therefore, their spatial location along the phase encoding axis can be determined (Buxton 2013).

By combining the information from both frequency and phase encoding, each slice can be divided into a 2D matrix of voxels to form an image.

1.1.4. Pulse sequences

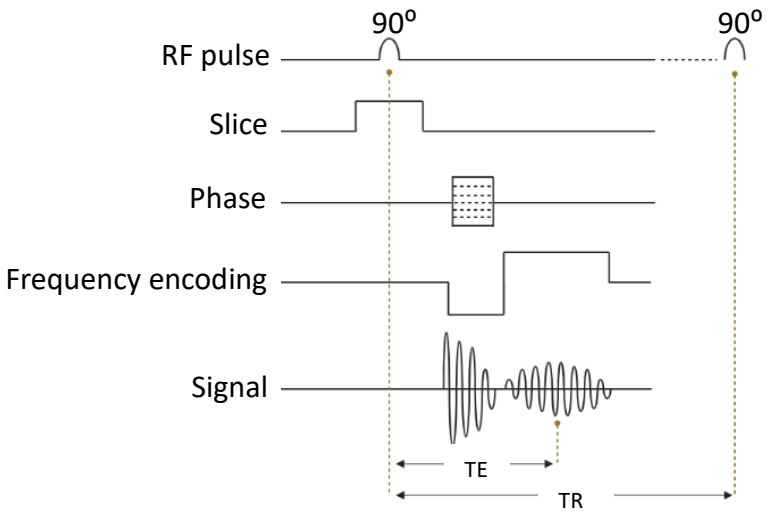

Figure 1.3: Schematic of gradient echo pulse sequence. 90° RF pulse applied whilst slice encoding gradient is applied along z-axis. Signal is phase-encoded along x-axis. Signal is initially dephased along frequency encoding axis before being brought back into phase by an opposing gradient during readout.

The basic steps involved in acquiring an MRI signal are outlined in figures 1.3 and 1.5. First, a RF pulse (B_1) is applied which rotates the spins and establishes a component of M_0 into the x-y plane, which precesses around the B_0 axis. When the B_1 field is removed, the nuclear spins begin to lose phase coherence due to local magnetic field inhomogeneities (T2* relaxation), and the transverse component of M_0 starts to decay. This precessing transverse component of M_0 induces a current in the receive coil. This signal is known as a free induction decay (FID) (Buxton 2013).

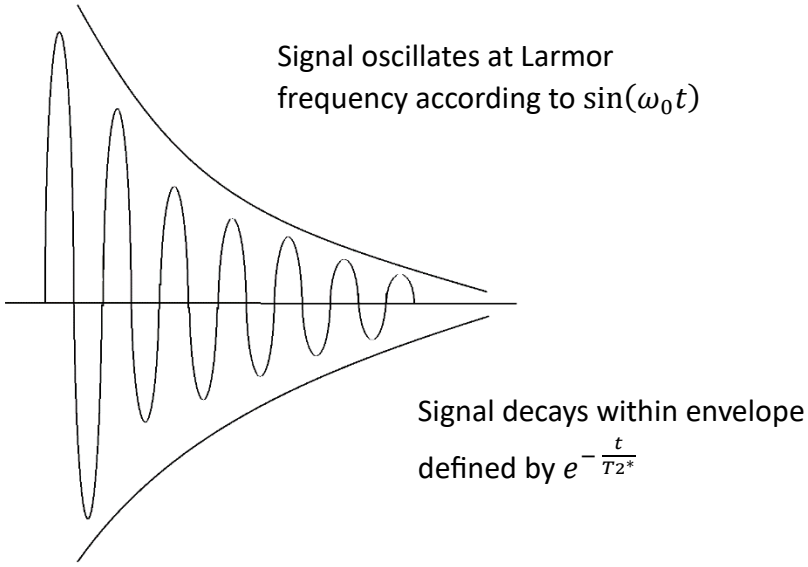

Figure 1.4: Example of free induction decay.

One of the most basic MRI pulse sequences involves the subsequent sequential application of two magnetic field gradients along the x-axis, which are equal in amplitude and duration but opposite in direction. The initial gradient accelerates phase dispersion. The second gradient then bring the spins back into phase, forming the free induction decay signal. When the spins are all back in phase, the FID reaches its maximum amplitude. The time at which this occurs is the echo time (TE). This pulse sequence is known as a gradient echo sequence (GRE) and is the basis of many MRI pulse sequences.

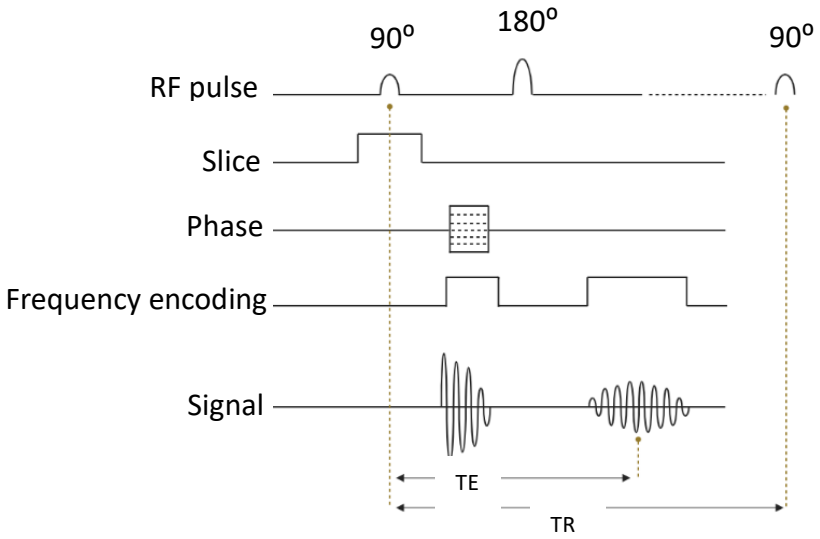

Figure 1.5 Schematic of spin echo pulse sequence. 90° RF pulse applied whilst slice encoding graident is applied along z-axis. Signal is phase-encoded along x-axis. 180° RF pulse at TE/2 refocuses the dephased FID.

Also commonly used in MRI is the spin-echo pulse sequence (Hahn 1950). After the initial 90° RF pulse, spins exposed to slightly higher magnetic fields precess faster and therefore gain phase relative to spins exposed to weaker fields. A short time (defined by TE/2) later, an additional RF pulse is applied which rotates the spins, and therefore M_0, by 180°. The spins exposed to stronger fields now have a phase deficit compared to those in weaker fields. Spins in stronger fields begin to regain phase coherence with those in weaker fields, and at time TE, all spins are once again in phase (Chappell 2017).

The echo can be thought of as the sum of multiple periodic functions, the frequencies of which correspond to the spatial location of the signal. The free induction decay signal, centred on TE, is detected by the receive coils which surround the imaging volume, and is processed to form an image. Multiple repetitions of the MRI sequence are performed with various phase encoding gradients to acquire enough information to decode the spatial position of each signal component. The time between each repetition is defined by the repetition time (TR).

Using the Block equations, the signal intensity, S, for any pulse sequence can be derived as a function of T1, T2, TR, TE and M_0. For example, for a spin-echo pulse sequence the signal can be represented as

$$S = M_0\, e^{-TE/T2}\,(1 - 2e^{-(TR-TE/2)/T1} + e^{-TR/T1}). \qquad (1.7)$$

The contrast between different tissues can be derived from such equations (Buxton 2013).

1.1.5. K-space

According to the Fourier theorem, any image can be decomposed into a series of plane waves of various amplitudes, frequencies, and phases. Similarly, a periodic function such as the free induction decay can be expressed as a sum of sine and cosine waves. The FID can therefore be decomposed into multiple periodic functions of various amplitudes, frequencies, and phases. The FID is repeatedly sampled, with various frequency and phase-encoding gradients applied, and the data stored as a spatial frequency distribution of the MRI signal. This is the so-called k-space representation of the data. Every point in k-space contains information about the spatial frequency and phase of the final MR image. The MRI image is formed by applying a Fourier transform to the k-space data (Buxton 2013).

K-space is traditionally filled row-by-row from right to left with each row corresponding to a different phase-encoding step. The centre of each row corresponds to the centre of the echo at TE and contains the highest amplitude information. The top and bottom rows correspond to high-order phase encode steps, whereas the middle rows correspond to low-order phase-encode steps. The amplitude of the signal corresponding to the middle row is therefore greatest. Consequently, the periphery of k-space corresponds to high spatial frequencies (representing edges and fine detail), and the centre corresponds to low spatial frequencies (representing amplitude and contrast) (Elster 2022).

Most MRI sequences step through k-space using cartesian coordinates. K-space can also be sampled using a spiral trajectory which is less sensitive to motion (Chang 2017), an important consideration when imaging the brainstem, which is especially susceptible to cardiorespiratory motion. Spiral readouts have also been demonstrated to improve the signal-to-noise ratio (SNR) because they preferentially sample the centre of k-space which contains the majority of the signal amplitude (Elster 2022).

Turbo spin-echo is an extension of conventional spin-echo. In conventional spin-echo, the initial 90^{o} RF pulse is followed by a 180^{o} pulse then a single line of k-space is filled by the phase-encoded echo. In turbo spin-echo, another 180^{o} pulse is applied after the initial echo is

read, then a different phase encoding gradient applied, and a second line of k-space is filled. Multiple further lines of k-space can be filled within a single TR in a similar way, limited by the decay of the transverse magnetisation due to T2 relaxation. The number of echoes sampled in a single TR is known as the echo train length (ETL). Turbo-spin echo reduces imaging time and reduces susceptibility related signal decay and artefacts. (Elster 2022).

Echo planar imaging (EPI) is a rapid spin or gradient-echo technique that is similar in principle to turbo-spin echo, but uses rapid gradient switching to step through k-space and sample as much as an entire slice in a single TR. EPI enables very rapid image acquisition and is commonly used in functional MRI where rapid imaging enables physiological changes to be studied (Buxton 2013). This comes at a cost of sensitivity to inhomogeneities in the main magnetic field, image distortion and signal drop out.

Both EPI and spiral acquisitions can be performed using multiple shots, which involves filling k-space over multiple TRs. This reduces readout time, reducing distortion, and potentially improves SNR because more acquisitions are performed, but at the risk of introducing more artefacts due to bulk-head motion between shots (Elster 2022).

1.1.6. Image contrast

Image contrast can be modified by varying TR and TE. As previously mentioned, different tissues have differing relaxation time constants. For example, fat has short T1 and T2 values, and water has long T1 and T2 values. If TR is short, M_0 from tissues with long T1, such as water, will not have sufficient time to re-establish in the longitudinal direction before the next 90^o RF pulse is applied. On the other hand, the longitudinal M_0 of tissues with short T1, such as fat, will be re-established. Therefore, fat appears as high signal and water as low signal on T1-weighted images. Contrast differentiation between tissues with differing T2 values can be achieved with a long TR and long TE. A long TR enables the longitudinal magnetisation of all tissues to re-establish between TR intervals, minimising T1-weighting. A long TE allows time for signal from tissues with short T2 values to decay relative to signal from tissues with longer T2 values. Water is therefore brighter than fat on T2-weighted imaging. In reality, multiple factors contribute concurrently to the contrast differences, including T1 and T2 relaxation as well as proton density, susceptibility effects and flow (tissue motion).

1.1.7. Parallel imaging

Parallel imaging involves the use of an array of receive coils to detect the MRI signal. Each element in the array is sensitive to signal originating from parts of the brain near to it. SNR can therefore be improved by combining information from each of the elements when forming an image. Information about the spatial location of each element can be used to spatially encode the data. The number of phase-encoding steps can therefore be reduced by a factor of R, where R is the acceleration factor. This subsequently reduces image acquisition time by a factor of R and suppresses susceptibility artefacts related to phase-related distortions. The penalty for this is a reduction in SNR of approximately $\sqrt{R}$, and the potential introduction of artefacts due to aliasing if the data is under sampled (Elster 2022), (Deshmane 2012).

1.2. BOLD fMRI

Since its inception in the early 1990s (Buxton 2013), blood oxygen level dependent (BOLD) fMRI has become the predominant MRI method of interrogating neural activity in the brain. Other non-invasive functional neuroimaging techniques such as electroencephalography (EEG) and magnetoencephalography (MEG) have a higher temporal resolution than BOLD. However, they are predominantly sensitive to cortical activity and have a low spatial resolution. BOLD can be used to probe whole-brain neural activity with a sub-millimetre resolution.

BOLD fMRI is based on localised temporal variations in the MRI signal which occur as a result of changes in local concentrations of deoxyhaemoglobin in brain tissue. Oxygenated haemoglobin in the arterial circulation is diamagnetic. Conversely, deoxyhaemoglobin, found in higher concentrations on the venous side of the circulation, is paramagnetic and induces local static magnetic field inhomogeneities which lead to accelerated MRI signal decay caused by a loss of phase coherence through T2* relaxation. The decay rate of the transverse magnetisation is denoted $R2^*$ and is the inverse of T2:

$$R2^* = \frac{1}{T2^*}. \qquad (1.8)$$

$R2^*$ can be separated into a component that depends on the concentration of deoxyhaemoglobin in the blood ($R2^*(dHb)$), and a component that represents the transverse decay rate in the absence of haemoglobin ($R2^*(0)$):

$$R2^* = R2^*(0) + R2^*(dHb). \quad (1.9)$$

Fluctuations in $R2^*(dHb)$ lead to measurable fluctuations in the BOLD signal, S, which in its simplest form can be represented by equation 1.10:

$$S = S_0 e^{-TE.R2^*}. \quad (1.10)$$

Where S_0 is the intrinsic local signal in the absence of signal decay. $R2^*$ can be modelled as a function of the local deoxyhaemoglobin concentration and blood volume:

$$R2^*(dHb) = kV[dHb]^{\beta}. \quad (1.11)$$

Where *k* is a proportionality constant that depends on the magnetic field strength, *V* is the blood volume, *[dHb]* is the concentration of deoxyhaemoglobin and β captures the added complexity of the effect of diffusion of water molecules through magnetic field gradients around small blood vessels, and the signal changes that arises from fluctuations in overall intravascular blood volume.

Increased neuronal activity leads to increased cerebral blood flow (CBF) in the local capillary network via a process known as neurovascular coupling (Phillips 2016). The fractional increase in CBF is higher than the fractional increase in the cerebral metabolic rate of oxygen ($CMRO_2$), and therefore, somewhat counterintuitively, the oxygen extraction fraction (OEF) from the arterial circulation is lower in regions of higher metabolic activity than in less metabolically active regions. Therefore, in metabolically active regions, the relative concentration of deoxyhaemoglobin is lower, the transverse decay rate $R2^*$ is reduced, and the MRI signal is increased (Buxton 2013), normally marking an increase in neuronal activity.

Fluctuations in blood volume and haemoglobin concentration lead to fluctuations in $R2^*$ which can be written as:

$$\Delta R2^* = k(V[dHb]^{\beta} - V_0[dHb]_0^{\beta}). \quad (1.12)$$

If dHb and V are normalised against their baseline values (dHb_0 and V_0, respectively), this can be rewritten as:

$$\Delta R2^* = kV_0[dHb]_0^{\beta}(vc^{\beta} - 1). \quad (1.13)$$

where $v = V/V_0$ and $c = [dHb]/[dHb]_0$. If the rate of oxygen consumption, $CMRO_2$, is assumed to be equal to the rate of oxygen delivery to the brain tissue, then:

$$CMRO_2 = E.CBF.[O_2]_{art}. \quad (1.14)$$

Where *E* is the oxygen extraction fraction and $[O_2]_{art}$ is the arterial concentration of oxygen. If the assumption is made that arterial haemoglobin is fully saturated, the BOLD signal can be written as:

$$\frac{\Delta S}{S_0} = M\left[1 - v\left(\frac{m}{f}\right)^{\beta}\right]. \quad (1.15)$$

where m and f are the normalised $CMRO_2$ and CBF values, respectively, and $M = k.TE.V_0.(E_0[dHb])^{\beta}$. From equation 1.15, it is evident that the magnitude of the BOLD signal is a function of several parameters including the magnetic field strength, echo time, baseline blood volume, baseline oxygen extraction fraction and baseline haemoglobin concentration through M, and to the normalised fluctuations in blood volume v, cerebral blood flow f and $CMRO_2$ m. M represents the maximum possible signal change in response to a stimulus. For example, if there was a such a large increase in CBF that no deoxyhaemoglobin remained in a voxel, equation 1.15 would reduce to $\frac{\Delta S}{S_0} = M$. Furthermore, M scales the BOLD signal response, such that the same changes in CBF, CBV and $CMRO_2$ can lead to different magnitudes of BOLD signal response if any of the parameters contained in M vary. For example, haematrocrit may vary between participants, leading to a different magnitude of

the BOLD signal response even if the same stimulus is applied. A full derivation of equation 1.15 can be found in Buxton (Buxton 2013).

The BOLD signal Is therefore governed by the haemodynamic response to changes In cerebral metabolism. It is not a direct measure of neuronal activity. Fluctuations in regional neuronal activity can be inferred from the BOLD signal response because neuronal activity is coupled to the haemodynamic response via several mechanisms (Phillips 2016). Neuronal activity requires energy, and it is currently thought that most of the energy demands of neurons is related to replenishment of postsynaptic neurotransmitters after neuronal firing (Buxton 2013). Ultimately, the BOLD signal is more closely correlated with the relatively slowly fluctuating local field potential that represents the electrophysiological changes in groups of neurons, rather than the action potentials of individual neurons (Logothetis 2002).

Changes in CBF, $CMRO_2$ and CBV all lead to a change in BOLD signal, and the interaction between these factors is complex. As demonstrated by equation 1.15, in isolation an increase in CBF tends to increase BOLD signal, whilst an isolated increase in $CMRO_2$ or CBV decreases BOLD signal (Buxton 2013). Vasoactive stimuli induce changes in BOLD signal independent of neuronal stimuli (Davis 1998). Studies which have compared the effect of vasoactive and neuronal stimuli have shown that the BOLD response to a purely neuronal stimulus is blunted compared to the response to a vasoactive stimulus (Buxton 2013), (Davis 1998). This is consistent with the opposing effects of increased CBF and increased $CMRO_2$ on the BOLD signal. This is pertinent to our attempt to use BOLD with a hypercapnic challenge to measure cerebrovascular reactivity, especially in the medulla where the respiratory control centres of the brainstem are located, as discussed below.

A further limitation to BOLD is that the magnitude of the BOLD response is limited by the baseline physiology of the participant. For example, regional differences in deoxyhaemoglobin concentration can influence the BOLD signal response independently of changes in $CMRO_2$. Caffeine restricts CBF and might therefore limit the CBF response, and therefore the BOLD response, to changes in $CMRO_2$ (Buxton 2013).

Finally, it is changes in deoxyhaemoglobin concentration in the venous side of the cerebral circulation which leads to BOLD signal change. Therefore, whilst BOLD can be used to index changes in CBF, it is non-quantitative and physiologically non-specific.

1.2.1. BOLD data processing methods

BOLD fMRI experimental design usually involves presenting a series of stimuli to the participant, interspersed with rest periods, and measuring the MRI signal change in response to these stimuli. This usually involves a block design (figure 1.6). The BOLD signal response does not conform exactly to the shape of the stimulus paradigm because, as previously discussed, the origin of the BOLD signal is multifactorial. The BOLD signal response is therefore represented by a haemodynamic response function that models the multifactorial nature of the BOLD signal. The haemodynamic response to a stimulus is not immediate due to the relatively slow CBF response to an increase in metabolic demand. A haemodynamic response function (HRF) is therefore used to model the delay and blurring of the BOLD response. The BOLD signal response is modelled using a general linear model (GLM) by convolving an appropriate haemodynamic response function with the experimental design paradigm. Voxelwise statistical analysis can be performed using a variety of analysis tools such as FSL (Woolrich 2009) and AFNI (Cox 1996), which compares the magnitude of the HRF to the random fluctuations in the BOLD signal that are induced by sources such as thermal and physiological noise, participant motion and scanner drift.

The BOLD response, Y, to m different stimuli can be modelled as the sum of the signal response, x_i, to each stimulus, s_i, weighted by the magnitude of each signal response, β_i;

$$Y = \beta_i x_i + \cdots + \beta_m x_m + \varepsilon. \qquad (1.16)$$

The variable ε represents the random variance in the signal introduced by physiological and thermal noise. The signal response $x_i$is the convolution of the stimulus function and the haemodynamic response function.

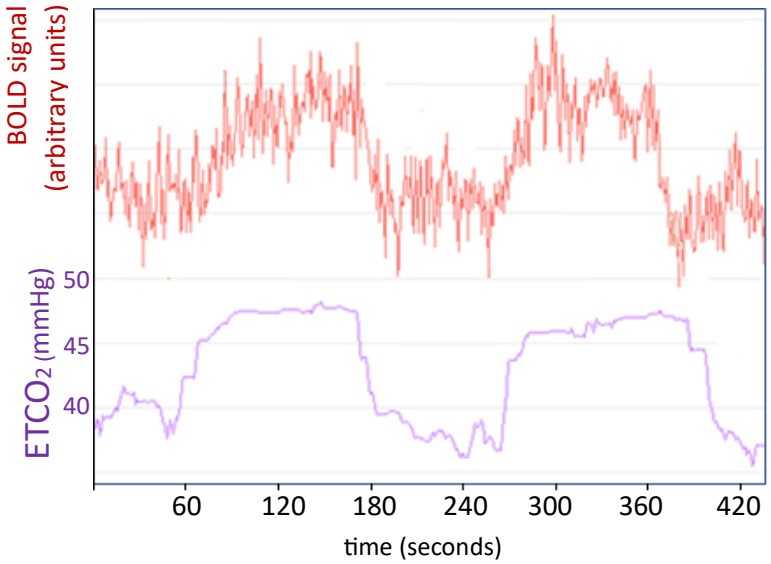

Figure 1.6: Block design – mean grey matter timeseries from a BOLD fMRI acquisition (red) demonstrates the BOLD signal response to variations in $ETCO_2$ trace (purple), induced via CO_2 administration. Paradigm involves 2 x 2 minute periods of hypercapnia, separated by 90 second period of normocapnia.

In its simplest format, a GLM can be applied to model the BOLD signal response to a single independent variable. For example, a GLM can be applied to BOLD data that has been acquired with a hypercapnic stimulus to derive measurements of CVR:

$$BOLD\ signal = \beta_1 \cdot ETCO_2 + \varepsilon. \quad (1.17)$$

The output of the GLM is a whole-brain map of the statistical parameter β_1, which represents the unit change in BOLD signal per unit change in end-tidal CO_2 ($ETCO_2$). These parameter maps can be converted to global maps of CVR, as discussed in chapter 2.

More complex GLMs can also be applied to model the signal response to multiple independent variables. For example, the model may comprise of a sensory stimulus, a motor stimulus, and a blood pressure response:

$$BOLD\ signal = \beta_1 \cdot sensory + \beta_2 \cdot motor + \beta_3 \cdot blood\ pressure + \varepsilon. \quad (1.18)$$

This model is applied independently to each voxel in the fMRI data. The resulting magnitude of the parameter estimate within each voxel reflects how well the model fits the

data in that voxel. The parameter estimates can be converted into test statistics by dividing the value of the parameter estimate by the uncertainty. It is then possible to determine which, if any, component of the model has a statistically significant fit to the data within each voxel.

It is also possible to compare the magnitude of the signal response to one independent variable compared to another. For example, the magnitude of the signal response to blood pressure relative to the response to the motor stimulus can be compared by subtracting the two parameter estimates β_2 and β_3, then converting the output into a map of test statistics.

1.3. Arterial spin labelling

Whilst BOLD can be used to measure CVR, a more specific method of measuring CBF is available in the form of arterial spin labelling (Buxton 2013). This involves magnetically 'labelling' a bolus of intravascular blood, which then travels into the tissue of interest enabling an estimation of tissue perfusion to be made. Once blood has been labelled with an inversion pulse, after a short time delay (termed the post-label delay (PLD)) to allow it to travel to the brain parenchyma, a 'tag' image is acquired. A 'control' image is then acquired, identical to the 'tag' image in all respects apart from the absence of the labelled bolus. Subtraction of the 'tag' and 'control' images theoretically leaves only signal from inverted blood, which represents perfusion information.

The first step in ASL is to apply a labelling pulse. There are two main labelling techniques which are currently in use. Pseudo-continuous ASL (PCASL) involves the application of a train of radiofrequency (RF) pulses together with a magnetic field gradient (applied in the direction of blood flow). As blood flows along the field gradient, the precession frequency of hydrogen nuclei sweeps through resonance with the applied RF pulse. The magnetisation vector of this blood therefore undergoes adiabatic inversion. The alternate approach, pulsed ASL, involves the application of a single RF pulse to the labelling volume which almost instantaneously inverts the net magnetisation of the H-nuclei within that volume.

The SNR of PCASL is generally higher than PASL for two reasons (Alsop 2015). Firstly, PCASL generally labels a larger volume of blood more efficiently than PASL. Secondly, T1

relaxation of the labelled blood beings as soon as the blood leaves the labelling plane. PASL labels a slab of blood, whereas with PCASL blood is labelled as it flows through a relatively thin plane. Blood labelled at the inferior edge of the PASL slab will have further to travel, and will therefore undergo more T1 relaxation, than blood labelled at the superior edge of the slab. The PCASL plane is positioned at the superior edge of the PASL slab and therefore all PCASL labelled blood undergoes the same amount of T1 relaxation. The ISMRM Perfusion Study Group and the European Consortium for ASL in Dementia have published a summary of their recommendations of the implementation of ASL in clinical settings, and for the above reasons PCASL is their recommended labelling method (Alsop 2015).

The time it takes for blood to travel from the labelling plane to brain tissue is known as the arterial transit time (ATT). ATT varies across brain regions (labelled blood must travel further to some brain regions) (D. L. Thomas 2006). A PLD that is slightly longer than the longest ATT is recommended (Alsop 2015) so that most of the labelled blood has reached the cerebral microvasculature before the 'tag' image is acquired. If the PLD is too short, labelled blood might still reside within the large intracranial arteries, leading to arterial transit artefacts which can confound CBF measurements. The PLD needs to be long enough to allow the labelled blood bolus to perfuse into brain tissue. However, as the PLD increases beyond the ATT, although a larger fraction of the labelled bolus will have transitioned from the intravascular space to brain tissue, this is at the cost of further T1 relaxation of the labelled blood. The choice of PLD is therefore a compromise between maximising the tissue and microvascular components of the labelled blood whilst minimising the macrovascular component, as well as minimising T1 relaxation of the labelled blood.

ATT is likely to vary somewhat between individuals, due to variations in flow dynamics and vascular anatomy, or due to vascular pathology (Al-Bachari 2014). In fact, ATT might be useful as a surrogate marker of cerebrovascular function (MacIntosh 2012), (Alsop 2015). Ideally, PLD would be tailored to each individual participant according to their ATT. Multi-PLD ASL involves acquiring ASL data at multiple delay times. A kinetic model is then fit to the data. This allows an estimation of ATT to be made, as well as generating perfusion values. It is less sensitive to differences in ATT between different brain regions and between subjects (Johnston 2015). However, SNR is generally lower because fewer tag-control pairs can be acquired per unit time compared to single-PLD acquisitions (Alsop 2015). Sampling at short PLDs also risks the presence of residual macrovascular signal confounding perfusion

measurements. This is a particular concern in the brainstem which is in close vicinity to the vertebral and basilar arteries.

A variety of readout approaches are available for ASL. As discussed above, spiral readouts oversample the centre of k-space and are therefore less sensitive to motion. This is an especially important consideration in the brainstem, which is susceptible to motion from cardiac pulsation and CSF flow (Brooks 2013). The choice of readout is discussed further in chapter 2.

In order to derive quantitative perfusion values, a kinetic model which describes the evolution of the labelled bolus over time must be applied to the data. A general kinetic model describes the labelled bolus as a function of its rate of delivery f, together with an arterial input function $a(t)$ which describes the evolution of the bolus as it arrives in the brain, and a residue function $r(t)$ which describes the decay of the bolus after it has arrived in the brain (Chappell 2017), (Buxton 2013). The form of the arterial input function is dictated by the labelling scheme, and it essentially resembles a boxcar function:

$$a(t) = 2M_{0a} \qquad 0 \leq t < \tau, and\ 0\ otherwise. \tag{1.19}$$

where M_{0a} is the magnetisation of blood in the labelling plane and τ is the label duration.

One of the assumptions of the simple kinetic model is that none of the labelled bolus leaves the brain. This is justified by the fact that bolus decay due to T1 relaxation occurs much more quickly than the time it takes for blood to transit from the tissue to the capillary bed to the venous circulation (Chappell 2017). The residue function therefore takes the form of an exponential decay curve governed by the longitudinal relaxation time of labelled water once it has been delivered to the brain tissue, T1:

$$R(t) = e^{-t/T_1}. \tag{1.20}$$

The kinetic model then takes the form:

$$\Delta M = 0 \qquad t < 0. \tag{1.21}$$

$$\Delta M = 2M_{0a} f T_{1b}\left(1 - e^{-t/T_{1b}}\right) \qquad 0 \leq t < \tau. \tag{1.22}$$

$$\Delta M = 2M_{0a} f T_{1b} e^{-t/T_{1b}}\left(e^{\tau/T_{1b}} - 1\right) \qquad \tau \leq t. \tag{1.23}$$

where ΔM is the magnitude of the signal from the tag-control subtracted image and T_{1b} is the T1 of arterial blood. This kinetic model can then be converted to a form that provides us with quantitative values of CBF:

$$CBF = \frac{6000.\lambda.\Delta M.e^{PLD/T_{1b}}}{2\alpha T_{1b} M_{0a}\left(1-e^{\tau/T_{1b}}\right).} \tag{1.24}$$

where λ is the partition coefficient that relates the density of water in tissue to the density of water in blood and α is the labelling efficiency. Arterial spin labelling can therefore be used to acquire perfusion information, and together with the application of a kinetic model, absolute values of CBF. A full derivation of the above can be found in Chappel et al. (Chappell 2017).

1.3.1. Brainstem ASL

ASL has not previously been widely applied specifically to measure brainstem perfusion. Warnert et al. (Warnert 2014) used 3T multi-TI pASL to investigate the kinetic curve and brainstem arrival time of the labelled bolus. They also used the same sequence to quantify brainstem cerebrovascular reactivity to hypercapnia, demonstrating that ASL can be used to detect significant global brainstem perfusion differences between two physiological states.

Other studies have reported regional differences in brainstem perfusion, measured using ASL, following drug administration, but these studies did not report CBF values. Viviani et al. (Viviani 2012) demonstrated, for group-averaged data, regional perfusion differences in the brainstem by using 3T ASL to investigate cerebral perfusion in healthy volunteers

randomised to receive buproprion and sertraline in a double-blind, placebo-controlled crossover study. These regional differences occurred at the sites of noradrenergic and serotonergic nuclei, including in the locus coeruleus, that are thought to be affected by these drugs. In a separate study, Marquand et al. (Marquand 2012) used ASL with multi-variate pattern recognition to demonstrate differential effects of the drugs methylphenidate and atomoxetine on regional CBF at various locations throughout the brain, including the midbrain. These studies give further encouragement that 3T ASL may be able to detect regional perfusion differences in the brainstem.

1.4. Cerebrovascular reactivity

Cerebrovascular reactivity (CVR) represents the capacity of a cerebral blood vessel to increase cerebral blood flow, via a change in vessel calibre, in response to a vasoactive stimulus. Measurement of CVR provides information on the functional reserve of the vascular system and is an important marker of the health of the cerebrovascular system. Impaired CVR has been associated with many diseases, including stroke, transient ischaemic attack (TIA) (Markus 2002) and multiple sclerosis (Marshall 2014). CVR correlates with angiographic measures of disease severity both in atherosclerotic and Moyamoya patients (Donahue 2014) and could therefore serve as an adjunct to angiography in selecting patients for revascularisation therapy. Measurement of CVR could also help in the assessment of the rehabilitation potential of brain regions affected by ischaemic stroke (Krishnamurthy 2021). CVR could be useful as a marker of neurovascular reserve in a variety of cerebrovascular diseases. For example, CVR measurements correlate with cognitive performance in patients with mild cognitive decline (Richiardi 2015), (Kim 2021), with the severity of regional arterial stenosis in Moyamoya (Federau 2017), and with the severity of motor symptoms in Parkinson's disease (Pelizzari 2021).

The assessment of brainstem CVR could also be useful in pre-surgical planning when the neurovascular coupling that underpins the BOLD signal response is compromised by brain pathology. For example, Pillai et al. demonstrated that low-grade gliomas can have preserved cerebral blood flow but impaired CVR, thus impeding evaluation of functional activity adjacent to the tumour due to the resultant neurovascular uncoupling (Pillai 2011), (Pillai

2015). This additional knowledge on the state of the local vasculature may help determine the necessity of intra-operative functional mapping. BOLD-CVR has also been used intraoperatively to determine whether there has been an immediate improvement in cerebral haemodynamics following arterial bypass graft surgery (Muscas 2022). The same technique has also been applied to assess CVR following tumour resection, and areas of impaired CVR have been shown to correlate with tumour recurrence on subsequent post-operative contrast-enhanced T1-weighted scans (Muscas 2022).

CVR is a complex phenomenon, and its evaluation requires multiple integrated steps. Hypercapnia is routinely used as a vasoactive stimulus in MRI studies of CVR (Fisher 2016), (Whittaker 2016). When the arterial partial pressure of CO_2 ($PaCO_2$) increases, CO_2 diffuses across the blood brain barrier and reduces the pH of the interstitial compartment (Willie 2014), (Liu 2019). This is thought to cause hyper-polarisation of smooth muscle and endothelial cells, resulting in smooth muscle relaxation and an increase in the release of endothelial factors such as nitric oxide. The end result is vasodilation.

Hypercapnia is induced by asking participants to breath a gas mixture that contains an increased concentration of CO_2. This increased CO_2 concentration ($FiCO_2$) translates to an increase in $PaCO_2$. However, the magnitude of the increase in $PaCO_2$ does not directly reflect the $FiCO_2$ due to the variability in alveolar ventilation between participants (Fisher 2016). Direct measurement of $PaCO_2$ is not possible using non-invasive methods. End-tidal CO_2 ($ETCO_2$) is therefore used as a surrogate marker of $PaCO_2$ (Hemmati 2012). $ETCO_2$ has been demonstrated to correlate well with direct measurement of $PaCO_2$ via arterial blood gas sampling in mechanically ventilated patients (Razi 2012).

There are several methods of inducing hypercapnia used in research practice – some involve the administration of CO_2 to the participant either by targeting a fixed CO_2 concentration in the expired gas, or by administering a fixed concentration in the inspired gas (Liu 2019). Fixed inspired systems involve less user and participant preparation, but do not result in accurate control of participants' $ETCO_2$. Fixed expired systems such as the Respiract Gas Control System (Fisher 2016) enable better control of $ETCO_2$ but can be expensive as a feedback system to the gas control is needed and they require additional participant calibration which might move baseline CO_2 away from its true value. There may then be a degree of uncertainty over whether subsequent CVR measurements are representative of the physiological baseline (Liu 2019). There are also other methods of inducing hypercapnia that

do not involve gas administration including a breath hold and volitional hyperventilation. These methods are simpler and do not require specialist breathing circuitry, but neither enables close control of $ETCO_2$, and both are highly dependent on participant compliance.

The response to hypercapnia can be measured using one of several methods. Transcranial Doppler ultrasound measurement of the change in flow velocity of blood in the middle cerebral artery in response to hypercapnia has previously been used, but only measures CVR related to one specific vessel, and therefore one arterial territory (McDonnell 2013). Phase-contrast contrast MRI similarly only enables blood flow measurement on a regional macroscopic scale. BOLD and ASL can be used to obtain whole brain maps of CVR. BOLD is widely applied in a research context but the multifactorial nature of the BOLD signal, as discussed in section 1.2, adds another layer of uncertainty to the CVR measurement.

Whilst CBF can be measured directly using ASL, contrast-to-noise is typically lower than BOLD, and labelling efficiency and ATT in PCASL decrease as a result of the increased flow induced by hypercapnia, which may reduce the magnitude of the measured change in CVR (Liu 2019). However, ASL has the advantage of providing a quantitative measure of CBF in mL/100g tissue/minute.

White matter CVR has been shown to be significantly lower than that of grey matter The brainstem contains a mixture of grey and white matter. Brainstem perfusion and CVR values are therefore expected to be lower than cortical grey matter values due to the increased white-matter content of the brainstem (Thomas 2014). CVR may also increase, rather than decrease as is the case with grey matter, with age (Thomas 2014). Furthermore, brainstem medullary chemoreceptors are sensitive to CO_2, and therefore increased activity in these chemoreceptors during hypercapnia may confound medullary CVR measurements made using BOLD (Pattinson 2009). These factors must be taken into consideration when interpreting brainstem CVR measurements.

1.4.1. Hypercapnia and increased CBF in hypertensives – safety considerations

Hypercapnia has been safely used in many previous studies to induce changes in cerebral blood flow in hypertensives, some of which included patients with other comorbidities such as stroke (Hajjar 2010). CO_2 administration has been safely used in many

other studies of CVR (Warnert 2016), (Maeda 1994), (Wong 2011), (Settakis 2003). There is in fact evidence that hypercapnia may provide benefits, rather than risks, under certain conditions. Zhou et al. suggest mild to moderate hypercapnia ($PaCO_2$ 60-100 mmHg) is neuroprotective during recovery after transient cerebral ischaemia in rats (Zhou 2010).

1.5. Magnetisation transfer imaging

Magnetisation transfer (MT) imaging is used in chapter 7 of this thesis to image the locus coeruleus. The physical process of MT involves transfer of energy between ^{1}H-nuclei that are 'bound' within macromolecules or water molecules closely associated with the surface of macromolecules, and ^{1}H-nuclei within 'free' water. 'Bound' ^{1}H-nuclei have a broad range of resonant frequencies, whereas 'free' ^{1}H-nuclei can only be excited by RF pulses at or near the Larmor frequency. MT-imaging involves the application of an off-resonance RF pulse that excites ^{1}H-nuclei in the 'bound' compartment. Energy is then transferred to the 'free' compartment via dipole-dipole interactions. This saturates signal from the 'free' water compartment when the brain is subsequently imaged, increasing contrast between the 'bound' and 'free' compartments.

1.6. MRI of the brainstem – challenges

The brainstem serves as a conduit for ascending and descending nerve tracts between the cerebral cortex and the spinal cord. The majority of cranial nerve nuclei are located in the brainstem. The brainstem also contains several autonomic centres that control blood pressure, heart rate and respiration. It is therefore a critically important structure.

MRI of the brainstem is challenging for several reasons. The brainstem is a small structure with an average volume of about 34 mL (Luft 1999). It can be subdivided into three constituent areas from rostral to caudal – the midbrain, pons and medulla. The average diameter of the smallest of these subdivisions, the medulla, is 14 mm (Raininko 1994) but brainstem substructures may measure less than 1 mm in diameter. For example, the nucleus tractus solitarius is less than 1 mm in diameter, and the locus coeruleus 1-2 mm in diameter (Sclocco 2017). Achieving sufficient SNR and spatial resolution to detect signal within these nuclei is therefore difficult even with ultrahigh field MRI. This problem is compounded by

brainstem co-registration inaccuracies, addressed in chapter 4. Inaccurate co-registration of the order of a single voxel might make group-level analysis of functional activity in individual brainstem nuclei very difficult. The use of anatomical atlases or masks is also reliant on accurate co-registration. Even if signal can be accurately localised to a small nucleus within an individual participant, subtle variations in brainstem size or internal architecture between participants might mean that the nuclei are not aligned, even with good co-registration to a common anatomical space.

The brainstem is especially susceptible to physiological noise. The change in the volume and position of the lungs during respiration causes fluctuations in the static magnetic field B_0 (Raj 2000). This causes misregistration of MRI signal and subsequent anatomic distortion. This effect decreases with the cube of the distance from the lungs, and therefore the brainstem is disproportionately affected (Sclocco 2017). The caudal location of the brainstem places it near to the paranasal sinuses and mastoid air cells. The magnetic susceptibility-induced gradient in B_0 caused by the air content of these sinuses causes distortions and signal drop out (Glover 2001). The brainstem is also surrounded by cerebrospinal fluid in the basal cisterns, and therefore subject to movement due to CSF pulsation (Sweetman 2010). The vertebrobasilar arteries which supply the brainstem and the posterior cerebral circulation run along the ventral surface of the brainstem. Cardiovascular pulsation transmitted via these vessels also contributes to brainstem movement (Beissner 2015). Physiological noise is proportional to the square of the magnetic field strength. Therefore, whilst increasing the strength of B_0 might increase the ratio of signal to thermal noise and enable higher resolution imaging, the disproportionate increase in physiological noise might outweigh these benefits when it comes to high-field brainstem imaging (Brooks 2013). Spatial smoothing is a commonly used post-processing technique which can increase SNR. However, care must be taken when applying this to the brainstem to avoid mixing signal from extra-axial structures such as CSF and blood vessels with brainstem signal.

The brainstem has a caudal and central location, placing it away from the receive elements of typical MRI head coils and further compromising SNR. For the above reasons related to the small size and complex anatomy of the brainstem, on most MRI sequences the brainstem appears to be relatively homogeneous, without distinction between white-matter tracts and grey-matter nuclei. Anatomical identification of brainstem nuclei to aid functional localisation is therefore challenging, though techniques such as magnetisation transfer

imaging has been used to identify nuclei that contain paramagnetic substances like neuromelanin or iron (Liu 2017).

There are also challenges specific to the application of arterial spin labelling in the brainstem. The arterial arrival time of the labelled bolus might be shorter in the brainstem. The post-label delay therefore needs to be optimised to ensure that there is no significant macrovascular signal component compromising CBF measurements, especially considering the proximity of the vertebrobasilar arteries to the brainstem. Whilst the brainstem is anatomically closer to the labelling plane than cortical grey matter, white matter has a longer ATT than grey matter (Macintosh 2010). The shorter physical distance to the brainstem may therefore be offset by the increased amount of white matter it contains compared to cortex.

1.7. Functional neuroanatomy of the brainstem

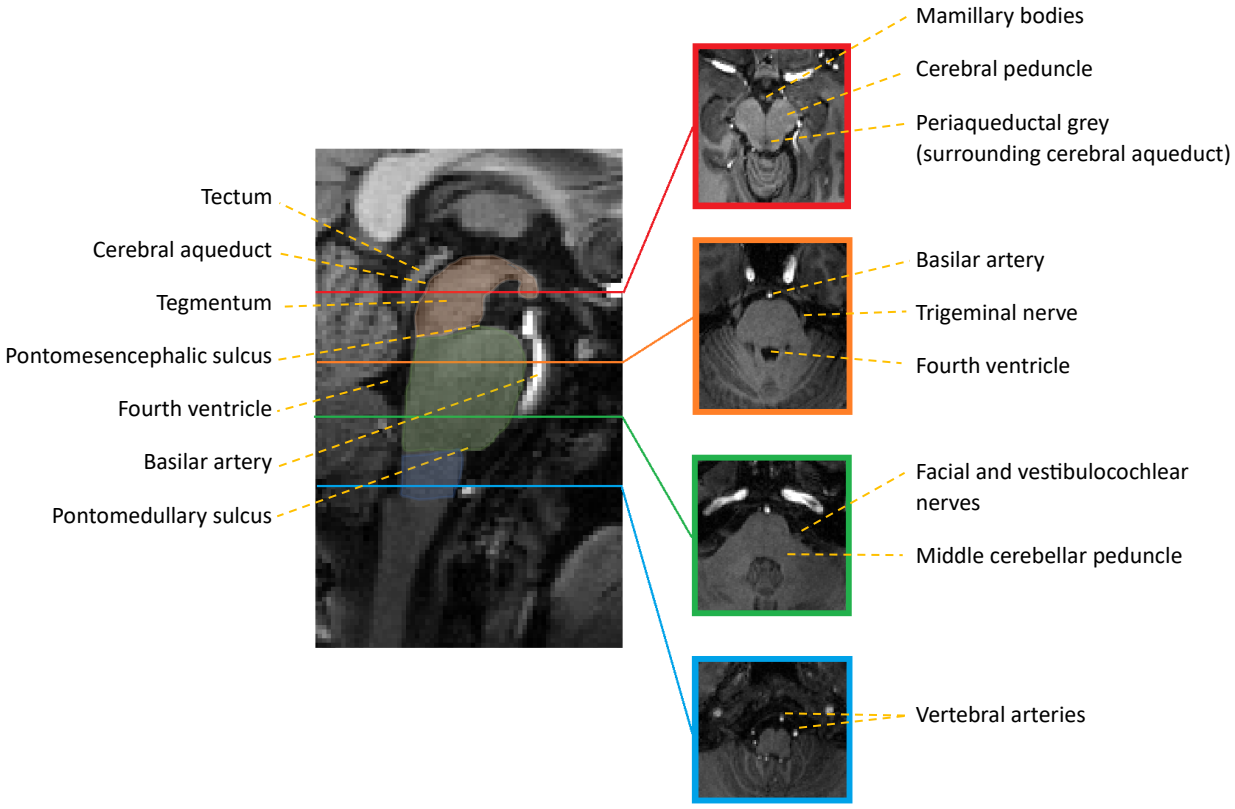

Figure 1.7: Brainstem anatomy outlined on T1 weighted mid-sagittal view (left). Midbrain (orange), pons (green) and medulla (blue). Selected axial cross-sections through the brainstem on the right.

The brainstem is a small structure consisting of three regions, the midbrain, pons and medulla (Luft 1999), (Naidich 2009), (Basinger 2022), (Shah 2019). The average diameter of

its smallest subdivision, the medulla, is 14 mm (Raininko 1994) and many brainstem nuclei measure less than 1 mm in diameter (Naidich 2009), (Basinger 2022), (Shah 2019). The cerebral aqueduct runs through the midbrain, connecting the third and fourth ventricles and separating the midbrain into the tectum dorsally, and the tegmentum and cerebral peduncles, which connect the midbrain to the cerebral hemispheres, ventrally. Notable structures within the midbrain include the substantia nigra (involved in reward and movement), the red nucleus (also involved in motor coordination), and the periaqueductal grey (involved in pain processing). Cranial nerves III and IV arise from the midbrain surface. The inferior boundary to the midbrain is defined by the pontomesencephalic sulcus (figure 1.7). Below this lies the pons, the largest subdivision of the brainstem. The ventral pons contains motor nuclei which communicate with the cerebellum via the middle cerebellar peduncle. Dorsally, the phylogenetically older tegmentum houses parts of the reticular formation (involved in arousal and wakefulness), including the locus coeruleus. The trigeminal nerve (cranial nerve V) arises from the pons. Cranial nerves VI, VII and VIII arise from the pontomedullary sulcus, which defines the boundary between the pons and medulla (figure 1.7). The most caudal subdivision of the brainstem, the medulla, merges with the spinal cord inferiorly. The pyramids, which contain motor fibres from the prefrontal cortex, decussate in the ventral medulla. Cranial nerves IX, X, XI and XII emerge from the surface of the medulla. The baroreceptor reflex is also mediated via the medulla, as discussed in section 1.12.1 below.

While the precise anatomy of the brainstem vasculature is somewhat variable (Akar 1994), arterial supply to the brainstem is via the vertebrobasilar arteries. The vertebral arteries originate from the subclavian arteries and extend superiorly through the neck, uniting on the ventral surface of the medulla to form the basilar artery. The basilar artery continues superiorly, running along the basilar groove on the surface of the pons until it bifurcates to form the posterior cerebral arteries at the circle of Willis. Several smaller arteries emerge from the vertebrobasilar system to supply the brainstem. These can be classified as anteromedial, anterolateral, lateral and posterior groups according to their penetration into the brainstem. The medulla receives its supply predominantly from the vertebral arteries via the anterior and posterior spinal arteries and anterior and posterior inferior cerebellar arteries. The precise anatomy of these vessels is somewhat variable (Akar 1994) but ultimately the majority of arterial supply to the brainstem is from the vertebrobasilar system.

1.8. Hypertension

Arterial blood pressure in the population is normally distributed and there is no definite level of transition between normal and high blood pressure (Warnert 2016). Each incremental increase in blood pressure leads to a corresponding increase in the risk of associated diseases such as stroke, myocardial infarction, chronic kidney disease, cognitive decline and premature death (NICE 2011) Adequate control of blood pressure significantly reduces the risk of many of these diseases and of subsequent mortality (Ettehad 2016).

The threshold value for high blood pressure varies between different health organisations. A healthy individual's blood pressure fluctuates throughout the day as a result of multiple factors, such as exercise, stress and even posture. Therefore, a single blood pressure measurement may not accurately reflect an individual's basal blood pressure. The National Institute for Health and Clinical Excellence (NICE) recommends that hypertension is diagnosed based on serial, rather than a single, blood pressure measurement (NICE 2011). NICE defines stage 1 hypertension (the least severe of their three hypertension categories) as a clinic blood pressure of greater than 140/90 mmHg with subsequent mean home or ambulatory blood pressure monitoring value greater than 135/85 mmHg.

As of 2015, 874 million adults worldwide had a systolic blood pressure that met NICE's stage 1 hypertension threshold (NICE 2011). The cost of medications for the management of hypertension in the United Kingdom amounted to £1 billion in 2006 (NICE 2011). The Global Burden of Disease Study 2015 found that elevated systolic blood pressure was the leading global risk factor in the loss of healthy life years (Ettehad 2016). Hypertension is therefore clearly an important global health issue.

Despite the high prevalence and morbidity associated with hypertension, in the majority of cases the aetiology is poorly understood (Hart 2016). There is evidence of a heritable component, with some estimates of the heritability of hypertension at over 50% (Hart 2016). Genome-wide association studies have so far identified genetic variations that account for 3.5% of the variance in blood pressure (Oparil 2018). Hypertension where a definite pathophysiological cause has been identified is termed secondary hypertension. Whilst there are a multitude of causes of secondary hypertension, they account for only 5-

10% of the overall incidence of the disease (Chiong 2008). The remainder of cases, where no definite underlying cause can be identified, are termed essential hypertension.

As discussed below, the regulation of systemic blood pressure is complex and depends on an interplay between multiple organs and feedback pathways that maintain cardiovascular homeostasis. Multiple environmental and genetic factors may adversely influence one of or more of the many physiological systems that regulate blood pressure, thus causing hypertension. One such system is the sympathetic nervous system, and as discussed below hypertension is associated with an increase in sympathetic nerve activity (SNA) to the cardiovascular system. The selfish brain mechanism proposes that the increase in SNA is a reflex mechanism driven by an increase in sympathetic outflow from the central nervous system. This increase in SNA might be an attempt to maintain adequate cerebral blood flow in response an insult that is compromising CBF.

1.9. Autonomic regulation of the cardiovascular system

Human blood pressure regulation involves several interlinked physiological systems. Blood pressure must be maintained at a level that is high enough to enable blood flow to meet the metabolic demands of various tissues, without being so high as to cause damage to the cardiovascular system.

Blood pressure (BP) is fundamentally a function of cardiac output (CO) and peripheral vascular resistance (PR):

$$BP = CO\,x\,PR \tag{1.25}$$

Cardiac output (CO) is a measure of the volume of blood ejected by the heart per minute and is related to heart rate (HR) and stroke volume (SV) (the volume of blood ejected by the left ventricle in each contraction) by the equation:

$$CO = HR\,x\,SV \tag{1.26}$$

The principal factors that govern each of these variables and how they are interlinked will be considered in turn.

1.9.1. Heart rate

Periodic spontaneous depolarisation of the sino-atrial node causes the heart to beat with an intrinsic automaticity at a rate of approximately 100-110 beats per minute (Textor 2012). The principal modulator of sino-atrial nodal activity is the autonomic nervous system (Kashour 2021). The autonomic nervous system is comprised of two arms – sympathetic and parasympathetic. An increase in the activity of the parasympathetic arm reduces the heart rate, whereas an increase in sympathetic activity increases the heart rate.

Short term modulation of heart rate in response to blood pressure changes occurs via several feedback mechanisms. The baroreceptor reflex, which is mediated via the autonomic nervous system, involves stimulation of stretch receptors in the carotid sinus, sited at the bifurcation of the common carotid arteries. Afferent signals are conducted by the glossopharyngeal nerve to the medulla, where several physiological centres act to modulate the balance between sympathetic and parasympathetic output. Pressure sensitive receptors situated in the atria also act via the autonomic nervous system to influence heart rate (Achilles 2013).

Fluctuations in heart rate occur in response to respiration. During inspiration, intrathoracic pressure reduces, causing an increase in venous return to the heart, which stimulates atrial pressure receptors and reduces the heart rate. The opposite occurs during expiration. Additionally, central respiratory centres are coupled to the autonomic nervous system and modulate autonomic activity according to respiratory rate. Peripheral chemoreceptors, which are sensitive to substrates such as oxygen and carbon dioxide, may also modulate the heart rate either indirectly via changes in respiratory rate and depth, or directly via modulation of autonomic output from the medulla (Achilles 2013).

1.9.2. Stroke volume

There are multiple factors that influence stroke volume. The force of left ventricular contraction during systole increases in response to an increase in left ventricular end-diastolic pressure (preload), for example due to an increase in venous return to the heart (Achilles 2013). An increased preload stretches the cardiac myocytes and increases sarcomere length, thus increasing the force of systolic ventricular contraction and thus the stroke volume. This is known as the Frank-Starling mechanism.

The afterload on the heart is related to the pressure against which systolic left ventricular contraction occurs. A higher afterload reduces stroke volume. Factors such as an increase in peripheral resistance or aortic pressure increase afterload. Preload and afterload are intrinsically linked. For example, an increase in peripheral vascular resistance will increase both venous return to the heart (preload) and afterload.

Extrinsic factors may also modify the Frank-Starling mechanism. If the pressure against which left ventricular contraction ejects blood from the heart is increased (an increase in 'afterload'), stroke volume will be lower for a given preload. The autonomic nervous system also modulates the Frank-Starling mechanism. An increase in sympathetic activity to the heart has a positively inotropic effect (the force of ventricular contraction is increased) whereas the parasympathetic nervous system has the opposite effect.

1.9.3. Peripheral vascular resistance

Peripheral vascular resistance is regulated via a number of intrinsic and extrinsic mechanisms (Achilles 2013). Intrinsic mechanisms originate within the vessels and act at a local level to maintain a relatively constant blood flow to an organ across a range of blood pressures, and to redirect blood flow to organs according to their metabolic demands.

The myogenic response occurs when an increase in blood flow through a peripheral artery causes perfusion pressure to increase (Achilles 2013). This initially causes passive dilation of the vessel. Vascular smooth muscle contraction then reduces vessel diameter, returning flow to its initial value.

Peripheral vascular resistance also changes in response to the production of local metabolic factors. In a region of high metabolic activity, for example a working muscle, an increase in metabolic products such as carbon dioxide (CO_2) causes smooth muscle relaxation, arteriolar vasodilation, a reduction in peripheral resistance, and finally an increase in local blood flow. Increased shear stress on the endothelial lining of arteries in response to an increase in flow stimulates release of various chemical mediators, including nitric oxide (NO) from the endothelial cells. These mediators act on vascular smooth muscle, causing vasodilation or vasoconstriction that aids in the maintenance of blood supply according to metabolic requirements (Achilles 2013).

Extrinsic mechanisms originate outside the vessel and act systemically (Achilles 2013). These include the autonomic nervous system and circulating hormones. The autonomic nervous system is described in more detail in section 1.12.

Catecholeamines (adrenaline and noradrenaline) modulate cardiovascular function at a systemic level by circulating in the bloodstream. Noradrenaline also acts as the principal post-synaptic peripheral sympathetic neurotransmitter that acts on target organs, including the vascular system (Klabunde 2021). Most of the noradrenaline that is released at sympathetic nerve terminals is taken up by the nerves and recycled. However, a small amount of noradrenaline makes its way into the intravascular space and acts as a humoral agent. A larger source of circulating catecholamines is the adrenal medulla, which produces both noradrenaline and adrenaline in response to stimulation of its sympathetic nervous supply.

Adrenaline preferentially binds to β-receptors on both the peripheral vasculature and on cardiac myocytes. An increase in circulating adrenaline therefore causes an increase in heart rate and peripheral vasodilation. Cardiac output increases, but peripheral resistance decreases, as per equations 1.29 and 1.30. Blood pressure is therefore largely unchanged, unless circulating adrenaline levels reach a level at which they also start to activate α-receptors, which causes a degree of peripheral vasoconstriction.

Noradrenaline preferentially binds to α_1 and β_1-receptors. This causes peripheral vasoconstriction, and a subsequent increase in blood pressure. Binding to β_1-receptors on cardiac myocytes causes an initial transient increase in heart rate. However, the increase in blood pressure stimulates the baroreceptor reflex, leading to a subsequent reduction in heart

rate. There is evidence that β-receptor mediated vasodilation protects premenopausal women from the vasoconstrictor effects of noradrenaline released from sympathetic nerve terminals (Hart 2011), (Hart 2009) This may partly explain the increased prevalence of hypertension amongst young men compared to young women (Burt 1995).

The renin-angiotensin-aldosterone (RAA) system is the other principal extrinsic modulator of peripheral vascular resistance (Weir 1999). Renin is released by the kidney in response to a reduction in renal perfusion, or by sympathetic stimulation of the kidney. Renin cleaves angiotensinogen to angiotensin-I, which is subsequently cleaved to angiotensin-II by angiotensin-converting enzyme (ACE). Angiotensin-II has several influences on the cardiovascular system. It increases adrenal production of aldosterone, a mineralocorticoid hormone which increases renal water and sodium retention. It stimulates release of noradrenaline from peripheral sympathetic nerve endings, as well as binding to angiotensin-1 receptor in the rostral ventrolateral medulla to increase brainstem sympathetic output. It also acts as a peripheral vasoconstrictor.

Two other hormones are important modulators of cardiovascular function (Klabunde 2021). Atrial natriuretic peptide (ANP) is a counter-regulatory hormone that is released by cardiac myocytes in response to atrial distension, sympathetic activity and other factors. It opposes the renin-angiotensin-aldosterone system and increases sodium excretion, thereby reducing blood volume and blood pressure. Antidiuretic hormone (ADH) is released by the posterior pituitary gland. Its main function is to act on the collecting system of the kidneys to increase water resorption. This increases blood volume and blood pressure.

Blood pressure regulation is therefore complex and multifactorial, but the sympathetic nervous system clearly plays an important role. In summary, an increase in SNA causes an increase in heart rate, and by equations 1.25 and 1.26 an increase in systemic blood pressure. The relationship between SNA and stroke volume is more complex. SNA increases stroke volume via an increase in preload and due to its positive inotropic effect, but also reduces stroke volume via an increase in afterload caused by increased peripheral vascular resistance. However, by equation 1.25, this increased peripheral vascular resistance also acts to increase blood pressure. Ultimately, the overall effect of an increase in SNA is an increase in blood pressure.

1.10. Cerebral autoregulation

Cerebral blood flow is dependent on a positive pressure gradient between the systemic arterial circulation and the cerebral venous system. This positive pressure, known as cerebral perfusion pressure (CPP), is maintained as long as mean arterial pressure (MAP) is sufficiently large to overcome the resistance to blood flow that is generated by intracranial pressure (ICP). ICP is often taken to be equivalent to the resistance generated by the cerebral venous system. Therefore:

$$CPP = MAP - ICP, \tag{1.27}$$

and

$$CBF = \frac{(MAP - ICP)}{cerebrovascular\ resitance}. \tag{1.28}$$

CBF is maintained to the brain across a range of perfusion pressures by cerebral autoregulation. Traditionally, CBF was thought to be held constant by cerebral autoregulation at normal cerebral perfusion pressure (MAP between approximately 50 and 150 mmHg). However, there is now evidence that CBF is only held constant in a much narrower range of MAPs, and that there is a degree of variation in CBF with changes in MAP (Willie 2014).

There are four main mechanisms subserving cerebral autoregulation. The myogenic response involves cerebrovascular smooth muscle contraction and relaxation in response to changes in pressure, mediated by activation of mechanically sensitive ion channels (Silverman 2022). Changes in cerebral perfusion leads to changes in local arterial concentration of O_2 and CO_2, which causes vasodilation or vasoconstriction (Willie 2014). Changes in blood flow stimulate release of a variety of vasoactive endothelial factors such as nitric oxide (Silverman 2022).

Finally, neurogenic mechanisms also mediate CBF. At a local level, changes in neuronal activity induce changes in CBF via neurovascular coupling – as described in the discussion of the BOLD mechanism in section 1.2. The cerebrovascular system is also innervated by sympathetic and parasympathetic fibres, and sympathetic ganglionectomy has been shown to

increase CBF (Willie 2014). There is evidence that sympathetic innervation to the anterior circulation is denser than to the posterior circulation, which includes the brainstem (Silverman 2022). In the presence of an increase in sympathetic nerve activity, regional differences between CBF to the anterior and posterior circulation of the brain might be partially driven by this difference in sympathetic innervation, rather than by pathology. Changes in CBF and CVR due to the effect of SNA on the cerebrovascular system might therefore be confounded by the effect of SNA on cerebral autoregulation.

1.11. Cerebrovascular function in hypertension

The selfish brain mechanism proposes that cerebrovascular abnormalities precipitate hypertension. However, hypertension is itself causally associated with pathological changes to small subcortical and cortical perforating cerebral blood vessels (Prins 2015) leading to chronic cerebral microangiopathy which contribute to reductions in CBF (Alosoco 2014). Muller et al. (Muller 2012) investigated the longitudinal association between blood pressure and cerebral blood flow over a four-year period. CBF was significantly reduced at follow up in untreated and poorly controlled hypertensives, compared to normotensives and controlled hypertensives. Therefore, in cross-sectional studies of patients with longstanding hypertension it might be difficult to dissociate changes in cerebral haemodynamics that are secondary to cerebrovascular disease precipitated by hypertension from those which may have played a role in causing hypertension via the selfish brain mechanism. Cross-sectional studies of the selfish brain mechanism might therefore focus on younger cohorts in the early stages of hypertension, before the onset of chronic small vessel disease. Ultimately, longitudinal studies are required to determine the direction of any relationship between brainstem haemodynamic dysfunction and systemic hypertension.

Several previous studies have applied a variety of techniques to measure CVR in hypertensives. Hajjar et al. used ASL with a hypercapnic challenge to measure CVR in five regions of interest – frontal, parietal, temporal, occipital and cerebellar. They found that, after accounting for stroke and white matter hyperintensity volume (which can be indicative of white matter ischaemic change due to small vessel disease), hypertensive participants had lower global vasoreactivity (0.43 ± 0.1 versus 1.11 ± 0.13 mL/100g/mmHg) (Hajjar 2010).

Warnert et al. used PC-MRA to measure the change in blood flow through the internal carotid and basilar arteries in response to hypercapnia (Warnert 2016) . This method revealed no significant difference in global CVR between normotensives (4.5 ± 0.7 mL/100 mL per min/%$ETCO_2$) and hypertensives (5.6 ± 0.6 mL/100 mL per min/%$ETCO_2$). However, this was a hetereogenous population of hypertensives who were receiving a variety of different antihypertensive medications with various mechanisms of action and different effects on the peripheral vasculature. This may have confounded any difference in CVR in the hypertensive group. The same study measured BOLD signal change in the occipital lobes in response to a visual stimulus task as a surrogate marker of CVR. No significant difference was found between hypertensives and normotensives, but hypertensive participants demonstrated a larger increase in blood pressure during the task. This raises the possibility that hypertensives are reliant on an increase in systemic blood pressure to maintain CBF, rather than local cerebrovascular vasodilation. In addition, participants who had vertebral artery hypoplasia plus an incomplete circle of Willis demonstrated lower occipital lobe CVR. This suggests a possible association between hypertension, posterior circulation vascular abnormalities and impaired CVR.

Transcranial Doppler ultrasound of the cerebral blood flow response to hypercapnia has also been used to demonstrate an impaired CVR in hypertensives compared to normotensives (Maeda 1994), (Ostrovskaya 2015). Wong et al. (Wong 2011) used transcranial Doppler to measure the middle cerebral artery blood flow velocity response to hypercapnia in children and found that CVR was lower in untreated hypertensives (2.56 ± 1.83 cm/s/mmHg) than in normotensives (4.26 ± 1.33 cm/s/mmHg). The findings of a blunted CVR in this young cohort of hypertensives gives weight to the idea that impaired CVR may not always be a result of chronic microvascular changes associated with longstanding hypertension.

Settakis et al. measured middle cerebral artery blood flow velocity and pulsatility index using transcranial doppler and found an impaired CVR to a 30 second breath hold task in adolescent hypertensives compared to normotensive controls (Settakis 2003). In a similar study that use hyperventilation as a hypocapnic stimulus, the results were equivocal, with no significant difference between the hypertensive and normotensive groups in the change in mean MCA flow velocity. However, $ETCO_2$ was not measured in either study, so there is

uncertainty regarding the efficacy of their stimulus, and the magnitude of the CVR could not be deduced (Settakis 2003).

Ivankovic et al. studied the influence of hypertension and diabetes with and without retinopathy on CVR (Ivankovic 2013). Comparing 30 hypertensives (without diabetes) with 30 normotensives, again measuring MCA flow using TCD and a 30 second breath-hold task, CVR in the hypertensive group was found to be approximately 29% lower. Ficzere et al. measured MCA flow velocity using TCD before and after intravenous injection of acetazolamide. They found that mean CVR was approximately 31% lower in a group of 25 severe hypertensives compared to 25 controls (Ficzere 1998).

The mean effect size of the difference in CVR between hypertensives and normotensives, using data from those studies that clearly reported CVR values (Warnert 2016), (Hajjar 2010), (Wong 2011) was Cohen's d = 1.92. If a similarly large effect size is applicable to the brainstem, the sample size required to achieve a statistical power of $\beta = 0.95$ with a significance threshold of $\alpha = 0.05$ is only 18 participants. Evaluation of CVR in hypertensives is therefore feasible with a relatively small sample size.

The effect of antihypertensive medications is a potential confounding factor when studying CVR and CBF. In a systematic review and meta-analysis of 35 studies investigating the effects of various vasodilating drugs on cerebral haemodynamics (Webb 2019), Webb et al. concluded that the effect of vasodilators on CVR and CBF was somewhat equivocal due to the low quality of the studies in the analysis. Webb estimates that vasodilators reduce CVR by a moderate amount, (standard mean difference between hypertensives and normotensives = 0.47 (weighted across studies by the inverse variance)), and only cause a minimal reduction or no significant change in CBF. However, this CVR estimate is based on only six studies. Rebrova et al. (Rebrova 2017) found no change in CVR to hypercapnia following six months of lisinopril treatment in a cohort of 15 patients with both hypertension and rheumatoid arthritis. In elderly male hypertensives, six months of valsartan treatment had no significant effect on CVR (Périard 2012).

1.12. The sympathetic nervous system

1.12.1. General anatomy and the brainstem's role

Preganglionic sympathetic neurones originate in the interomediolateral (IML) cell column in the lateral horn of the spinal cord between the levels of the first thoracic and second lumbar vertebrae. Preganglionic neurones project to ganglia in the sympathetic chains either side of the spine via the ventral roots of spinal nerves exiting the spinal cord. Here they synapse with post-ganglionic neurones, which send projections to their effector target organs including the heart and peripheral vasculature.

Sympathetic and parasympathetic preganglionic neurones are cholinergic – they utilise acetylcholine as a neurotransmitter. Most sympathetic postganglionic neurones, including those projecting to the cardiovascular system, are noradrenergic, utilising noradrenaline as a neurotransmitter. All parasympathetic postganglionic neurones are cholinergic (Samuels 2008).

There are several types of noradrenergic receptor, each of which respond differently to noradrenaline. Activation of α_1 and β_1 -receptors results in an excitatory response, whereas activation of α_2-receptors leads to an inhibitory response (Ritter 2007), (Samuels 2008).

Pre-ganglionic sympathetic neurones in the IML are influenced by many different parts of the central nervous system, including parts of the brainstem (Paton 2009). The rostral ventrolateral medulla (RVLM) is a physiological centre situated in the medulla, and is an important source of excitatory sympathetic input to the cardiovascular system (Lunblad 2014). It is a believed to be a central component in the generation of basal sympathetic tone (Feldman 2013). The baroreceptor reflex arc is also mediated via the brainstem (Dampney 2002). Sensory afferents from baroreceptors in the carotid sinus and aortic arch are transmitted to the nucleus tractus solitarii (NTS) in the medulla. The NTS sends excitatory neuronal projections to the caudal ventrolateral medulla (CVLM) where neuronal signals are converted from excitatory to inhibitory. Finally, the CVLM sends inhibitory projections to the RVLM. The net result of activation of the baroreceptor reflex arc is therefore inhibition of sympathetic output from the RVLM, and a reduction in systemic blood pressure.

Traditionally, the baroreceptor reflex arc was thought to only be involved in short-term modulation of blood pressure. However, more recent evidence suggests that chronic resetting of the baroreflex occurs (Kougias 2010). Resetting involves a reduction in the sensitivity of the baroreceptor reflex arc to fluctuations in MAP. The baroreflex is therefore less responsive and elevations in systemic blood pressure are maintained rather than immediately dampened. The pathophysiological mechanism underlying such a reset is uncertain, and might involve changes to the sensitivity of the peripheral baroreceptors, or functional impairment to their afferent sensory neurons (Kougias 2010). Alternatively, it is theoretically possible that functional impairment of the central component of the baroreceptor reflex arc in the medulla might be a factor.

In addition to modulating blood flow via the cardiovascular system, the RVLM may also influence cerebral perfusion via neuronal projections to the cerebral cortex. Excitation of sympathetic neurones in the RVLM induced by hypoxia or ischaemia is believed to elicit a widespread increase in cerebral blood flow (Golanov 2004).

There are several other noradrenergic nuclei in the brainstem which send projections to the IML. The locus coeruleus is the largest of these (K. Y. Liu 2017), (Samuels 2008). It is located in the dorsal pons near the pontomesencephalic junction, and on average measures in humans 14.5 mm in length and 2.5 mm in thickness (K. Y. Liu 2017). One of its main functions is regulation of autonomic activity (Samuels 2008). It has extensive projections throughout the CNS, including to parasympathetic and sympathetic centres in the brainstem and spinal cord.

Noradrenegric output from the locus coeruleus inhibits parasympathetic activity via activation of α_2-receptors in the dorsal motor nucleus of the vagus (DMV) and the nucleus 42utomatiz (NA), both situated in the medulla. The locus coeruleus also has an inhibitory effect on the RVLM, but it sends excitatory projections to preganglionic sympathetic neurones in the IML. The resultant increase in IML sympathetic activity outweighs medullary sympathetic inhibition. The net effect of an increase in locus coeruleus activity is therefore an increase in sympathetic, and a decrease in parasympathetic, supply to the cardiovascular system (Samuels 2008).

1.12.2. Central autonomic network

As well as the brainstem, several other parts of the central nervous system are involved in autonomic regulation. These are interlinked by a complex network of neurones sending feedback between the different areas and projecting to the spinal sympathetic neurones and cardiovascular system. The paraventricular nucleus of the hypothalamus has emerged as an important part of this network (Dougherty 2020). It has neuronal projections to the RVLM, sympathetic neurons in the spinal cord and to cardiac nuclei amongst others (Coote 2004). The limbic system, which includes the amygdala and hippocampus, also forms part of the network via its connection with the hypothalamus (Dougherty 2020). The insula cortex is associated with modulation of heart rate (Coote 2004), and is interlinked with the limbic system. A meta-analysis of neuroimaging studies that have investigated the central autonomic network has implicated many cortical and subcortical regions as part of this network, including the hypothalamus, thalamus, amygdala and insula (Beissner 2013).

1.13. Blood pressure, the sympathetic nervous system and hypertension

There is an established association between hypertension and elevated sympathetic nerve activity (SNA). Spontaneously hypertensive rats have been shown to have elevated sympathetic nerve activity (Hart 2016), and various studies in humans, using both microneurography and noradrenaline spillover techniques, have shown elevated sympathetic nerve activity in hypertensives (Grassi 2016). Muscle sympathetic nerve activity has been shown to be elevated in participants with high-normal blood pressure, borderline-hypertension and early-stage hypertension (Hart 2016), (Seravalle 2015), (Smith 2004) and plasma catecholamines are elevated in young hypertensives (Goldstein 1983). Hart et al. (Hart 2013) found that renal denervation caused a reduction in both SNA and systolic blood pressure in rats. In humans, results were equivocal (overall there was no reduction in the mean systolic blood pressure or mean SNA of a group of 9 patients who underwent renal denervation), but four of the patients did show a 10% reduction in systolic blood pressure at 6 months. There is also evidence that sympathectomy can be successfully used as a method of treating resistant hypertension (Hart 2016), (Seravalle 2015). Young adults with a resting tachycardia have been shown to be at higher risk of developing hypertension, and an

elevation in plasma adrenaline has been suggested to be a predictor of the development of hypertension (Grassi 2016).

The finding that SNA is elevated in pre-hypertensive and borderline-hypertensive populations raises the possibility that SNA increases before the onset of hypertension. Furthermore, the fact that interventions such as alpha- and beta-blockade, sympathetic ganglion blockage and renal sympathetic denervation all reduce blood pressure in hypertensives is also supportive of a causal link between elevated SNA and hypertension (Esler 2010). However, a causal relationship between elevated SNA and hypertension is yet to be definitively established (Grassi 2016), and the aetiology of elevated SNA in hypertension remains uncertain. There is evidence that hyperinsulinaemia that occurs in obesity might play a role, via the sympatho-excitatory effect of insulin in the CNS (Seravalle 2022). Angiotensin-II also drives an increase in sympathetic activity via the CNS, and therefore overactivity of the renin-angiotensin-aldosterone system might be a contributory factor. The selfish brain mechanism might also play a role in increasing SNA and driving hypertension.

1.13.1. The selfish brain mechanism

The selfish brain mechanism proposes that hypertension is a compensatory mechanism that aims to maintain CBF by increasing systemic blood pressure through an increase in cardiovascular sympathetic tone. According to the selfish brain mechanism, if CBF is compromised for some reason, increased neuronal activity in regions of the brain which modulate sympathetic nerve activity, such as the medulla and other components of the central autonomic network, elevates cardiovascular sympathetic tone and subsequently increases systemic blood pressure. This helps to restore and maintain CBF by increasing CPP, as per equation 1.28.

The theory behind the selfish brain mechanism originated with the work of Harvey Cushing, who demonstrated in 1901 that a reduction in cerebral blood flow (induced by an increase in intracranial pressure) caused an increase in systemic blood pressure in dogs (Hart 2016). In the 1950s, John Dickinson found an inverse correlation between post-mortem vertebral artery flow and ante-mortem blood pressure, with a weaker correlation in the

internal carotid arteries (Paton 2009). This suggested a correlation between posterior cerebral circulation vascular resistance and blood pressure.

Since then, several further studies have demonstrated an association between various cerebrovascular abnormalities and changes in cerebral haemodynamics. For example, an association between vertebral artery hypoplasia (congenital narrowing of the vertebral arteries) and reduced CBF has been found. Thierfelder et al. found that blood flow to the posterior inferior cerebellar artery territory was lower in patients with vertebral artery hypoplasia (Thierfelder 2014). Occipital and temporal lobe perfusion, measured using arterial spin labelling, has been found to be reduced in hypertensives, suggesting a possible correlation between posterior circulation hypoperfusion and hypertension (Alosoco 2014).

Warnert et al. demonstrated an increased prevalence of posterior circulation anatomic variants, including vertebral artery hypoplasia (VAH), in hypertensive patients compared to normotensives (Warnert 2016). They also found total and regional CBF, including to the brainstem, to be lower in hypertensives. Total cerebrovascular resistance was also higher in hypertensives. Hypertensives with vertebral artery hypoplasia (defined as a diameter of <2 mm uniformly throughout the visualised V2, V3 and V4 segments of either verterbral artery) had higher cerebrovascular resistance and lower total CBF compared to hypertensives without VAH. Furthermore, cerebrovascular resistance, but not muscle sympathetic nerve activity, was found to be elevated in a borderline hypertensive group, suggesting that elevated cerebrovascular resistance may precede elevated SNA in the generation of hypertension.

Waki et al. found that occlusion of caudal medullary draining veins reduced blood flow and oxygenation to the medulla of normotensive rats. This induced a significant increase in arterial blood pressure in baroreceptor reflex dennervated rats (Waki 2011). In humans, ischaemic damage to the medulla has been shown to be associated with cardiovascular autonomic dysfunction (Meglic 2001). Thus it is conceivable that hypoperfusion of the medulla coupled with dysfunctional baroreceptor mechanism may lead to hypertension and could underpin the selfish brain mechanism.

Waki et al. have also demonstrated an over-expression of leukotriene B4, a pro-inflammatory molecule, in the medulla of spontaneously hypertensive rats. Blockade of the leukotriene B4 receptor, BTS1, lowered arterial blood pressure in spontaneously hypertensive

rats, but not in normotensive controls (Waki 2014). This raises the possibility that an inflammatory process in the brainstem could act as a trigger to systemic hypertension via the selfish brain mechanism.

It is therefore possible that elevated systemic blood pressure in a subset of patients with so-called 'essential' hypertension is driven by the selfish brain mechanism. The pathophysiological mechanism that triggers the hypothesised initial reduction in CBF is uncertain, but current evidence suggests that hypoperfusion of the posterior circulation, and specifically of the autonomic centres in the medulla, may be involved.

1.14. Conclusion

Cerebrovascular and cardiovascular homoeostasis are clearly very complex and involve multiple interlinked physiological mechanisms. The brainstem plays an important role via mediation of autonomic activity to the cardiovascular system. This thesis aims to validate, optimise and apply a variety of MRI-based methods of probing brainstem functional activity, which may then be used in future studies to further investigate the selfish brain mechanism. Firstly, methods of measuring brainstem CBF and CVR are optimised using ASL, BOLD and a hypercapnic challenge. The reliability and reproducibility of these methods are demonstrated in a pilot study. Next, existing data is explored to study the association between vertebral artery hypoplasia and CBF to the brainstem and other parts of the central autonomic network in hypertensives and normotensives. Brainstem co-registration is then automated and optimised using machine learning. The UK Biobank dataset is also explored to study differences in the amplitude of low-frequency fluctuations (ALFF) in the BOLD signal, a potential surrogate index of CVR, between hypertensives and normotensives. Following this, the relationship between ALFF and CVR is investigated to validate ALFF as a surrogate marker of CVR. Finally, a pilot study of functional MRI in the locus coeruleus, an important noradrenergic brainstem nucleus that is integral to the central autonomic network, is undertaken. The thesis concludes with a general discussion of the results of the above studies and outlines a potential future study of CVR in a hypertensive cohort.

2. Development of non-invasive measurements of regional brainstem CVR

2.1. Introduction

Cerebrovascular reactivity (CVR) is a measure of the responsiveness, tone and functional reserve of the vascular system and is often regarded as an important marker of the health of the cerebrovascular system (Krishnamurthy 2021), (Richiardi 2015), (Kim 2021). CVR is important in the context of the selfish brain mechanism because brainstem functional vascular reserve might be impaired even if perfusion is maintained. For example, if there is a pathophysiological mechanism impeding brainstem CBF, compensatory mechanisms such as cerebral autoregulation and/or the selfish brain mechanism might correct CBF up to a point. CBF might therefore be measured as normal in a hypertensive cohort. However, if there is a further increase in metabolic demand from the brain, the capacity of the cerebral vasculature to dilate further to meet the associated increased CBF requirement might be impaired, which might manifest as a reduction in CVR.

As discussed in section 1.4, CVR can be assessed by measuring the change in cerebral blood flow in response to a vasoactive stimulus such as carbon dioxide, (Fisher 2016), (Whittaker 2016), and there are a variety of methods of measuring the change in CBF. BOLD and ASL allow whole brain maps of CVR to be obtained. The change in CBF in response to hypercapnia can be measured directly using arterial spin labelling (ASL) or inferred indirectly via a change in BOLD signal. However, the challenges involved in brainstem MRI that were discussed in section 1.6 apply to both brainstem BOLD and brainstem ASL. Furthermore, ASL is an inherently low SNR technique. Reliable measurement of brainstem CBF and CVR is therefore challenging. In this chapter an ASL sequence is optimised to measure brainstem CBF and then used with a hypercapnic challenge to measure regional brainstem CVR. BOLD can be used instead of ASL to measure CVR, but as outlined in section 1.2 the origin of the BOLD signal is multifactorial, and therefore BOLD is not a specific measurement of CBF. The advantage of BOLD is its higher SNR compared to ASL. In a subset of participants BOLD CVR was also measured and compared to ASL CVR, to validate the ASL CVR measurements. The ultimate goal is to apply these methods in a future study of brainstem CVR in hypertensives (see appendix 1 for a summary of the proposed study protocol).

As discussed in the chapter 1.6, there are several challenges inherent to functional imaging of the brainstem. The brainstem is a relatively small structure and contains several physiological centres, cranial nerve nuclei and white matter tracts all in close proximity to each other. It is important therefore to achieve an acceptable balance between spatial resolution and SNR. The brainstem is surrounded by vascular structures and cerebrospinal fluid (CSF) spaces and is therefore susceptible to physiological noise from vascular and CSF pulsation. Due to its caudal location, it is also particularly susceptible to off-resonance B_0 effects due to the changes in concentration and spatial distribution of oxygen with respiration. The paranasal sinuses and mastoid air cells are close to the brainstem, and it is therefore susceptible to distortion and signal dropout. Image acquisition parameters must be selected to minimise these confounding effects, or correction techniques must be applied during post-processing. Variation in brainstem substructure between subjects will confound attempts to make groupwise comparisons of functional activity with any great precision, because small brainstem structure such as the rostral ventrolateral medulla (RVLM) may not overlap following co-registration to standard space. Spatial smoothing might help with this, but too much smoothing risks introducing signal from CSF in the basal cisterns surrounding the brainstem.

There are also several important considerations that are specific to the use of ASL to investigate cerebral perfusion and CVR, especially when it comes to the brainstem. The choice of label location is important because the vertebral arteries that supply the brainstem are tortuous, and their precise anatomy varies between participants. Suboptimal label placement might confound inter-participant CBF measurements. For example, labelling might be inefficient if the labelling plane is placed so that the vertebral artery is running parallel rather than perpendicular to it. The post-label delay must be long enough to minimise arterial transit artefacts in the form of residual intravascular labelled bolus in the vertebrobasilar arteries. At the same time, if the PLD is too long SNR will be lost due to decay of the labelled bolus through T1 relaxation. The choice of ASL readout is also important when imaging in the vicinity of the brainstem to minimise magnetic susceptibility-induced signal loss and distortion from the nearby paranasal sinuses and mastoid air cells. These challenges are considered in more detail in the brainstem ASL optimisation section below.

Only a few previous studies have specifically focussed on ASL to measure differences in brainstem perfusion between different patient groups (Viviani 2012) (Warnert 2014).

Warnert et al. (Warnert 2014) used 3T multi-TI pASL to investigate the kinetic curve and brainstem arrival time of the labelled bolus. The same study also used pASL to quantify brainstem cerebrovascular reactivity to hypercapnia. A multi-TI ASL sequence was used because of the desire to measure arrival time, whereas a single-TI sequence might confer improved SNR, and spatial resolution was relatively low, with a voxel size of 3 x 3 x 7 mm. Furthermore, a fixed label location 1 cm inferior to the imaging plane was used, therefore variations in vascular anatomy in the neck might lead to inefficient labelling, potentially confounding CBF measurements. Finally, only overall mean brainstem CVR was reported rather than CVR values in sub-regions of the brainstem (medulla, pons and midbrain).

While Warnert's study looked at perfusion averaged over the brainstem as a whole, other studies purport to have measured regional differences in brainstem blood flow between different experimental conditions. For example, Viviani et al. (Viviani 2012) have found evidence suggestive of regional perfusion differences, measured using 3T ASL, in the brainstem in healthy volunteers randomised to receive buproprion and paroxetine in a double-blind, placebo-controlled crossover study. These regional differences occurred at the sites of noradrenergic and serotonergic nuclei that are thought to be affected by these drugs, including in the locus coeruleus. In a separate study, Marquand et al. (Marquand 2012) used ASL with multivariate pattern recognition to demonstrate differential effects of the drugs methylphenidate and atomoxetine on regional CBF at various locations throughout the brain, including the midbrain. However, neither of these studies tailored their approach towards the brainstem – for example neither study reports using an individually tailored label location. To date, no studies have attempted to measure regional CVR within the brainstem.

There are existing methods other than ASL of measuring brainstem perfusion, for example Hougard et al. used dynamic contrast-enhanced MRI to measure perfusion in a region of interest in the mid-pons and found a mean of 18.1 mL/100g/min (Hougard 2017). However, ASL does not involve the administration of an intravenous contrast medium and is therefore safer and more practical in a research setting. CVR measurement also has potential utility in the clinical setting. Measurement of CVR could help in the assessment of the rehabilitation potential of brain regions affected by ischaemic stroke (Krishnamurthy 2021). CVR measurements correlate with cognitive performance in patients with mild cognitive decline (Richiardi 2015), (Kim 2021), and with the severity of motor symptoms in Parkinson's

disease (Pelizzari 2021), and could therefore be and useful tool to investigate neurodegenerative diseases. If it is possible to optimise CVR to make accurate regional brainstem CVR measurements, the technique could be applied to guide management of patients with brainstem stroke or to aid diagnosis of neurodegenerative diseases that involve brainstem substructures, such as progressive supranuclear palsy or multisystems atrophy.

2.1.1. Summary of aims

In summary, the aims of this chapter are:

1. To build on the work of previous studies and optimise an ASL sequence to enable reliable and reproducible measurement of regional brainstem CBF.
2. To use this ASL sequence together with a hypercapnic challenge to demonstrate the feasibility of measuring regional brainstem CVR (in the medulla, pons and midbrain).
3. To measure regional brainstem CVR using BOLD with a hypercapnic challenge in order to validate the ASL measurements, and to determine whether BOLD or ASL CVR is the preferred method to be used in a future study of hypertensive patients.

2.1.2. Signal to noise measurement

There are two main sources of noise in MRI: thermal and physiological noise. Thermal noise is caused by various sources such as random fluctuations in the electrical hardware and dielectric effects in the human body (Buxton 2013). According to work by Triantafyllou et al. at a field strength of 3T and a voxel volume of approximately 27 mm^3, which is of the order of the ASL voxel size under consideration in this chapter, the relative contributions of physiological and thermal noise are approximately equal (Triantafyllou 2005).

There are three main factors that affect the signal-to-noise ratio in MR imaging. The first of these is the transverse magnetisation M_{perp} at the time of image acquisition. As discussed in section 1.1, M_{perp} is directly proportional to the external magnetic field strength B_0. SNR therefore increases in direct proportion to the magnetic field strength. The number of spins in each voxel also affects SNR. A larger voxel contains more spins and therefore makes

a larger contribution to the MRI signal. Voxel volume, ΔV, is therefore also a factor. Finally, the time taken to acquire the image, T, which is a product of the acquisition time (the time taken to sample the free-induction decay) and the number of repetitions of the acquisition, is also a factor. SNR is therefore proportional to:

$$SNR \propto M_{perp} \Delta V \sqrt{T}. \quad (2.1)$$

Signal-to-noise ratio (SNR) is a key parameter in determining the effectiveness of an MRI sequence. It is used to evaluate the quality within single imaging studies and to compare images acquired using different sequence parameters or hardware. Three common methods of estimating MRI SNR are (Dietrich 2007):

1. Comparison of the mean signal within a region of interest (ROI) within the brain parenchyma with the mean or standard deviation of the signal in a ROI outside the brain:

$$SNR_{spatial} = \frac{S_{brain}}{S_{outside}} \; or \; SNR_{spatial} = \frac{S_{brain}}{SD_{outside}}. \quad (2.2)$$

where *S* = signal and *SD* = standard deviation

2. Comparison of mean signal with a parenchymal ROI with the temporal standard deviation of the signal within the same ROI.

$$SNR_{temporal} = \frac{S_{brain}}{SD_{temporal}}. \quad (2.3)$$

3. Acquisition of two identical images, followed by subtraction of the images, then using the residual signal as an estimate of background noise.

The use of a ROI outside the brain to estimate background noise within the brain assumes that noise is distributed uniformly across the imaging volume. This is not necessarily the case, for example thermal noise is not homogenously distributed when a phased array coil is used (Cardenas-Blanco 2008). The method of subtracting two identical images overcomes this and

is more exact (Firbank 1999), but it is impractical because of the necessity of acquiring two images. Estimating noise by calculating the voxelwise temporal variance across multiple acquisitions ($SNR_{temporal}$) may be a more robust method (Dietrich 2007). Furthermore, $SNR_{temporal}$ might capture more information about physiological noise due to temporal variance introduced by respiration and cardiac pulsation. It is also the most relevant definition of noise for analysis of timeseries data such as ASL and BOLD fMRI. $SNR_{temporal}$ was therefore used to assess brainstem SNR in this study.

2.2. Methods

2.2.1. General procedure

All MRI data was acquired using a Siemens 3T Magnetom Prisma scanner (Siemens Healthcare GmbH, Erlangen, Germany). Brainstem ASL optimisation was initially undertaken by scanning healthy volunteers and is described in detail below (see section 2.2.3). After deciding on the optimal sequence parameters, ten healthy volunteers under the age of 40 were scanned to demonstrate the feasibility of measuring regional brainstem CVR. Participants were recruited internally within Cardiff University Brain Research Imaging Centre (volunteer PhD students and postdoctoral researchers – see appendix 2 for a full list of inclusion and exclusion criteria). Informed consent was obtained from all participants under pre-existing ethical approval from Cardiff University School of Psychology.

All data were analysed in their original functional (ASL or BOLD) space to minimise interpolation errors which might be introduced by spatial transformation of functional data. High-resolution whole brain structural scans were obtained and co-registered to functional space using FSL FLIRT (Jenkinson 2001). Co-registration accuracy was visually assessed, and in cases where brainstem co-registration was inaccurate landmark-based co-registration was applied (as discussed in section 4.1.3). BOLD and ASL data were motion corrected using FSL MCFLIRT (Jenkinson 2002), which co-registers each volume in a MRI dataset against a reference volume (by default the middle volume in the timeseries).

Perfusion weighted images, derived by subtracting tag and control images, were translated into absolute cerebral blood flow measurements (in units of mL/100g/minute) by scaling to M_{0b}, the equilibrium magnetization of arterial blood, and subsequently applying a kinetic model using using oxford_asl. Oxford_asl is a command line tool that is part of the Bayesian Inference for Arterial Spin Labeling (BASIL) toolbox for analysis of ASL data (Chappell 2009). A separately acquired proton-density weighted image (M_0 image) is used to derive an estimate of M_{0b}.

The Freesurfer image analysis suite (Fischl 2012), together with the 'Brainstem Substructures' module (Iglesias 2015), was used to perform segmentation of the brainstem. The 'Brainstem Substructures' module uses a probabilistic atlas that has been constructed following manual delineation of brainstem regions using well-defined anatomical landmarks to subdivide the brainstem into midbrain, pons and medulla. The result of this segmentation process was used to generate binary masks of the three brainstem regions. The Harvard-Oxford cortical atlas, available via the FSL software package, was used to generate a frontal grey matter mask in MNI-space. These masks were co-registered to functional (ASL or BOLD) space using the matrices derived from the co-registration process described above. The co-registered masks were eroded using fslmaths with a 2 mm spherical kernel to prevent encroachment of extra-axial structures.

2.2.2. SNR measurement

ASL-SNR was calculated as follows. An uncalibrated perfusion map was generated by taking the mean across all of the tag-control subtracted ASL images. The mean signal within a brainstem mask (generated by combining the individual medulla, pons and midbrain masks discussed above) was then calculated (S_{brain}). For single-TI acquisitions, $SD_{temporal}$ was the temporal standard deviation across all the tag-control subtracted images. For multi-TI acquisitions, $SD_{temporal}$ was temporal standard deviation across the set of tag-control images at each TI. The mean of the value of $SD_{temporal}$ at each TI was then used in equation 2.3 to calculate $SNR_{temporal}$.

2.2.3. Optimisation of brainstem ASL

The ISMRM Perfusion Study Group have published a set of consensus recommendations on the use of ASL in the clinical setting. These recommendations were used to help guide choice of hardware, sequence parameters and post-processing methods. Initial work focussed on a PCASL acquisition with a single PLD and an EPI readout.

Hardware optimisation

Field strength

Some of our choices were constrained, for example we were restricted to 3T ASL because a 7T ASL sequence had not been fully developed at the time of the study.

Coil selection

The ISMRM Perfusion Study Group (Alsop 2015) recommends a multichannel receive head coil. This enables the use of parallel imaging to reduce the echo time and readout duration, improving SNR. Unfortunately, the medulla lies at the periphery of the receive sensitivity of available MRI head coils. To determine which of three available coils would provide the best sensitivity for the brainstem a comparison of multi-TI PCASL data was made between a 32-channel head coil, 64-channel head and neck coil, and a 20-channel C-spine coil, in 2 participants. The craniocaudal variation in temporal SNR for each coil along a line that runs vertically through the brainstem is displayed on figure 2.1. The magnitude and craniocaudal variation in $SNR_{temporal}$ are similar for all three coils, and gradually reduces from the cortical grey matter, down through the centre of the brain and into the brainstem.

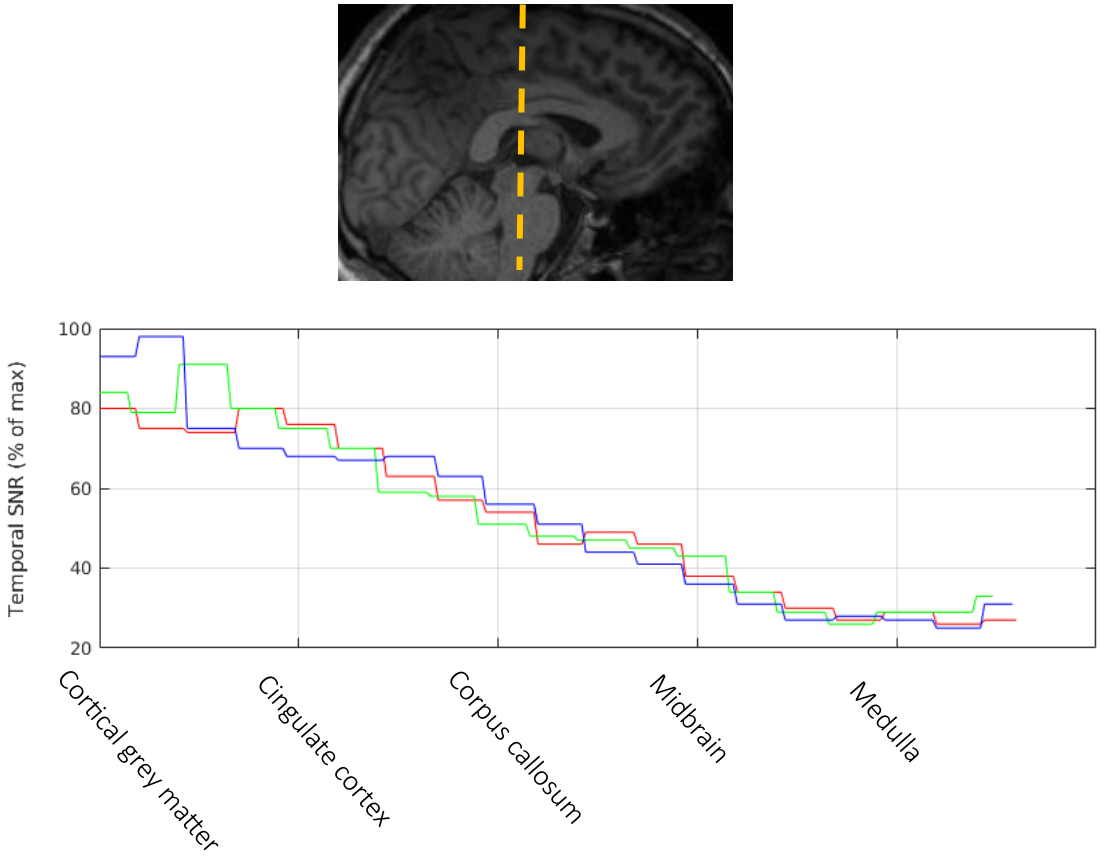

Figure 2.1: Top: The temporal SNR (as a percentage of maximum) along the dashed yellow line running vertically from the cerebral cortex through the brainstem to the cervicomedullary junction was measured on a mid-sagittal slice for three coils (the line is displayed overlying a MPRAGE image for reference). Bottom: Plot of the SNRt along the dashed yellow line, with approximate positions of selected anatomical landmarks on the x-axis. Blue - 20-channel C-spine coil, single participant. Red - 32-channel head coil, two participants. Green - 64-channel head and neck coil, two participants.

The 64-channel coil was expected to be best for combined brainstem and whole-brain imaging due to the extent of its coverage in the craniocaudal direction, and the presence of three dedicated transmit elements in the neck. A comparison of brainstem $SNR_{temporal}$ is shown in table 2.1 for the three coils. This is admittedly a very small sample, and whilst brainstem $SNR_{temporal}$ is low for all three coils, it is higher in the brainstem using a 64-channel coil. In the absence of any discernible difference in craniocaudal coil sensitivity gradient, the 64-channel coil was therefore selected.

Table 2.1: Comparison of brainstem SNR in three head coils.

Coil	Brainstem $SNR_{temporal}$
20 channel	Participant 1 = 0.08
32 channel	Participant 1 = 0.17 Participant 2 = 0.22 Mean 0.20
64 channel	Participant 1 = 0.14 Participant 2 = 0.35 Mean = 0.25

Sequence optimisation

Labelling method

All sequences that were available for testing during this study were based on PCASL. Alternate labelling methods such as PASL were not tested, but PCASL is the labelling method recommended by the ISMRM Perfusion Study Group (Alsop 2015). The SNR of PCASL is generally higher than PASL for two reasons. Firstly, PCASL generally labels a larger volume of blood more efficiently than PASL. Secondly, T1 relaxation of the labelled blood begins as soon as the blood leaves the labelling plane. PASL labels a slab of blood, whereas PCASL labels a relatively thin plane as blood flows through it. Blood labelled at the inferior edge of the PASL slab will have further to travel, and will therefore undergo more T1 relaxation, than blood labelled at the superior edge of the slab. The PCASL plane is positioned at the superior edge of the PASL slab and therefore all PCASL labelled blood undergoes the same amount of T1 relaxation. One disadvantage of PCASL is that magnetisation transfer effects may confound CBF measurements. Off-resonance RF energy from the labelling pulse is transferred to the imaging plane via interaction with free water molecules. This alters the signal amplitude in the tag image. The absence of a labelling pulse in the control image acquisition means there is no such effect on the control image. The tag-control subtracted image therefore contains information related to magnetisation transfer as well as blood flow from the label plane. Magnetisation transfer was a greater problem for continuous ASL (CASL), the precursor to

PCASL. PCASL utilises a series of brief RF pulses, rather than the continuous RF pulse utilised in CASL. This reduces the magnetisation transfer effect to the tag image. For the above reasons PCASL is the labelling method recommended by the ISMRM Perfusion Study Group (Alsop 2015).

Bolus duration

The choice of label duration is a compromise between the higher SNR and the increase in tissue energy deposition associated with a longer label duration. The dependence of the signal on tissue T1 also increases with increasing label duration. The current recommendation, which was followed here, is for a PCASL label duration of 1800 ms (Alsop 2015).

Post-label delay

It is recommended that PLD be set just longer than the arterial transit time (ATT) (Alsop 2015). If the PLD is too short, labelled blood might not have had sufficient time to travel from the labelling plane to the brain tissue and might still reside within large intracranial vessels, leading to erroneously low cerebral perfusion measurements and to the presence of arterial transit artefacts. As the PLD increases beyond the ATT, a larger fraction of the labelled bolus will transition from the intravascular space to brain tissue, at the cost of further T1 relaxation of the labelled blood. The choice of PLD is therefore a compromise between maximising the tissue and microvascular components of the labelled blood whilst minimising the macrovascular component, as well as minimising signal decay related to T1 relaxation of the labelled blood. Due to the brainstem's proximity to the vertebrobasilar arteries, it is especially important to ensure that the PLD is sufficiently long to minimise contamination of brainstem perfusion measurements by residual vertebrobasilar macrovascular signal.

ATT varies somewhat between individuals, due to variations vascular anatomy and in flow dynamics, some of which might be driven by pathology (Linder 2023). Ideally, PLD would be tailored to each individual participant according to their ATT, prior to performing a whole-brain perfusion scan. ATT can be estimated by using a multi-PLD ASL sequence. In theory, an

estimation of ATT could be made within each individual, and the PLD tailored accordingly. However, this is time consuming and impractical. Therefore, we assessed the ATT to the midbrain, medulla and pons from eight multi-TI PCASL acquisitions made across five different individuals using oxford_asl. The overall mean brainstem ATT was 1.31 ± 0.16 seconds. The mean ATT in each brainstem region is displayed in table 2.2.

Table 2.2: Mean ATT in the brainstem

Region	ATT (seconds)
Medulla	1.34 ± 0.15
Pons	1.30 ± 0.18
Midbrain	1.28 ± 0.15

The basilar artery is in very close proximity to the pons, and any residual signal within it will significantly confound brainstem CBF estimates, either through partial voluming of arterial transit artefacts or by its inclusion within imperfectly co-registered brainstem ROIs. The mean signal (as a percentage of the maximum) within a manually defined basilar artery ROI was plotted against the PLD. As expected, basilar artery signal can be seen to peak early then decay to a plateau by roughly 1500 ms (figure 2.2).

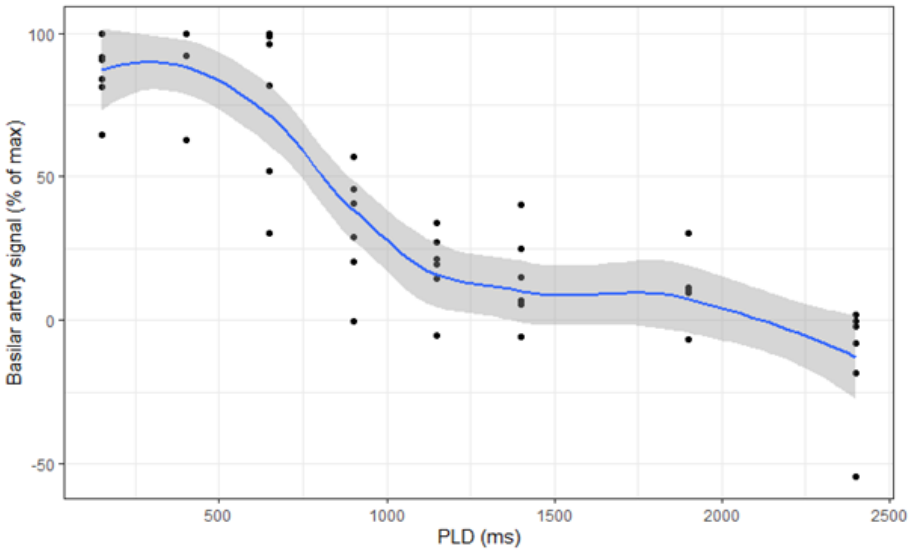

Figure 2.2: Basilar artery signal peaks early then gradually reduces, reaching an approximate plateau around 1500 ms.

A post label delay of 1.8 seconds is recommended in healthy subjects under the age of 70 (Alsop 2015). Based on the above observations, a PLD of 1.8 seconds should give sufficient time for the labelled bolus to transition from the macrovascular to the microvascular brainstem circulation in all participants. At the same time there should be minimal residual signal remaining in the basilar artery. A PLD of 1.8 seconds was therefore chosen for this study. A slightly longer PLD of 2.0 seconds is recommended in the clinical adult population (Alsop 2015), but increasing the PLD further beyond 1.8 seconds risks compromising SNR.

Label location

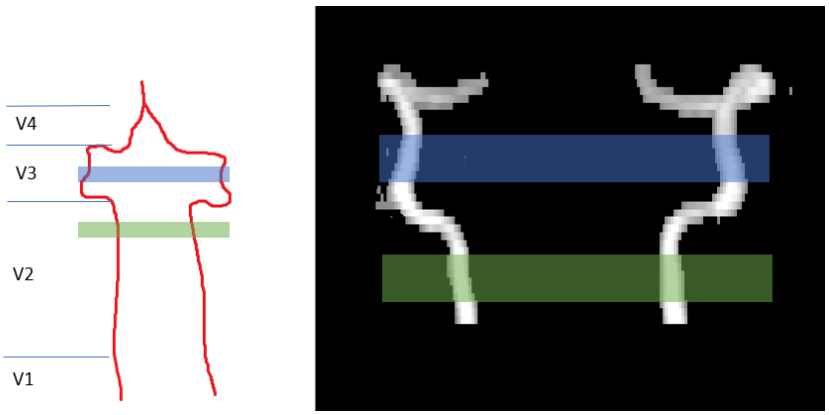

Figure 2.3: Left – schematic representation of the vertebral artery segments. Right – coronal maximum intensity projection, taken from a PC-MRA acquisition, of segment V3 and superior part of segment V2. V3 label plane in blue, V2 label plane in green.

Positioning the labelling plane as close as possible to the brain will minimise signal decay due to T1 relaxation in the labelled bolus. To achieve efficient labelling of blood, the labelling plane should be positioned away from areas of B_0 inhomogeneity (such as near the paranasal sinuses) and so that the traversing blood vessels are relatively perpendicular to it (Alsop 2015). The vertebral arteries that supply the brainstem have a tortuous course in the neck (see figure 2.3). A phase-contrast angiogram of the cervical vasculature was acquired for each participant and used to plan the position the labelling plane. Two labelling locations were compared. A superior labelling location was placed across the V3 vertebral artery segment, which is closer to the brain but where the vertebral arteries are not as consistently straight. The inferior labelling location was placed across the superior aspect of the V2 segment, which is further from the brain but also further from the effects of the paranasal airspaces. Two acquisitions using a PCASL EPI sequence were made at each labelling location (see table 2.3).

Table 2.3: SNRt according to label location

Label location	Brainstem SNRt
V2	0.22±0.07 (n=2)
V3	0.26±0.04 (n=2)

Overall, brainstem SNRt was similar between label location. Subsequent data were therefore acquired with the label located at the superior aspect of V2, to minimise the effects of the paranasal sinuses and to ensure that the vessels were as perpendicular as possible to the label plane.

Background suppression

ASL is an inherently low SNR technique. The magnitude of the difference in signal between the 'tag' and 'control' images is of the order of 1% (Alsop 2015). Subject motion between the acquisition of tag and control pairs can have a significant detrimental effect on SNR. The magnitude of the signal due to subject motion is proportional to the signal in the

unsubtracted images and is therefore much greater than the perfusion signal. Background suppression aims to remove the signal that originates from static tissues, therefore negating the effect of any such subject motion, and improving the SNR of the perfusion image. This is done by applying a series of inversion pulses before the acquisition of each tag-control pair. Background suppression inversion pulses are not always 100% efficient and can cause a reduction of as much as 5% in ASL signal (Alsop 2015). Nonetheless, when using a 3D readout the consensus review recommends the use of background suppression because it is possible to time the application of the background suppression pulses so that the longitudinal magnetisation of static background tissue passes through the null point at the same time as ASL image acquisition begins. Another benefit of a 3D readout is that background suppression is more uniform when compared to a 2D readout.

Spatial resolution

Maximising spatial resolution is important to enable differentiation between regions of the brainstem and to minimise partial voluming from CSF and vascular structures in the basal cisterns surrounding the brainstem. However, the inherently low SNR of brainstem MRI dictates that voxel size is not so small that noise dominates the signal. The dimensions of brainstem sub-structures are typically smaller in the axial plane than they are craniocaudally, therefore slice thickness was relaxed slightly for both BOLD and ASL acquisitions, whilst retaining the maximum possible in plane resolution.

Readout

Segmented 3D readouts are recommended because they provide better background suppression than 2D readouts (Alsop 2015). Vidoretta et al. have developed a PCASL sequence with a 3D turbo spin-echo readout (Vidorreta 2017). They have demonstrated the ability of this sequence to obtain high-resolution whole-brain CBF maps in a clinical population. The sequence uses an interleaved spiral acquisition, and each interleaf can be acquired sequentially within a single TR (single-shot) or over multiple TRs (multi-shot). In theory, single-shot acquisitions provide better temporal resolution. This might be useful in a

functional study that utilises a rapid-onset task. In the present study, the CBF response to hypercapnia occurs over a period of minutes and temporal resolution is therefore less important than spatial resolution, with the caveat that a lower temporal resolution might exacerbate physiological noise contributions and/or the effect of participant head motion. This sequence was tested in 2 participants using 2 in-plane interleaves acquired over 2 shots compared to 4 interleaves acquired over 4 shots, with spatial resolution of 2.5 x 2.5 x 3.1 mm. Ultimately, the 4-shot acquisition was found to provide superior brainstem SNRt ($SNRt_{4\text{-shot}}$ = 1.39 ± 0.08, $SNRt_{2\text{-shot}}$ = 0.67 ± 0.25, table 2.4. A further benefit of spiral readouts is that they are less sensitive to motion than cartesian readouts, an important consideration in the vicinity of the brainstem (Block 2014).

Table 2.4: SNRt compared between a 2-shot and 4-shot acquisition.

Participant	Shots	Brainstem SNRt
1	2	0.84
1	4	1.44
2	2	0.50
2	4	1.33

Parallel imaging

Parallel imaging involves the use of multiple receive coil elements to detect the MRI signal. Information about the spatial position of each element combined with its sensitivity is used to aid image reconstruction whilst enabling undersampling of k-space. This enables faster image acquisition (Elster 2022) with a shorter TE. The 3D spiral readout described above (Vidorreta 2017) applies parallel imaging with generalized autocalibrating partially parallel acquisitions (GRAPPA) reconstruction (Griswold 2002) to shorten TE, resulting in reduced through-plane blurring (figure 2.4), faster image acquisition, and subsequently enabling higher spatial resolution. Shorter TE might also help reduce susceptibility artefacts around the brainstem.

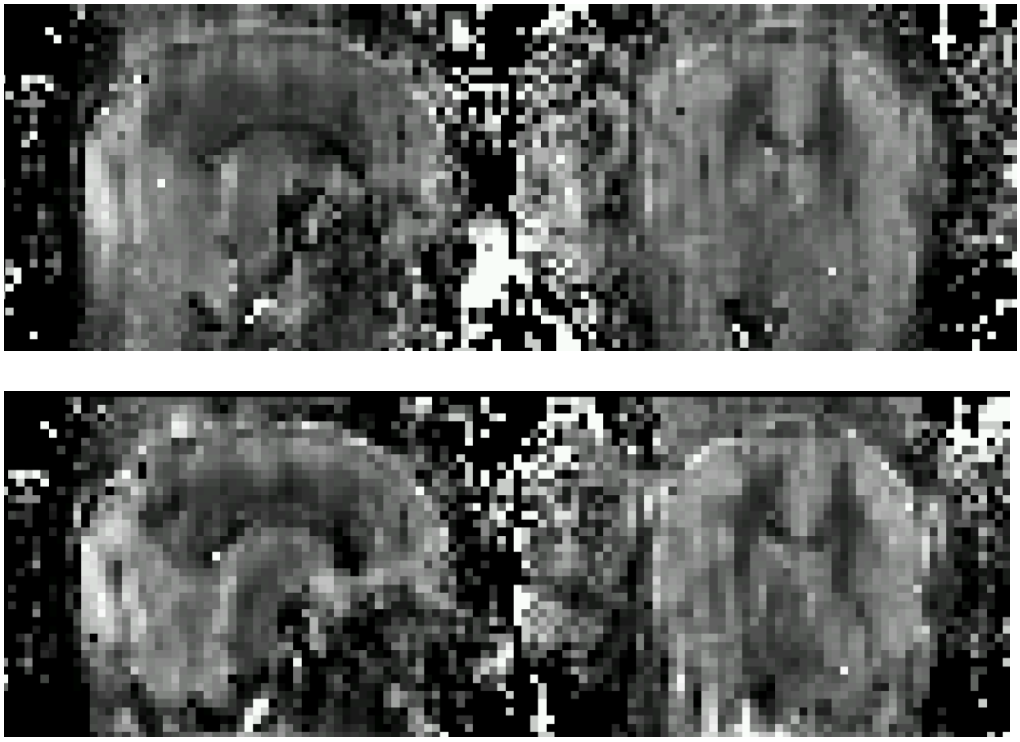

Figure 2.4: 1D-acceleration with GRAPPA = 2 (bottom) reduces blurring in the superior-inferior direction compared to no acceleration (top), as exemplified by the improved grey-white matter differentiation seen on the sagittal view in the lower image.

Post-processing optimisation

In addition to the processing methods discussed in section 2.2.1, regions containing cerebrospinal fluid were removed from calibrated perfusion maps using a mask that was generated using tissue-type segmentation (performed using FSL FAST (Zhang 2001)) of the structural data, subsequently co-registered to functional space.

2.2.4. Measurement of brainstem ASL

Based on the considerations discussed above a PCASL sequence with background suppression and a 3D RARE (turbo spin-echo) Stack-Of-Spirals readout (Vidorreta 2017) was used, with the following sequence parameters. 3D RARE spiral readout with 4 in-plane interleaves acquired over 4 shots (see figure 2.5), repetition time (TR) = 4250 ms, echo time (TE) = 10 ms, matrix =96 x 96, voxel size = 2.5 x 2.5 mm^3, slice thickness = 3.1 mm, flip angle = 90°, whole brain coverage. Shimming was performed using a manually defined region of

interest centred on the brainstem to maximise B_0 field homogeneity around the brainstem. Perfusion weighting was performed with single-TI PCASL labelling scheme, bolus duration = 1800 ms, post-label delay = 1800 ms, 10 tag/control pairs with an acquisition time (TA) of 7 mins. A phase-contrast sequence (TR = 40.7 ms, TE = 5.6 ms, FA = 10°, resolution = 0.47 x 0.47 x 1.3 mm, covering the V2 segments of the vertebral arteries and the cervical portions of the internal carotid arteries) was acquired to guide ASL label placement. The label was placed across the superior aspect of the V2 segment as shown in figure 2.3.

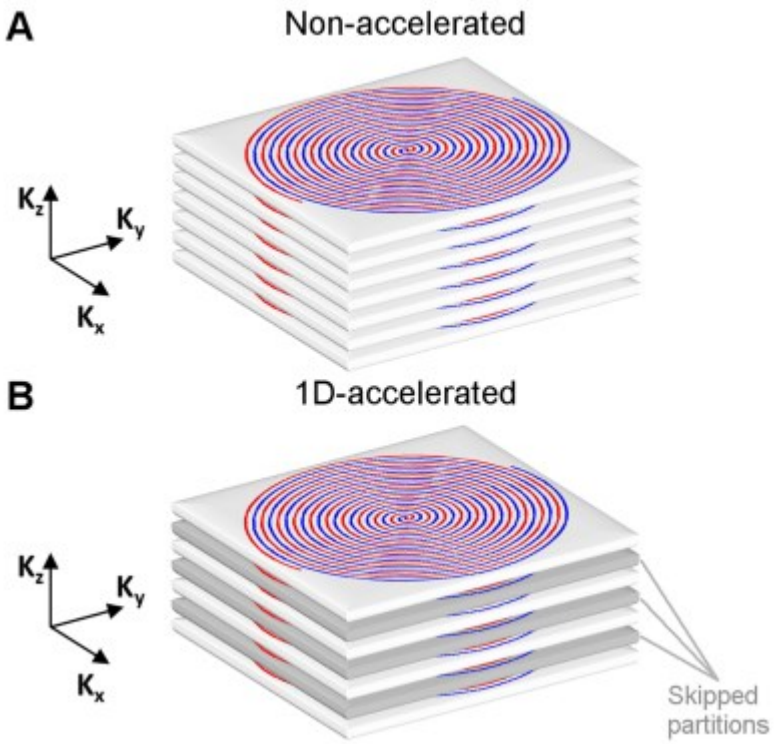

Figure 2.5: from (Vidorreta 2017). 1D acceleration is applied in the k_z direction using GRAPPA. Each k_z partition is divided into several spiral interleaves. In a single-shot acquisition all interleaves are acquired sequentially using a turbo-spin echo acquisition within a single TR. In a multi-shot acquisition each spiral is acquired after separate 90° RF pulses.

As Whole-brain calibrated perfusion maps were generated using the command-line version of the BASIL toolkit (oxford_asl) (Chappell 2009) as previously described.

Regional perfusion values were then obtained by applying brainstem and frontal grey matter masks co-registered to functional space to the calibrated perfusion data. To further control for noise contributions, voxels that contained perfusion values less than zero or

outlying perfusion values (defined as values 1.5 times above or below the interquartile range) were excluded from calculation of the mean.

2.2.5. Measurement of cerebrovascular reactivity

For the first five participants, hypercapnia was induced via the Respiract gas delivery system (Fisher 2016), with a target $ETCO_2$ approximately 8 mmHg above the participant's baseline. As discussed in the introductory chapter of this thesis, there are two types of CO_2 delivery systems used in research practice (Liu 2019). In theory, fixed expired systems such as the Respiract system enable better control of $ETCO_2$, The Respiract system involves a calibration process which aims to fix the participant's baseline $ETCO_2$. This involves delivering a slightly increased concentration of CO_2 to the participant to enable the concentration of inspired CO_2 ($FiCO_2$) to be modulated in response to fluctuations in $ETCO_2$. In our experience, this process consistently elevated participants' baseline $ETCO_2$ away from its true value. There is evidence that both BOLD and ASL-CVR are sensitive to baseline levels of arterial CO_2 (Halani 2015). There may then be a degree of uncertainty whether subsequent CVR measurements obtained using the Respiract system are physiologically representative. Furthermore, participants were subsequently less tolerant to a further increase in 8 mmHg in their $ETCO_2$ above an already elevated baseline. For these reasons, an in-house gas delivery system was used for the final five participants. A Matlab script was used to control the concentration of gases from four gas cylinders located in the MRI control. These gases subsequently passed through mixing and humidification chambers, then into a breathing circuit connected to a facemask covering the participant's nose and mouth. A sampling line connected to the facemask was used to monitor $ETCO_2$ and ETO_2. During normocapnia participants breathed medical air (20.9% oxygen with the remainder being nitrogen). To induce hypercapnia a mixture of medical air with 5% CO_2 was administered. Baseline $ETCO_2$ was measured at the start of each scan session with participants breathing medical air for approximately 5 minutes.

Two separate ASL acquisitions were obtained. The first was acquired with the participant breathing medical air at normocapnia. Following this a gas mixture containing 5% CO_2 was administered. The participant's increased $ETCO_2$ was allowed to stabilise and then a second ASL acquisition was obtained in hypercapnia. To calculate regional CVR, regional mean

CBF during normocapnia was subtracted from CBF during hypercapnia and subsequently divided by the difference between the mean normocapnic and hypercapnic $ETCO_2$.

For BOLD-CVR, a single BOLD acquisition was obtained, with a hypercapnic stimulus paradigm consisting of two separate two-minute periods breathing 5% CO_2, interspersed with three two-minute periods of normocapnia. BOLD-CVR maps were generated as described below.

2.2.6. Physiological monitoring

ETO_2 and $ETCO_2$ were continuously monitored via a sampling line connected to the facemask. Heart rate was continuously monitored via photoplethysmography, and respiratory rate via a pneumatic respiratory belt.

2.2.7. BOLD sequence parameters

A BOLD echo planar imaging fMRI sequence with the following parameters was utilised: TR = 1200 ms, TE = 30 ms, voxel size = 2 x 2 x 2.5 mm, multiband factor = 4, GRAPPA = 4 to minimise acquisition time and susceptibility artefacts.

Physiological noise correction was performed using linear regression to remove signal variance related to heart rate, respiratory volume per unit time and fluctuations related to the phase of the respiratory and cardiac cycles (RETROICOR) (Glover 2000). Distortion correction was performed using a pair of phase-encode reversed images and the FSL tool topup. To remove scanner drift BOLD data was high-pass filtered with a cutoff of 240 seconds (240 s = twice the length of a single hypercapnia/normocapnia cycle in the stimulus paradigm). There is a lag between changes in $ETCO_2$ and BOLD signal and therefore the $ETCO_2$ trace was time-shifted to maximise correlation with the mean BOLD timeseries in the frontal grey matter (see figure 2.6), as previously described by Yezhuvath et al. (Yezhuvath 2009). The shifted $ETCO_2$ trace (in units of mmHg) convolved with a haemodynamic response function was used as a regressor in general linear model (using FSL FEAT) (equation 2.4). The mean BOLD timeseries from a manually drawn CSF mask was also included in the GLM as a covariate.

$$BOLD\ signal = \beta_1 \cdot PETCO_2 + CSF + \varepsilon \quad (2.4)$$

where ε represents the variance in the BOLD signal not explained by the statistical model. The output of the GLM is a whole-brain map of the statistical parameter β_1, which represents the unit change in BOLD signal per unit change in $ETCO_2$. These parameter maps were converted to CVR maps in units of % change in BOLD signal per mmHg CO_2 by dividing them with the mean of the BOLD timeseries, then multiplying by 100:

$$CVR\ (\%\Delta BOLD/mmHgCO_2) = 100\ x\ \frac{\beta_1}{mean\ BOLD\ timeseries}. \quad (2.5)$$

Only clusters where there was a statistically significant fit of the model to the data were retained. Finally, regional CVR (medulla, pons, midbrain and frontal grey matter) was calculated by applying ROI masks to the CVR maps.

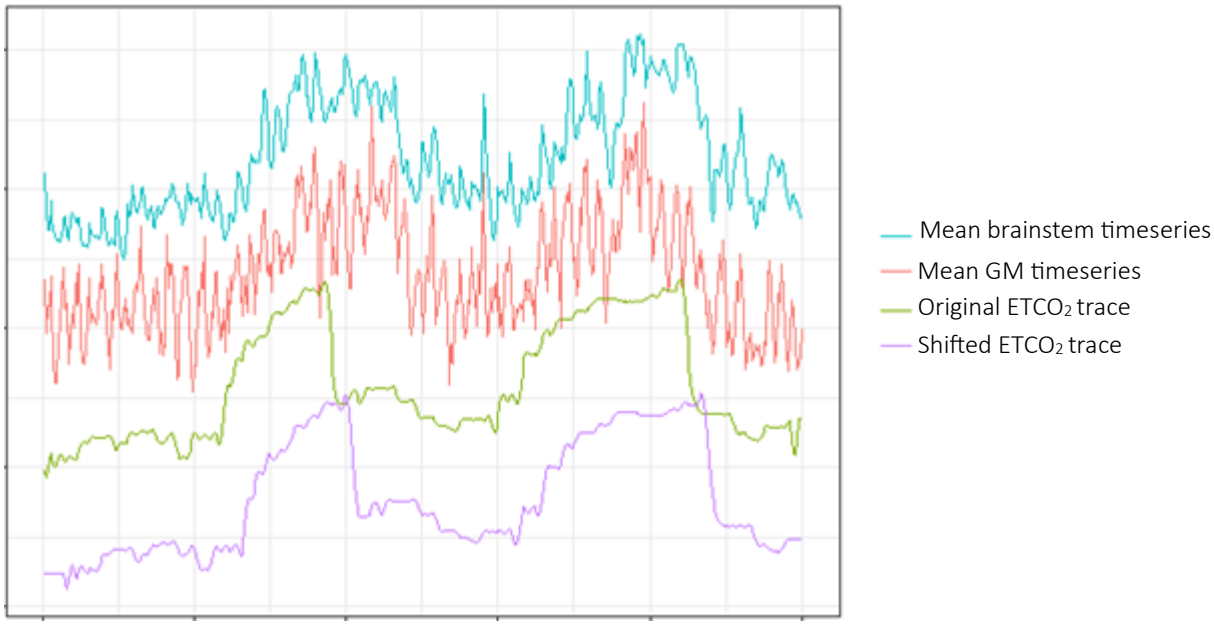

Figure 2.6: Representative example of $ETCO_2$ trace before (green) and after (purple) shifting to account for lag between changes in $ETCO_2$ and BOLD signal. Mean GM (blue) and brainstem (red) timeseries.

2.2.8. Statistical analysis

Statistical analysis was performed using the R software package (R-core-team 2022). Regional ASL CBF data was compared using two-way ANOVA with brain region and CO_2 status (hypercapnic or normocapnic) as independent variables. An interaction term between region and CO_2 status was also included to examine whether CVR varied according to region, or whether the regional variation in CBF varied between normocapnia and hypercapnia. BOLD data were analysed using a GLM in FSL FEAT as described above. Unless otherwise specific, values are specified as mean ± standard error (SE) and standard deviation (SD).

2.3. Results

2.3.1. Measuring brainstem CBF using ASL

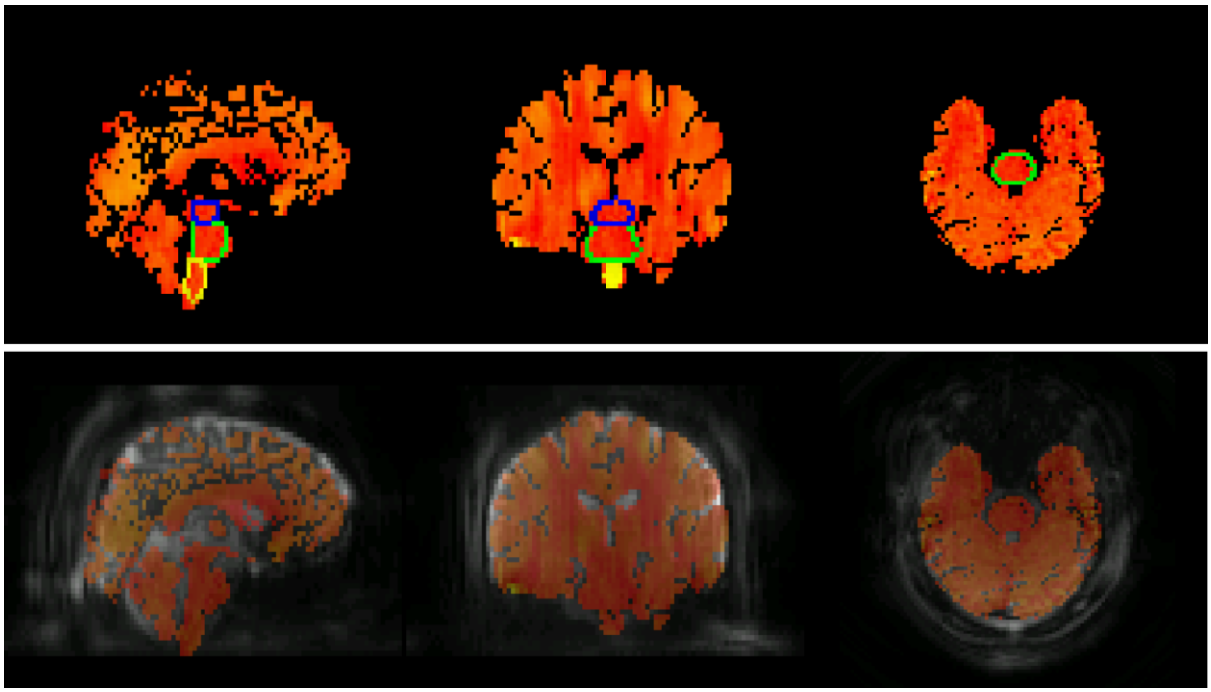

Figure 2.7: Calibrated perfusion map with outlines of brainstem ROIs (medulla = yellow, pons = green and midbrain = blue), demonstrating accuracy of co-registration between the ROI masks and perfusion data. The ROIs are aligned with the brainstem and do not encroach on extra-axial structures such as the adjacent basal cisterns.

The mean $ETCO_2$ during hypercapnia (48.8 ± 0.4SE,2.5SD mmHg) was significantly higher than during normocapnia (41.0 ± 0.2SE,1.5SD) ($t = 16.6$, $df = 65.0$, p-value $< 2.2 \times 10^{-16}$). Mean frontal grey matter CBF during normocapnia was 40.84 mL/100g/minute ±

1.3SE,10.0SD, and mean brainstem CBF during normocapnia was 37.4 mL/100g/minute ± 1.6SE,12.2SD.

Two-way ANOVA with hypercapnia/normocapnia status and brain region as dependent variables revealed that mean CBF across all regions was significantly higher during hypercapnia than during normocapnia ($CBF_{hypercapnia}$ = 45.9 mL/100g/minute ± 12.0SE, 1.9SD v $CBF_{normocapnia}$ = 33.6 mL/100g/minute ± 9.9SE, 1.6SD, F(1) =26.8, p = 2.0 x 10^{-6}, partial η^2 = 0.27). Post-hoc paired t-tests with a Holm correction for multiple comparisons revealed that CBF is significantly higher in hypercapnia in all four ROIs (figure 2.8 and table 2.5). Furthermore, each regional increase in CBF during hypercapnia corresponds to a large effect size (table 2.5). Figure 2.9 demonstrates that CBF was increased within each participant during hypercapnia, except for one participant in whom there was a reduction in brainstem CBF during hypercapnia.

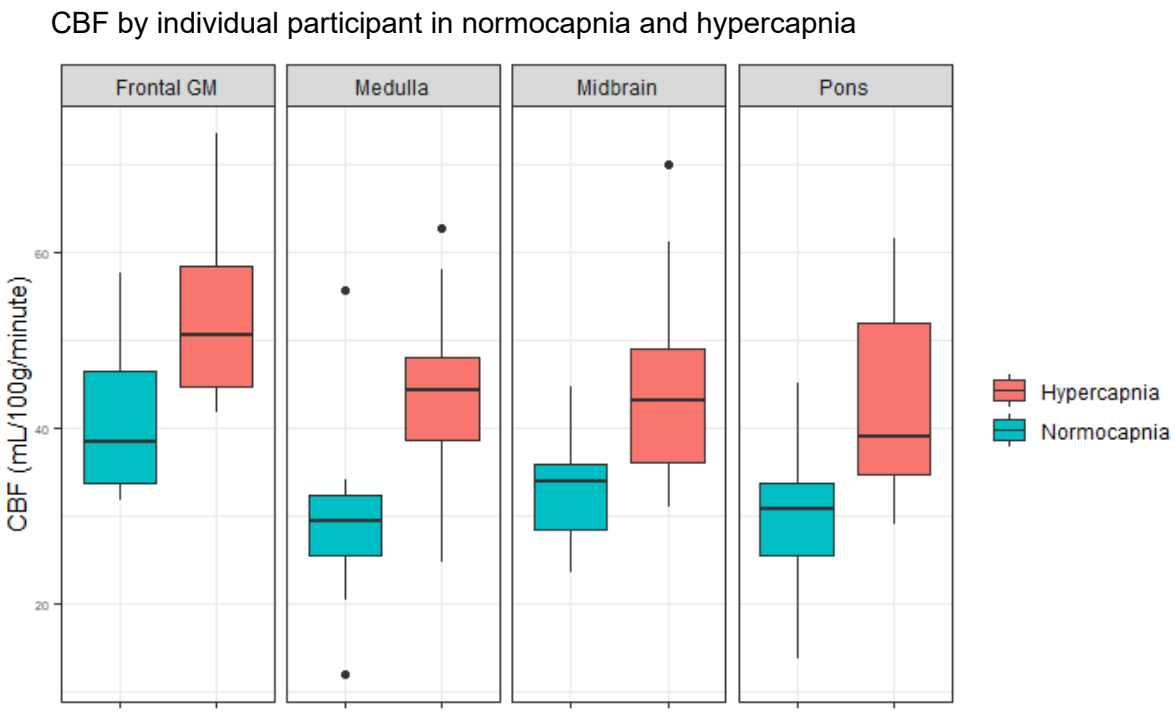

Figure 2.8: Regional CBF according to CO_2 status. Regional CBF is significantly higher in hypercapnia.

Table 2.5: CBF is significantly higher, and the effect size is large, in all four ROIs during hypercapnia.

Region	Normocapnia CBF (mL/100g/minute)	Hypercapnia CBF (mL/100g/minute)	t	dF	Cohen's d	p	Holm threshold for p
Frontal GM	**40.83**	**52.52**	6.91	9	**1.18**	**7×10^{-5}**	0.05/4 = 0.0125
Midbrain	**33.60**	**45.27**	4.33	9	**1.16**	**0.002**	0.05/3 = 0.0166
Pons	**30.44**	**42.70**	3.82	9	**1.15**	**0.004**	0.05/2 = 0.0125
Medulla	**29.60**	**43.20**	3.71	9	**1.15**	**0.005**	0.05/1 = 0.0500

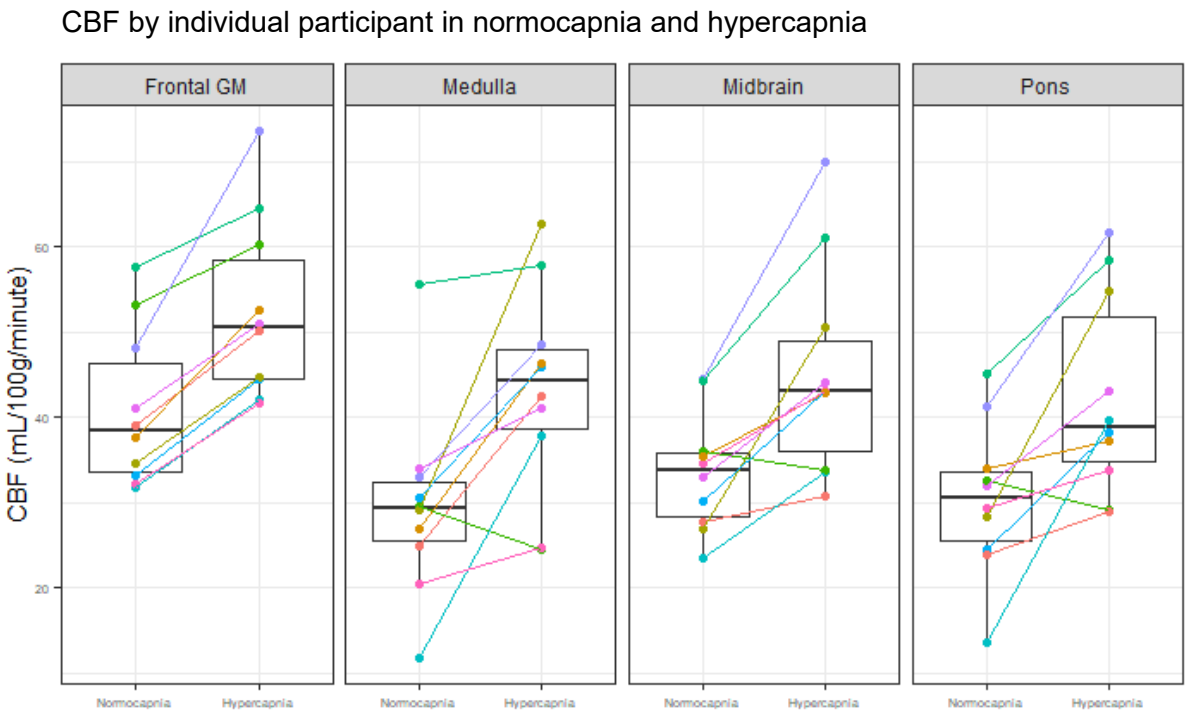

Figure 2.9: CBF is increased in hypercapnia in all datasets except for one. In this one exception, brainstem CBF was measured to be lower during hypercapnia.

ANOVA comparing CBF across the brain regions were also applied separately to the normocapnia and hypercapnia data, which revealed a pattern of non-significant regional variation in CBF (tables 2.6 and 2.7).

Table 2.6: Pairwise t tests comparing regional CBF, data from normocapnia only.

Mean CBF (mL/100g/minute)		t	dF	p	Holm threshold for p
Frontal GM = 40.84	Pons = 30.44	2.57	17.99	**0.019**	0.008
Frontal GM = 40.84	Medulla = 29.60	2.44	17.30	**0.025**	0.010
Frontal GM = 40.84	Midbrain = 33.61	1.98	16.83	**0.064**	0.013
Midbrain = 33.61	Medulla = 29.60	0.96	15.07	**0.354**	0.017
Pons = 30.44	Midbrain = 33.61	-0.88	17.03	**0.390**	0.025
Pons = 30.44	Medulla = 29.60	0.19	17.12	**0.855**	0.05

Table 2.7: Pairwise t tests comparing regional CBF, data from hypercapnia only.

Mean CBF (mL/100g/minute)		t	dF	p	Holm threshold for p
Frontal GM = 52.52	Pons = 42.47	2.00	17.79	**0.061**	0.008
Frontal GM = 52.52	Medulla = 43.19	1.82	17.62	**0.086**	0.010
Frontal GM = 52.52	Midbrain = 45.28	1.40	17.59	**0.178**	0.013
Pons = 42.47	Midbrain = 45.28	-0.52	17.96	**0.611**	0.017
Midbrain = 45.28	Medulla = 43.19	0.38	18.00	**0.709**	0.025
Pons = 42.47	Medulla = 43.19	-0.13	17.97	**0.897**	0.05

There is no significant effect of the interaction between CO_2 status and brain region on CBF ($F(3) = 0.37$, $p = 0.99$, partial $\eta^2 = 0.002$). This implies that the difference in CBF between normocapnia and hypercapnia (i.e. ASL CVR) does not significantly vary between brain regions. It also implies that the pattern of regional distribution in CBF does not significantly vary between normocapnia and hypercapnia.

Table 2.8: Sub-group comparison of Respiract v in-house gas delivery system for $ETCO_2$ and CBF. There is no statistically significant difference in frontal GM or brainstem CBF between the Respiract and in-house systems during normocapnia or hypercapnia. $ETCO_2$ is significantly higher during hypercapnia when using the in-house system, possibly due to tighter control of the target $ETCO_2$ that is possible with the Respiract (reflected in the lower standard deviation of the hypercapnic $ETCO_2$ values of the Respiract system compared to the in-house system).

	Normocapnia					Hypercapnia				
	Respiract	In-house	t	df	p	Respiract	In-house	t	df	p
$ETCO_2$ (mmHg)	40.74 ± 1.10	41.34 ± 1.88	1.39	38.72	0.17	47.24 ± 1.18	50.28 ± 2.56 ±	5.39	33.58	$5x10^{-5}$
Mean frontal GM CBF (mL/100g/minute)	39.35 ± 8.22	42.33 ± 10.77	0.49	7.48	0.64	49.88 ± 7.29	55.14 ± 13.51	0.77	6.14	0.47
Mean brainstem CBF (mL/100g/minute)	29.30 ± 3.02	33.13 ± 12.03	0.69	4.50	0.52	39.07 ± 10.54	48.23 ± 10.60	1.37	8.00	0.21

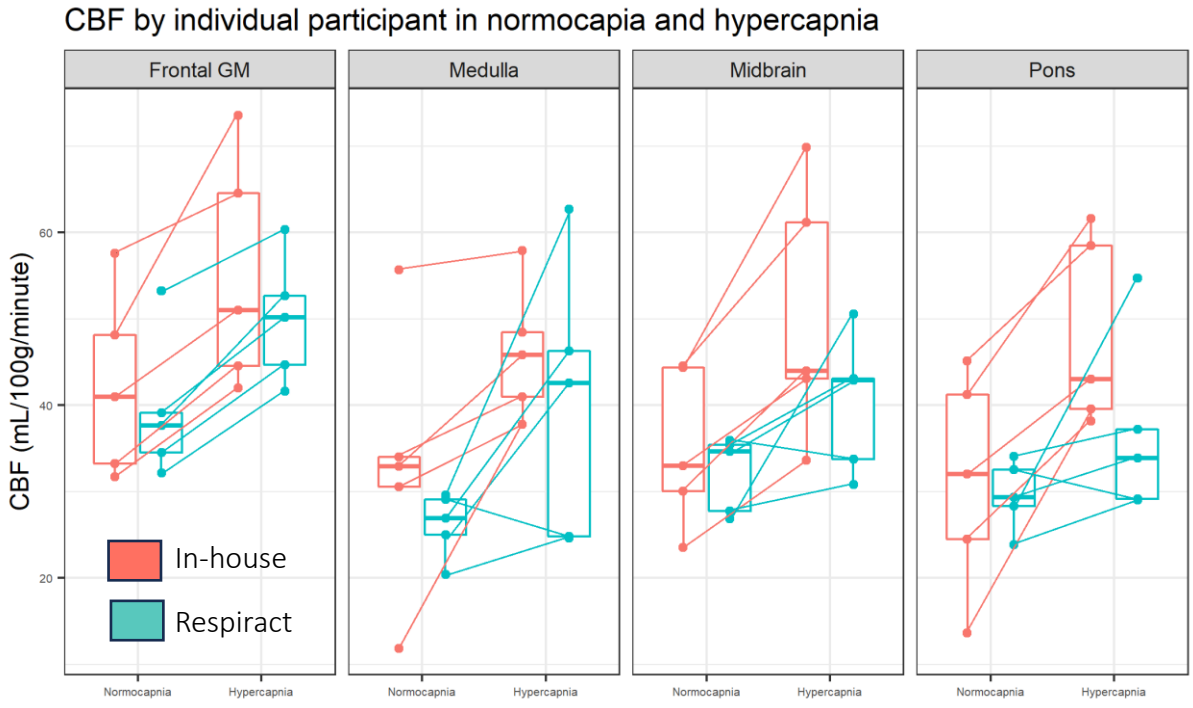

Figure 2.10: CBF is increased in hypercapnia in all datasets acquired using the in-house gas delivery system. The only datasets in which there is a reduction in CBF during hypercapnia was acquired using the Respiract system.

2.3.2. ASL CVR

Regional mean ASL CVR values are as follows: frontal grey matter CVR = 3.82 %ΔCBF/mmHg ± 0.40SE,1.28SD, medulla CVR = 6.50 %ΔCBF/mmHg ± 2.12SE,6.72SD, pons CVR = 5.67 %ΔCBF/mmHg ± 1.80SE,5.70SD, midbrain CVR = 4.35 %ΔCBF/mmHg ± 1.18SE,375SD. One-way ANOVA revealed no statistically significant difference in CVR between the four regions of interest ($F(3) = 0.28$, $p = 0.98$, partial $\eta^2 = 0.006$).

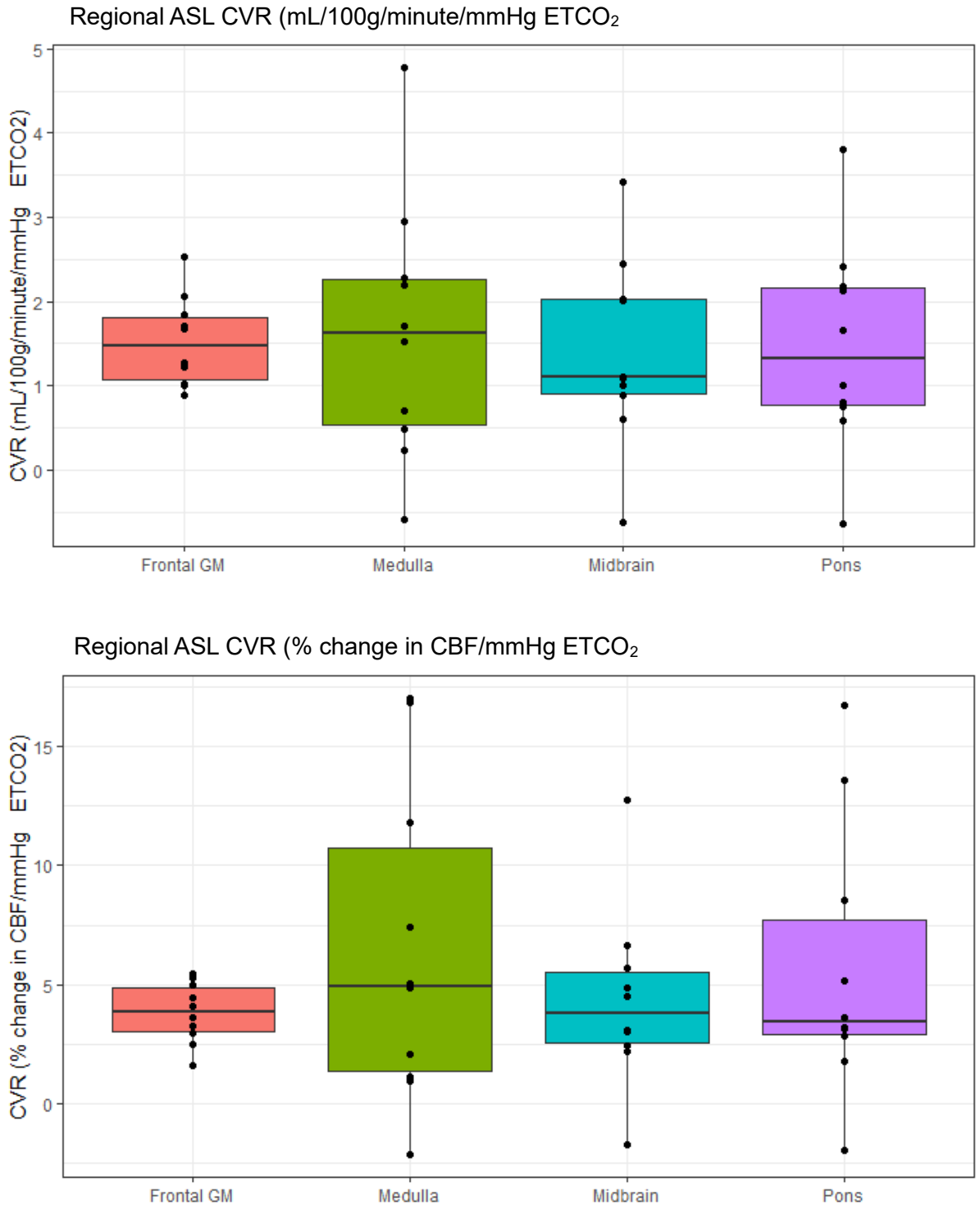

Figure 2.11: CVR in units of mL/100g/minute/mmHg CO_2 (top) and, to facilitate comparison with BOLD CVR measurements, % change in CBF per mmHg (bottom). Two-way ANOVA revealed no statistically significant difference in CVR across the four regions.

There is no significant difference in ASL CVR between the Respiract and in-house gas delivery cohorts in the frontal grey matter (in-house mean = 3.52 %ΔCBF/mmHg, Respiract mean = 4.12 %ΔCBF/mmHg, t =-0.72, df = 6.52, p=0.49) or in the brainstem (in-house mean = 5.98 %ΔCBF/mmHg, Respiract mean = 7.02 %ΔCBF/mmHg, t =-0.23, df = 7.74, p=0.82) (figure 2.12).

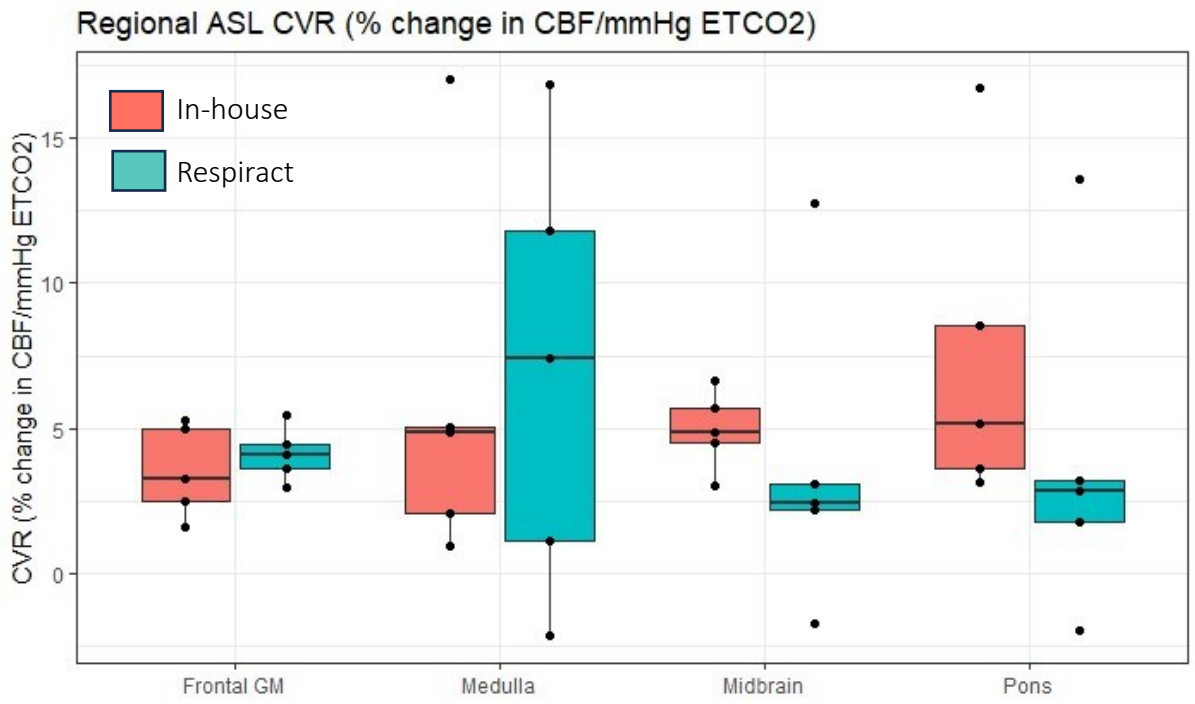

Figure 2.12: Comparison between ASL CVR values obtained using the Respiract system and the in-house gas delivery system (expressed as % change in CBF per mmHg). There is no statistically significant difference between frontal grey matter or brainstem ASL CVR values obtained using the two systems.

2.3.3 BOLD CVR

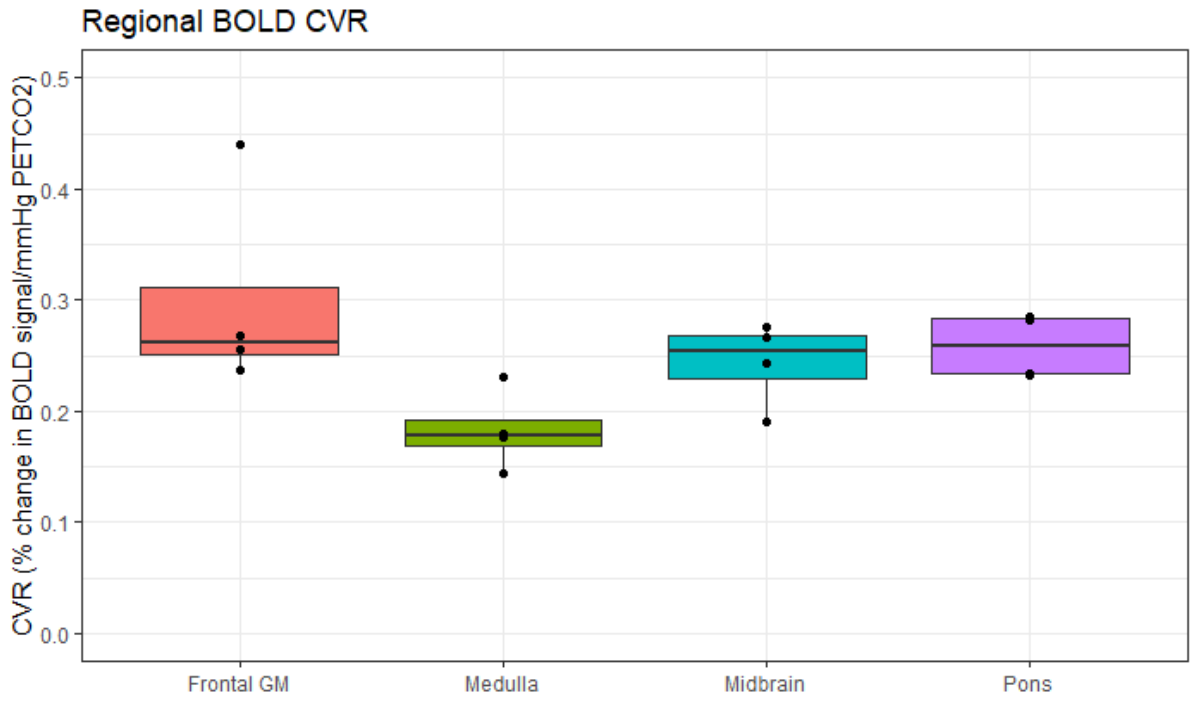

Figure 2.13: BOLD CVR in four participants. BOLD signal increased during hypercapnia across all brain regions in all four participants. CVR values are in agreement with previous measurements in the literature.

Regional mean BOLD values are as follows: frontal grey matter CVR = 0.30 %ΔBOLD/mmHg ± 0.05SE,0.09SD, medulla CVR = 0.18 %ΔBOLD/mmHg ± 0.02SE,0.04SD, pons CVR = 0.26 %ΔBOLD/mmHg ± 0.01SE,0.03SD, midbrain CVR = 0.24 %ΔBOLD/mmHg ± 0.02SE,0.04SD. One-way ANOVA revealed no statistically significant difference in CVR between the four regions of interest ($F(3) = 3.05$, $p = 0.07$, partial $\eta^2 = 0.44$).

In summary, hypercapnia induces a significant increase in CBF in the frontal grey matter and all three brainstem regions, and the corresponding effect size is large. Regional brainstem ASL CBF is consistently increased in hypercapnia in every participant except for one case in which brainstem ASL CBF was lower during hypercapnia. There is no significant regional difference in ASL CVR or in BOLD CVR.

2.4. Discussion

We have successfully applied ASL to measure regional brainstem CVR. The ISMRM Perfusion Study Group's consensus recommendations were used as a guideline, and we explored various hardware and sequence parameters to ensure that the ASL sequence was tailored towards measuring brainstem CBF. Three head coils were compared to ensure that hardware selection was optimal. The optimal post label delay was explored using measurements of brainstem ATT made using a multi-TI ASL acquisition. A PLD of 1800 ms is consistent with ISMRM recommendations (Alsop 2015) and is long enough to avoid contamination from residual basilar artery signal and allow transition of the labelled arterial bolus to the microvascular circulation. Label location was selected based on comparison between label placement at two locations along the vertebral arteries. The superior aspect of the V2 vertebral artery segment was selected over the tortuous V3 segment where vessels running parallel to the imaging plane might lead to suboptimal labelling. The fast spin-echo readout employed by the ASL sequence enables rapid imaging and high temporal resolution. With a spatial resolution of 2.5 x 2.5 x 3.1 mm we were able to demonstrate a significant hypercapnia-induced increase in ASL CBF in the medulla, pons and midbrain in nine out of ten participants (see figures 2.8 and 2.9 and table 2.5). In the tenth participant, whilst grey matter CBF increased during hypercapnia, brainstem CBF was measured as being lower (figure 2.9). As previously discussed, brainstem ASL SNR is inherently low, therefore any within-participant factor (for example movement or perhaps variations in anatomy that place the brainstem outside the area of maximal coil sensitivity) that further compromises SNR might defeat our attempt to elicit a robust brainstem CBF response to hypercapnia. Accurate measurement of brainstem CBF and CVR on the scale of small brainstem nuclei which are of the order of millimetres in size is unlikely to be feasible using the currently available ASL sequence parameters at 3T. We decided to focus on optimising accurate measurements within the three larger regions of interest (medulla, pons and midbrain) so that we can be confident that our CBF and CVR measurements are accurate and robust, rather than obtaining voxelwise maps of brainstem CBF and CVR that are potentially unreliable. The CBF response to hypercapnia is temporally delayed (Rostrup 2000), especially in white matter, therefore high spatial resolution is more important than temporal resolution. ASL data was therefore acquired with 4 in-plane interleaves acquired over 4 shots to reduce signal loss due to T2 and

T2* decay, improving SNR and enabling higher spatial resolution (Vidorreta 2017). In regions such as the brainstem which are especially vulnerable to susceptibility artefact due to B_0 inhomogeneity this might also reduce signal dropout and distortion (Vidorreta 2017). There is a risk of head motion between multiple shots, but in a comparison of 4- and 2-shot acquisitions, brainstem $SNR_{temporal}$ using a 4-shot acquisition was higher. Rigorous post-processing methods were also applied to ensure CBF estimates were as accurate as possible. Data were retained in their original functional space to avoid interpolation errors. Regions of interest were analysed using masks generated from each individual participant's high-resolution structural scan. Co-registration to functional space was repeated using landmark-based co-registration in cases where affine co-registration was suboptimal. CSF spaces were masked to minimise contamination of brainstem signal from structures in the basal cisterns.

Only a few previous studies have been identified that used ASL to measure absolute values of CBF in the brainstem (Warnert 2014), (Warnert 2016). Brainstem perfusion values measured here are comparable to those previously reported. Mean frontal grey matter CBF during normocapnia was 40.84 mL/100g/minute which is towards the lower end of the expected range of 40 – 100 mL/100g/minute (Alsop 2015). Mean brainstem CBF is lower than grey matter CBF (but not significantly (tables 2.6 and 2.7)), and comparable to previously reported values (37.4 mL/100g/minute ± 1.6SE,12.2SD compared to 29.1 ± 0.9 mL/100g/minute (Warnert 2016) and 31.4 ± 10.1 mL/100g/minute (Warnert 2014).

This is the first study to demonstrate the feasibility of using ASL with a hypercapnic challenge to measure regional brainstem CVR. Grey matter ASL CVR values (3.82 ± 0.40 %ΔCBF/mmHg) are in agreement with previous studies (table 2.8). Brainstem ASL CVR (5.51 ± 0.99 %ΔCBF/mmHg) is comparable to the only identified study to have previously measured brainstem ASL CVR (3.8 ± 1.8 %ΔCBF/mmHg) (Warnert 2014). A wide range of BOLD CVR values is reported in the literature (table 2.9). Frontal grey matter CVR values measured in this study (0.30 ± 0.05SE,0.09SD %ΔBOLD/mmHg) fall within the expected range. Brainstem CVR using BOLD has been studied previously (Butterbaugh 2015), (Foster 2015), but regional values were not reported.

Table 2.9: Grey and white matter ASL and BOLD CVR from previous studies

Study	Cohort	Grey matter ASL CVR (%ΔCBF/mmHg)	White matter ASL CVR (%ΔCBF/mmHg)	Grey matter BOLD CVR (%ΔBOLD/mmHg)	White matter BOLD CVR (%ΔBOLD/mmHg)
(Warnert 2014)	*10 healthy 30.7 ± 5.0 years*	3.5 ± 1.9 %			
(Leoni 2017)	*10 healthy, 30 ± 7 years*	3.28±1.43			
(Tancredi 2012)	*10 healthy, 24–33 years*	4.4 ± 0.2			
(Taneja 2020)	*32 healthy, mean age 22*	5.6 ± 0.4	5.1 ± 0.4	0.33 ± 0.01	0.19 ± 0.01
(Zhou 2015)	*16 healthy, 37.8 ± 14.3 years*	5.11 ± 0.87		0.23±0.04	
(Pelizzari 2021)	*13 healthy, 66.3 ± 10.1 years*	2.6 (1.7-3.5)		0.22 ± 0.01	
(Halani 2015)	*18 healthy, 26.3 ± 6.5 years*	1.9 ± 0.4	1.1 ± 0.3	0.05 ± 0.01	0.03 ± 0.01
(Bhogal 2016)	*16 healthy, 28 ± 3 years*			0.26 ± 0.07	0.04 ± 0.02
(Thomas 2014)	*15 healthy, 27±1.4*			0.22 ± 0.01	0.03 ± 0.002

There was no significant regional difference in ASL CVR or BOLD CVR in this study, although sample size, particularly for BOLD CVR, was low. Brainstem BOLD CVR (0.23 %ΔBOLD/mmHg ± 0.01SE,0.05SD) was non-significantly lower than grey matter CVR (0.30 ± 0.05SE,0.09SD %ΔBOLD/mmHg), whilst brainstem ASL CVR (5.51 ± 0.99 %ΔCBF/mmHg) was non-significantly higher than grey matter ASL CVR (3.82 %ΔCBF/mmHg ± 0.40). Previous studies have found BOLD CVR in white matter to be lower than in grey matter (Bhogal 2016), (Halani 2015), (Taneja 2020). White matter CVR wasn't measured in the present study, but the brainstem contains a mixture of grey and white matter. Brainstem CVR might therefore be expected to exhibit some of the same properties as subcortical white matter. Interestingly, Taneja et al. compared BOLD CVR and ASL CVR and found that whilst BOLD CVR values were significantly lower in subcortical white matter than cortical grey matter (GM CVR = 0.33 ± 0.01

%/mmHg, WM CVR = 0.19 ± 0.01 %/mmHg), there was no significant difference in ASL CVR between grey and white matter (GM ASL CVR = 5.6 ± 0.3% /mmHg, WM ASL CVR = 5.1 ± 0.4 %/mmHg) (Taneja 2020). Lower white matter BOLD CVR could be due to the confounding effect of the concurrent increase in venous blood volume that occurs alongside the increased CBF during the BOLD response. Taneja et al. suggest that although white matter may have fewer blood vessels than grey matter (Thomas 2014), this may not necessarily equate to lower vascular reactivity. Furthermore, Thomas et al. have shown that the BOLD signal response to hypercapnia is temporally delayed in white matter compared to grey matter – this might also contribute to an underestimation of BOLD CVR in regions containing white matter, including the brainstem, and could also explain lower white matter BOLD CVR (Thomas 2014). Brainstem medullary chemoreceptors are sensitive to CO_2, and therefore increased activity in these chemoreceptors during hypercapnia may also confound measurements of BOLD CVR (Pattinson 2009).

The effect of baseline physiology on CVR must also be considered when applying these methods. Halani et al. have found that baseline vascular tension affects the vasodilatory response to hypercapnia, and that this response is different when measured using BOLD and ASL CVR. The BOLD vasodilatory response was higher at resting vascular tension than during predilation or preconstriction, whereas the CBF vasodilatory response was similar at rest and during predilation, but lower during preconstriction. This has implications for measurement of CVR in pathological states such as hypertension. An elevated mean arterial pressure might increase vascular tension (Willie 2014). BOLD might therefore underestimate CVR in hypertensives compared to ASL according to Halani's findings. BOLD and ASL CVR measurements might be biased in different ways in the presence of hypertension.

2.4.1. Limitations

In our sample of ten healthy participants, there was a consistent increase in brainstem CBF in response to hypercapnia except for one case. As previously discussed, ASL is a low SNR technique, and the brainstem is especially sensitive to motion and physiological noise. Visual assessment did not reveal any obvious qualitative problem with this dataset, but it is possible that physiological noise and/or participant movement may have overwhelmed the ASL signal

response to hypercapnia in this single case. This highlights the importance of optimising ASL sequence parameters and post-processing methods when studying the brainstem and suggests that despite the efforts made here there is still room for improvement. In our experience, induced hypercapnia is generally well tolerated but can induce a sensation of breathlessness in some participants, which might contribute to head motion in the scanner. Future studies that apply ASL CVR to the brainstem might also include BOLD CVR, an inherently higher signal technique, as an adjunct to guard against loss of data in cases where ASL CVR fails. However, BOLD CVR is a complex measure of cerebral haemodynamics that is less specific to changes in cerebral blood flow.

ASL provides a direct quantitative measurement of cerebral blood flow, overcoming the confounds associated with BOLD CVR. The limitations of ASL CVR are primarily related to the inherently low SNR of ASL. Only 1% of the volume of a voxel of grey matter is made up of fresh inflowing blood in ASL (Chappell 2017). Therefore, the magnitude of the ASL signal of interest is only 1% of the overall signal intensity. Additionally, PCASL labelling efficiency is flow dependent, so the increased flow induced by hypercapnia may reduce labelling efficiency and therefore the magnitude of the CBF response to hypercapnia. Brainstem perfusion values are expected to be lower than cortical grey matter values due to the increased white-matter content of the brainstem (Thomas 2014) (a non-significant trend towards a reduced brainstem CBF was observed in this small sample). BOLD has a higher SNR but as previously discussed, it provides a non-specific measure of CBF and is itself subject to numerous confounds. The inherent challenges associated with brainstem MRI, such as physiological noise, the small size of the brainstem, artefact from adjacent vessels and CSF spaces, also confound attempt to accurately measure brainstem CVR.

2.5. Conclusion

Careful optimisation of a PCASL sequence, together with robust post-processing techniques, enables regional brainstem CBF and CVR measurements to be made. There are limitations to the application of ASL in the brainstem, and BOLD CVR might serve as an adjunct due to its higher SNR. The techniques developed in this chapter could feasibly be

applied in a future study of hypertensives to investigate the selfish brain mechanism (see Appendix 1).

3. Vertebral artery hypoplasia and brainstem blood flow in patients with hypertension

3.1. Introduction

As discussed in chapter 1, the selfish brain mechanism proposes that hypertension is a compensatory mechanism that aims to correct cerebral blood flow (CBF) to the brain by increasing systemic blood pressure via an increase in sympathetic nerve activity. The medulla plays a central role in autonomic regulation of the cardiovascular system (Varner, 1991), (Klabunde 2021), (Cechetto, 2014) – it houses the rostral ventrolateral medulla (RVLM) which, as well as being a central component of the baroreceptor reflex, is believed to be important in the generation of basal sympathetic tone (Feldman 2013). Blood supply to the medulla, and to the brainstem as a whole, is via the vertebrobasilar arteries. The paired vertebral arteries arise from the subclavian arteries before ascending in the neck, uniting at the pontomedullary junction to form the basilar artery, which subsequently ascends along the ventral surface of the pons to supply the posterior circulation of the brain via the circle of Willis.

Our group has previously demonstrated an increased prevalence of narrowing of the vertebral arteries (vertebral artery hypoplasia (VAH)) in hypertensives compared to normotensives (Warnert 2016). In the same study, whole-brain CBF was measured by calculating the flow through the vertebral and carotid arteries using phase-contrast MRI, revealing a statistically significant difference in whole-brain CBF between those with and without VAH, but only in the presence of hypertension (figure 3.1). No significant difference in whole-brain CBF between normotensives with and without VAH was found. These findings suggest an association between hypertension, VAH and a global reduction in CBF. Since the vertebral arteries predominantly supply the posterior circulation, it would be interesting to know if VAH in hypertension is specifically associated with compromised CBF to the posterior circulation, rather than to the whole brain. If this is the case, it is of further interest to determine if brainstem CBF is especially affected by VAH. VAH is associated with an increased risk of posterior circulation infarction, and there is an increased prevalence of VAH in patients with posterior circulation infarcts compared to those with anterior circulation infarcts (Park. JH, 2007). This suggests that people with VAH are susceptible to compromised posterior

circulation blood flow, whilst blood flow to other vascular territories is preserved. The brainstem is supplied by branches of the vertebrobasilar arterial system proximal to the circle of Willis, therefore unlike the cerebrum it might not benefit from collateral flow from the anterior circulation via the circle of Willis. The brainstem might therefore be especially susceptible to a reduction in CBF if VAH is present. Hypoperfusion of the brainstem could lead to dysfunction of the medullary centres involve in autonomic regulation of the cardiovascular system, which include the central components of the baroreceptor reflex arc (of which the RVLM is a key part), and in turn trigger the selfish brain mechanism.

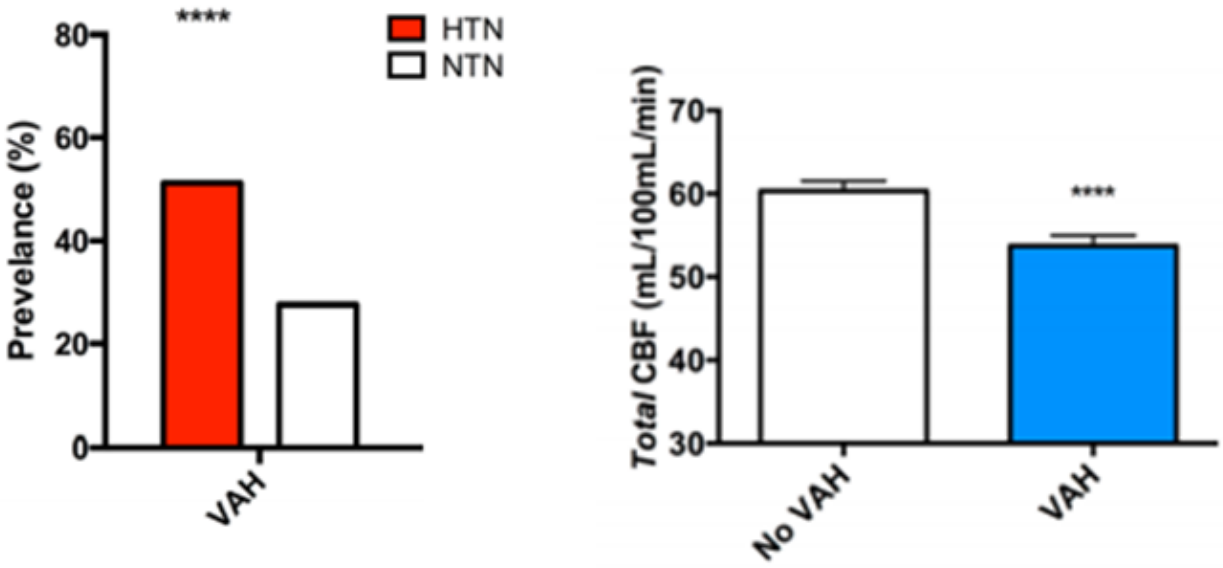

Figure 3.1: There is an increased prevalence of VAH in hypertensives (left), and whole-brain CBF, measured using phase-contrast MRI, is reduced in hypertensives with VAH (right) (Warnert 2016).

The original analysis of this data focused on whole-brain CBF values which were obtained by measuring flow through the basilar and internal carotid arteries using phase-contrast MRI. The data was revisited to investigate whether there is an association between VAH and *regional* CBF, focusing on the posterior circulation, the brainstem and other cortical centres involved in autonomic regulation of the cardiovascular system (regions that are part of the central autonomic network (see section 1.12.2)), and whether this association (if any) varies according to blood pressure status. We hypothesise that hypertensives with VAH will have lower CBF to the posterior circulation, and specifically to the brainstem, compared to

the anterior circulation. Because of the complexity of cerebral haemodynamics there are a number of scenarios compatible with the selfish brain mechanism even if our analysis does not support our primary hypothesis. For example, even if posterior circulation CBF is compromised by VAH, it remains possible that this will be masked by compensatory collateral blood flow from the anterior circulation. If this is the case, we present a secondary hypothesis that CBF will be lower across all regions in hypertensives with VAH compared with normotensives with VAH, rather than exclusively in the posterior circulation or brainstem. Similarly, the selfish brain mechanism may mask compromised cerebral haemodynamics in hypertensives by restoring CBF towards normal limits. In this case we hypothesise a significant reduction in posterior circulation CBF in participants with VAH, independent of blood pressure status. Finally, it is also possible that CBF is impaired in hypertensives due to a factor other than VAH, in which case we hypothesise a significant reduction in posterior circulation CBF in hypertensives independent of VAH.

Cerebral perfusion deficits are also associated with structural changes in the brain in the form of volumetric changes in grey and white matter density (Siepmann, 2017), (van Dalen, 2016), (Wolters, 2017), (Denier, 2013). If VAH is responsible for reduced posterior circulation CBF in hypertensives, structural changes might be seen predominantly in the posterior circulation. As a secondary objective in this chapter, volumetric analysis of grey matter density on T1-weighted data was performed. We hypothesise an association between regional cerebral blood flow deficits and volumetric changes to grey matter and expect lower grey matter density in the posterior circulation of hypertensives with VAH.

3.1.1. Summary of aims

1. To investigate whether there is an association between VAH and regional CBF in the brainstem and other cortical centres involved in autonomic regulation of the cardiovascular system.
2. To determine whether this association (if any) varies according to blood pressure status.
3. To investigate whether there is any association between grey matter density and regional cerebral blood flow deficits in the above regions.

3.2. Methods

3.2.1. Participants

Data were available for 103 participants in total. Participants had previously been recruited from University Hospitals Bristol NHS Foundation Trust following ethical approval by the National Health Service Research Ethics Committee and local Research and Development approval. All participants had provided written informed consent. Inclusion and exclusion criteria are detailed in appendix 3.

Hypertension was defined as ambulatory BP ≥ 135/85 mmHg. Normotension was defined as ambulatory blood pressure ≤ 135/85 mmHg. Treated hypertension was defined as ambulatory blood pressure ≤ 135/85 mmHg and currently being treated for hypertension (receiving at least one medication for the treatment of hypertension, including a calcium-channel blocker, beta-blocker, angiotensin-converting enzyme (ACE) inhibitor, aldosterone-receptor blocker, thiazide diuretic, potassium-sparing diuretic and/or renin inhibitor). Participant characteristics are further outlined in tables 3.1 and 3.2.

Participants had previously been grouped according to the presence or absence of VAH, which had been defined as a diameter of <2 mm uniformly throughout the visualised V2, V3 and V4 segments of either vertebral artery, as measured on time-of-flight angiography by a Radiologist with at least 6 years' experience.

15 datasets were excluded after visual quality inspection due to incomplete coverage of the brainstem within the field of view. 15 treated but uncontrolled hypertensives were also excluded from the analysis. The remaining 73 participants were subdivided into 27 normotensives, 34 untreated hypertensives and 12 treated hypertensives, to try and account for the possible confounding effects of antihypertensive medications on CBF (Webb 2019). It was not possible to consider the specific effects of individual antihypertensive medications because of the wide variety of treatment regimens in the study population, which consisted of a variety of different medications with various physiological mechanisms and vasoactive properties. Furthermore, doses and patient compliance were not known. Therefore, all treated hypertensives were considered as a single cohort, and treated but uncontrolled hypertensives were excluded.

3.2.2. MRI data analysis

3D PCASL ASL data had been previously acquired (spin echo read-out, TR/TE = 1522/4.3 ms, labelling plane 1 cm below imaging volume, voxel size 1.8 x 1.8 x 3 mm, field of view 240 x 240 x 180 mm^3, post-labelling delay 1500 ms) as part of another study (Warnert 2016). The main differences between this protocol and the protocol optimised in chapter 2 are the use of a fixed labelling position (compared to the use of a phase-contrast angiogram to tailor the label position to each participant in chapter 2), the lower voxel size of 1.8 x 1.8 x 3 mm (2.5 x 2.5 x 3.1 mm in chapter 2) and the shorter post-label delay of 1500 ms (1800 ms in chapter 2). High resolution T1-weighted structural scans were also available for each participant (voxel size 1 x 1 x 1 mm, field of view of 256 x 256 x 155 mm^3, TR/TE = 7.9/3.0 ms). The vertebral arteries had been assessed using a 3D time of flight angiogram (TR/TE = 24/2.7 ms, flip angle = 20°, voxel size = 0.34 x 0.34 x 0.5 mm, field of view = 192 x 192 x 85 mm^3), and classified as either hypoplastic (at least one vertebral artery measuring <2 mm in diameter along its entire length) or normal. The available PCASL MRI data had already been pre-processed by Warnert et al. as previously described (Warnert 2016). Whole brain cerebral blood flow values had been calculated in mL/100g/minute by applying the standard Buxton model (Buxton 2013) to the mean tag-control subtracted PCASL images (see introductory chapter).

Regions of interest for the medulla, midbrain and pons were generated separately for each participant from the high-resolution T1-weighted scan using Freesurfer's Subcortical segmentation package (Iglesias 2015). Image co-registration was performed using landmark-based registration tailored to the brainstem, as summarised below, and described in detail in chapter 4. These methods help to reduce the uncertainty introduced by i) inter-participant variations in brainstem size and structure causing a mismatch between individual ASL datasets and the standardised brainstem Harvard-Oxford atlas templates, and ii) mis-registration between the brainstem ROIs and PCASL data which could lead to non-brainstem structures such as the basilar artery or CSF being encompassed by these ROIs, which could significantly impact CBF estimates.

Brainstem perfusion was compared to other cortical and subcortical ROIs that are part of the central autonomic network. A cortical grey matter ROI in the anterior circulation (frontal grey matter) and another in the posterior circulation (occipital pole) are also included

as reference regions. Brainstem regional perfusion values were obtained using the ROIs derived from Freesurfer, as described above. The other cortical and subcortical perfusion values were obtained through co-registration of the ASL data to MNI-space, followed by application of the Harvard-Oxford cortical and subcortical structural atlases which are include as part of the FSL software package (Woolrich 2009). The Harvard-Oxford atlas contains regions of interest for the following parts of the brain that are involved in the central autonomic network; thalamus, amygdala, hippocampus, insula.

Grey matter volumetric analysis of brain-extracted T1-weighted structural images was also performed. FSL VBM was used to generate fractional grey matter density values for the regions involved in autonomic activity. Unfortunately, brainstem GM density values could not be reliably obtained using this method, possibly because of the lower grey matter density and the less distinct grey-white matter differentiation in the brainstem compared to the cortex. Mean grey matter density in each region of interest was output by applying ROIs in a similar process to that described below (see section 3.2.3 below).

3.2.3. Image co-registration

Landmark-based co-registration (LBC) is a method developed by Napadow et al. (Napadow 2006). It has been shown to improve the accuracy of brainstem co-registration between high-resolution structural data and the MNI-template. In chapter 4 we demonstrate that LBC can also be used to co-register lower resolution functional data to high-resolution structural data, resulting in an improvement in brainstem co-registration accuracy compared to a global intensity-based co-registration using FSL FLIRT. For the analysis of brainstem perfusion, LBC was therefore applied to co-register the ASL data to the T1-weighted structural data. The LBC process involves defining nine brainstem anatomical landmarks (see figure 3.2) on both the structural data and the M_0 volume of the ASL dataset. The M_0 dataset was then co-registered to the structural dataset using AFNI's 3dTagalign program (Cox 1996), using these landmarks as reference points. 3dTagalign rotates and translates the input image (the M_0 dataset) and uses the least squares method to minimise the distance between the landmarks on the M_0 dataset and those on the structural image. The transformation matrix generated by this co-registration process was then used to co-register the calibrated

perfusion data to structural space. Figure 3.3 demonstrates the improved accuracy of both brainstem and cortical registration of ASL data using this approach.

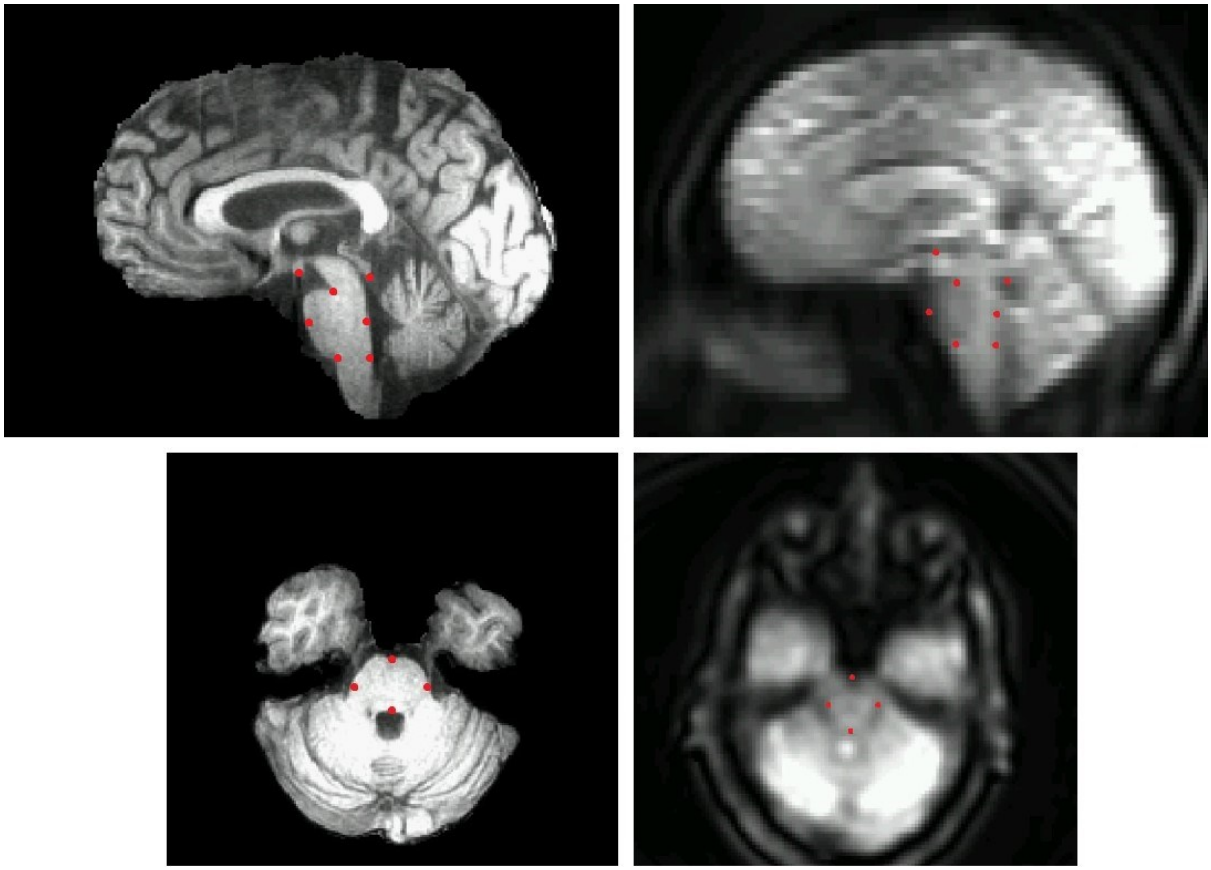

Figure 3.2: Sagittal (top) and axial (bottom) views depicting anatomical landmarks (red points) on MPRAGE (left) and M_0 (right) images, used in the landmark-based co-registration process.

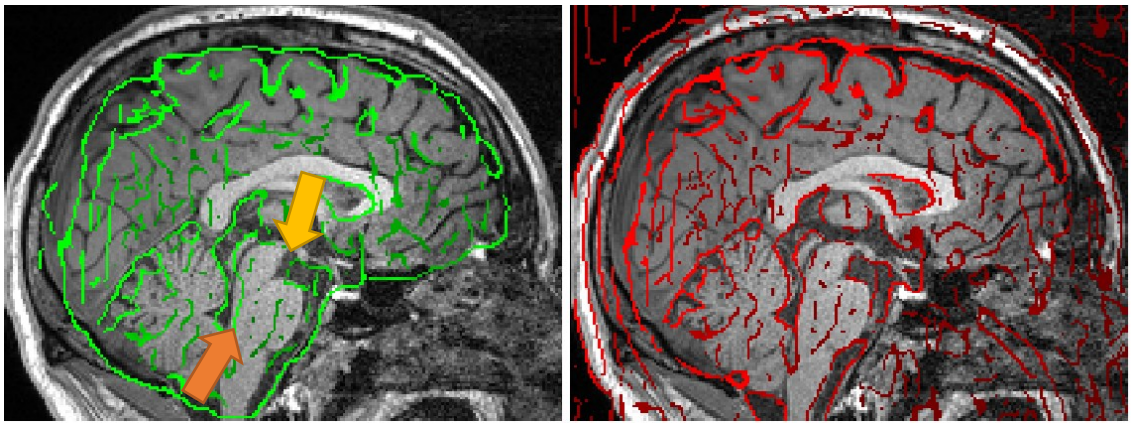

Figure 3.3: Representative example of the improved accuracy of landmark-based co-registration. The outline of the ASL data co-registered to the anatomical data are displayed overlying the anatomical image. Global intensity-based co-registration using FSL FLIRT results in misalignment of the brainstem. This is exemplified by misalignment of the ventral midbrain (yellow arrow) and dorsal surface of the brainstem (orange arrow). This is corrected by LBC (red).

LBC is tailored specifically to optimise brainstem co-registration; therefore, the cortical and subcortical perfusion values were generated after separately applying a global intensity-based two-step co-registration using FSL FLIRT. The M_0 dataset was co-registered to the structural image, and the structural image was separately co-registered to MNI-space. The affine transformation matrix generated by these two steps were then applied to the ASL data to co-register it to MNI-space.

3.2.4. Image segmentation

The Freesurfer image analysis suite (Fischl 2012), together with the 'Brainstem Substructures' module (Iglesias 2015)was used to perform segmentation of the brainstem. The 'Brainstem Substructures' module uses a probabilistic atlas that has been constructed following manual delineation of brainstem regions using well-defined anatomical landmarks to subdivide the brainstem into midbrain, pons and medulla. The result of this segmentation process was used to generate binary masks of the three brainstem regions. Brainstem masks were eroded to ensure that they were wholly within the brainstem and to exclude peripheral brainstem voxels, within which partial voluming of CSF or vascular signal may occur. These masks were applied to the perfusion data to output mean perfusion values across cortical grey matter, the medulla, pons and midbrain.

3.2.5. Statistical analysis

Statistical analysis was carried out using the R statistical package v 4.0.1 (R Core Team, 2017). Figures were generated using the tidyverse package (Wickham H, 2019).

A preliminary three-way ANCOVA comparing the effect of VAH (present or absent), blood pressure group (normotensive, treated hypertensive or untreated hypertensive) and brain region on CBF, with age, BMI and sex included as covariates, was performed to check that the assumptions of parametric statistical testing were met. Visual inspection of a QQ plot (which draws a correlation between the data residuals and the normal distribution) suggests that the model residuals are not normally distributed (figure 3.4). CBF data are inevitably zero-bounded resulting in a positive skew, which seems to be further exaggerated by outlying data-points at very high absolute CBF values (figure 3.5). Visual inspection did not reveal any

qualitative problems with the data, and therefore outliers could not be justifiably excluded from the analysis. The relatively small sample size may also be contributing to the deviation from normality. The Fligner-Killeen test (a non-parametric test of homogeneity of variance which is robust against departures from normality (STHDA 2023)) for heteroscedasticity was non-significant (chi-squared = 799.22, df = 812, p-value = 0.62).

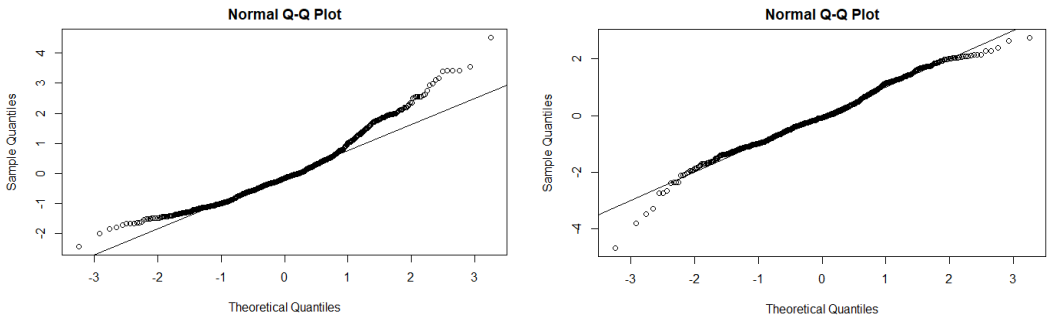

Figure 3.4: QQ plot of absolute CBF values (left) demonstrates deviation from the normal distribution. This is improved following a log transformation (right). Shapiro-Wilk test was not performed because this test is highly sensitive to even small deviations from normality if the sample size is large enough (Field 2012).

To address the non-normality of the data, a log transformation was applied to CBF values. The log transformed CBF data is negatively skewed (figure 3.5), but a QQ plot suggests a closer fit to a normal distribution (figure 3.4). Therefore, considering the improved fit to the assumption of normality after log transformation, the data was analysed by conducting ANCOVA of log CBF data.

The geometric mean is less susceptible to outliers than the arithmetic mean, and better represents the skewed data. Therefore, CBF values are expressed in terms of the geometric mean.

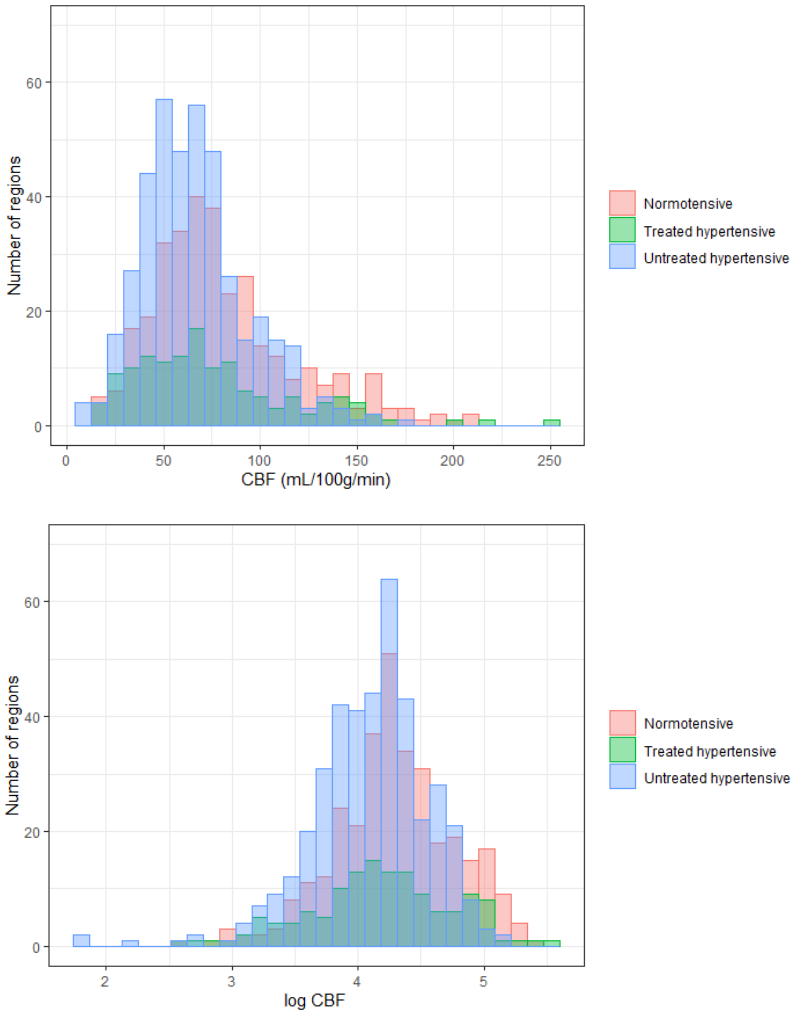

Figure 3.5: A histogram of all the mean regional CBF values across all participants (top) demonstrates the positive skew of the raw data, which is improved by applying a log transformation (bottom).

3.2.6. Standardised regional CBF, blood pressure group and vertebral artery hypoplasia.

In normotensive individuals the expected normal range of CBF is 40-100 mL/min/100 mL (Alsop 2015). As demonstrated in figures 3.5-3.8, there are many CBF values which fall outside this range and might be classed as outliers. The reason for this wide distribution in CBF values is not certain, but physiological and thermal noise might be contributing factors. If the participant moves their head between the acquisition of the tag and control ASL images, this may impact the tag-control subtracted image and subsequently the accuracy of calibrated perfusion data. The signal-to-noise ratio of ASL is inherently low because the labelled arterial bolus contributes only approximately 1-2% to the overall signal intensity in the imaging volume (Chappell 2017). Even small head movements that cause a misalignment of a few

voxels between the tag and control images might therefore significantly affect perfusion estimates. As previously discussed, the CBF data used in this analysis had already been pre-processed (Warnert 2016) but it is not stated whether pre-processing steps such as motion correction and spatial smoothing were applied. Motion correction is important to ensure accurate alignment between tag and control images before they are subtracted. Too much spatial smoothing could cause partial-voluming of non-perfusion signal, such as signal from CSF spaces in the basal cisterns and cortical sulci, into voxels at the edge of the brain.

Standardisation can alleviate some of the erroneous inter-participant variability in the global MRI signal. For example, head movement might introduce noise that confounds global CBF quantification. Head movement might affect some participants more than others and could account for at least some of the unexpectedly high CBF estimates. Issues like this that affect all parts of the brain to a similar degree may be addressed by standardising CBF values against, for example, cortical grey matter CBF. However, whilst some factors such as head movement might affect the MRI signal on a global level, if there are regional factors that vary between participants, standardisation might not help. For example, brain anatomy is variable, and some participants have bigger heads with the brainstem positioned further towards to the lower edge of the MRI head coil which could disproportionately affect brainstem SNR relative to cortical SNR. Brainstem perfusion estimates in such participants might be artificially low. Therefore, standardisation will not correct all the factors that might be confounding absolute perfusion estimates but might help to correct sources of uncertainty that affect the signal on a global level and improve our sensitivity to detect regional differences in CBF.

Therefore, to try and account for some of the inter-participant uncertainty in the absolute CBF values, a separate analysis of standardised CBF values was performed. This analysis was restricted to standardised posterior circulation CBF (specifically CBF to the brainstem and occipital pole) in order to further address the hypothesis that posterior circulation CBF is lower than anterior circulation CBF in participants with VAH. Standardisation was performed by dividing occipital pole and brainstem CBF by frontal cortical grey matter CBF within each participant. A two-way ANCOVA was conducted to compare the effect of VAH (present or absent) and blood pressure (normotensive, treated hypertensive or untreated hypertensive) on standardised posterior circulation CBF. The interaction between blood pressure group and VAH status was also modelled. Age, BMI and sex were again included as

covariates. In this analysis assumptions of normality and homoscedasticity were met, therefore no transformation of the data was necessary.

3.3. Results

*Table 3.1: Summary of participant characteristics by blood pressure group. * p < 0.05 v Normotensive group, ᵗ p < 0.05 v Untreated hypertensive group.*

	Normotensive (n=27)	Untreated hypertensive (n=34)	Treated hypertensive (n=12)
Female sex	20 (74%)	15 (44%)*	7 (58%)
Age (years)	45.5 ± 13.4	56.8 ± 12.0*	56.7 ± 8.2*
BMI (kg/m^2)	25.2 ± 3.5	27.9 ± 4.5*	28.2 ± 4.5
Ambulatory systolic BP (mmHg)	118.9 ± 8.8	147.0 ± 10.6*	124.6 ± 9.2ᵗ
Ambulatory diastolic BP (mmHg)	74.8 ± 6.2	89.6 ± 9.8*	81.8 ± 6.6*
Number with VAH	9 (33%)	19 (55%)	5 (42%)

*Table 3.2: Summary of participant characteristics according to the presence or absence of VAH. * p <0.05 v no VAH group.*

	No VAH (n=40)	VAH (n=33)
Female sex	22 (55%)	20 (61%)
Age (years)	49.8 ± 14.5	55.9 ± 10.3*
BMI (kg/m^2)	26.9 ± 4.0	26.9 ± 4.8
Ambulatory systolic BP (mmHg)	128.5 ± 13.1	130.2 ± 17.5
Ambulatory diastolic BP (mmHg)	80.2 ± 7.6	81.8 ± 12.1
Normotensive	18	9
Untreated hypertensive	15	19
Treated hypertensive	7	5

3.3.1. Absolute CBF

A three-way ANCOVA comparing the effect of VAH (present or absent), blood pressure group (normotensive, treated hypertensive or untreated hypertensive) and brain region on log CBF, with age, BMI and sex included as covariates, was performed.

There was no statistically significant three-way interaction between VAH, blood pressure group and region ($F(35) = 0.6$, $p = 0.97$, partial $\eta^2 = 0.02$) on CBF. Likewise, there was no significant two-way interaction between region and blood pressure ($F(22) = 0.2$, $p = 0.99$, partial $\eta^2 = 0.005$) or between region and VAH ($F(11) = 0.07$, $p = 0.99$, partial $\eta^2 = 0.01$).

However, there was a significant interaction between VAH and blood pressure group ($F = 8.81$, $df = 2$, $p = 0.0002$, partial $\eta^2 = 0.02$). Therefore, post-hoc tests were performed to compare the effect of VAH on CBF within each of the three blood pressure groups, and to compare CBF between the three blood pressure groups in the presence or absence of VAH. Three separate one-way ANCOVA tests were performed (normotensives, treated hypertensives, and untreated hypertensives) with VAH as the independent variable and age, sex and BMI as covariates. A Holm correction was applied, with the threshold for statistical significance set at an alpha level of 0.017 (that is $\alpha = 0.05/3$ for 3 blood pressure groups)). The effect of VAH is significant in normotensives ($p = 1.6 \times 10^{-6}$) but not in treated ($p = 0.99$) or untreated ($p = 0.83$) hypertensives (figure 3.6). Subsequent pairwise comparison confirms that mean CBF is significantly higher in normotensives with VAH (mean $CBF_{normotensive+VAH}$ = 83.0 mL/100g/min, standard deviation = 28.6, standard error = 2.9) than in normotensives without VAH (mean $CBF_{normotensive+noVAH}$ = 65.6 mL/100g/min, standard deviation = 38.3, standard error = 2.7).

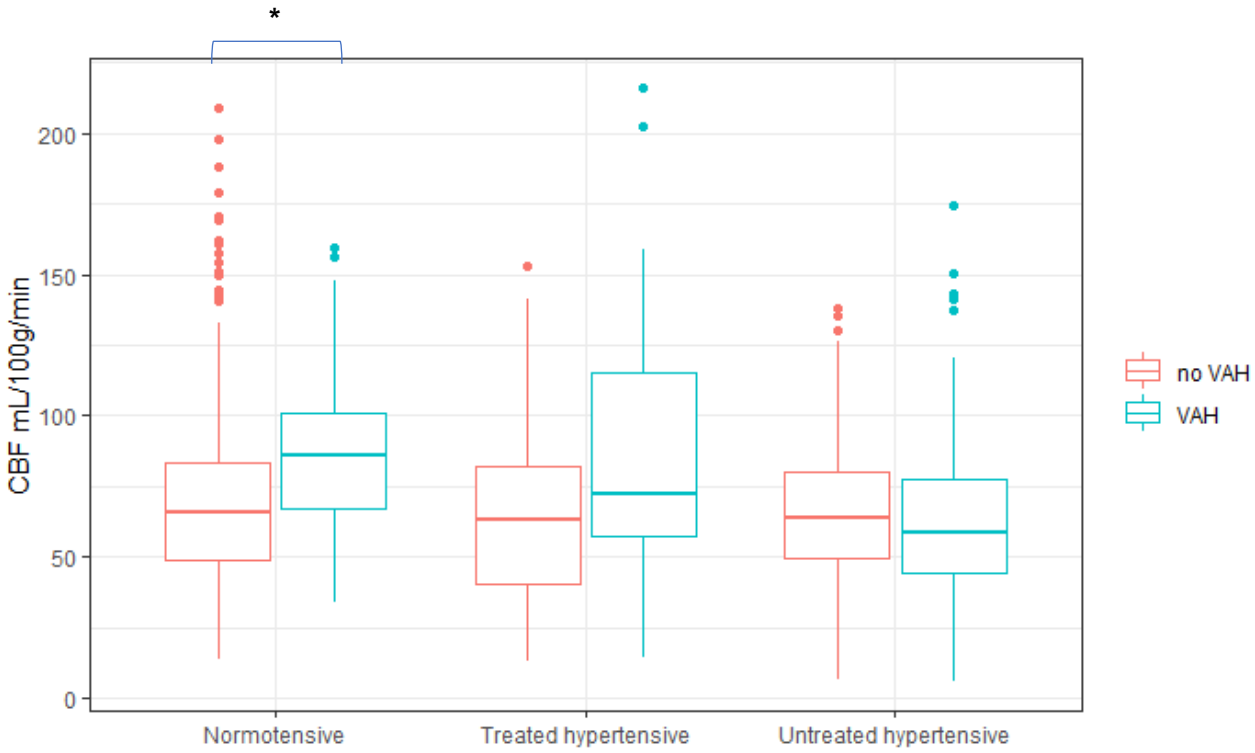

Figure 3.6: Mean CBF is significantly higher in normotensives with VAH (83.0 mL/100g/min, standard deviation = 28.6, standard error = 2.9) than in normotensives without VAH (65.6 mL/100g/min, standard deviation = 38.3, standard error = 2.7) (*).

Likewise, two separate one-way ANCOVA tests were performed (VAH and no VAH) with blood pressure group as the independent variable and age, sex and BMI as covariates, with the Holm-adjusted threshold for statistical significance set at 0.05/2 = 0.025. The effect of blood pressure group is significant in participants with VAH (p = 0.007), but not in those without VAH (p = 0.38) (figure 3.7). Pairwise comparison reveals that CBF is significantly lower in untreated hypertensives with VAH (mean $CBF_{untreated+VAH}$ = 57.6 mL/100g/min, standard deviation = 27.8, standard error = 1.9) than in normotensives with VAH (mean $CBF_{normotensive+VAH}$ = 83.0 mL/100g/min, standard deviation = 28.6, standard error = 2.9) (p = 1.4×10^{-9}), as well as in untreated hypertensives compared to treated hypertensives (mean $CBF_{treated+VAH}$ = 75.9 mL/100g/min, standard deviation = 44.9 standard error = 6.1) (p = 2.7×10^{-4}), with no significant difference between normotensives and treated hypertensives (p = 0.26).

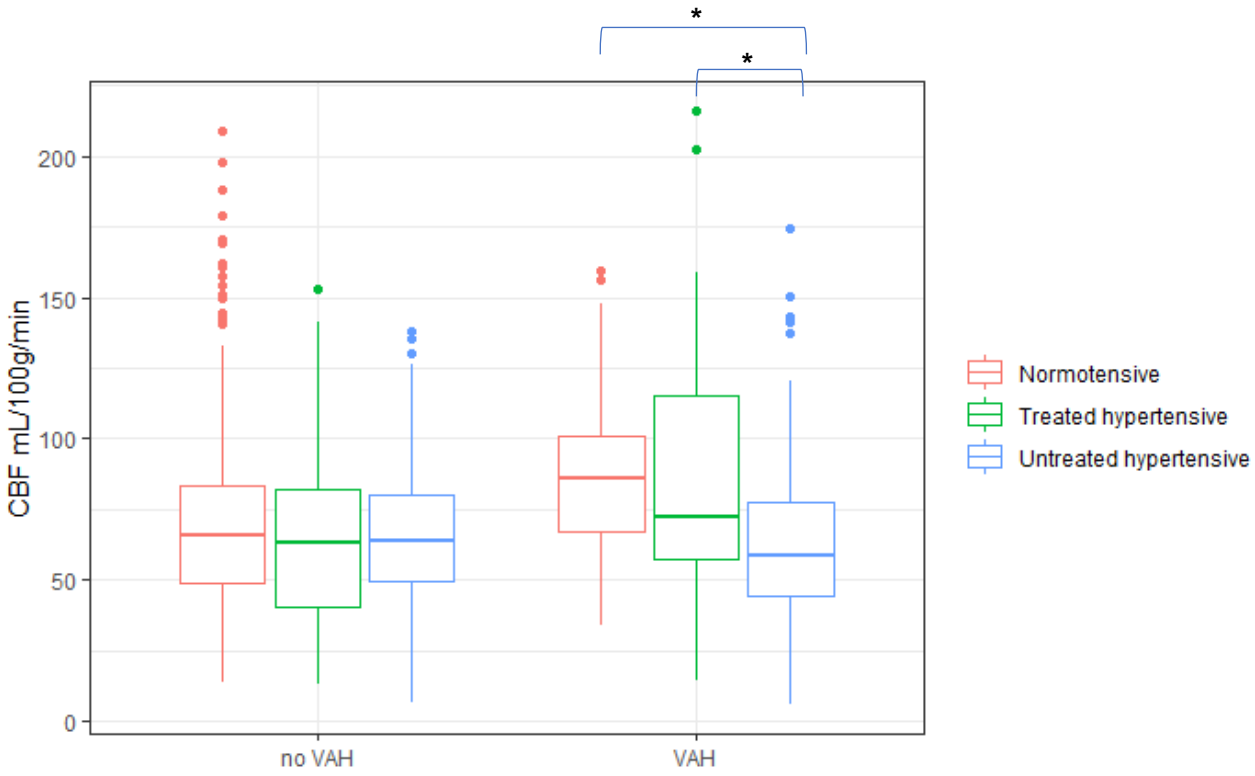

Figure 3.7: In participants with VAH, mean CBF is significantly lower in untreated hypertensives (*) compared to both normotensives and treated hypertensives. There is no significant difference in mean CBF in those without VAH.

In summary:

1. There is no statistically significant three-way interaction between VAH, blood pressure group and region.
2. There is no significant two-way interaction between region and blood pressure or between region and VAH.
3. Mean CBF is significantly higher in normotensives with VAH.
4. Mean CBF is significantly lower in untreated hypertensives compared to normotensives and treated hypertensives in the presence of VAH.

3.3.2. Standardised CBF

A two-way ANCOVA comparing the effect of VAH (present or absent) and blood pressure group (normotensive, treated hypertensive or untreated hypertensive) on

standardised posterior circulation (occipital pole plus brainstem) CBF, with age, BMI and sex included as covariates, was performed.

There was no significant variation in standardised posterior circulation CBF between those with and without VAH ($F(1) = 0.003$, $p = 0.95$, partial $\eta^2 = 0.00$) or between the three blood pressure groups ($F(2) = 0.04$, $p = 0.96$, partial $\eta^2 = 3.0 \times 10^{-4}$), (figure 3.8). Furthermore, there was no significant effect of the interaction between blood pressure group and VAH status ($F(2) = 0.03$, $p = 0.97$, partial $\eta^2 = 3.0 \times 10^{-4}$).

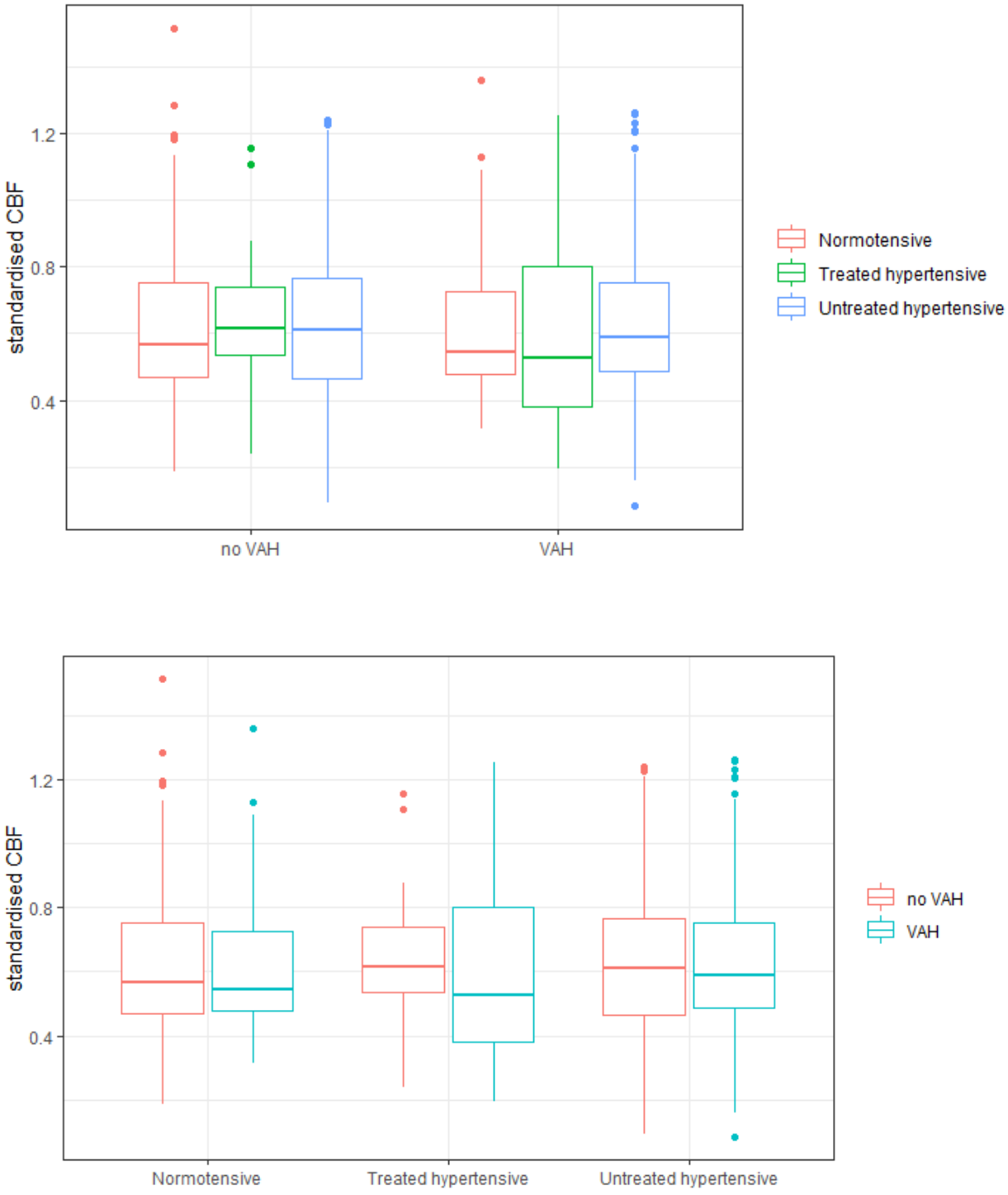

Figure 3.8: No significant difference in posterior circulation standardised CBF between the blood pressure groups with and without VAH (top), or between those with and without VAH in any of the blood pressure groups (bottom).

3.3.3. Relationship between grey matter density and blood pressure, brain region and VAH

A three-way ANCOVA comparing the effect of VAH (present or absent), blood pressure (normotensive, treated hypertensive or untreated hypertensive) and brain region on fractional GM density, with age, BMI and sex included as covariates, found that fractional GM density significantly varied across brain regions ($F(6) = 979.9$, $p < 2 \times 10^{-16}$, partial $\eta^2 = 0.93$). There was no statistically significant difference in fractional GM density between blood pressure groups ($F(2) = 1.9$, $p = 0.16$, partial $\eta^2 = 0.006$) or between those with and without VAH ($F(1) = 0.3$, $p = 0.58$, partial $\eta^2 = 6 \times 10^{-4}$). Furthermore, there was no significant two-way interaction between VAH and blood pressure group ($F(2) = 2.4$, $p = 0.09$, partial $\eta^2 = 0.01$), between VAH and region ($F(7) = 0.6$, $p = 0.75$, partial $\eta^2 = 0.01$) or between region and blood pressure group ($F(14) = 0.9$, $p = 0.53$, partial $\eta^2 = 0.03$), and no significant three-way interaction between VAH, blood pressure and region ($F(23) = 0.8$, $p = 0.78$, partial $\eta^2 = 0.03$) on GM density.

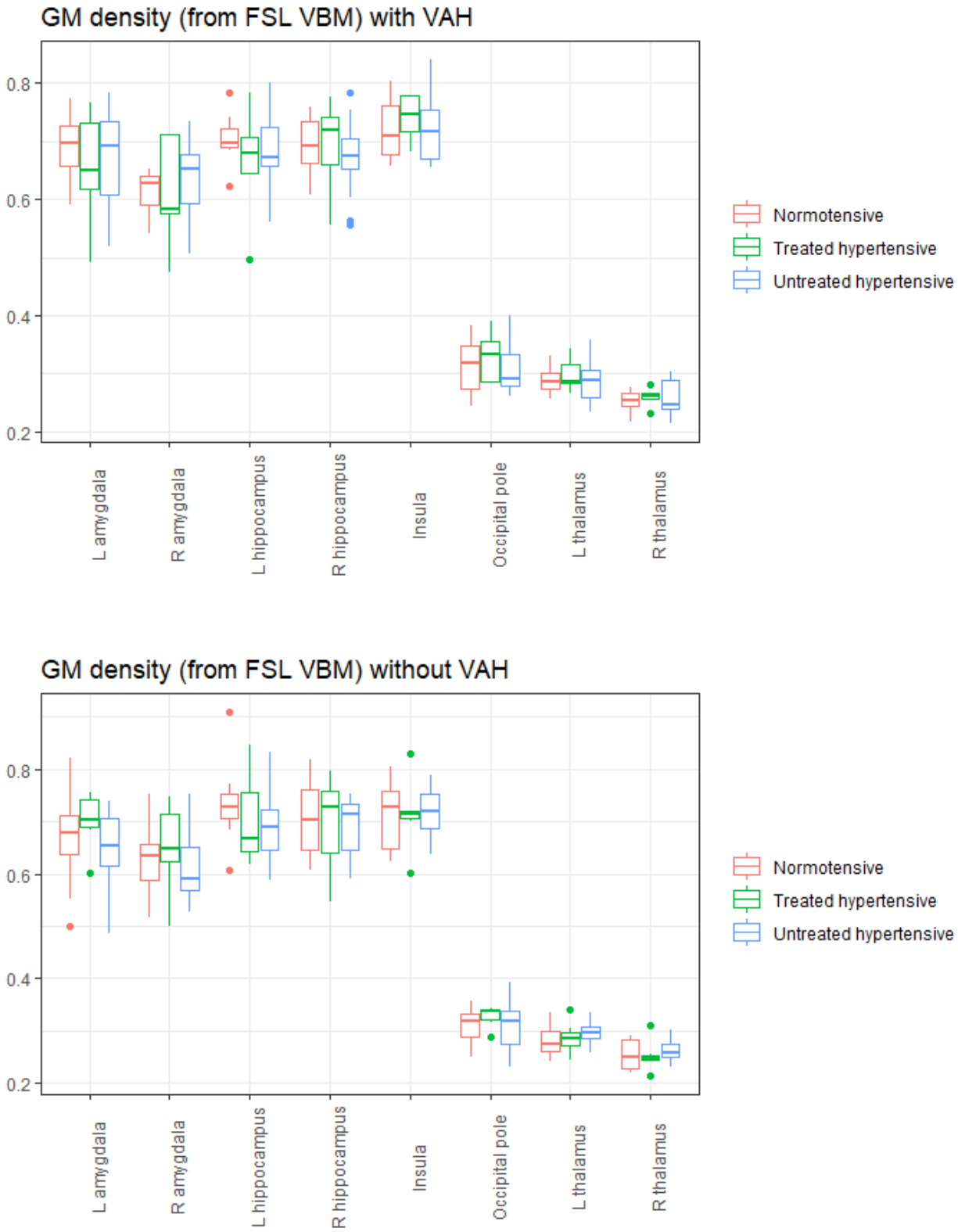

Figure 3.9: Regional grey matter density by blood pressure group in participants with (top) and without (bottom) VAH. There is no significant variation between the blood pressure groups within each region.

Figure 3.10 and table 3.3 shows that there is no correlation between CBF and GM density in any of the regions of interest studied here.

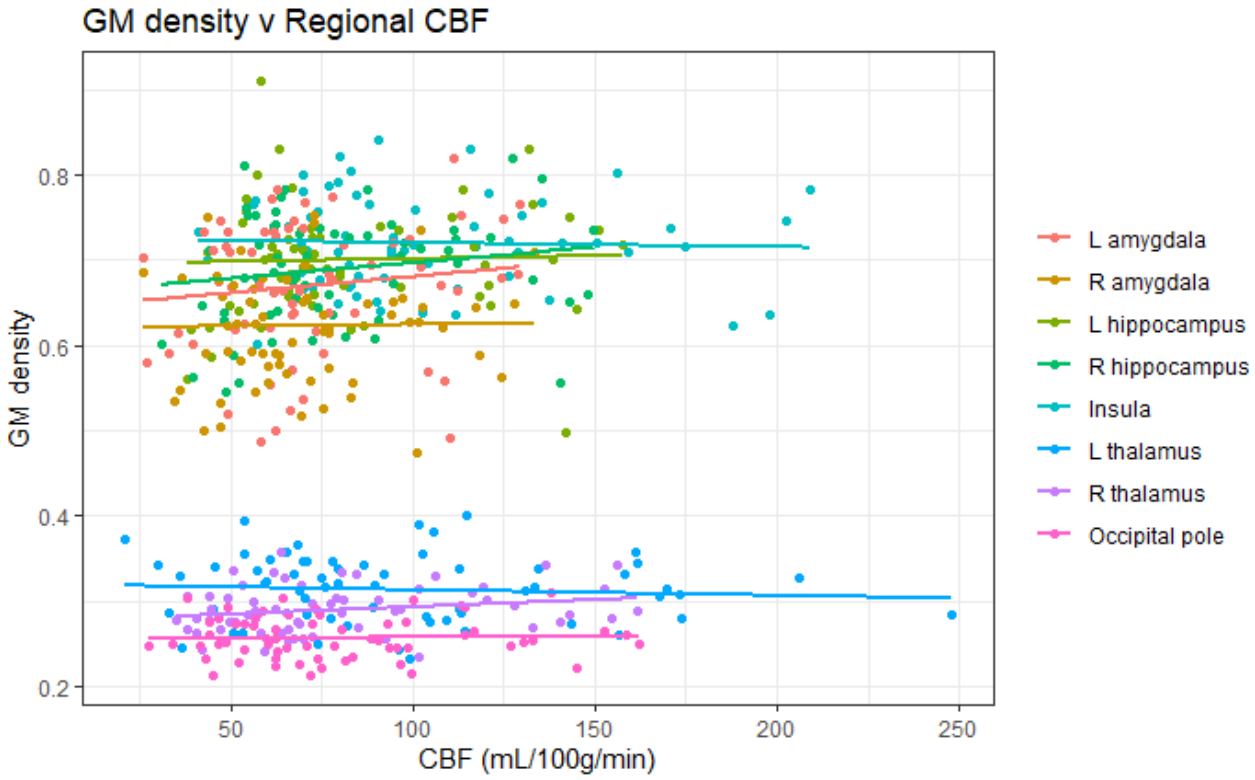

Figure 3.10: Relationship between regional grey matter density and CBF.

Table 3.3: Regional correlation between grey matter density and CBF (Spearman's correlation was used due to the non-parametric nature of the CBF data). No statistically significant correlation was found in any of the regions of interest under investigation.

Region	Spearman's rho	p-value
L thalamus	0.16	0.18
R thalamus	0.01	0.96
L amygdala	0.13	0.30
R amygdala	-0.05	0.66
L hippocampus	0.07	0.58
R hippocampus	0.16	0.19
Occipital pole	-0.11	0.38
Insula	-0.06	0.61

3.4. Discussion

The relationship between regional brainstem CBF, blood pressure and vertebral artery hypoplasia was investigated using PCASL MRI data from a group of hypertensives and normotensive participants. Participants were sub-divided into three groups (normotensive, untreated hypertensive and treated hypertensive) to explore the impact of antihypertensive medication on CBF. Our primary hypothesis was a reduction in CBF to the posterior circulation and brainstem in hypertensives with VAH. We found no evidence of a statistically significant three-way interaction between regional CBF, VAH and blood pressure to support this hypothesis. Similarly, there is no significant two-way interaction between region and VAH or between region and blood pressure group. In the context of the selfish brain mechanism, if CBF is compromised by congenital vertebral artery hypoplasia we expected lower CBF in the posterior circulation than in the anterior circulation. These results suggest that there is no difference between posterior and anterior circulation CBF according to VAH or blood pressure status. The analysis of standardised posterior circulation CBF, which revealed no significant

difference between the blood pressure groups or between those with and without VAH, and no interaction between VAH and blood pressure group, supports this. Alternatively, it is possible that VAH *is* compromising CBF to the posterior circulation, but that flow from the anterior circulation via the circle of Willis is compensating for this, or that, in the hypertension group at least, the selfish brain mechanism has corrected CBF to the posterior circulation. Alternatively, the increased prevalence of vertebral artery narrowing in hypertensives might not be due to hypoplasia, but rather caused by pathological stenosis secondary to atherosclerosis, for which hypertension is a known risk factor (Solberg 1983), (Alexander 1995). Vertebral artery narrowing may therefore be a result of hypertension, rather than a cause. If hypertension precedes and causes vertebral artery narrowing because of cerebrovascular disease, we might expect CBF to both the anterior and posterior circulation to be similarly affected because in a group comparison cerebrovascular disease would probably affect the internal carotid arteries to the same extent as the vertebral arteries. Yet another possibility is that patients with congenital vertebral artery hypoplasia develop hypertension, which subsequently causes global cerebrovascular disease, ultimately leading to a global reduction in CBF. There are clearly many possibly permutations, and the only way to determine the sequence of events with certainty would be through a longitudinal study over many years or even decades, which is obviously beyond the scope of this PhD thesis.

Contrary to the expectations of our secondary hypothesis, mean CBF across the ROIs is *higher* in normotensive participants with VAH compared to those without VAH. There is no significant difference in mean CBF between those with and without VAH in treated or in untreated hypertensives (figure 3.6). This is contrary to the findings of Warnert et al. who found whole-brain CBF, calculated from the flow in the internal carotid and basilar arteries on phase-contrast MRI, to be *lower* in hypertensives with VAH. It is also contrary to our hypothesis that VAH negatively affects CBF. The VAH group is significantly older, which makes the finding even more surprising because age is associated with a global reduction in CBF (Braz, 2016), (Biagi, 2007). BMI is not significantly different between those with and without, and neither is the proportion of males to females. This is also surprising from a physiological perspective, because vascular narrowing is associated with a reduction in flow, not an increase (Wei 2019). Perhaps this normotensive population have somehow overcompensated for VAH and overcorrected their CBF. Perhaps, during development of the cerebral vasculature, the carotid arteries supplying the anterior circulation overdevelop to

compensate for VAH and to enable sufficient collateral blood supply to the posterior circulation via the circle of Willis. Those with VAH who do not develop this supposed collateral supply might then be at risk of posterior circulation hypoperfusion, and of hypertension, if they acquire any further insults that affect the posterior circulation. However, the fact that there was no significant difference in the pattern of regional variation in CBF according to blood pressure group or VAH presence casts significant doubt on this idea.

Otherwise, the unexpected result might be due to the large uncertainty in the data and the relatively small sample size. A direct comparison with the findings of Warnert et al. is complicated by several factors. Firstly, the sample of participants is different between the two analyses - some of the participants were excluded from the present analysis due to the brainstem being outside the field of view on ASL images. Warnert also compared global CBF, whereas only certain ROIs implicated in central autonomic function, together with reference frontal and occipital ROIs, were included in this chapter. Furthermore, CBF was calculated from PCASL data in this analysis, compared to phase-contrast MRI for Warnert et al.'s analysis. Global CBF measurements obtained using phase-contrast MRI have previously been demonstrated to be systematically higher and more variable than those obtained using PCASL, and the correlation between CBF measurements obtained using the two modalities is far from perfect (Dolui, et al.., 2016). Dolui et al. propose several factors that might explain disagreement between the two methods. If a fixed label location is chosen for each participant, as was the case with this data, variations in vascular anatomy might contribute to PCASL labelling inefficiency (for example if the vertebral or carotid artery is not running perpendicular to the labelling plane) (Dolui, et al., 2016). As discussed in section 2.2.3 and illustrated in figure 2.3, the vertebral arteries are especially tortuous, and therefore a fixed label location risks suboptimal label placement and inefficient labelling of blood flowing to the posterior circulation. The internal carotid arteries follow more of a straight path through the neck until they reach the skull base, therefore there is less risk of inefficient labelling of blood flowing to the anterior circulation. Label placement is therefore critical when comparing perfusion in the anterior and posterior cerebral circulation. Labelling efficiency may also be negatively affected by an increase in flow velocity (Aslan 2010). If this is the case, PCASL estimates of posterior circulation CBF in patients with VAH, in whom flow velocity would be expected to be higher, may be too low. There are other variables that are not accounted for by the Buxton model which was used to process the PCASL data here. For

example, the T1 of blood depends on haematocrit and varies between participants (Dolui, et al., 2016) but is assumed to be constant by the Buxton model. Finally, although an effort was made to optimise brainstem co-registration using LBC, inaccurate co-registration can also confound analysis of ASL data, whilst measurement of CBF from phase contrast MRI is not susceptible to co-registration inaccuracies.

In the presence of VAH, mean CBF was found to be significantly lower in untreated hypertensives than both treated hypertensives and normotensives (figure 3.7). Discounting the previously discussed finding of an elevated CBF in those with VAH, in isolation this finding is potentially compatible with the selfish brain mechanism. VAH could be causing a reduction in CBF thus triggering the selfish brain mechanism, but the resultant increase in systemic blood pressure might be insufficient to fully correct CBF. On the other hand, CBF is significantly lower in untreated compared to treated hypertensives. This is contrary to the selfish brain mechanism, in the context of which treatment of hypertension might be expected to have a negative effect on CBF, because lowering systemic blood pressure would remove the compensatory mechanism that is aiming to restore CBF back to normal. This finding is also contrary to that of Warnert et al., who found that whole-brain CBF measured using phase-contrast MRI was significantly lower in treated rather than untreated hypertensives. The disagreement between the two analyses again raises questions about the uncertainty in the absolute PCASL CBF values, and about the correlation between PC MRA and PCASL CBF estimates. The different sample populations in each analysis might also again be a factor in the disagreement.

There are limitations to the data under consideration in this exploratory analysis. As demonstrated in figure 3.6 there is a large degree of uncertainty in absolute CBF values, with several outliers lying greater than 1.5 times above the interquartile range. Visual inspection of the source images related to these outliers did not reveal any obvious qualitative problems with the data, and therefore there was no justifiable reason to exclude these data-points from the analysis. There are many possible reasons for the uncertainty in the CBF values. Absolute values of cerebral blood flow within an individual inevitably vary with time due to natural fluctuation in physiological parameters such as P_aCO_2 and P_aO_2. Extrinsic factors such as sleep and the use of recreational substances such as caffeine and alcohol may also influence CBF (Clement, 2017). In a review of studies that measured CBF using both ASL and PET, Fan et al.

assessed the between-scan reproducibility of absolute CBF values measured using ASL and found the coefficient of variation (defined as the standard deviation divided by the mean) to be 8.6% (Fan AP, 2016). A minimum uncertainty of at least 8.6% in absolute CBF values might therefore be expected. This uncertainty may contribute towards, but cannot fully account for, the variance in the data. At least some of this additional variance may be explained by confounds such as age, sex and BMI. Raw ASL data was not available for qualitative assessment or analysis and therefore pre-processing steps such as motion correction and physiological noise correction could not be optimised towards maximising brainstem CBF accuracy. The fixed label location that was used might also have confounded CBF measurements due to the tortuosity of the vertebral arteries in the neck. The importance of carefully optimising label placement is reinforced by figure 3.11 below, which demonstrates the effect of inefficient labelling secondary to suboptimal label placement. Blood flow velocity is highly sensitive to vessel diameter and therefore the increase in velocity that results from vertebral artery narrowing might also reduce labelling efficiency.

Participants were classified as having vertebral artery hypoplasia if they had a single hypoplastic vertebral artery, as defined in section 3.2.1, under the assumption that a single hypoplastic vertebral artery may compromise brainstem haemodynamics. However, it is possible that the normal contralateral vertebral artery could compensate for any flow impairment in the hypoplastic artery and provide adequate blood supply to the brainstem and posterior circulation. An acquired vertebrobasilar pathology such as arterial dissection or stenosis might cause a more severe haemodynamic compromise to the brainstem, especially if the basilar artery and/or both vertebral arteries are affected. It is therefore possible that acquired vertebrobasilar pathology, rather than longstanding well-compensated VAH, might trigger the proposed selfish brain mechanism. Future studies could include a cohort of hypertensives with acquired vertebrobasilar pathology to compare brainstem CBF with participants with unilateral VAH.

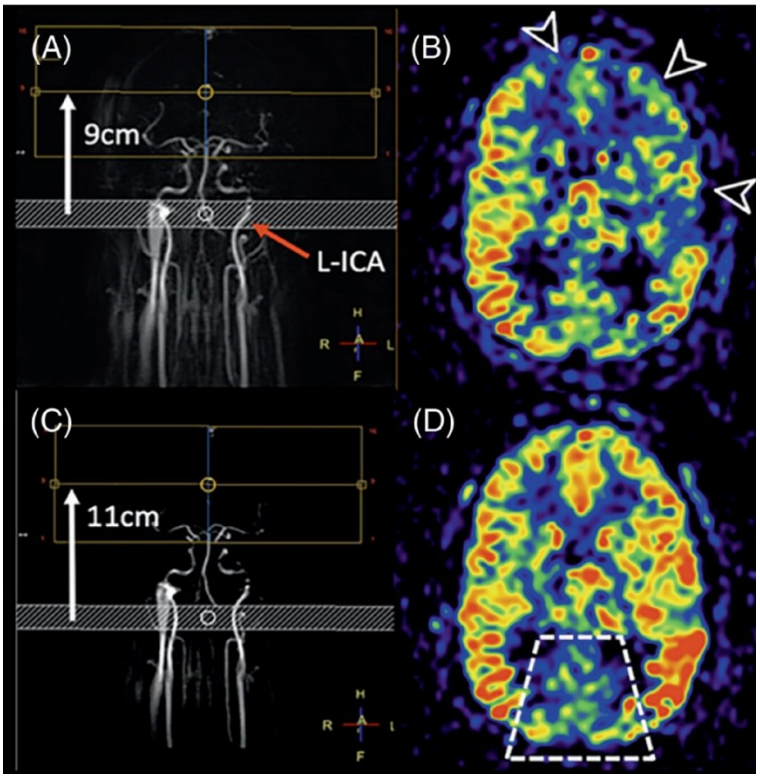

Figure 3.11: (taken from Lindner et al., "Current state and guidance on arterial spin labelling perfusion MRI in clinical neuroimaging" (Linder 2023)). In B) there is apparent hypoperfusion of the left middle cerebral artery and bilateral anterior cerebral artery territories, considered to be due to inefficient labelling secondary to the oblique orientation of the left internal cerebral artery through the labelling plane on the planning angiogram in A). In C), the labelling plane has been moved caudally and subsequently D) demonstrates more uniform cortical perfusion. The dashed box in D) demonstrates pseudo-hypoperfusion of the posterior circulation due which is though to be due to inefficient labelling of the vertebral arteries, which demonstrate a tortuous course through the labelling plane in C).

Volumetric analysis of regional grey matter density was also performed. There is a statistically significant difference in grey matter density according to brain region (figure 3.9). There is a normal physiological variation in GM density throughout the brain which might account for this. Partial voluming of non-grey matter structures into the generic Harvard-Oxford atlas ROIs might also contribute and may explain the lower thalamic and occipital pole values seen in figure 3.9. There was no significant association between regional grey matter density and blood pressure group, the presence or absence of VAH, and no significant correlation between grey matter density and absolute regional CBF. The lack of any significant difference in posterior circulation GM density in hypertensives with VAH is consistent with the outcomes of the CBF analysis. However, the lack of correlation between regional GM density and CBF (figure 3.10) suggests that even in the presence of a significant reduction in posterior circulation CBF, GM density might not necessarily be affected.

3.5. Conclusion

Three-way ANCOVA was performed to investigate the relationship between regional CBF and vertebral artery hypoplasia in normotensives, untreated hypertensives and treated hypertensives. Mean CBF across the ROIs is *higher* in normotensive participants with VAH compared to normotensives without VAH. This finding is unexpected, contrary to our hypothesis that VAH negatively affects CBF, and cannot be fully explained. There is some uncertainty in the data and limitations to the analysis which might be contributing to the unexpected results. In the presence of VAH, mean CBF is significantly lower in untreated hypertensives compared to normotensives and treated hypertensives. This suggests that treatment of hypertension is beneficial to CBF, which is also somewhat contrary to the selfish brain mechanism. There was no significant two-way interaction between region and VAH or between region and blood pressure group, which suggests that there is no significant difference between posterior and anterior circulation CBF according to VAH or blood pressure status. Separate analyses of standardised posterior circulation CBF and of regional grey matter density support these findings. A longitudinal study is required to clarify the relationship between VAH and hypertension.

4. Implementation of a convolutional neural network for brainstem landmark detection and co-registration

4.1. Introduction

4.1.1. Co-registration

Co-registration between functional and anatomical datasets is an important step in any functional MRI analysis. The spatial resolution and signal-to-noise and contrast-to-noise ratio of functional MRI data is often relatively low. Co-registration with a higher resolution, high SNR/CNR anatomical dataset aids with localising functional information to specific regions of the brain. For example, in chapters 2 and 3 high-resolution anatomical datasets were segmented into regions of interest (ROIs), then applied to co-registered ASL data in order to output regional cortical and subcortical perfusion values. High-resolution structural scans can also be used to help localise functional activity to specific regions of the brain. In chapter 7 a magnetisation transfer weighted acquisition co-registered to a BOLD acquisition is used to localise functional activity in the locus coeruleus. The accuracy of co-registration is especially important in the case of brainstem functional imaging. Brainstem nuclei such as the RVLM and locus coeruleus are of the order of millimetres in size, therefore small inaccuracies in co-registration between functional and structural data will compromise measurements of regional brainstem functional connectivity and reduce sensitivity to detect significant activation in a group level analysis. Furthermore, the brainstem is surrounded by CSF spaces, and the basilar artery is closely opposed to its anterior surface. Mis-registration between functional and structural datasets may lead to incursion of CSF or vascular signal into brainstem regions of interest.

Co-registration of MRI data is commonly performed by optimising a cost function that measures intensity and/or boundary-based differences between two images. This generates an affine registration matrix that describes the linear transformation between the coordinate spaces of the two images. Optimisation of the cost function is usually performed on a global level, across the whole of the brain, and is primarily aimed at maximising the accuracy of cortical registration. Global co-registration methods may therefore be less successful in accurately co-registering sub-regions of the brain, such as the brainstem. FSL and AFNI both

contain implementations of affine intensity-based co-registration (Jenkinson 2002), (Jenkinson 2001), (Greve 2009), (Cox 1996), (Cox 1997).

4.1.2. Brainstem-weighted co-registration

Napadow et al. have developed a method of co-registration between anatomical images and the MNI-152 template that is tailored to the brainstem (Napadow 2006) known as automated brainstem co-registration (ABC). The method involves two steps. Firstly, a global affine intensity-based co-registration is performed. The resulting data then undergoes a second affine co-registration, this time with the cost-function weighted towards the brainstem by applying a generic brainstem mask, generated from the MNI-152 template. The accuracy of this method was demonstrated by calculating the root-mean squared error (RMSE) between a set of 12 brainstem landmarks on the co-registered anatomical data and the MNI-152 data. Compared to global-affine registration (3.26 ± 0.81 mm), RMSE was significantly lower with ABC (1.22 ± 0.39 mm, $p < 1 \times 10^{-16}$).

Low resolution functional datasets are usually co-registered to MNI space in two steps. First, they are co-registered to a high-resolution anatomical dataset before then being co-registered to the MNI template for group level analysis. The resultant MNI-space functional data is useful if group-level analysis is to be performed. Certain analyses may benefit from being performed in the anatomical space of the individual subject, rather than relying on a generic MNI-template. For example, the brainstem can be segmented on a high-resolution structural scan within each individual participant then co-registered and applied to the ASL data, rather than applying a generic MNI-space brainstem mask which may not accurately reflect the true size, shape, and location of the brainstem within each individual. Napadow's ABC method was developed and tested using high-resolution (1.0 x 1.0 x 1.3 mm) T1-weighted structural MR scans co-registered to the generic MNI-152 template. It has not been tested for the co-registration of relatively low-resolution functional data to within-participant anatomical data.

The weighting of the cost-function in the ABC method requires a brainstem mask. This is not a problem when co-registering to the MNI-152 dataset because the same pre-existing MNI-space brainstem mask can be used for every individual. To maximise the accuracy of co-registration from functional to anatomical space, a new brainstem mask based on that

individual's anatomical dataset must be created for each individual. Manual definition of a brainstem mask is possible but time consuming and highly user dependent. Alternatively, a segmentation package such as Freesurfer can be employed (Dale 1999), but this is also time consuming as well as computationally expensive. For ABC to be practically applicable for co-registration of functional to anatomical data, a fast, reproducible, and computationally inexpensive method of defining a brainstem region of interest on anatomical MRI data is required.

4.1.3. Landmark-based brainstem co-registration

The signal and contrast characteristics of functional and structural datasets are often very different, and therefore intensity-based cost function optimisation methods may not always be optimal for co-registration. In addition to ABC, Napadow et al. also developed an alternative co-registration method that can be used to troubleshoot problematic datasets that failed the ABC process. This involves manual identification and labelling of 12 brainstem landmarks on both an input and reference dataset. Co-registration is then performed by translation of the input dataset to the reference dataset, with the aim of minimising the mean squared error between the two sets of landmarks. This method, known as landmark-based co-registration (LBC), has been successfully applied to register contrast-enhanced T1-weighted baseline and follow-up images in patients with brain tumours (Demir 2010).

LBC can achieve co-registration accuracy on a par with ABC (Napadow 2006). However, the process of landmark selection is both time consuming and highly user dependent. An automated method of identifying and labelling these brainstem landmarks would remove these limitations.

4.1.4. Deep learning and convolutional neural networks

Deep learning is a branch of artificial intelligence that involves the application of a computational neural network to learn and make predictions about a dataset. The aim in this chapter is to use deep learning and an artificial neural network to automatically generate a brainstem mask and to automatically detect brainstem landmarks, thus automating the ABC and LBC methods.

A neural network is a model that consists of several computational nodes arranged in many layers, through which data is repeatedly passed. Within each layer, the data undergoes a series of linear and non-linear transformations, before reaching the output layer which contains the prediction of the neural network. With each training iteration, the neural network adjusts a set of parameters associated with each node to optimise the fit of the model to the data. By feeding the network with a large volume of training data, it is possible to train it to recognise patterns within the data, and subsequently to make predictions about test data.

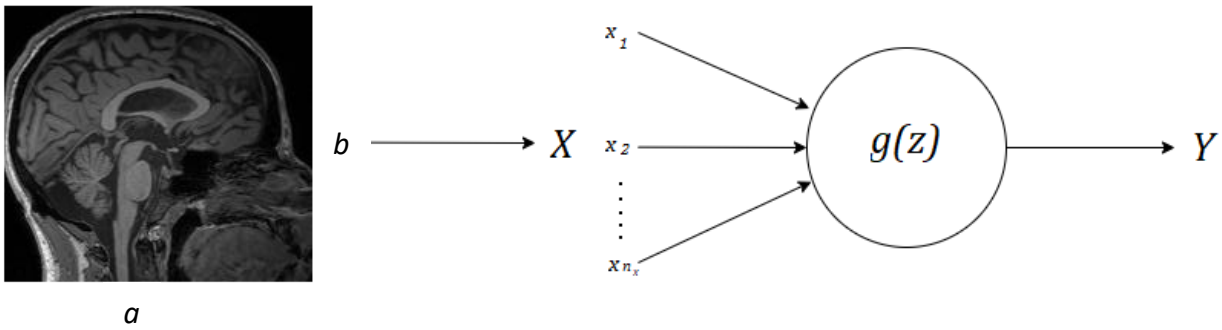

Figure 4.1: Simple neural network. A single 2D MRI slice is unrolled into a vector of length n_x. This is fed into a single computational node where it undergoes a linear transformation with output z. A-linear function g is applied subsequently applied to z. The output is represented by the vector Y.

In its simplest form, a neural network consists of an input layer, a single computational node, and an output layer (figure 4.1). In the case of a single 2D MRI slice of dimensions $a \times b$, the input layer consists of a feature vector X of length $n_x = a \times b$. For a set of m training sets X is then a $m \times n_x$ matrix.

The input feature vector X is passed to the computational node, and a linear function of the form demonstrated in equation 4.1 is applied to the input data.

$$z = \omega . X + b \qquad (4.1)$$

ω and b are matrices containing the parameters used to describe z in terms of X. A non-linear activation function, g, is also subsequently applied to z. The activation function can take any of a number of forms depending on the aims of the neural network. The most commonly used function is the ReLU function (Brownlee 2021):

$$ReLU(z) = \begin{cases} z, & z > 0 \\ 0, & otherwise. \end{cases} \quad (4.2)$$

The output of the computational node then takes the form:

$$a = ReLU(z). \quad (4.3)$$

The purpose of this non-linear function is to enable the neural network to make complex non-linear predictions about the data. Without it, the network would be limited to simpler linear predictions, regardless of how structurally complex it is (Strika 2019).

The goal of the neural network is to make predictions about the data. Once the data reaches the output layer it is amalgamated into a vector of the form that represents the prediction that is to be made by the network. For example, the goal might be to predict the coordinates of an anatomical landmark on the 2D MRI slice. The output layer would therefore consist of a $2 \times m$ matrix, represented by Y, containing the two coordinates corresponding to each of the m input datasets.

A deep neural network consists of many nodes and layers (see figure 4.2 for a simplified example). Each feature of the input layer is fed into each node in the first hidden layer of the network. The output of each node in the first layer is fed into each node in the second layer, and so on. This type of neural network is termed 'fully connected'. Increasing the complexity of the network increases the number of parameters in the model, which allows increasingly complex predictions to be made.

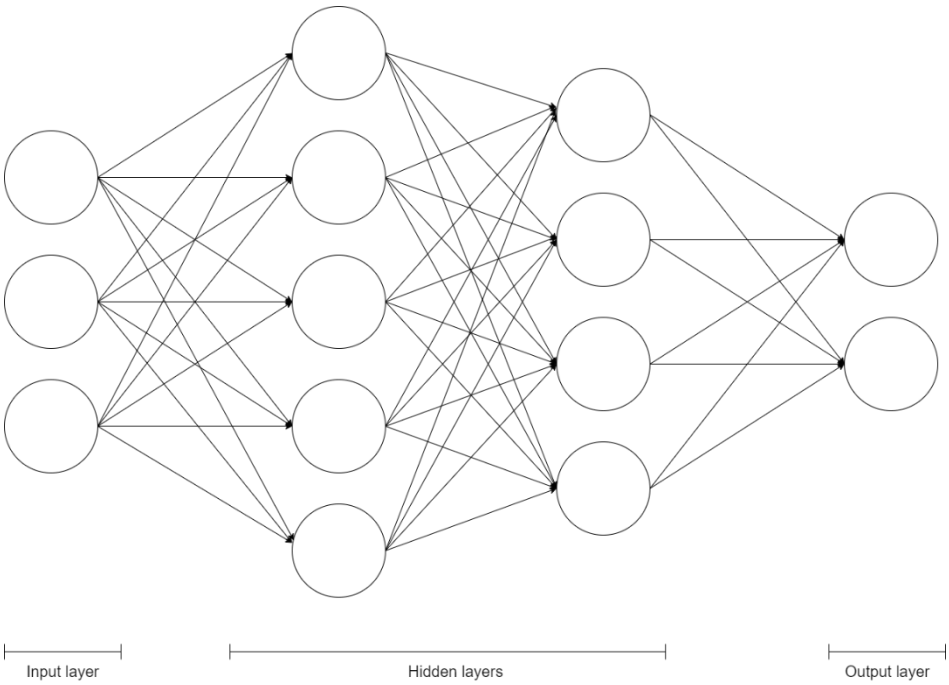

Figure 4.2: Representative example of a simple neural network with more than one layer. A deep neural network may contain many more hidden layers, each containing several nodes.

The goal of the network is to optimise the parameters ω and b such that the output of the network is as close as possible to the ground truth. When the data is first passed through the network, its parameters have not been optimised and therefore the output is unlikely to accurately represent the ground truth. The accuracy of the network is measured using a loss function, L. The loss function can take many forms, but here is depicted as the mean square error between the CNN's predictions and the ground truth. In training the network, the aim is to minimise this loss function. This is done by calculating the derivative of L with respect to the parameters ω and b in a process called gradient descent. The parameters are then updated incrementally, and the data is passed through the network again. Over several iterations (epochs), the loss function tends towards a minimum, the parameters are updated and optimised accordingly, and the accuracy of the network improves.

The most common method of training a neural network is via supervised learning (Lundervold 2019). This involves supplying the neural network with a dataset that has been pre-labelled with the ground truth information. In the context of brainstem landmark detection, the ground truth is the set of coordinates of the anatomical landmarks of interest.

A neural network's performance is assessed by comparing the accuracy of the predicted coordinates against the ground truth, as defined by the loss function.

4.1.5. Convolutional neural networks

A typical high-resolution anatomical MRI scan might have a resolution of 256 x 256 x 128. The input vector of this data would therefore contain over 8 million features. This leads to a huge number of parameters in each layer of the network, which is very computationally expensive and time consuming to train. Convolutional neural networks are a specific type of neural network that use filters to detect features in the data and to help reduce the number of parameters in the network, and to preserve spatial information about the data (Kanghan 2019). CNNs are therefore well suited to the analysis of MRI data.

Instead of unravelling the 3-dimensional MRI data into a 1-dimensional vector before feeding it into a fully connected neural network, a CNN preserves the 3D structure of the data. Within each layer of the CNN, several filters are applied. These filters are matrices containing a set of parameters. For example, figure 4.3 demonstrates the use of a vertical edge detection filter.

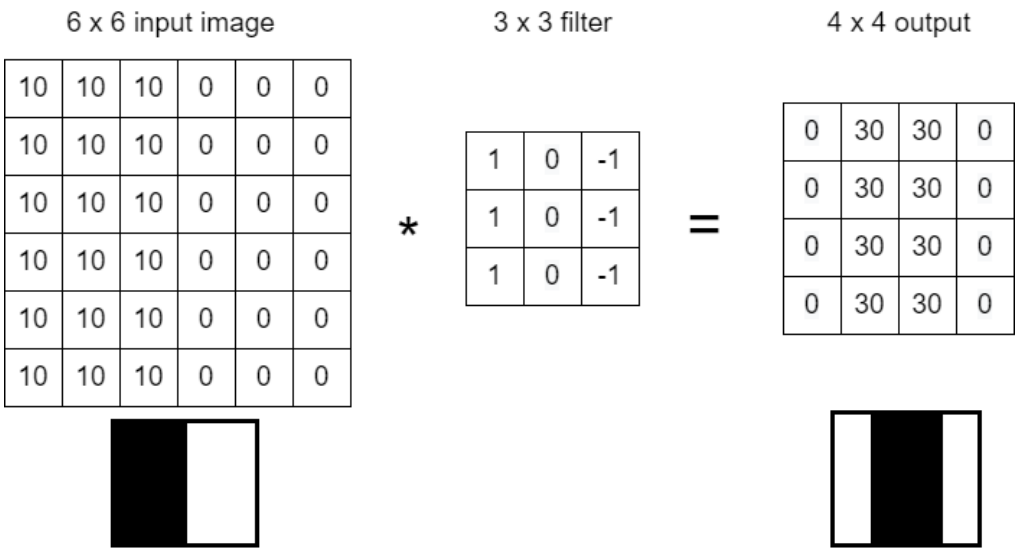

Figure 4.3: Vertical edge detection filter. A 6 x 6 greyscale image is convolved with a 3 x 3 filter which outputs a 4 x 4 greyscale image displaying the position of the vertical edge in the input image.

In the above example, the 6 x 6 input data is convolved with the 3 x 3 vertical edge detection filter. The output is a 4 x 4 matrix that represents the location of the vertical edge in the input data. In a CNN this convolution step replaces the linear function in equation 4.1. The output subsequently undergoes a non-linear transformation such as a ReLU activation function. An example of a single layer of a CNN is shown in figure 4.4.

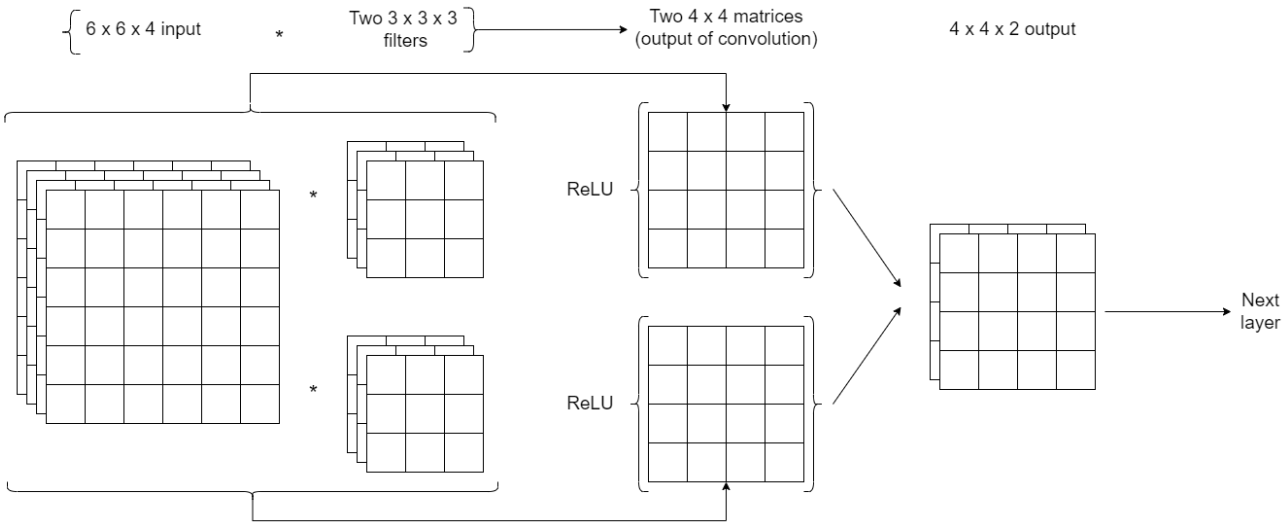

Figure 4.4: Example of a single layer of a CNN. The 6 x 6 x 4 input is convolved with two 3 x 3 x 3 filter matrices. The ReLU activation function is applied to each of the two 4 x 4 output matrices. These are then passed to the next layer.

Note that the output matrix in figure 4.4 is smaller than the input matrix. To preserve the spatial dimensions of the input matrix, extra data can be added around the edge of the input matrix, a process known as padding. For example, a border of zeros can be added around the input matrix. Without padding, there is an upper limit on the number of layers in a CNN because the output matrix continues to shrink with each layer. Padding also preserves information at the edge of the input matrix – without padding the pixels at the edge of the image undergo fewer convolutions and information about the edge of the image is lost.

The types of filters in a CNN that might be relevant to the data do not have to be pre-specified, and the parameters of the filters do not have to be pre-defined. Instead, the parameters are optimised in a data-driven manner and the CNN 'learns' to identify features such as edges, contrast differences etc that are relevant to that dataset.

In a CNN, the parameters of each filter have translation invariance – the parameters remain the same regardless of which part of the input data they are applied to. This has two benefits. Firstly, the number of parameters is dramatically reduced, which reduces computational load and training time. Secondly, translation invariance enables the filters to detect similar features at different locations in the data. For example, a filter that has been optimised to detect vertical lines can do so at the top and at the bottom of an image. Another advantage of a CNN is sparsity of connections between layers. In a fully connected neural network, such as figure 4.2, the output of each node in each layer depends on the input from every node in the preceding layer. In a convolutional neural network, due to the nature of the convolution between the filter and input data, the output of each layer depends only on a small number of inputs. This helps to prevent overfitting of the network to the training data. It also improves translational invariance, which is an especially desirable feature in analysing imaging data. For example, the brainstem may be shifted to different parts of the field of view depending on a participant's head position. A robust CNN that has translational invariance can overcome this and identify the brainstem regardless of its relative position in the field of view.

A CNN is trained in a similar manner to a traditional neural network, by forward propagation of the training data through the CNN followed by gradient-descent to iteratively update and optimise the parameters of the filters. In this process, the filters learn different features of the dataset. The final layer of a CNN is typically a fully connected layer like that of a simple neural network, which computes the output in the desired format.

4.2. Aims

In this chapter, a convolutional neural network (CNN) was developed and tested to try and further automate the process of co-registration between functional and anatomical space. The CNN were based on a CNN that had previously been developed to perform facial keypoints detection (detecting certain landmarks on people's faces, such as the outline of the eyes, nose and mouth) (Chen 2021). Firstly, a 2D CNN was trained to automatically predict the location of four brainstem landmarks on a mid-sagittal slice of a high-resolution structural MRI and on lower-resolution functional MRI data. These landmarks were then used to co-register the functional data to structural space using the LBC process described above. Once a

2D CNN had been successfully developed, the 2D CNN was expanded into a 3D CNN and reconfigured to predict the anatomical boundaries of the brainstem. These boundaries were used to generate a cuboidal mask encompassing the brainstem, and this mask was used as part of the ABC process as previously described. These methods are henceforth referred to as 2D-CNN LBC and 3D-CNN ABC, respectively. The accuracy of brainstem co-registration between functional and anatomical space using these two methods was compared to a commonly used intensity-based affine co-registration using FSL FLIRT (affine-FLIRT) and to LBC using manually defined brainstem landmarks (ground-truth LBC).

4.2.1. Summary of aims

1. Develop a 2D CNN to accurately label four anatomical landmarks on the brainstem on a mid-sagittal slice.
2. Develop a 3D CNN to accurately define the anatomical boundaries of the brainstem.
3. Compare the accuracy of brainstem co-registration using the outputs of these CNN as part of the LBC and ABC methods previously described with FSL FLIRT and LBC using manually defined ground-truth brainstem landmarks.

4.3. Methods

4.3.1. Convolutional neural network structure

First, a 2D-CNN was developed to identify brainstem landmarks. The structure of the CNN was based on a facial keypoints detection 2D deep neural network (Chen 2021) which itself was based on the LeNet architecture (LeCun 1998). The benefit of the LeNet model is that it is a relatively simple CNN with a small memory footprint and is therefore quick to train (Naimish 2017). The network contains four convolution layers feeding into a fully connected layer, and an output layer with dimensions *m* x 8 which contains the coordinates of the four brainstem landmarks on the input mid-sagittal MRI slice, where *m* is the number of input datasets (figure 4.5). There is also a subsampling max pooling layer. This runs a 2 x 2 filter across the data and takes the maximum value from each 2 x 2 region. This improves translation invariance and serves to downsample the data, further reducing the number of

parameters, thus reducing computation time and preventing overfitting (Ng 2020). For the 2D CNN, the first layer of the network was reconfigured to accept a 2D image with the dimensions of a single mid-sagittal MRI slice, where the brainstem is readily visible and anatomical landmarks can easily be identified and labelled.

This 2D-CNN was then reconfigured to accept 3D MRI data in the NIFTI format. The output layer was adjusted to a *m* x 5 vector containing the superior, anterior, posterior, right and left boundaries of the brainstem. The inferior boundary was defined as the inferior edge of the field of view to reduce the computational load of predicting a sixth boundary. This boundary-predicting 3D-CNN employed the same structure as the landmark-predicting 2D-CNN (figure 4.5), apart from the conversion from 2D to 3D. The models were all recreated in pytorch and implemented in Google Colab.

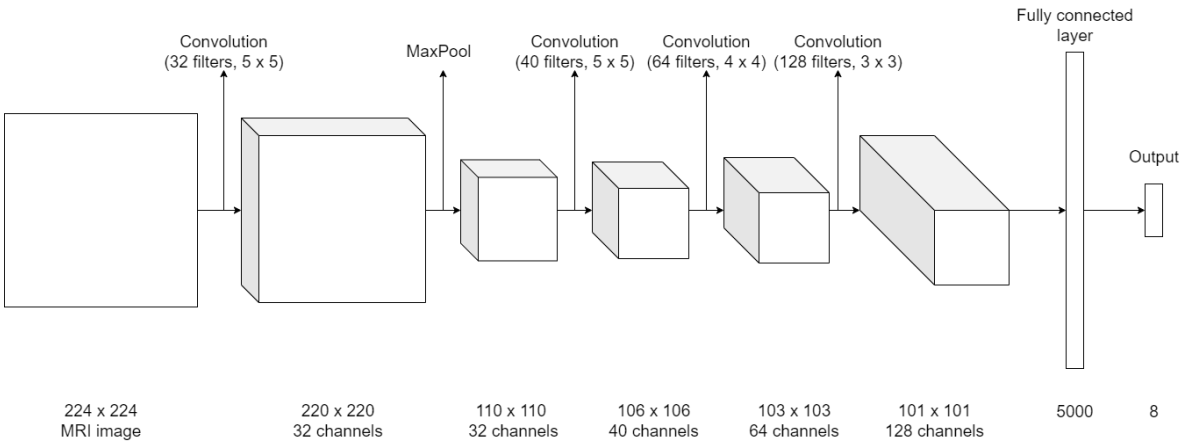

Figure 4.5: Outline of the CNN architecture. The number of output channels in each layer is equal to the number of filters applied to the preceding layer.

4.3.2. Training and test data

123 anatomical images were manually labelled with four brainstem landmarks (figure 4.6); mid-sagittal ventral pontomesencephalic notch, mid-sagittal ventral pontomedullary notch, apex of the fourth ventricle and mid-sagittal mamillary body.

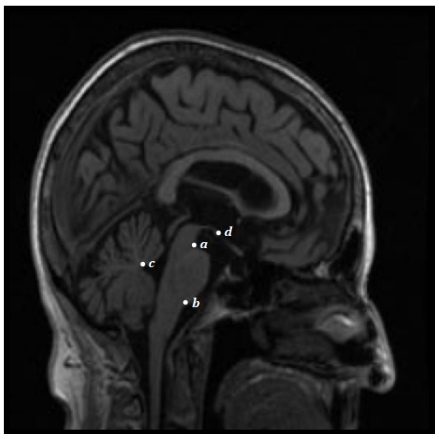

Figure 4.6: Four brainstem landmarks labelled on a mid-sagittal anatomical MRI slice. A) mid-sagittal ventral pontomesencephalic notch, b) mid-sagittal ventral pontomedullary notch, c) apex of the fourth ventricle, d) mamillary body.

113 of these MPRAGE images were used to train the landmark-predicting 2D-CNN, with 10 withheld for testing. The reason for only labelling 4 brainstem landmarks rather than the 12 used by Napadow et al. was to minimise the time required to manually label the training data, and because part of the aim of this initial 2D-CNN was to serve as a proof-of-principle. Figure 4.7 shows an example of an ASL dataset co-registered to a high-resolution structural dataset with LBC (using 4 manually labelled landmarks as per figure 4.6). There is very good subjective alignment in all three planes at the level of the medulla, midbrain and pons between the outline of the structural dataset in red and the co-registered ASL dataset. This demonstrates that accurate LBC can be achieved in all three planes using only 4 anatomical landmarks in the mid-sagittal plane, justifying the decision to reduce the number of brainstem landmarks from 12 to 4, and the decision to use landmarks in only one plane.

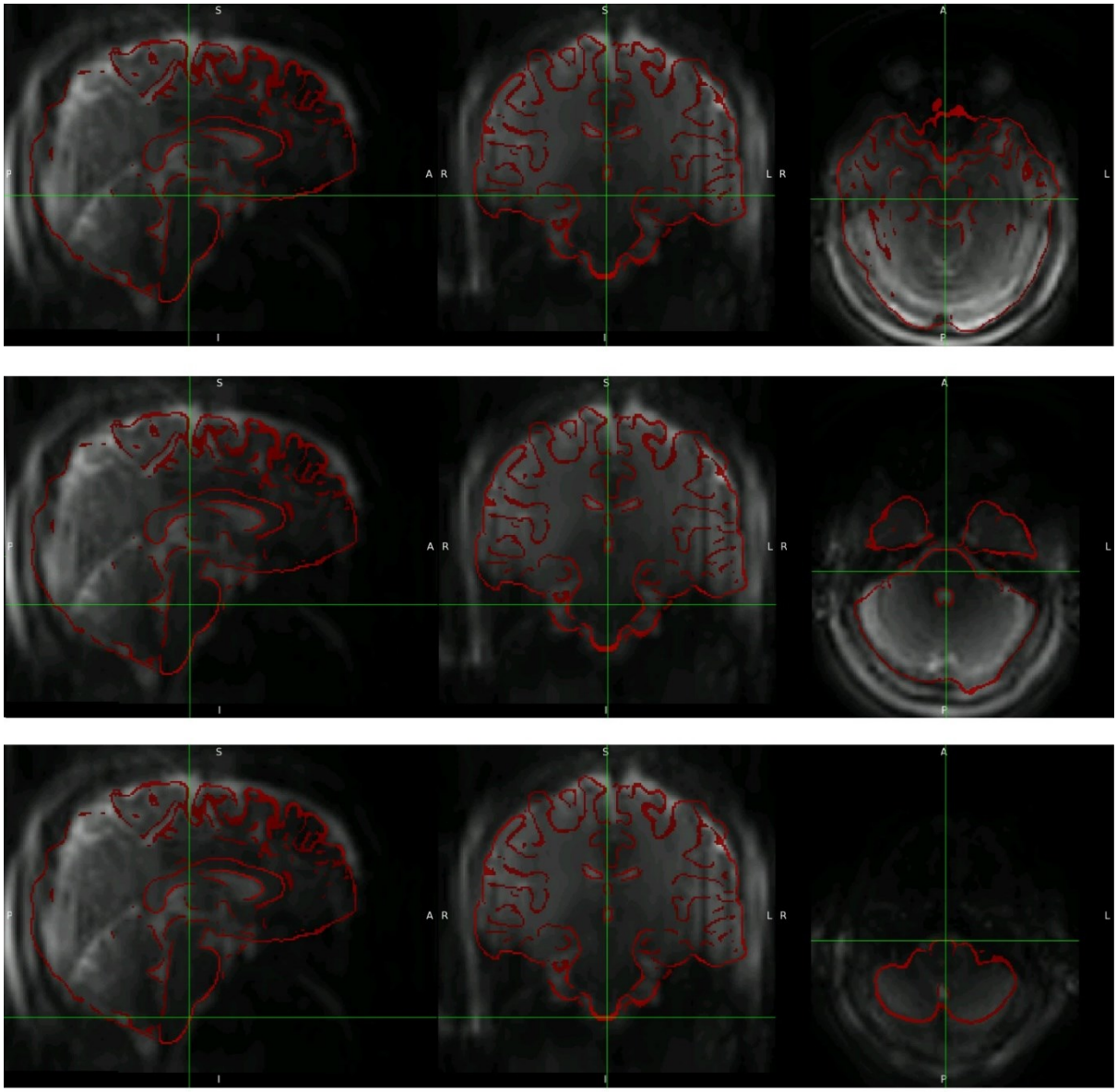

Figure 4.7: There is good subjective agreement in all three between an ASL dataset co-registered to a structural MPRAGE dataset using four manually defined mid-sagittal brainstem landmarks (as depicted in figure 4.6). The green lines denote the position of each plane. Axial views on the right demonstrate that alignment is maintained at the level of the midbrain (top), pons (middle) and medulla (bottom). Note also that there is good alignment not only of the brainstem but of the cerebral cortex, corpus callosum (sagittal plane) and ventricles (coronal plane).

MRI data consisted of a mixture of personally acquired data from other studies and data from the Alzheimer's Disease Neuroimaging Initiative (ADNI), an opensource dataset that is available online (ADNI 2021). To make the model as generalisable as possible, some ADNI MRI data from participants with cognitive impairment was included in the training data, as well as cognitively normal participants. Input MRI data were normalised to the range [0, 1],

and labels transformed into the range [-1, 1]. This helps to improve training efficiency by restricting the magnitude of the model's loss during training (Chen 2021).

49 resting-state BOLD EPI datasets from the UK Biobank database were also manually labelled with the same four brainstem landmarks. The landmark-predicting 2D-CNN that had been pre-trained with anatomical data was subsequently re-trained using 39 of these functional datasets, with 10 reserved for testing.

For the 3D-CNN, the training dataset consisted of 39 anatomical datasets each individually labelled with the superior, inferior, anterior, posterior, right and left boundaries of a cuboidal region encompassing the brainstem. An additional 10 datasets were used for testing.

For both CNNs, training data were augmented with random shear, random brightness and random crop techniques. Data augmentation serves to provide the network with more training data by introducing random variations into the dataset (Naimish 2017). The CNN is essentially a regression model with a set of real numbers (coordinates) as the output. A mean square error loss function was therefore chosen (Brownlee 2019). Each 2D-CNN was trained for 10,000 epochs. The 3D-CNN was trained for 1000 epochs due to the increased computational time associated with the conversion to 3D.

4.3.3. Co-registration methods

Unweighted affine intensity-based co-registration using FSL FLIRT.

FSL FLIRT achieves co-registration between different modalities (e.g. BOLD to MPRAGE) using an affine transformation and by optimising an intensity-based cost function between two images (Jenkinson 2002), (Jenkinson 2001), (Greve 2009). The functional and anatomical data were first brain-extracted, then co-registered using FLIRT. The affine co-registration matrix generated by this process was then used to register the non-brain-extracted functional data to anatomical space. The non-brain-extracted functional data was used for all subsequent analyses because of the variable performance of brain extraction, especially around the brainstem.

3D-CNN ABC

This global co-registration step was then optimised using a second intensity-based affine co-registration, again using FSL FLIRT. This time, co-registration was weighted towards the brainstem using a cuboidal mask. The boundaries of this mask were predicted using the boundary-predicting 3D-CNN.

2D-CNN LBC

The landmark-predicting 2D-CNNs described above were used to predict four brainstem landmarks on an anatomical and a functional scan. 3dTagalign, which is part of the AFNI software (Cox 1996) performs co-registration by rotating and translating the functional dataset and using a least squares algorithm to minimise the distance between the specified anatomical and functional landmarks (Napadow 2006).

Ground-truth LBC

The same four brainstem landmarks were also manually labelled. These were considered ground-truth landmarks against which the accuracy of the CNNs were measured. 3dTagalign was again used to co-register the functional and anatomical datasets using these ground-truth landmarks.

4.3.4. Assessment of accuracy

The performance of the landmark-predicting 2D-CNNs was assessed by using it to predict the brainstem landmarks on 10 test datasets. The RMSE between the predicted landmarks and the manually defined ground truth landmarks was calculated. Similarly, the accuracy of the boundary-predicting CNN was assessed by calculating the RMSE between the predicted and manually defined ground truth boundaries on another set of 10 test data.

Subjective visual assessment of co-registration accuracy was demonstrated by overlaying the outline of the structural dataset on to the co-registered functional dataset. The

brainstem outline was generated using the AFNI tool 3dedge (Cox 1996). Objective assessment of co-registration accuracy was performed by evaluating the RMSE between the four ground truth brainstem landmarks on the co-registered functional data and the ground truth anatomical landmarks.

4.4. Results

4.4.1. 2D-CNN to identify brainstem landmarks

Figures 4.8 and 4.9 demonstrate the performance of the 2D-CNN before and after it was trained with the MPRAGE dataset. As expected, the RMSE after training is significantly improved compared to before training (RMSE pre-training = 44.1 ± 11.9 (standard deviation), RMSE post-training = 2.5 ± 0.8 (standard deviation) voxels. Two sample t-test, t=11.1, df = 9.1, $p=1.4 \times 10^{-6}$). The low standard deviation of the RMSE post-training indicates that the CNN is robust and performs with a similar accuracy across all 10 test datasets.

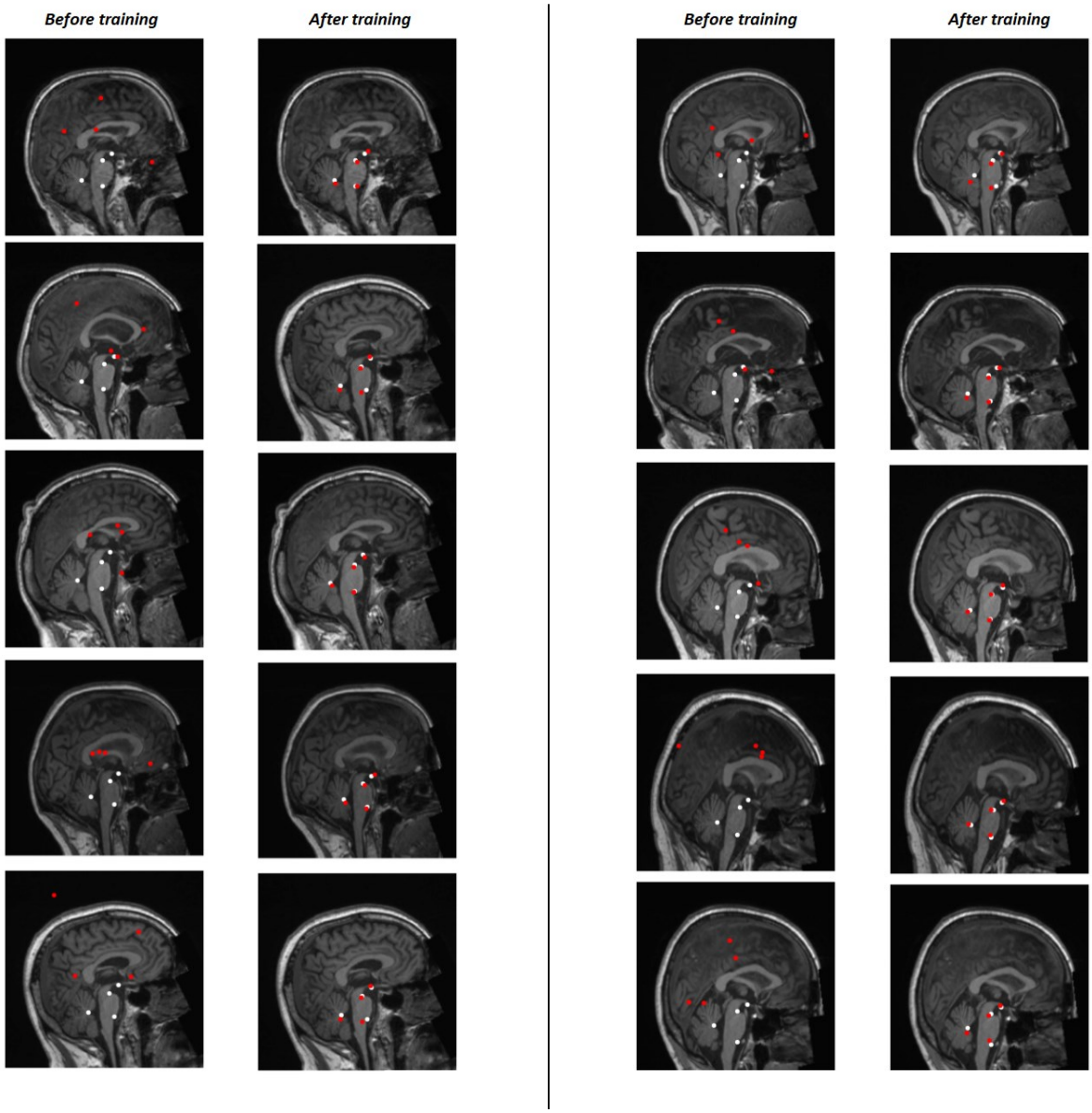

Figure 4.8: Mid-sagittal slice from ten representative MPRAGE datasets. Four brainstem anatomical landmarks are labelled, predicted by the CNN in red and ground-truth in white, before and after training with a 2D CNN.

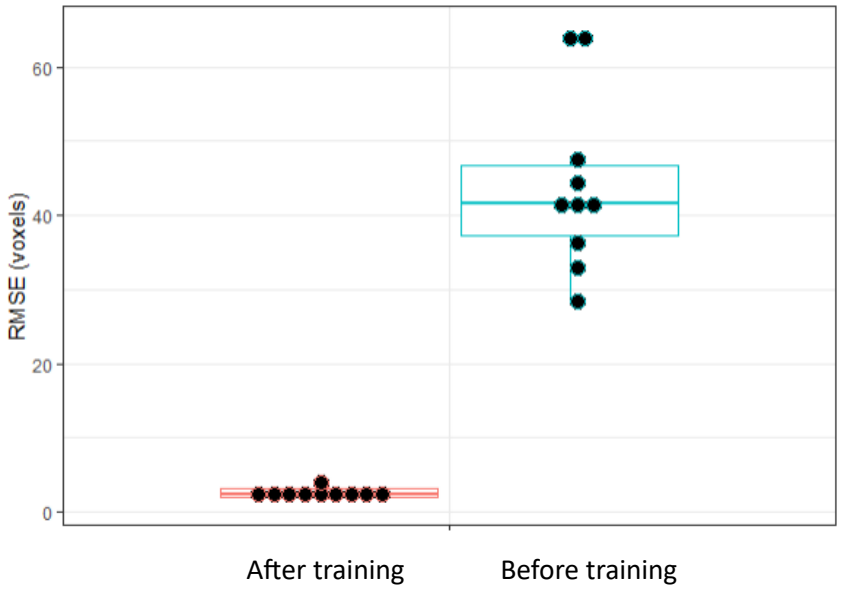

Figure 4.9: Boxplot demonstrating performance of CNN after training (red) compared to before training (blue).

Figure 4.10 demonstrates the performance of the 2D-CNN in predicting landmarks on 10 BOLD test datasets (five representative examples are displayed) before training, after training with the MPRAGE data, and after additional training with BOLD data. The RMSE of the CNN trained with MPRAGE data (9.5 ± 3.9 voxels) is significantly smaller than the RMSE before training (42.0 ± 9.6 voxels) (Two-sample t-test with Holm correction for multiple comparison, $t = 9.9$, $df = 12.0$, $p = 4.2 \times 10^{-7}$). There is a further significant improvement in the RMSE after re-training the CNN with BOLD data (4.4 ± 1.4 voxels), when compared to the CNN trained with only MPRAGE data (Two-sample t-test with Holm correction for multiple comparison, $t = 3.8$, $df = 11.3$, $p = 0.003$). The low standard deviation of the RMSE again indicates that the CNN is robust across subjects.

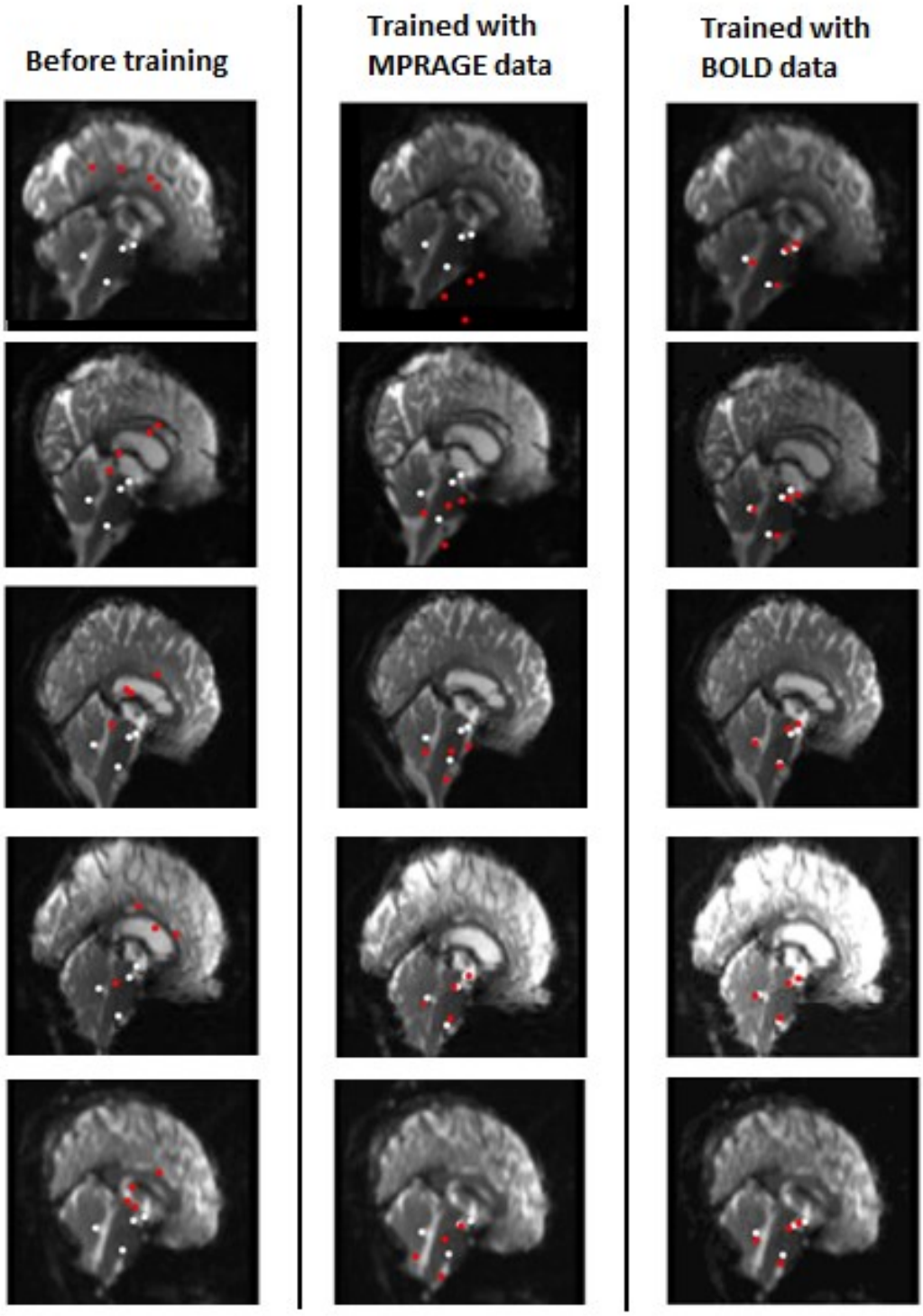

Figure 4.10: Mid-sagittal slice from five representative BOLD datasets. Four brainstem anatomical landmarks are labelled, predicted by the CNN in red and ground-truth in white. Before training (left column), CNN trained only with MPRAGE data (middle column), CNN re-trained with BOLD data (right column).

4.4.2. 3D CNN to generate brainstem ROI

The 3D-CNN was tested using 10 MPRAGE test datasets. There is good subjective agreement between the predicted and ground truth boundaries (figure 4.11). The RMSE of the predicted boundaries compared to the ground truth boundaries is significantly lower after training (Mean RMSE before = 31.1 ± 7.7 voxels (standard deviation), mean RMSE after = 6.4 ± 3.0 voxels, t = 9.49, df = 11.6, p = 8 x 10-7).

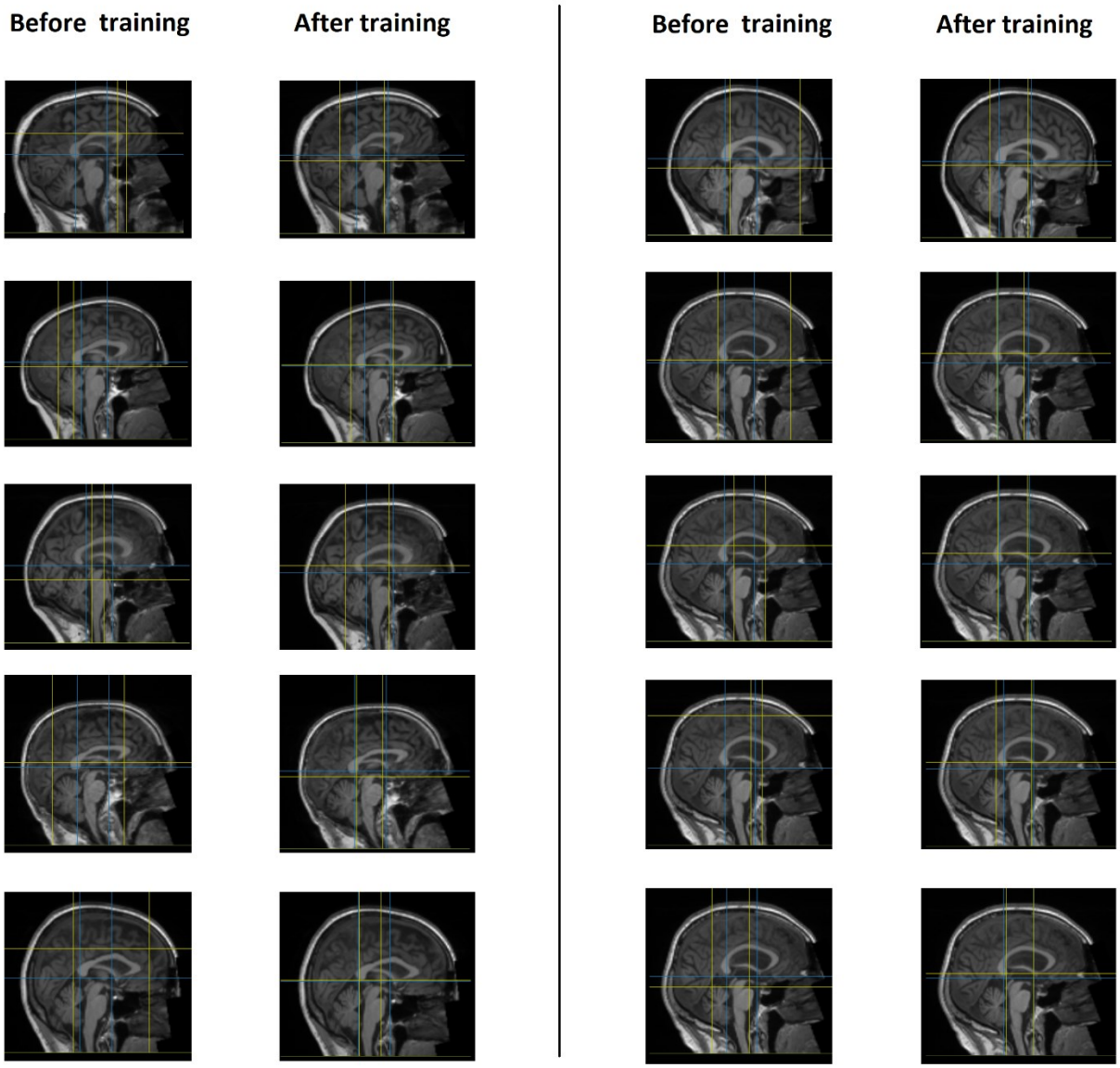

Figure 4.11: Mid-sagittal slice from ten MRPAGE datasets before and after training. The ground truth (blue) and predicted (yellow) boundaries of the brainstem region of interest are shown.

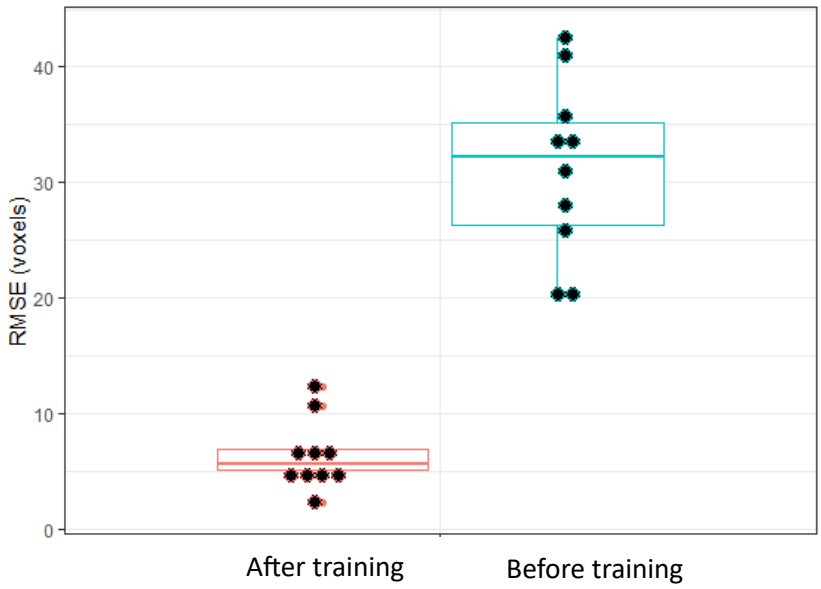

Figure 4.12: Boxplot demonstrating performance of 3D-CNN after training (red) compared to before training (blue).

4.4.3. Comparison of co-registration methods

A comparison was made of the accuracy of brainstem co-registration between functional (BOLD) and anatomical (MPRAGE) data using:

i) Affine intensity-based co-registration using FSL FLIRT
ii) 3D-CNN ABC
iii) 2D-CNN LBC
iv) Ground-truth LBC using 4 landmarks

Figure 4.13 demonstrates representative examples of the results of the four co-registration methods. Co-registration using ground-truth LBC subjectively outperforms affine intensity-based co-registration using FSL FLIRT in all cases. Napadow et al. demonstrated similar results when co-registering structural data to MNI-space (Napadow 2006). Co-registration using 2D-CNN LBC and 3D-CNN ABC subjectively outperforms affine intensity-based co-registration using FSL FLIRT in most cases. However, the last column demonstrates

that co-registration using 2D-CNN LBC doesn't always outperform affine intensity-based co-registration. Furthermore, whilst 3D-CNN ABC performed well in most cases, co-registration of one of the ten test datasets was very inaccurate (see * on figure 4.13).

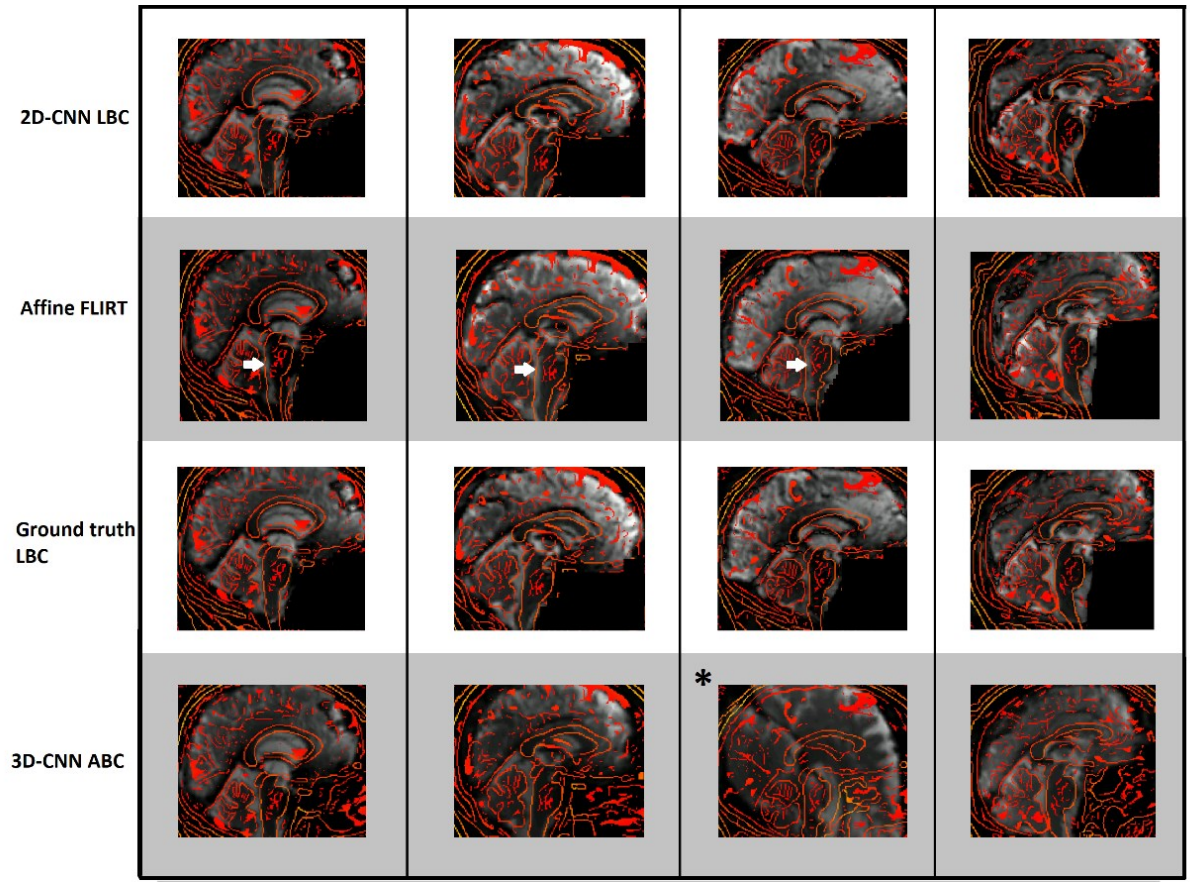

Figure 4.13: Examples of results of 2D-CNN LBC (top row), affine registration using FSL FLIRT (second row), ground-truth LBC (third row) and 3D-CNN ABC (bottom row). The outline of the anatomical MPRAGE scan is overlaid in red. In most cases, alignment with the posterior edge of the brainstem is clearly inferior using FLIRT (white arrows).

Table 4.1 and figure 4.14 summarise the RMSE of the four models. Planned two-sample t-tests (adjusted for multiple comparisons with a Holm-correction) revealed that when applied to these 10 test datasets, ground truth LBC significantly outperforms both affine intensity-based co-registration using FSL FLIRT ($t = -5.39$, $df = 14.75$, $p = 8.03 \times 10^{-5}$) and 2D-CNN LBC ($t = 2.97$, $df = 16.76$, $p = 0.009$). There was no significant difference in performance between 2D-CNN LBC and affine intensity-based co-registration using FSL FLIRT, nor between 3D-CNN ABC and any of the other three models, even after exclusion of the inaccurate dataset in the 3D-CNN ABC group (table 4.2).

Method	Mean RMSE	SD RMSE
Ground-truth LBC	2.18	0.77
2D-CNN LBC	3.38	1.02
3D-CNN ABC	6.12 (3.51 excluding outlier)	8.39 (1.48 excluding outlier)
FLIRT Affine co-registration	4.73	1.28

Table 4.1: RMSE (mean and standard deviation) of the four co-registration methods.

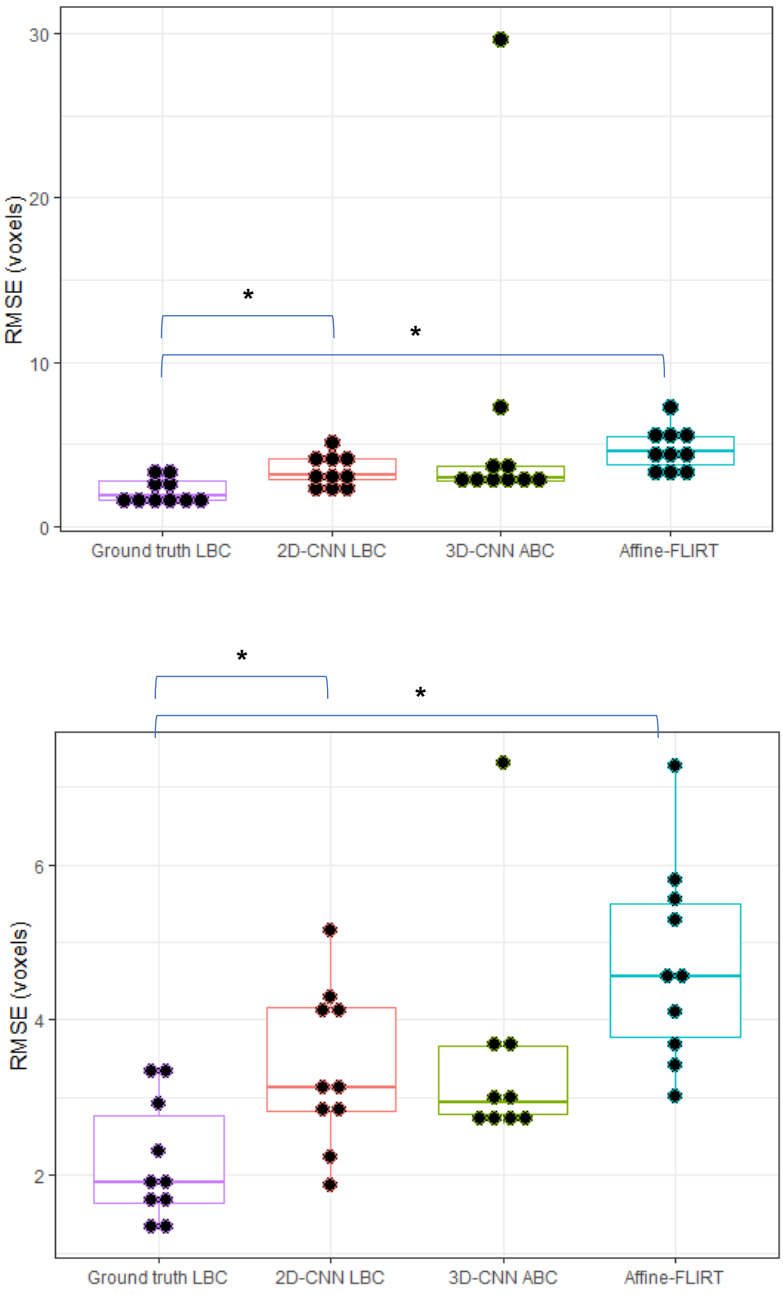

*Figure 4.14: Comparison of RMSE of the four co-registration methods. * Ground-truth LBC significantly outperforms 2D-CNN LBC and Affine-FLIRT. Top: Co-registration of one of the test datasets in the 3D-CNN ABC group was very inaccurate (see outlying datapoint). Bottom: Comparison of the methods after exclusion of this outlier.*

Comparison	t	df	p	Significance threshold (Holm corrected)
Ground-truth LBC v Affine *	-5.39	14.75	8.03×10^{-5}	0.008
2D-CNN LBC v Ground-truth LBC *	2.97	16.76	0.009	0.010
2D-CNN LBC v Affine	-2.61	17.12	0.018	0.0125
Ground-truth LBC v 3D-CNN ABC	-1.48	9.15	0.172	0.017
3D-CNN ABC v 2D-CNN LBC	1.03	9.27	0.330	0.025
3D-CNN ABC v Affine	-0.52	9.42	0.614	0.050

Table 4.2: Planned post-hoc t-tests were performed to compare the four models. In this small sample, ground-truth LBC significantly outperforms both affine FLIRT co-registration and 2D-CNN LBC. The remainder of the comparisons do not reach the threshold for statistical significance. This data includes the outlier in the 3D-CNN ABC group.

Comparison	t	df	p	Significance threshold (Holm corrected)
Ground-truth LBC v Affine *	-5.39	14.75	8.03×10^{-5}	0.008
2D-CNN LBC v Ground-truth LBC *	2.97	16.76	0.009	0.010
2D-CNN LBC v Affine	-2.61	17.12	0.018	0.0125
Ground-truth LBC v 3D-CNN ABC	-2.42	11.78	0.033	0.017
3D-CNN ABC v Affine	-1.91	16.00	0.074	0.025
3D-CNN ABC v 2D-CNN LBC	0.22	14.03	0.826	0.050

Table 4.3: Even after exclusion of the outlier in the 3D-CNN group, the results of comparing the four models remains similar. Ground-truth LBC again significantly outperforms both affine FLIRT co-registration and 2D-CNN LBC.

4.5. Discussion

There are many possible approaches to registration using deep learning (Boveiri 2020). The approach taken in this chapter was chosen because i) Napadow et al. have previously demonstrated the accuracy of brainstem co-registration using LBC and ABC but both methods were open to further automatisation, ii) pre-existing CNNs (previously trained to detect landmarks on people's faces) were available that could be tailored to facilitate and further automate Napadow's methods and iii) once successfully tailored to facilitate brainstem co-registration, the same CNNs could potentially be retrained to facilitate co-registration of other small brain structures.

Initially therefore, a 2D convolutional neural network was developed and trained using MPRAGE and BOLD data to predict the coordinates of four brainstem landmarks. These landmarks were used to perform brainstem co-registration between the BOLD and MPRAGE data. This 2D CNN was partly intended as a proof of principle, but despite being limited to two dimensions was itself found to be capable of facilitating brainstem co-registration that was subjectively more accurate than whole-brain affine co-registration using FSL FLIRT. A 3D convolutional neural network was also subsequently developed, which predicted the boundaries of a cuboidal region of interest around the brainstem. This region of interest was used to create a brainstem mask which was subsequently used to refine affine intensity-based co-registration by weighting the cost-function towards the brainstem. The performance of these methods was compared to unweighted affine intensity-based co-registration using FSL FLIRT, and to landmark-based co-registration using manually defined ground-truth brainstem landmarks.

The 2D-CNN can predict the four brainstem landmarks on MPRAGE data accurately and robustly (to within 2.5 ± 0.8 voxels of the ground truth). Landmark prediction using the 2D-CNN when applied to BOLD data is less accurate (4.4 ± 1.4 voxels). The CNN that was developed to make predictions about BOLD data had been pre-trained with MPRAGE data – pre-training is advantageous because many of the features identified in the MPRAGE data are likely to be transferable to the BOLD data (Tajbakhsh 2016). However, the BOLD data is lower resolution and fewer BOLD training datasets were used which may have biased the model towards MPRAGE data. As previously discussed, the parameters of the filters are not pre-

defined when constructing a CNN. Instead, the CNN 'learns' the optimal values for the parameters that minimises the mean square error between the predicted and ground-truth values in the training dataset. The user has no control over the values of these parameters, therefore there is some uncertainty as to which features of the data the model identifies and uses to make its predictions. Some of the filters that performed well with high resolution MPRAGE data might not perform as well with the lower resolution BOLD data. For example, there is a sharp transition between CSF and brainstem on the higher resolution MPRAGE dataset. Therefore, the CNN trained with MPRAGE data might develop a filter that identifies vertical edges, similar to figure 4.3. In the lower resolution BOLD data, the transition from brainstem to CSF is less well defined, and therefore the same vertical edge detection filter may perform less well.

The 3D-CNN is less accurate than the 2D-CNNs. It can predict the boundaries of the brainstem region of interest with an accuracy of 6.3 ± 3.0 voxels. Despite this, overall brainstem co-registration accuracy using 3D-CNN ABC is not significantly different to any of the other three methods. Accurate definition of the four brainstem landmarks that are employed by LBC is critical to the success of co-registration because LBC involves minimising the RMSE between these landmarks. For ABC, the accuracy of a brainstem ROI is not as critical, because the coordinates of the ROI boundaries are not themselves used as part of the co-registration process. Instead, the ROI is used to weight a cost-function towards the brainstem. The ABC process might therefore be more forgiving of inaccuracies in defining the boundaries of the brainstem mask.

In addition, whilst LBC requires landmarks to be defined in both anatomical and functional space, ABC does not need a brainstem mask in functional space, only in structural space. The initial co-registration from functional to structural space is a global intensity-based registration. A brainstem mask in structural space is then used to weight a second affine co-registration step between the output of the first step and the anatomical scan in structural space. The 3D-CNN therefore does not need to be able to make predictions using the lower resolution BOLD data.

The main problem with the 3D-CNN ABC method is that whilst the CNN itself is capable of defining a ROI around the brainstem with reasonable accuracy, the brainstem weighted co-registration process does not seem to be robust in its current form. 3D-CNN ABC

performed well in nine out of ten test datasets but failed completely in the tenth (figure 4.13). A co-registration failure rate of one-in-ten is not acceptable, especially if this model were to be applied to a large dataset.

A potential limitation of the 2D-LBC CNN is that it only outputs landmarks in a single plane. Therefore, any subsequent affine co-registration that uses these landmarks won't involve right-left/left-right translation or axial-rotation. This could be a problem if the participant's head is rotated to the side in the scanner. In this chapter, the LBC-CNN was restricted to 2D to simplify the development process, and to minimise training time and computational cost. This enabled proof-of-principle of this method to be demonstrated. A simple 2D CNN can also be more easily translated for use in co-registering other parts of the brain. Users could manually label anatomical landmarks on a single 2D slice of, for example, the hippocampus.

The fact that 3D-CNN ABC does not make direct use of brainstem landmarks during the co-registration process is its weakness as well as its strength. There are factors other than the accuracy of the landmarks that dictate co-registration accuracy. The 3D-CNN ABC method is still dependent on the ability of FLIRT to accurately co-register using intensity-based cost-function minimisation. If there are inaccuracies in other steps such as brain extraction this might also affect the accuracy of cost-function minimisation. LBC is not susceptible to these issues and is potentially more robust because the co-registration process is constrained by the requirement of minimise the MSE between only four brainstem landmarks. However, it is critical that the landmarks are accurately predicted. If one of these methods is to be applied to the analysis of a large dataset, refinement of the 2D-LBC CNN might be the best option because it is potentially more robust.

As discussed in section 4.3.3, co-registration accuracy was performed by evaluating the RMSE between the four ground truth brainstem landmarks on the co-registered functional data and the ground truth landmarks on the target structural dataset. However, this method is dependent on the accuracy of ground-truth labelling and might not be fully representative of co-registration accuracy. For example, evaluation of co-registration accuracy in the mid-sagittal plane might not capture misalignment at the lateral aspects of the brainstem. A potentially more robust method of objectively measuring co-registration accuracy would involve manual volumetric segmentation by an expert radiologist, which

would enable the overlap between the co-registered functional data and the structural data to be evaluated using a dice similarity coefficient or Jaccard coefficient (Mohan 2019). Any future studies that aim to improve on the work outlined in this chapter might use such methods.

4.6. Conclusion

LBC using manually defined landmarks (ground truth LBC) remains the gold standard for brainstem co-registration, but we have demonstrated that CNNs have the potential to automate both ABC and LBC. Both the 2D and 3D CNNs performed well after training with relatively few datasets, which is promising for the development of further CNNs tailored towards other regions of the brain. The LeNet architecture developed here was chosen for its relative simplicity, and the default hyperparameters (the variables that control the behaviour of the CNN, including the loss function and number of training epochs) used by Chen et al. were retained (Chen 2021). Experimentation with more complex network architectures as well as further hyperparameter optimisation might further improve CNN performance. A neural network with a similar architecture could be retrained to facilitate co-registration of other small structures in the brain.

5. Amplitude of low-frequency fluctuations, cerebral perfusion and arrival time in hypertensives – retrospective analysis of UK Biobank rsfMRI and ASL data

5.1. Introduction

As discussed in the introductory chapter, the selfish brain mechanism proposes that hypertension is a compensatory mechanism that aims to maintain cerebral blood flow (CBF) by increasing systemic blood pressure through an increase in cardiovascular sympathetic tone. The mechanism that triggers this hypothesised reduction in CBF is uncertain. Although the findings of chapter 3 were not supportive of previous work which had implicated VAH as a factor that might drive the selfish brain mechanism, there is evidence from animal studies of an association between brainstem haemodynamic impairment and hypertension. An accumulation of pro-inflammatory mediators has been demonstrated in the medulla of spontaneously hypertensive rats (SHR), and it has been proposed that localised brainstem inflammation may cause obstruction of the microvasculature supplying the sympathetic centres in the medulla, thus causing hypoxia and triggering the selfish brain mechanism (Waki 2010). Furthermore, surgical occlusion of veins draining the medulla of SHR has been shown to cause localised tissue hypoxia and a subsequent increase in systemic blood pressure (Waki 2011). Therefore, it is possible that local haemodynamic dysfunction due to inflammatory microvascular disease, rather than a more widespread reduction in CBF secondary to macrovascular anomalies such as VAH, might be responsible for triggering the selfish brain mechanism. In this context measurements of the functional reserve of the cerebral vasculature such as cerebrovascular reactivity (as discussed in section 1.4), as well as measurements of CBF, are of interest. Therefore, in this chapter we investigate the association between hypertension and regional variations in various parameters which may be markers of cerebrovascular function.

5.1.1. Background

As discussed in section 1.2, the physiological origin of the BOLD signal is multifactorial. Increased regional brain activity leads to increased metabolic demand resulting in an increase

in oxygen demand. CBF and CBV to that region increase to meet this demand. The increase in CBF and CBV to the region overcompensates for the cerebral metabolic rate of oxygen consumption ($CMRO_2$). The oxygen extraction fraction (OEF) in metabolically active regions is therefore lower in active regions, as is the deoxyhaemoglobin concentration. Therefore, the BOLD signal to neuronally active regions increases. The magnitude of the BOLD signal is a function of several physical and physiological variables including the magnetic field strength of the MRI scanner, the echo time of the BOLD sequence, the baseline blood volume, baseline oxygen extraction fraction and baseline haemoglobin concentration as well as fluctuations in blood volume, CBF and $CMRO_2$.

Most of the power of the resting state BOLD signal in the brain lies in the lower frequencies, due to the intrinsically slow response of the haemodynamic response function to changes in neural activity (Bijsterbosch 2017). The precise origin of low-frequency fluctuations (LFFs) in the BOLD signal is uncertain. Biswal et all have demonstrated a strong correlation between resting state fMRI functional connectivity maps generated from low-frequency fluctuations in the motor cortex and fMRI activation maps induced by a motor task. This suggest that the LFFs are driven by the same mechanisms that drive task-induced changes in BOLD signal, and that spontaneous fluctuations in neuronal activity contribute to LFFs. Subsequent studies have replicated these findings in other somatosensory areas (Lowe 1998), (Cordes 2000). Simultaneous measurements of fluctuations in EEG and BOLD signal also support this (Zhan 2014), (Horovitz 2008). Logothetis et al used direct electrophysiological measurements of neuronal activity and showed a correlation between local field potentials and BOLD signal changes (Logothetis 2001), which also suggests that fluctuations in neural activity contribute to resting-state BOLD fluctuations.

Haemodynamic and metabolic fluctuations might also contribute to LFFs. For example, Obrig et al (Obrig 1996) have used near infrared spectroscopy to demonstrate spontaneous low-frequency fluctuations below 0.1 Hz in cerebral oxygenation. Wise et al demonstrated that fluctuations in $ETCO_2$ in the frequency range 0-0.05 Hz correlate with fluctuations in the resting-state BOLD signal (Wise 2004).

Spontaneous low-frequency fluctuations in arterial blood pressure are known as Mayer waves, which are thought to represent oscillations in sympathetic vasomotor tone which are modulated by the baroreceptor response (Julien 2006). Mayer waves characteristically occur

at a frequency of 0.1 Hz. These spontaneous cardiovascular fluctuations might therefore contribute to LFFs in BOLD signal. Spontaneous fluctuations in arterial blood pressure have been found to correlate with cerebral blood flow velocity using Doppler ultrasound of the middle cerebral artery (Diehl 1998), (Panerai 2000). However, it is unlikely that Mayer waves alone are responsible for BOLD LFFs. Cerebral autoregulation modulates cerebral haemodynamic fluctuations induced by Mayer waves, as suggested by the work of Katura et al (Katura 2006). In their study, Katura used optical tomography to study the relationship between low-frequency oscillations in haemoglobin concentration, arterial blood pressure and heart rate and found that low-frequency oscillations in blood pressure and heart rate could only account for a fraction of the oscillations in cerebral haemoglobin concentration. Zhang et al (Zhang 2000) studied the relationship between continuous arterial blood pressure measurement and middle cerebral artery flow velocity using transcranial Doppler ultrasound. They found, amongst other things, that oscillations in flow velocity were partially attenuated at lower frequencies, which also suggests that cerebral autoregulation modulates the cerebral haemodynamic response to cardiovascular fluctuations.

Physiological and thermal noise may also contribute to LFFs in the BOLD signal. Respiratory and cardiac sources of variance in the rsfMRI signal are significant, contributing approximately 8.6% and 6.3% to the total variance in grey matter LFFs at a regional level (Bianciardi 2009). Reassuringly, spontaneous neuronal fluctuations appear to contribute a much greater proportion of the variance in spontaneous rsfMRI signal fluctuations than cardiac pulsations (figure 5.1). Bianciardi also demonstrated that signal drifts at frequencies < 0.01 Hz make a significant contribution to LFFs, possibly due to head motion, slow changes in baseline physiology or changes in the baseline MRI scanner conditions. At a voxel level, thermal noise also significantly contributes to LFFs (up to 38% in grey matter), but when region of interest analysis is considered, the thermal contributions are negligible.

The biophysical origin of these low-frequency resting-state BOLD fluctuations is therefore non-specific. Nevertheless, the amplitude of the low frequency fluctuations (ALFF) in the resting-state BOLD signal has previously been found to vary between various physiological and pathophysiological states. For example, Yang et al. found ALFF in the visual cortices to be significantly higher with the eyes open than with the eyes closed (Yang 2007). Other studies have suggested regional differences in ALFF between different diseases such as major

depressive disorder (J. Liu 2014), mesial temporal lobe epilepsy (Zhang 2010), Alzheimer's (Yang 2018), and migraine (Wang 2016). ALFF is therefore a potentially useful index of neurovascular function, with the caveat that it is non-specific because of the multifactorial nature of the BOLD signal and the variety of factors that drive low-frequency fluctuations in it. Spontaneous fluctuations in neuronal activity, fluctuations in metabolic parameters including ETO_2 and $ETCO_2$, fluctuations in cerebral blood flow and cerebral blood volume driven by systemic arterial blood pressure variability modulated by cerebral autoregulation, and sources of physiological and thermal noise are all likely to contribute.

Interestingly, cerebrovascular reactivity (CVR) has also been linked to low frequency fluctuations in the BOLD signal. As discussed in section 1.4, CVR represents the capacity of a cerebral blood vessel to change calibre in response to a stimulus. Measurement of CVR provides information on the functional reserve of the vascular system. Assessment of CVR usually requires the administration of a vasoactive substance such as carbon dioxide or acetazolamide to modulate CBF. Golestani et al have previously demonstrated a significant association in the motor and executive control networks between CVR maps, generated by measuring the CBF response to a hypercapnic challenge, and ALFF in the 0.008 – 0.09 Hz range (Golestani 2016). Furthermore, Ni et al have demonstrated a significant widespread correlation between CVR maps derived from resting-state BOLD data and ALFF in the 0.01 – 0.08 Hz range (Ni 2022). Low-frequency fluctuations in the rsfMRI signal may therefore contain information on CVR.

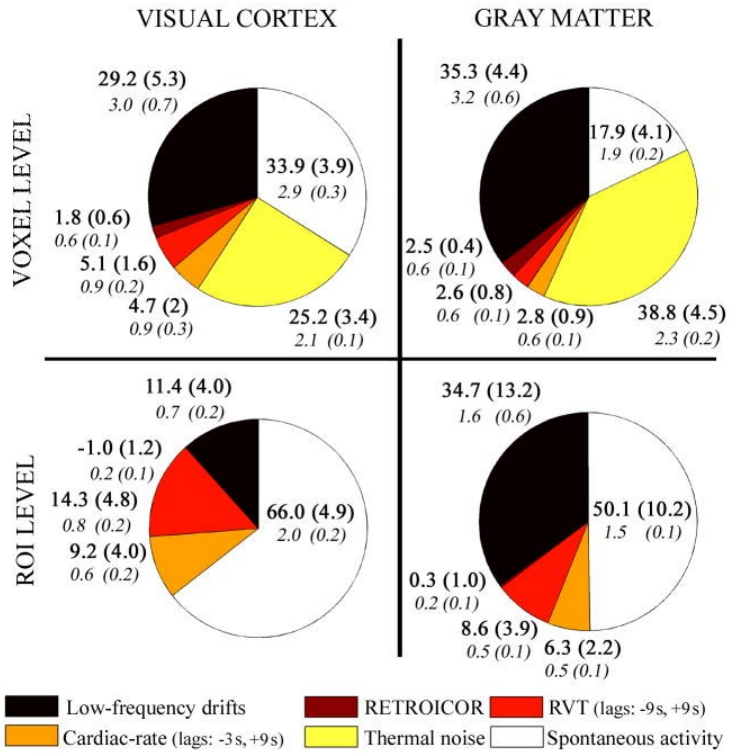

Figure 5.1: Bianciardi et al. demonstrated the relative contribution of various sources to low-frequency fluctuations in rsfMRI signal at the voxel and regional level (taken from (Bianciardi 2009)).

Fluctuations in the resting state BOLD signal due to physiological processes have been shown to contaminate ALFF measurements. Qi-Hong Zou et al (Zou 2008) have previously demonstrated that high-powered fluctuations within the CSF spaces will dominate over lower powered fluctuations in the brain parenchyma, reducing the sensitivity of the ALFF analysis (Zou 2008) to detect spontaneous brain activity (figure 5.2). To address this, a fractional correction to ALFF can be applied by calculating the ratio of the power at each frequency to the mean power across the whole frequency spectrum. This ratio, known as fractional ALFF (fALFF), suppresses contributions from the CSF spaces and large vessels, improving the sensitivity to detect variations between brain regions.

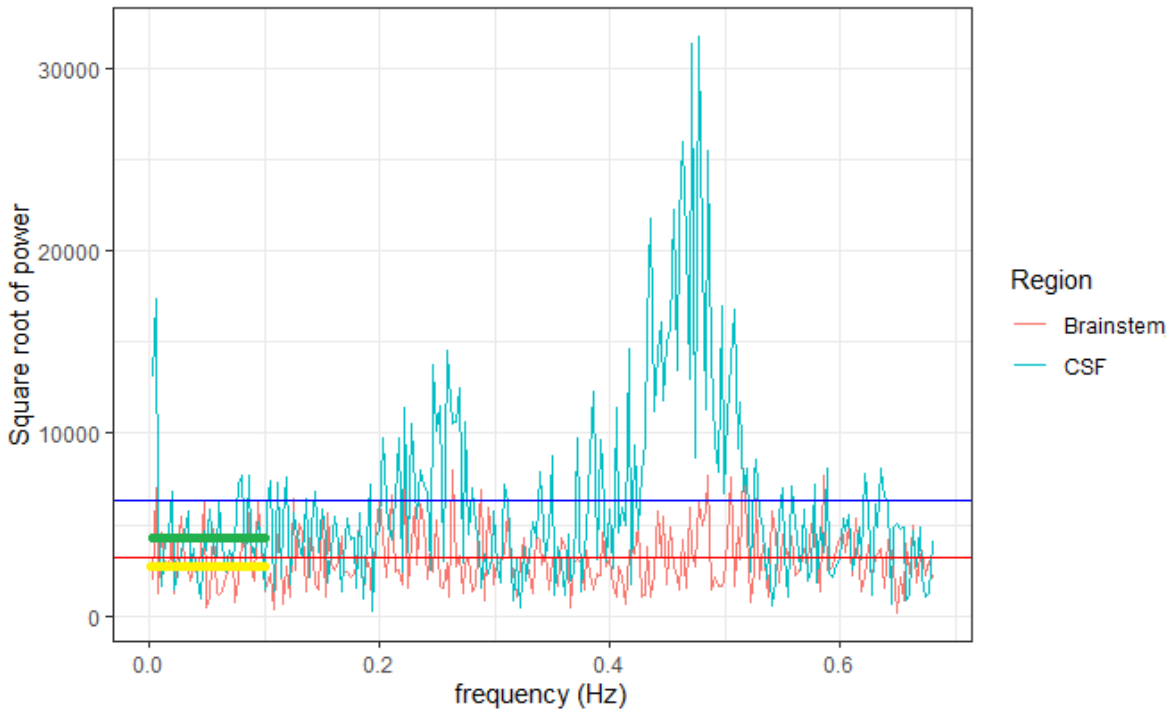

Figure 5.2: Brainstem (red) and CSF (blue) voxel power spectrum. The power in the CSF voxel is higher across the entire frequency spectrum, but especially at higher frequencies. Blue line = mean power in CSF voxel, red line = mean power in brainstem voxel. The ALFF in the CSF voxel (green line) is higher than the ALFF in the brainstem (yellow line). However, the ratio of ALFF to the mean amplitude of the power spectrum (i.e. fractional ALFF) is higher in the brainstem than in the CSF. Therefore CSF fALFF is suppressed relative to brainstem fALFF by the fractional correction.

UK Biobank is a large biomedical database containing genetic and health information on over 500,000 participants. rfMRI and ASL data for a group of hypertensive participants and a group of normotensive controls was downloaded from this repository and processed to generate regional fALFF values. The selfish brain mechanism proposes that cerebrovascular abnormalities precipitate hypertension. However, hypertension is itself causally associated with pathological changes to small subcortical and cortical perforating cerebral blood vessels (Prins 2015) leading to chronic cerebral microangiopathy (Alosoco 2014). Whilst a causal relationship between fALFF and hypertension cannot be established by the cross-sectional approach taken in this chapter, cerebrovascular disease caused by hypertension would be expected to affect the anterior and posterior circulation reasonably equally. If impaired cerebrovascular function specifically involving the posterior circulation (mediated by vertebral artery hypoplasia) or the medulla (mediated by, for example, localised brainstem

inflammation) plays a causal role in the development of hypertension, a significant differential between CVR in the posterior circulation and/or medulla compared to the anterior circulation would be expected. Therefore, our primary hypothesis was that fALFF in the posterior circulation, and specifically the medulla, would be lower in hypertensives. We also analysed a set of ASL data to evaluate CBF and arterial arrival time (AAT), with the hypothesis that CBF would be reduced and AAT increased in the hypertensive medulla. An association between impaired medullary cerebrovascular reactivity and hypertension would be consistent with the selfish brain mechanism, and such a finding would support the development of further longitudinal research to elucidate the direction of any such association.

5.1.2. Summary of aims

1. Compare regional CBF and AAT, derived from ASL data, between hypertensives and normotensives.
2. Compare regional ALFF, derived from resting-state BOLD fMRI data, between hypertensives and normotensives.

5.2. Methods

5.2.1. UK Biobank

High-resolution structural T1 and resting state functional MRI data is available for 44097 UK Biobank participants. Arterial spin labelling data is available for 1174 participants. Approval was obtained to download and analyse rsfMRI and ASL data for the purpose of addressing the hypotheses relevant to this chapter.

International Statistical Classification of Diseases and Related Health Problems revision-10 (ICD-10) diagnostic codes from hospital inpatient records were used to classify participants as hypertensive or normotensive. UK Biobank includes a data-field containing the diagnoses listed in participants' hospital records (data-field 41204). All participants with a recorded diagnosis of 'essential (primary) hypertension' were included. Participants with a recorded diagnosis of 'secondary hypertension', including 'renovascular hypertension',

'hypertension secondary to other renal disorders', 'hypertension secondary to endocrine disorders', 'other secondary hypertension', or 'secondary hypertension, unspecified', were excluded.

Participants were also asked at the assessment centre about their past medical history, including a history of hypertension and when this was first diagnosed. Self-reported hypertension is recorded as either 'hypertension' or 'essential hypertension'. There is no reference to 'secondary hypertension' in the assessment centre data, and no further detail on how the diagnosis of 'hypertension' or 'essential hypertension' was reached, and which (if any) investigations to exclude secondary hypertension were performed. The hypertension status of each participant was therefore determined solely based on ICD-10 criteria.

5.2.2. MRI analysis

UK Biobank rsfMRI data were acquired with the following parameters – spatial resolution = 2.4 mm isotropic, 88 x 88 x 64 matrix, 6 minutes duration (490 timepoints), TR = 0.735 s, TE = 39ms, GE-EPI with x8 multi-slice acceleration, no iPAT, flip angle 52°, fat saturation.

UK Biobank ASL data were acquired using a multi-PLD acquisition with five PLDs (400, 800, 1200, 1600 and 2000 ms). Pseudo-continuous ASL used to label the arterial bolus (bolus duration 1800 ms), with a GRASE readout (1 tag-control pair per PLD, EPI factor 48, turbo factor 12, 3.4 x 3.4 x 4.5 mm resolution, TR 4220 ms, TE 29.4 ms). An uncalibrated perfusion image was generated by taking the mean of the tag-control subtracted data at each PLD. This was visually inspected to confirm that the tag-control subtracted data contained perfusion information. Next, oxford_asl was used to generate whole-brain maps of perfusion and arrival time. As discussed in section 1.3, oxford_asl is a command line tool that is part of the Bayesian Inference for Arterial Spin Labeling (BASIL) toolbox for analysis of ASL data (Chappell 2009). BASIL fits a kinetic curve to multi-PLD ASL data and generates voxel-wise estimates of cerebral perfusion. Voxelwise calibration of the perfusion data was performed using an M_0 acquisition. Oxford_asl also generates voxel-wise estimates of AAT.

High resolution T1-weighted structural images (1mm^3 isotropic resolution) were available from UK Biobank in pre-processed form (Alfaro-Almagro 2018). This included tissue-type segmentation using FAST (FMRIB's Automated Segmentation Tool) (Zhang 2001), and co-registration to a MNI152 template in standard space using a combination of linear and non-linear transformations which were subsequently combined into a single structural-to-MNI non-linear warp field.

Generic pre-processing steps were applied to all ASL and rsfMRI data. Data were motion-corrected and brain extracted using FSL MCFLIRT and BET, respectively. Spatial smoothing was applied with a kernel full-width half maximum (FWHM) equal to twice the voxel size of the functional data. Co-registration from each individual's subject space to their structural image was performed using FSL FLIRT. The structural-to-MNI non-linear warp field available from UK Biobank was then used to co-register the functional dataset to a standard MNI152 template.

5.2.3. ALFF and fractional ALFF

Previous studies have utilised ALFF using various bandpass frequencies (J. e. Zhan 2016) but the majority of the literature on ALFF has focused on a narrower frequency range between 0.01 and 0.08 Hz. Recent work by Liu et al (Liu 2021) used the global mean rsfMRI time course, bandpass filtered between various frequencies, as a regressor in multiple general linear models (GLM) to investigate which frequency range of the rsfMRI time course led to rsCVR maps with the strongest correlation with CVR maps generated using a hypercapnic challenge. A frequency range of 0 to 0.1164 Hz was found to have the strongest correlation. Therefore, we initially selected the broadest frequency range (between 0 and 0.1164 Hz) suggested by the literature to maximise sensitivity to detect differences in CVR between hypertensives and normotensives. However, low-frequency fluctuations in respiration, heart rate (Shmueli 2007) and systemic blood pressure (Julien 2006) might contribute to ALFF in this frequency range. Therefore, to confirm that the results of the analysis in the 0 to 0.1164 Hz frequency range were not significantly affected by the above confounds, the same 2054 hypertensive and 1724 normotensive rsfMRI datasets were re-analysed using the narrower frequency band of 0.01 to 0.08 Hz.

Voxelwise fALFF was calculated as follows. Firstly, the linear trend in the data was removed (to address the possible confound of low frequency drifts in the MRI signal) and the data were de-meaned then bandpass filtered between 0 and 0.1164 Hz. The voxelwise bandpass filtered data were transformed to voxelwise power spectra using *fslpspec*. The power of a frequency component is proportional to the square of the amplitude at that frequency. The square root of the voxelwise power spectrum data was obtained, and the mean of this between 0 and 0.1164 Hz calculated to give the ALFF between these frequencies. The fractional ALFF correction was then applied as follows. Unfiltered rsfMRI data were transformed to voxelwise power spectra using fslpspec. The mean amplitude of the power spectra across the entire frequency range (0 to 0.680 Hz) of the rsfMRI signal was calculated (the upper frequency limit of the rsfMRI data is defined according to the Nyquist limit and the sampling rate of the rsfMRI acquisition (TR = 0.735 s)). The voxelwise mean ALFF maps were then divided within each participant with these maps to produce maps displaying voxelwise ALFF as a fraction of the mean amplitude of signal fluctuations across the entire rsfMRI frequency spectrum (fALFF). These values were then converted to z-scores (using mean frontal grey matter fALFF as a reference).

Because we are interested in whether there is a differential between anterior and posterior circulation fALFF in hypertensives, we standardised against the anterior circulation ROI (frontal grey matter). If posterior circulation CVR is indeed impaired in the presence of hypertension, standardisation of fALFF against a whole brain ROI might reduce our sensitivity to detect a significant difference between the anterior and posterior circulation. The standardised subcortical fALFF values could also then be compared against the standardised visual cortex fALFF to determine if there is a regional difference in fALFF z-scores within the posterior circulation, to test our primary hypothesis that medullary fALFF is lower in hypertension. Mean frontal grey matter ALFF was subtracted from the voxelwise ALFF, then this was divided by the standard deviation of the frontal grey matter fALFF, to generate a map of fALFF z-scores. These were transformed to MNI space using the spatial registration matrices generated during the pre-processing stage.

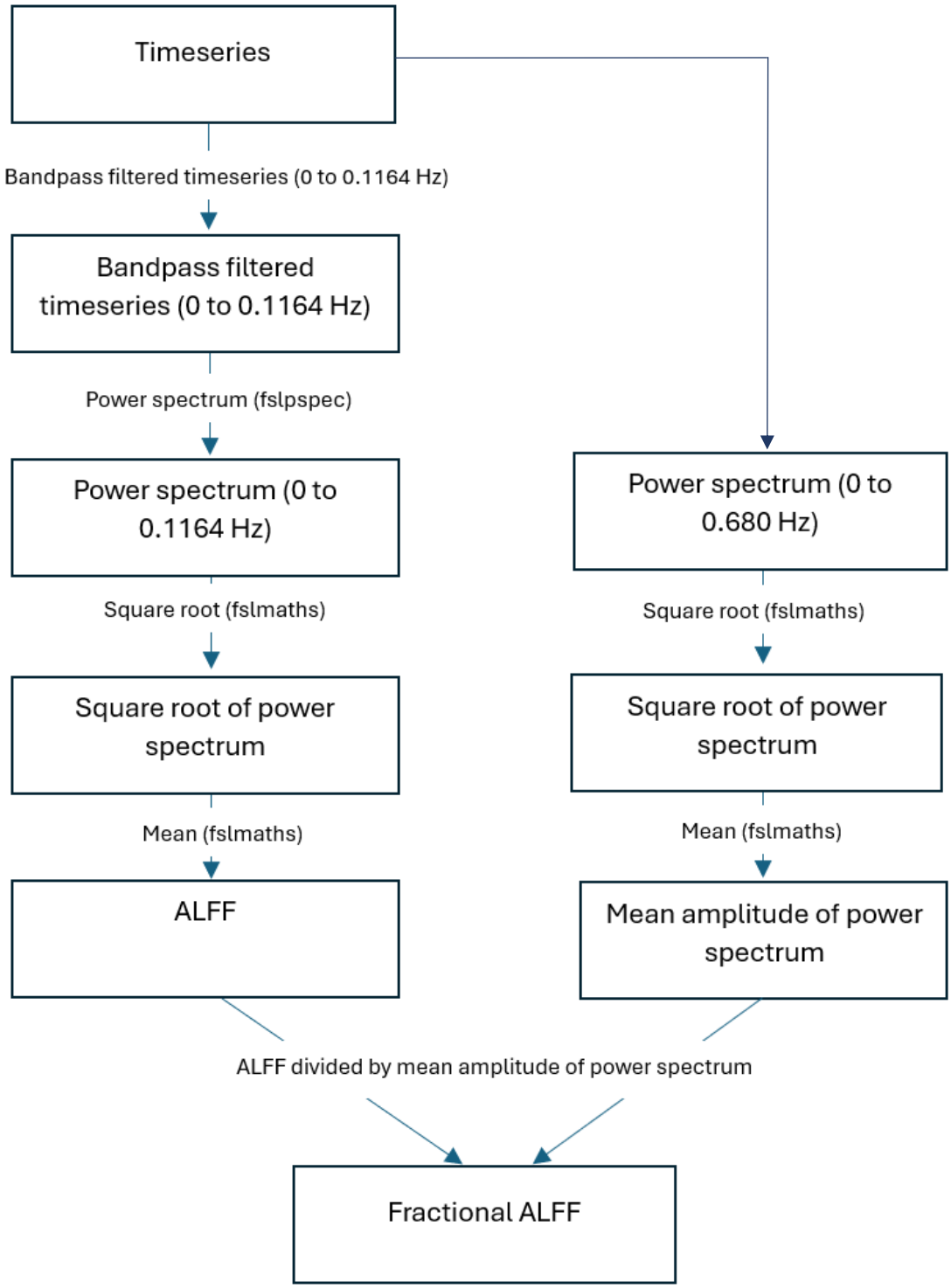

Figure 5.3: Outline of fALFF calculation.

Regional brainstem masks were generated by segmentation of the MNI152 template using FreeSurfer (Fischl 2012) Harvard-Oxford cortical atlas was used to generate masks for

the other regions of interest. Using these masks, mean regional CBF, ATT and fALFF values were calculated.

5.2.4. Regional analysis

Three brainstem (medulla, pons and midbrain), five subcortical (thalamus, hypothalamus, hippocampus, amygdala and insula – all components of the central autonomic network) and two reference (frontal grey matter and visual cortex grey matter) regions of interest (ROI) were included in the analysis. ROI analysis was chosen over voxelwise analysis because i) we are testing a specific hypothesis and ii) ROI analysis minimises the contribution of thermal noise to ALFF (Bianciardi 2009).

Preliminary analysis revealed several participants with CBF and/or ATT close to zero. Visual inspection of these data did not reveal any obvious qualitative problems. However, very low values of arrival time and CBF do not make physiological sense. Outliers were defined as datapoints greater than 1.5 times lower (or higher) than the lower (or upper) interquartile range. No CBF values met these criteria, but 5 low-lying arrival time values were excluded from the analysis. Similarly, 4 outlying fALFF values were excluded.

5.2.5. Statistical analysis

Age, sex and BMI are all associated with blood pressure variability and are all risk factors for the development of hypertension (Pinto 2007), (Collaboration 2021), (Cheng 2022), (Reckelhoff 2001), (Drøyvold 2005). Preliminary exploration of this data revealed a significant difference in these variables between the hypertensive and normotensive groups which could confound the analysis of ALFF/fALFF between hypertensives and normotensives. These variables were therefore included as covariates in the statistical model. Propensity score matching is a technique applied to observational data which matches participants between experimental groups according to their baseline characteristics. This creates two experimental groups which share similar baseline characteristics and helps to eliminate the effect of confounding variables on the outcome variable. In this case, the R software package

'MatchIt' was used to create a normotensive group which matched the hypertensive group according to age, sex and BMI in order to control their effect on between-group differences in ALFF/fALFF.

Three separate two-way ANCOVAs were applied (initial analysis of small dataset 0-0.1164 Hz, largescale analysis 0-0.1164 Hz and largescale analysis 0.01-0.08Hz) to each of the three dependent variables of interest (CBF, AAT and fALFF), with blood pressure group (normotensive or hypertensive) and brain region as independent variables. To control familywise error rate across the three ANOVA tests, a Bonferroni correction was applied, and the significance level set at 0.0167. Age, BMI and sex were included as covariates. The results of parametric testing are outlined in appendix 4 and 5.

Following on from the results of the fALFF analysis of 242 participants, a power calculation was performed to determine the sample size required to achieve a power of 0.8 with a type-II error probability of 0.05 in relation to detecting a significant effect of the interaction between region and BP group. The software package G*power (Faul 2007) was applied, and the required sample size estimated to be 3461. A second fALFF region of interest analysis with 2054 hypertensives and 1724 matched normotensives (total sample size of 3778) was subsequently performed.

We limited the analysis to a subset of UK Biobank participants, whilst ensuring that the sample size was above that dictated by our power calculation, because of limitations in computational processing time and data storage capacity. 2054 hypertensive rsfMRI datasets were obtained from the UK Biobank database. These were propensity matched against 2054 normotensive datasets. Unfortunately, a number of these matched normotensive rsfMRI datasets had failed UK Biobank quality control and were marked as 'unusable' and were therefore excluded from the present analysis, leaving 1724 normotensive rsfMRI datasets. The sample size was still well above the threshold calculated in our power calculation. The calculation of regional fALFF subsequently followed the same steps as those previously outlined. Two-way ANCOVA was again applied, with fALFF as the dependent variable and blood pressure group (normotensive or hypertensive) and brain region as independent variables. Age, BMI and sex were included as covariates.

5.3. Results

Within the UK Biobank repository, 8706 participants with rfMRI data and 142 participants with ASL data are classed as having 'essential hypertension'. One of the ASL datasets was excluded due to also being labelled with an ICD-10 diagnosis of 'secondary hypertension', leaving 141 hypertensive ASL datasets (see figure 5.4).

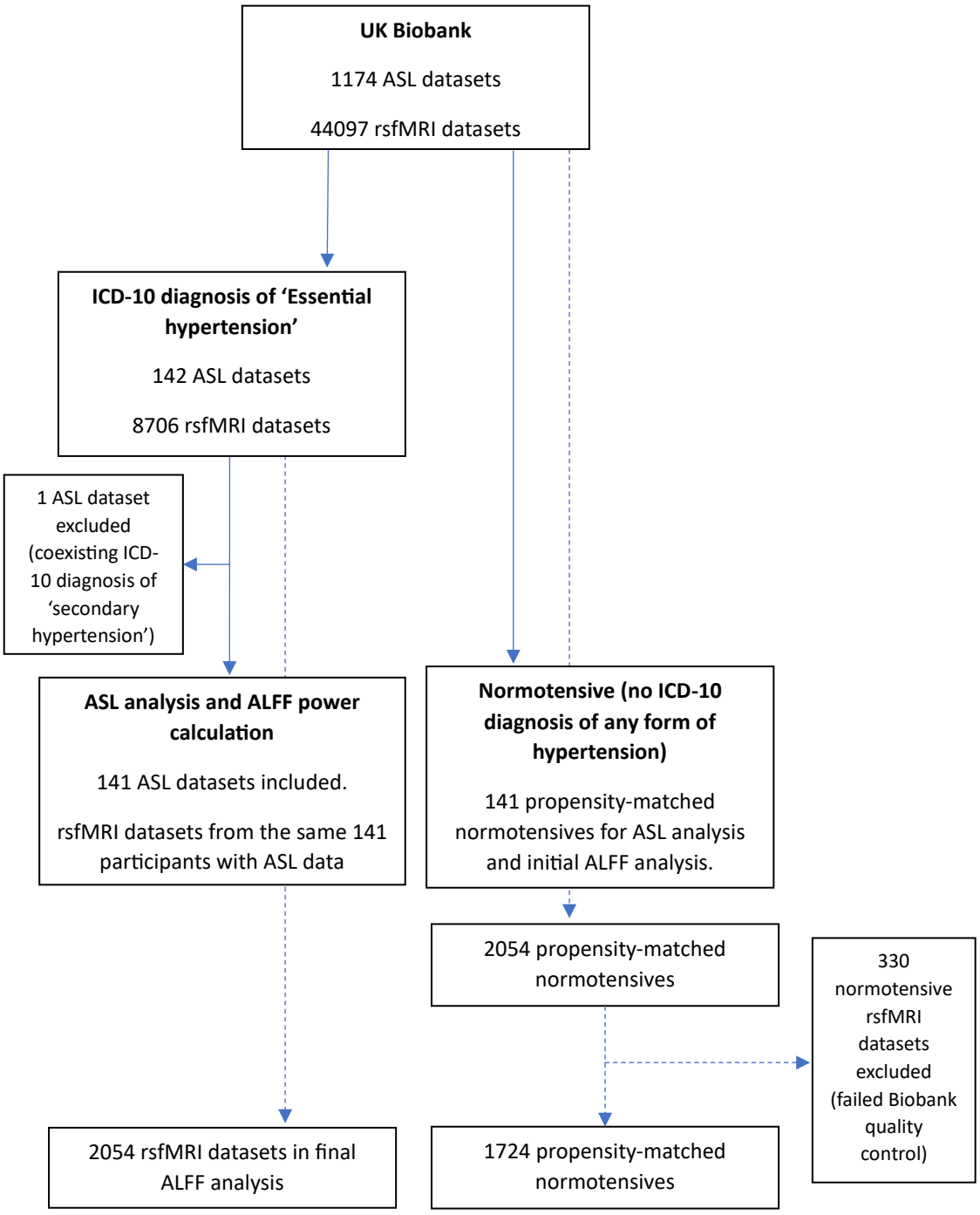

Figure 5.4: Participant selection from the UK Biobank repository.

Initially, we analysed ASL and rsfMRI data from the 141 hypertensives for whom ASL data was available, as well as 141 matched normotensive controls. This facilitated a direct comparison of ALFF, CBF and AAT within this group of 242 participants. However, whilst the number of ASL datasets is limited, there are 8706 hypertensive rsfMRI datasets in the UK Biobank database. Therefore, the results of the initial analysis of 242 datasets were used in a power calculation to determine the sample size required to achieve a power of 0.8 with a type-II error probability of 0.05 in relation to detecting a significant effect of the interaction between regional ALFF and blood pressure status. This yielded a required sample size of 3461 participants (including both hypertensives and normotensive controls). Subsequently, a largescale analysis of 2054 hypertensive rsfMRI and 1724 matched normotensive rsfMRI datasets was performed. Due to limited data storage space it was not possible to analyse all 8706 hypertensive rsfMRI datasets.

5.3.1. Initial analysis of 141 hypertensives and 141 normotensives

Tables 5.1 and 5.2 summarise the baseline demographic information of the hypertensive and normotensive groups before and after propensity score matching. Before matching, the hypertensive group is significantly older, contains significantly more males, and has a significantly higher BMI. After matching there is no significant difference in age, sex, or BMI between the two groups.

Table 5.1: Baseline characteristics before matching. 812 normotensive datasets were initially acquired from the UK Biobank database, and these were used in the subsequent propensity matching process, the results of which are outlined in table 5.2 below. Age, BMI and sex significantly differ between groups. Values are specified as mean ± standard deviation.

	Hypertensive (141)	Normotensive (812 initially obtained from UK Biobank)	p-value
Age (mean)	54.7 ± 7.6	49.6 ± 7.5	$<6.5 \times 10^{-13}$
BMI (mean)	28.5 ± 4.3	26.1 ± 4.5	2.9×10^{-9}
Proportion male	0.62	0.40	(chi-square) 1.8×10^{-9}
BP systolic (mmHg)	147.6 ± 18.8	129.9 ± 16.4	$<2.2 \times 10^{-16}$
BP diastolic (mmHg)	88.4 ± 17.5	78.9 ± 9.4	$<2.2 \times 10^{-16}$

Table 5.2: Baseline characteristics after matching. No significant difference in age, sex or BMI between the groups. Values are specified as mean ± standard deviation.

	Hypertensive (141)	Normotensive (141)	p-value
Age (mean)	54.7 ± 7.6	54.6 ± 7.5	0.85
BMI (mean)	28.5 ± 4.3	28.4 ± 4.6	0.66
Proportion male	0.62	0.61	(chi-square) 0.60
BP systolic (mmHg)	147.6 ± 18.8	137.4 ± 16.4	$<6.9 \times 10^{-6}$
BP diastolic (mmHg)	88.4 ± 17.5	82.9 ± 9.4	$<2.4 \times 10^{-5}$

A two-way ANCOVA comparing blood pressure (normotensive or hypertensive) and brain region on fALFF z-score, with age, BMI and sex included as covariates, found that mean fALFF z-score across all regions in hypertensives (-0.538 (standard deviation 0.521, standard error 0.01) is significantly higher than in normotensives (-0.615 (standard deviation 0.487, standard error 0.01), $F(1) = 30.03$, $p = 4.6 \times 10^{-8}$, partial $\eta^2 = 0.008$). There is a significant regional difference in fALFF z-score across all participants ($F(14) = 91.72$, $p < 2 \times 10^{-16}$, partial

$\eta^2 = 0.26$). The age, sex and BMI covariates also significantly predict fALFF z-score. However, there was no statistically significant effect of the interaction between brainstem region and blood pressure group on fALFF z-score ($F(14) = 0.639$, $p = 0.83$, partial $\eta^2 = 0.002$).

5.3.2. Largescale fALFF analysis 0-0.1164 Hz

As previously discussed, the results of the initial analysis of 242 participants prompted a largescale fALFF analysis. Table 5.3 demonstrates that there is no significant difference in baseline demographics between the hypertensive and normotensive groups included in the largescale analysis.

Table 5.3: Baseline characteristics after matching. No significant difference in age, sex or BMI between the groups.

	Hypertensive (2054)	Normotensive (1724)	p-value
Age (mean)	57.7 ± 6.7	57.5 ± 6.9	0.37
BMI (mean)	27.8 ± 4.0	27.6 ± 4.4	0.48
Proportion male	0.60	0.61	(chi-square) 0.22
BP systolic (mmHg)	149.0 ± 18.1	137.0 ± 17.0	$<2.2 \times 10^{-6}$
BP diastolic (mmHg)	87.0 ± 10.6	81.2 ± 9.7	$<2.2 \times 10^{-6}$

Figure 5.5 demonstrates a summary of regional fALFF z-scores between the blood pressure groups in the largescale analysis. A two-way ANCOVA comparing blood pressure (normotensive or hypertensive) and brain region on fALFF z-score, with age, BMI and sex included as covariates, found that the mean fALFF z-score across all regions in hypertensives (-0.66 (standard deviation = 0.56, standard error = 0.003)) is significantly higher than in normotensives (-0.67 (standard deviation = 0.56, standard error = 0.004), $F(1) = 11.95$, $p = 0.0005$), although the effect size is extremely small (partial $\eta^2 = 0.0002$).

There is a significant regional difference in fALFF z-score ($F(14) = 1126.17$, $p < 2 \times 10^{-16}$, partial $\eta^2 = 0.22$). Age, BMI and sex also significantly predict fALFF z-score. However, there

was no statistically significant effect of the interaction between brainstem region and blood pressure group on fALFF z-score ($F(14) = 0.23$, $p = 0.99$, partial $\eta^2 = 8 \times 10^{-5}$).

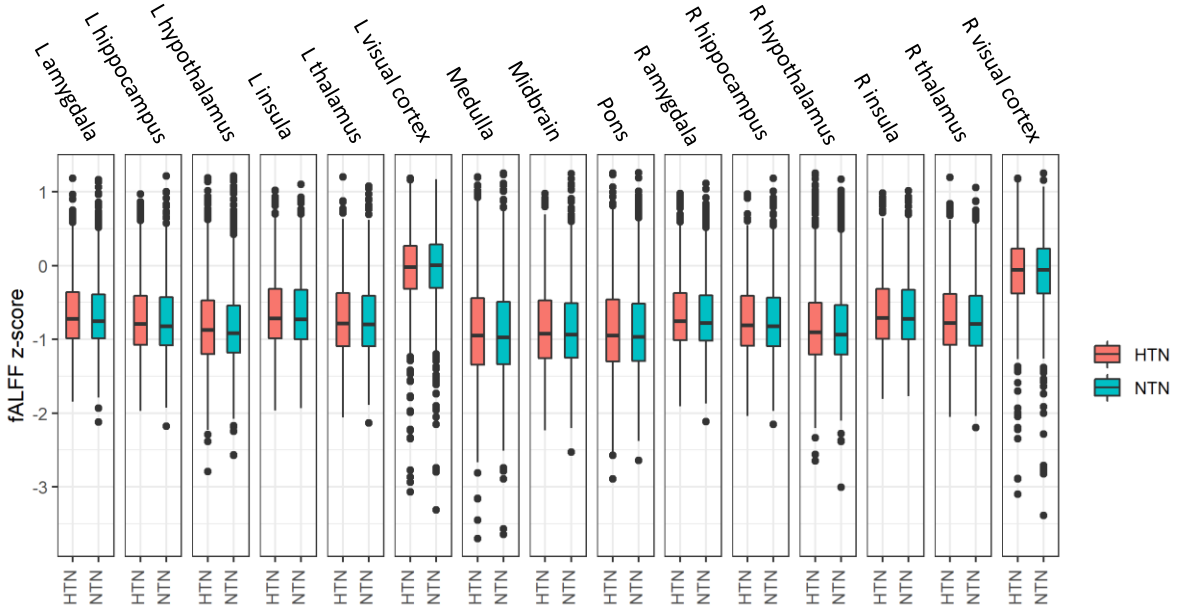

Figure 5.5: Regional fALFF z-score (0 – 0.1164 Hz) varies across the brain in both hypertensives and normotensives. There is no significant difference in the pattern of regional variation between the hypertensive and normotensive groups.

5.3.3. Largescale fALFF analysis 0.01 to 0.08 Hz

Figure 5.6 demonstrates a summary of regional fALFF z-scores (in the frequency range 0.01 – 0.08 Hz) between the blood pressure groups in the largescale analysis. A two-way ANCOVA comparing blood pressure (normotensive or hypertensive) and brain region on fALFF z-score, with age, BMI and sex included as covariates, found no significant difference between mean fALFF z-score across all regions in hypertensives (-0.605 (standard deviation = 0.508, standard error = 0.003)) and normotensives (-0.613 (standard deviation = 0.509, standard error = 0.003), $F(1) = 3.94$, $p = 0.047$, partial $\eta^2 = 0.0001$) after a Bonferroni correction for multiple comparisons (with $p < 0.0167$ set as the threshold for statistical significance).

Once again there is a significant regional difference in fALFF z-score ($F(14) = 1222.85$, $p < 2 \times 10^{-16}$, partial $\eta^2 = 0.26$). Age, BMI and sex also significantly predict fALFF z-score. As with the analysis of the broader frequency range, there is no statistically significant effect of

the interaction between brainstem region and blood pressure group on fALFF z-score (F(14) = 0.29, p = 0.99, partial η^2 = 0.0001).

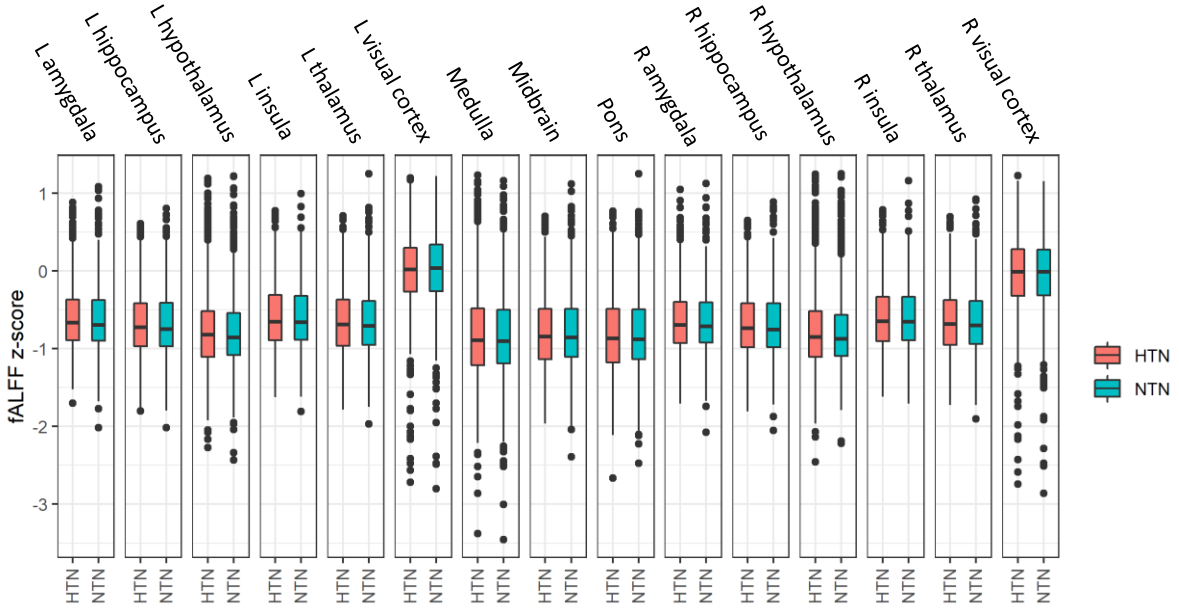

Figure 5.6: Regional fALFF z-score (0.01 – 0.08 Hz) varies across the brain in both hypertensives and normotensives. There is no significant difference in the pattern of regional variation between the hypertensive and normotensive groups.

5.3.4. Regional cerebral blood flow in hypertensives and normotensives

A two-way ANCOVA comparing the effect of blood pressure (normotensive or hypertensive) and brain region on CBF, with age, BMI and sex included as covariates, found that total CBF across all ROIs under consideration is significantly lower in the hypertensive group, although the effect size is small (figure 5.7, mean hypertensive CBF = 23.2 (standard deviation = 11.4, standard error = 0.3), mean normotensive CBF = 24.2 mL/100g/min (standard deviation = 11.0, standard error = 0.2), F(1) = 16.8, p = 4 x 10^{-5}, partial η^2 = 0.004). There is also a significant variation in CBF between brain regions (figure 5.8, F(16) = 261.8, p < 2 x 10^{-16}, partial η^2 = 0.49). The covariates (age, sex and BMI) also significantly predict CBF. There was no statistically significant effect of the interaction between region and blood pressure group on CBF (F(16) = 0.48, p = 0.96, partial η^2 = 0.002).

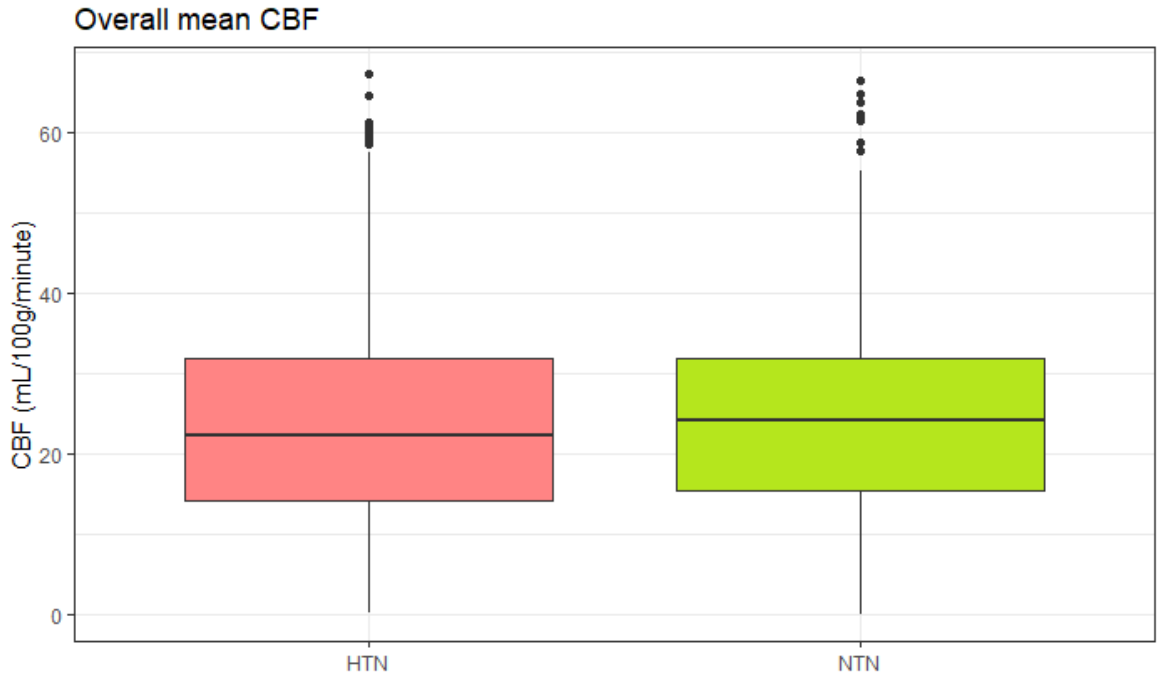

Figure 5.7: Mean CBF across all ROIs is significantly lower in the hypertensive group compared to the normotensive group.

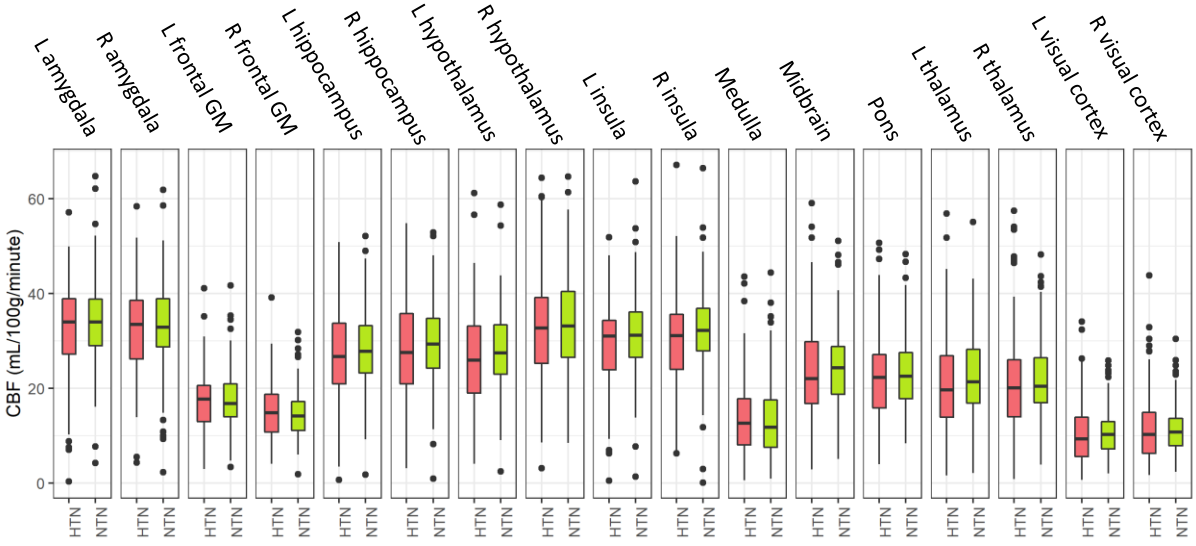

Figure 5.8: CBF (mL/100g brain tissue/minute) to regions of the brain implicated in sympathetic function, and to reference regions (frontal and occipital grey matter), in hypertensives and normotensives.

5.3.5. Regional arterial arrival times in hypertensives and normotensives

A two-way ANCOVA comparing the effect of blood pressure (normotensive or hypertensive) and brain region on arrival time, with age, BMI and sex included as covariates, reveals no statistically significant difference in arrival times between normotensives and hypertensives (figure 5.9, mean arrival time in hypertensives = 1.21 s (standard deviation 0.10, standard error 2.30×10^{-3}) vs normotensives = 1.21 s (standard deviation 0.11, standard error 2.38×10^{-3}), $F(1) = 0.77$, $p = 0.38$, partial $\eta^2 = 0.002$).

However, there is a significant difference in arrival time across brain regions (figure 5.10, ($F(16) = 136.1$, $p < 2 \times 10^{-16}$, partial $\eta^2 = 0.49$). The covariates age and sex also significantly predict arrival times. There is also a statistically significant effect of the interaction between brain region and blood pressure group on arrival time ($F(16) = 3.41$, $p = 4.4 \times 10^{-6}$, partial $\eta^2 = 0.01$).

Analysis of the simple main effect of blood pressure group within each region was subsequently performed by grouping the data by region and performing one-way ANCOVA for blood pressure group with age, sex and BMI as covariates. A Holm correction was applied, with the initial threshold for statistical significance set at an α-level of 0.003 (that is $\alpha = 0.05/17$ for 17 ROIs)). There was no statistically significant difference in arrival time in the medulla between hypertensives and normotensives (medulla mean arrival time in normotensives = 1.26 s (standard deviation 0.10, standard error 0.01) and in hypertensives = 1.22 s (standard deviation 0.11, standard error 0.01), $p = 0.01$) or in any of the other regions of interest (table 5.4). Analysis of the simple main effect of region in each blood pressure group was similarly performed. There is a significant regional variation in ATT within each blood pressure group. This is expected given the significant regional variation across all participants. The pattern of regional variation is very similar between the two blood pressure groups, as demonstrated in figure 5.10.

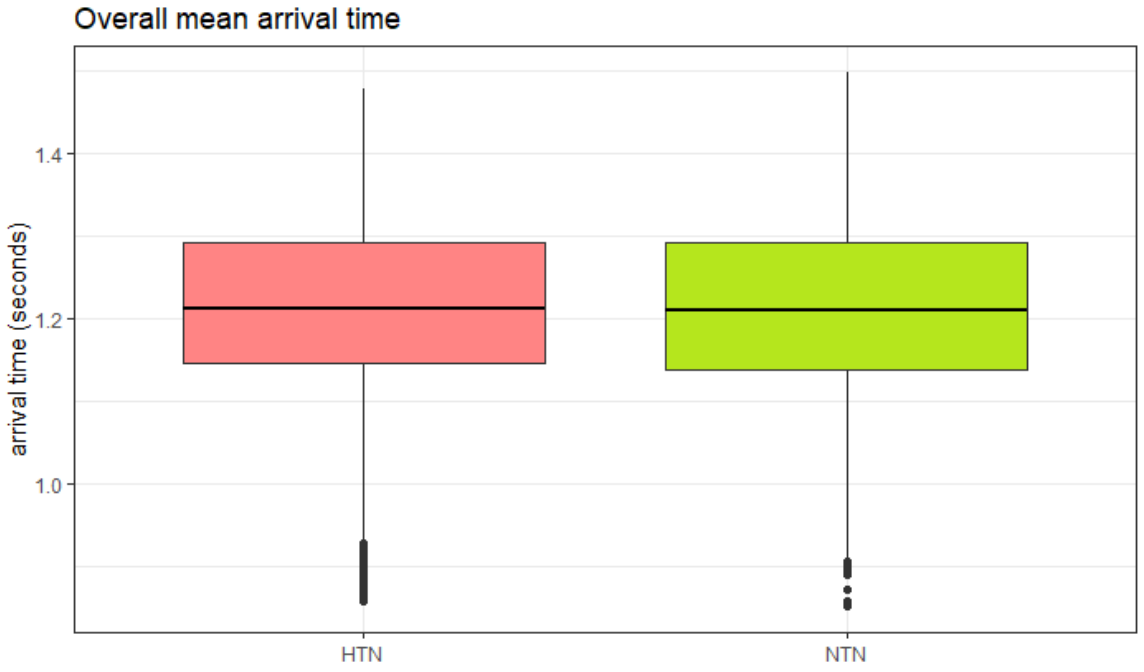

Figure 5.9: There is no significant difference in arrival time across all ROIs between hypertensives and normotensives.

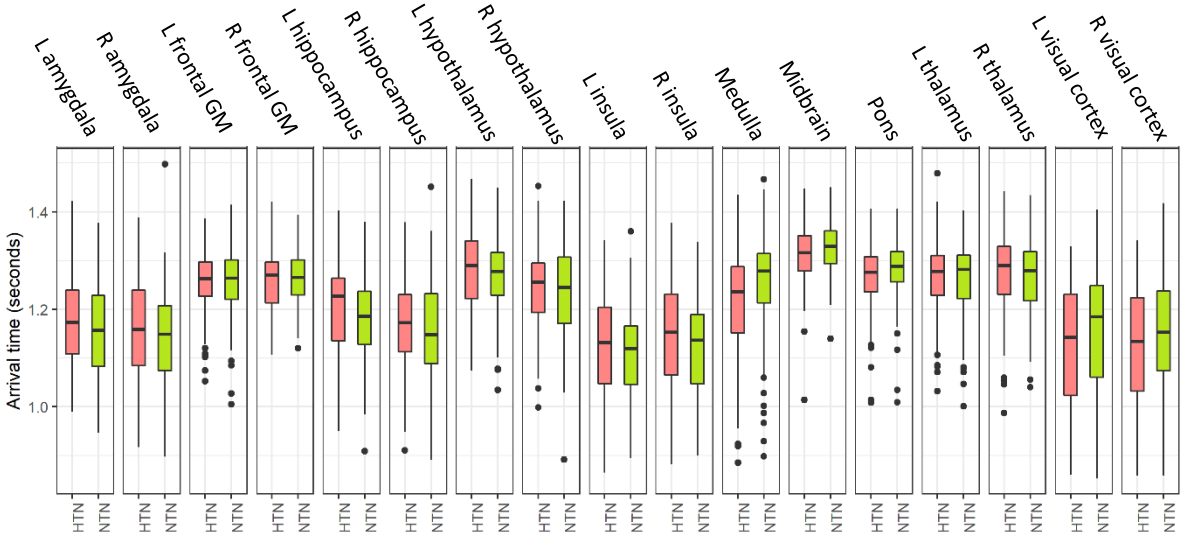

Figure 5.10: Regional arrival time varies across the brain in both hypertensives and normotensives, and there is a statistically significant interaction between region and blood pressure group.

	Arrival time (NTN) (seconds ± stdev)	Arrival time (HTN) (seconds ± stdev)	Deg. Of freedom	F	p	Significance threshold (Holm corrected)
Medulla	1.26 ± 0.10	1.22 ± 0.11	252	9.46	0.004	0.003
R insula	1.12 ± 0.09	1.15 ± 0.10	261	5.07	0.015	0.003
L hippocampus	1.18 ± 0.08	1.20 ± 0.09	260	5.11	0.025	0.003
L visual cortex	1.15 ± 0.13	1.13 ± 0.13	234	3.82	0.058	0.004
Pons	1.28 ± 0.06	1.27 ± 0.07	260	3.63	0.058	0.004
Midbrain	1.33 ± 0.05	1.31 ± 0.06	261	3.37	0.068	0.004
R amygdala	1.14 ± 0.10	1.16 ± 0.10	261	3.29	0.071	0.005
L amygdala	1.15 ± 0.10	1.18 ± 0.10	261	2.96	0.086	0.005
L hypothalamus	1.26 ± 0.06	1.28 ± 0.06	261	2.73	0.100	0.006
L insula	1.11 ± 0.10	1.13 ± 0.10	260	2.31	0.130	0.006
R frontal GM	1.26 ± 0.06	1.25 ± 0.06	256	2.01	0.158	0.007
R hippocampus	1.15 ± 0.09	1.17 ± 0.09	261	1.75	0.188	0.008
R visual cortex	1.15 ± 0.12	1.14 ± 0.13	238	1.64	0.202	0.010
R hypothalamus	1.24 ± 0.06	1.25 ± 0.06	261	0.69	0.406	0.013
R thalamus	1.27 ± 0.08	1.27 ± 0.08	260	0.35	0.554	0.017
L thalamus	1.26 ± 0.08	1.26 ± 0.08	260	0.02	0.881	0.025
L frontal GM	1.26 ± 0.07	1.26 ± 0.06	257	0.00	0.989	0.050

Table 5.4: Summary of mean regional arrival times in hypertensive and normotensives. Analysis of the simple main effect of blood pressure group in each region did not reveal any statistically significant differences between hypertensives and normotensives after a Holm correction to the significance threshold.

5.4. Discussion

In this chapter we have investigated whether fALFF, CBF and AAT in the medulla, as well as other parts of the central autonomic network, vary between hypertensives and normotensives using data from UK Biobank. A regional analysis was performed rather than voxelwise analysis to specifically test our hypothesis that the hypertensive medulla is differentially affected, and to mitigate the contribution of thermal noise to the fALFF. fALFF in the medulla, normalised against the frontal grey matter, was compared to several subcortical regions of interest that are part of the central autonomic network, as well as to a control region in the visual cortical grey matter. In the first instance a preliminary analysis of a small subset (n = 242) of participants was performed, and the results used in a power calculation to determine the sample size required to detect a significant effect of the interaction between

regional ALFF and blood pressure status. Subsequently, regional fALFF between 0 and 0.1164 Hz was compared in 2054 hypertensives and 1724 normotensives. In summary, in the frequency range 0 to 0.1164 Hz, there is a statistically significant difference in mean fALFF across all ROIs between hypertensives and normotensives, but the effect size is so small as to be almost inconsequential. Furthermore, when the analysis was repeated using a narrower frequency band (0.01 – 0.08 Hz), the difference in mean fALFF did not reach the threshold for statistical significance, which suggests contributions from respiratory, cardiac and blood pressure fluctuations may be confounding fALFF in the broader frequency range. Similarly, there is a significant regional variation in fALFF (at both 0 – 0.1164 Hz and 0.01 – 0.08 Hz), but this regional variation does not differ between hypertensives and normotensives, suggesting that regional fALFF is not predictive of hypertension.

The regional variation in fALFF demonstrated in figures 5.5 and 5.6 is interesting, and might reflect regional differences in the contributions of physiological and thermal noise and neuronal and haemodynamic fluctuations to fALFF. The brainstem and the other subcortical grey matter structures that were included in the analysis are more caudally located and might be more susceptible to noise from cardiac, CSF and respiratory fluctuations, which might explain the difference in fALFF between these regions and the visual cortex.

This regional difference in fALFF was the same in hypertensives and normotensives, which is contrary to our primary hypothesis. However, the results do not necessarily disprove our primary hypothesis that brainstem CVR may be differentially affected in hypertension, because fALFF may not be a sufficiently specific marker of cerebrovascular function. Despite its lack of specificity, fALFF might be useful as a screening tool that can be applied retrospectively in an exploratory manner to large datasets such as UK Biobank, and to guide the direction of more specific studies with targeted hypotheses. In chapter 6 we go on to explore whether ALFF and fALFF are indeed valid surrogate markers of CVR.

The mean CBF across all the ROIs under consideration was found to be lower in hypertensives. This is consistent with previous studies which have demonstrated a global reduction in CBF in hypertensives (Muller 2012), (E. e. Warnert 2016), (Nobili 1993). CBF significantly varies between different ROIs. This is to be expected considering regional variations in grey and white matter content, and regional variations in AAT which may affect ASL labelling efficiency. There is no statistically significant interaction between brain region

and blood pressure group. This implies that there is a consistent difference in CBF between hypertensives and normotensives across all parts of the central autonomic network, and that regional differences in CBF follow a similar pattern in hypertensives and normotensives. Therefore, CBF to the medulla is not differentially affected in hypertensives according to this analysis. This is consistent with previous work by our group which demonstrated a consistent reduction in CBF across all brain regions in hypertensives (E. e. Warnert 2016). Based on the results of this chapter, it does not appear that CBF to any one central autonomic region is differentially affected in hypertensives.

The reduction in total CBF across all regions implies that systemic hypertension is unable to fully correct the reduced CBF that is hypothesised to precede hypertension. However, there are other possible explanations for the globally reduced CBF in hypertensives. 19 out of 141 hypertensives for whom ASL data was available self-reported as receiving antihypertensive medication, 75 denied receiving antihypertensive medication, and 47 gave no definitive answer, and our group has previously found that patients receiving antihypertensive medication have significantly lower CBF than untreated and healthy young normotensives (E. e. Warnert 2016) (though we were unable to replicate this finding in a subsequent analysis of the data (see chapter 3)). Hypertension is also strongly associated with cerebrovascular disease (Y. Liu 2018), (Li 2018), which may have precipitated the reduction in CBF. Age and hypertension have both been found to correlate with incidental subcortical MRI lesions that are thought to be secondary to chronic cerebrovascular disease (Awad 1986). Such lesions are common above the age of 40 (Awad 1986), and the mean age in this study was 54.7 and 54.6 in the hypertensive and normotensive groups respectively. It is therefore likely that, independent of the selfish brain mechanism, there is a greater cerebrovascular disease burden in the hypertensive group in this study, which is consistent with the global CBF reduction in this group. Elucidating the direction of the causal relationship between hypertension and cerebrovascular dysfunction is one of the central challenges of investigating the selfish brain mechanism, and as previously discussed can only truly be addressed with a longitudinal study.

Arrival time is dependent on location of the labelling plane in the neck, which varies between studies, but the values here are in broad agreement with those previously estimated using ASL (Y. Chen 2012), (Macintosh 2010). There is no statistically significant difference in

global arrival time between normotensives and hypertensives in this set of participants. There is a significant difference in arrival times across the brain regions, which is expected considering the labelled bolus must travel different distances to different regions of the brain. Brainstem white matter might also prolong arrival time. The interaction between brain region and blood pressure group was statistically significant in the initial two-way ANCOVA model, but post-hoc testing did not reveal a significant difference in regional arrival time between the blood pressure groups.

De Vis et al compared the spatial variation in ALFF and fALFF (frequency range 0.01-0.08Hz) with that of BOLD CVR induced by both hypercapnia and hyperoxia and found Pearson's R^2 of 0.61 and 0.31 for ALFF v hypercapnia and hyperoxia BOLD CVR respectively. This is encouraging from the point of view of using ALFF as a surrogate for CVR, because it suggests that a large proportion of the spatial variation in ALFF is consistent with the spatial variation in BOLD CVR. However, hyperoxia BOLD CVR maps also correlate with ALFF maps, suggesting that variations in venous blood volume may also contribute to ALFF. This latter point is further evidence that ALFF is multifactorial and, at best, a non-specific surrogate for CVR.

5.4.1. Limitations

Our aim was to use fALFF as a surrogate for CVR, and a frequency range between 0 and 0.1164 Hz was initially selected because it has been previously suggested that LFFs in this range might contain information related to CVR. However, the physiological basis of fALFF is likely to be multifactorial, containing contributions from spontaneous fluctuations in neuronal activity (H. e. Yang 2007), (Biswal 1995). Bianciardi et al demonstrated that signal drifts at frequencies < 0.01 Hz make a significant contribution to LFFs, possibly due to head motion, slow changes in baseline physiology or changes in the baseline MRI scanner conditions (Bianciardi 2009). An attempt was made to mitigate for such low frequency drifts by removing the linear trend in the data prior to the fALFF calculation. Normal respiration occurs at about 0.25 Hz, which is above our cut-off frequency of 0.1164 Hz. However, the respiratory rate could drop below this cut-off frequency in some cases. Furthermore, low-frequency

fluctuations in heart rate (Shmueli 2007) and systemic blood pressure (Julien 2006) in the range < 0.1Hz have been shown to correlate with fluctuations in rsfMRI signal, just below our cut-off frequency of 0.1164 Hz. It therefore possible that respiratory fluctuations, cardiac pulsation or systemic blood pressure fluctuations may contribute to the LFFs between 0 and 0.1164 Hz. The results of our analysis between 0 and 0.1164 Hz were not replicated in the narrower frequency range 0.01 to 0.08 Hz, which further suggests that signal contamination from cardiac, respiratory or blood pressure fluctuations may have adversely affected the analysis in the 0 to 0.1164 Hz frequency range.

We applied fALFF rather than ALFF because of our desire to suppress low-frequency fluctuations in the basal cisterns in order to improve the sensitivity of our metric to detect significant variations between hypertensives and normotensives within the adjacent brainstem. However, cerebrospinal fluid (CSF) fluctuations are thought to be at least partly driven by haemodynamic oscillations such as vessel wall movement and changes in cerebral blood volume in the low frequency range (H. e. Yang 2022). The application of this fractional correction might therefore suppress some of the vascular contributions to fALFF and reduce our sensitivity to detect changes in vascular reactivity.

The mean CBF value of 22.4 mL/100g/min in hypertensives and 23.5 mL/100g/min in normotensives is lower than expected. Whilst the relatively low brainstem CBF inevitably contributes to this low overall mean, of greater concern is the fact that frontal and visual cortical grey matter values are even lower (below 20 mL/100g/minute, figure 5.8). Grey matter CBF measured using ASL is usually between 40 and 100 mL/100g/min (Alsop 2015). The ASL acquisition contains a limited number of measurements (only one measurement per PLD) which probably compromises the SNR of the data, and calls into question the validity of the CBF measurements from this ASL dataset. A possible explanation for the fact that subcortical ROIs demonstrate larger CBF values than the visual cortex and frontal grey matter is that these subcortical ROIs are in areas which are particularly susceptible to physiological noise. If the SNR of the ASL data is so low that noise dominates over perfusion information, ROIs in areas which are subject to more noise might demonstrate an apparently higher CBF than areas subject to less noise.

As discussed in section 1.4, there are several methods of assessing CVR by measuring the haemodynamic response to one of a variety of vasoactive stimuli. These may all be more

robust methods of measuring CVR than using a metric such as fALFF, but unfortunately they are not typically present in large biomedical databases. They are also technically challenging to acquire compared to rsfMRI data. A surrogate marker of vascular reactivity such as fALFF is therefore potentially valuable as a tool to explore large datasets before applying a more robust measure of CVR in a prospective study.

Finally, this was a retrospective study using data from the UK Biobank database. The UK Biobank database contains a very large number of participants, but the ASL sequence has only recently been introduced, and there are only a limited number of ICD-10 diagnosed hypertensives with ASL data available, which limited the sample size of CBF and ATT analysis in this study. Categorisation of participants as hypertensive was made based on ICD-10 diagnoses derived from clinical records, but as detailed in tables 5.2 and 5.3 the measured blood pressure in some of the participants designated as normotensive might lie within the hypertensive range, therefore there may be some undiagnosed hypertensives in the normotensive population. Finally, we were unable to fully ascertain the medication history of the participants, and therefore couldn't study the impact of antihypertensive medication.

5.5. Conclusion

In this study we investigated the association between fALFF and hypertension in the context of the selfish brain mechanism. Mean fALFF in the frequency range 0 – 0.1164 Hz across the brainstem, amygdala, hippocampus, hypothalamus, thalamus, insula cortex and visual cortex, calculated from resting state BOLD signal, is significantly higher in hypertensives, but the effect size is extremely small. There is a significant regional variation in fALFF across the brain but here was no association between regional fALFF and hypertension. fALFF in the medulla does not seem to have a specific association with hypertension. The physiological basis of fALFF is uncertain, and it is unlikely to be useful as a specific distinguishing marker of cerebrovascular reactivity in the context of hypertension, but might useful as a general measure of cerebrovascular function in other cerebrovascular pathologies.

Allowing for the limitations of the data, total cerebral blood flow across all the ROIs was lower in hypertensives than normotensives, which is consistent with previous work.

There was no significant effect of the interaction between blood pressure group and region on fALFF or CBF. In the context of the selfish brain mechanism, the findings suggest that there is a global reduction in CBF in hypertensives, rather than haemodynamic compromise being restricted to one autonomic region such as the medulla. If the selfish brain mechanism is indeed a cause of hypertension, these results are more consistent with a generalised CBF reduction, for example due to vertebral artery hypoplasia, acting as a trigger, rather than a local CBF reduction, for example due to local microvascular inflammation in the medulla. Furthermore, whilst there is an association between hypertension and a global reduction in CBF, there are limitations to the data, and the cross-sectional nature of the data precludes any inference about the direction of the causal relationship, if any, between hypertension and CBF. Further prospective longitudinal studies of cerebral haemodynamics in hypertensives and normotensives are required to investigate the selfish brain mechanism. The utility of fALFF as a surrogate of CVR is also in doubt, and this is further explored in the following chapter.

6. Validation of the amplitude of low frequency fluctuation (ALFF) in resting-state fMRI data as a surrogate marker of cerebrovascular reactivity

6.1. Introduction

Following on from the outcomes of chapter 5, which cast doubt over the utility of fALFF in the frequency range 0 – 0.1164Hz as a surrogate marker of CVR, in this chapter we investigate whether an association between ALFF/fALFF and CVR can be isolated to a specific frequency range. As previously discussed, whilst neural activity can cause an increase in the BOLD signal by inducing an increase in CBF to meet the metabolic demands of the brain, BOLD signal changes also occur in the absence of neural activity, in response to purely haemodynamic effects. For example, an increase in arterial carbon dioxide concentration (at levels which are not believed to influence the cerebral metabolic rate of oxygen consumption ($CMRO_2$)) induces an increase in BOLD signal by causing cerebral vasodilation, an increase in CBF, and a subsequent reduction in OEF and deoxyhaemoglobin concentration. As previously discussed, CO_2 is commonly administered as a vasoactive stimulus to assess cerebrovascular reactivity (CVR), typically by measuring the BOLD or ASL signal response to hypercapnia. Measurable fluctuations in the BOLD signal have also been demonstrated in response to low-frequency fluctuations in resting arterial CO_2 concentration- Wise et al observed fluctuations of 0.110 ± 0.033% BOLD signal change per mmHg CO_2 for grey matter and 0.049 ± 0.022% per mmHg in white matter that correlated with peak end-tidal carbon dioxide ($ETCO_2$) fluctuations of ±1.1 mm Hg in the frequency range 0–0.05 Hz (Wise 2004). Furthermore, CVR maps have been derived from resting-state BOLD data by using end-tidal CO_2 ($ETCO_2$) as a regressor in a general linear model (GLM) and using the parameter estimate, β, as an indicator of CVR (Lipp 2015). Golestani et al demonstrated that whole-brain maps of the amplitude of low frequency fluctuations (ALFF) in the resting-state BOLD signal were qualitatively similar to the standard CVR maps obtained by modulating the BOLD signal through a sinusoidal variation of the inspired CO_2, and that global grey matter ALFF significantly correlates with standard CVR measurements.

Therefore, despite the multifactorial nature of the biophysical origin of the BOLD signal, it follows that low frequency fluctuations in the resting-state BOLD signal, driven by natural haemodynamic fluctuations such as those which occur with resting fluctuations in arterial CO_2 concentration, or due to variations in other parameters which affect cerebral autoregulation, could be used to assess CVR. It might be possible to derive a metric of CVR from resting-state BOLD data in the absence of $ETCO_2$ measurements.

CVR is conventionally assessed by measuring the BOLD or ASL signal response to a vasoactive stimulus, such as the administration of CO_2. This requires specialist breathing apparatus to administer CO_2, as well as continuous physiological monitoring to enable measurement of $ETCO_2$. It is also dependent on participant compliance, and hypercapnia can be uncomfortable. Validation of a metric of CVR that is non-invasive and does not require the patient to perform a task is therefore desirable. This would widen the scope of applying CVR in both the research and clinical settings, with minimal input from MRI operators and participants, and would open the door to retrospective analysis of previously acquired data.

Previous studies that have evaluated whether metrics of CVR can be derived from resting-state BOLD data have all used BOLD CVR as the gold-standard, with variable results. As discussed, the origin of the BOLD signal is not purely related to changes in CBF, and it is therefore difficult to draw firm conclusions when comparing different metrics of CVR that have all been derived from BOLD data. By comparing resting-state BOLD data with data that is much more closely aligned with cerebral blood flow, such as ASL, it might be possible to further evaluate whether resting-state BOLD data can be used to derive accurate metrics of CVR. In this chapter, we further evaluate whether ALFF is a useful metric of CVR by comparing it to both ASL CVR and BOLD CVR data.

ALFF and fractional ALFF (fALFF) are compared to ASL and BOLD CVR within the cortical grey matter, where BOLD and ASL signal-to-noise is at its highest, in order to maximise the sensitivity of our statistical analysis. The relationship between ALFF/fALFF and CVR is also investigated in the brainstem, to test whether ALFF and/or fALFF are sensitive enough to overcome the challenges inherent in brainstem MRI, as discussed in the introductory chapter to this thesis, and to verify whether they are of use as tools to investigate alterations in CVR in the brainstem in the context of hypertension. We attempted to determine which, if any, bandpass-frequency range yields regional ALFF/fALFF values that correlate most strongly with

ASL CVR and/or BOLD CVR values. We also attempt to reproduce the findings of previous work that has demonstrated a significant positive correlation between ASL CVR and BOLD CVR (Zhou 2015).

Following this, the within-subject relationship between regional fALFF and regional BOLD and ASL CVR is also investigated to determine whether fALFF maps accurately represent the spatial distribution of CVR. This is an important consideration if fALFF is to be useful as a clinical tool to assess regional differences in CVR that might arise due to brain pathology. We focus on regions of interest that form parts of the central autonomic network, again in an effort to evaluate ALFF/fALFF as a potential surrogate of CVR in the context of investigating the selfish brain mechanism.

We hypothesise a positive correlation between both ALFF and fALFF with ASL and BOLD CVR both within the cortical grey matter and in the brainstem. Within each subject we also expect a positive correlation between regional fALFF and regional ASL and BOLD CVR.

6.1.2. Summary of aims

1. Determine which, if any, bandpass-frequency range yields brainstem and cortical grey matter ALFF and/or fALFF values that correlate most strongly with ASL and/or BOLD CVR.
2. Verify a positive correlation between ASL CVR and BOLD CVR.
3. Investigate whether there is a significant within-subject correlation between the regional distribution of ALFF and/or fALFF with ASL and/or BOLD CVR.

6.2. Methods

The data used in this chapter came from two sources (see figure 6.1). Firstly, data from the study described in chapter 2 was revisited. Secondly, data from an additional ten healthy males sourced from the study outlined in appendix 1 were used. See appendix 1 and 2 for a full list of inclusion and exclusion criteria. As discussed in section 2.2.1 data from the former study was acquired under pre-existing ethical approval from Cardiff University School of Psychology. Full ethical approval by the National Health Service Research Ethics Committee

and local Research and Development had been obtained in advance of the latter study, which was ultimately abandoned due to problems with recruitment of hypertensive patients. Informed consent was obtained from all participants.

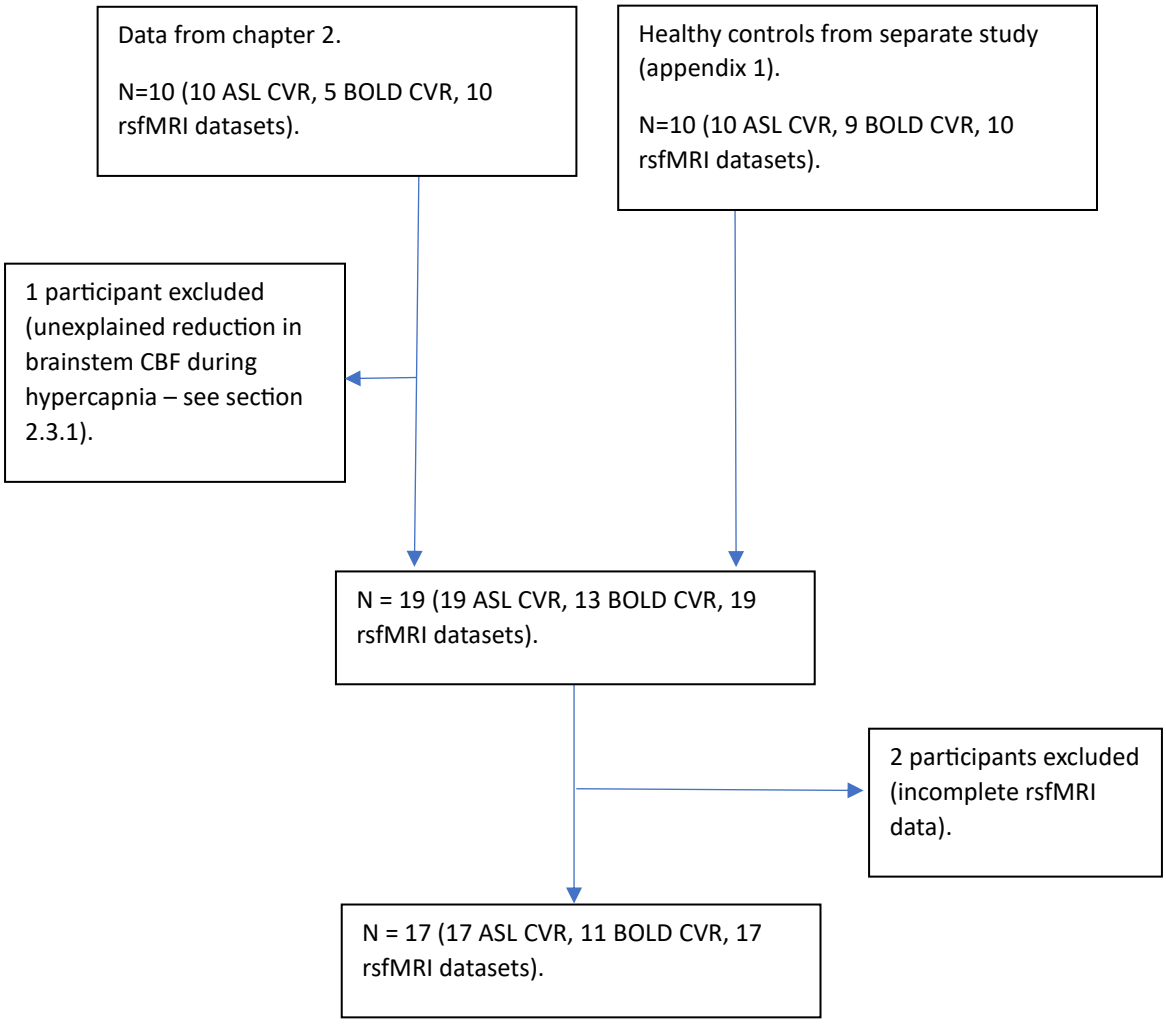

Figure 6.1: Outline of the sources of data analysed in this chapter.

The precise details of the PCASL and BOLD EPI sequences used are discussed in sections 2.2.4 and 2.2.7, respectively. Resting-state BOLD data were acquired with the participant's eyes open, staring at a fixed cross projected on a screen inside the scanner room.

As discussed in chapter 2, ASL CVR was measured by first acquiring two ASL datasets, one with the participant breathing medical air at normocapnia, and another during

administration of a gas mixture containing 5% CO_2. To calculate regional CVR, regional mean CBF during normocapnia was subtracted from CBF during hypercapnia and divided by the difference between the mean normocapnic and hypercapnic $ETCO_2$, yielding a measurement of CVR in units of ΔCBF/mmHg. As discussed in section 2.2.5, five of the ASL CVR datasets were acquired using the Respiract Gas Delivery System (Fisher 2016) and five were acquired using an in-house system. One of the ASL CVR datasets acquired using the Respiract system was excluded due to an unexplained reduction in brainstem CBF during hypercapnia, as discussed in section 2.3.1. All data from the second pool of participants (the healthy control population from the separate study) were acquired using the in-house system.

For BOLD CVR, a single BOLD dataset was obtained, with a hypercapnic stimulus paradigm consisting of two separate two-minute periods breathing 5% CO_2, interspersed with three two-minute periods of normocapnia. BOLD CVR maps were subsequently generated by applying a GLM with the end-tidal CO_2 ($ETCO_2$) trace, convolved with a gamma haemodynamic response function, as the predictor variable, yielding parameter maps that were converted to CVR maps in units of % change in BOLD signal per mmHg (see section 2.2.7 for further details). All BOLD CVR data were acquired using the in-house gas delivery system.

All data were analysed in their original functional space to minimise interpolation errors which might be introduced by spatial transformation of functional data. Functional data were co-registered to a high-resolution whole brain structural scan using FSL FLIRT. The structural data were subsequently co-registered to MNI space. The transformation matrices generated by each of the two co-registration steps were concatenated then inverted to enable co-registration from MNI to functional space.

Masks of the medulla, pons and midbrain were generated by segmentation of each individual's structural dataset using FreeSurfer (Fischl 2012), as previously described in chapter 2. These were combined to form a single brainstem mask. 22 further cortical and subcortical masks (see figure 6.2 showing a visual representation of these masks) were generated from the Harvard-Oxford cortical atlas, available via the FSL software package. These included the thalamus, hippocampus, amygdala, hypothalamus, and insula, which are all involved in the central autonomic network, and are therefore relevant in the context of the selfish brain mechanism. Masks of the 12 cortical grey matter regions of interest were combined to form a single cortical grey matter mask (6 bilateral regions – the precentral

gyrus, frontal poles, occipital poles, superior parietal lobule, temporal poles and superior frontal gyrus). These masks were co-registered to functional space using the inverted transformation matrix described above. The co-registered brainstem masks were eroded using fslmaths with a 1 mm spherical kernel to prevent encroachment of extra-axial structures. The accuracy of mask co-registration to functional space was visually assessed for any overlap between the masks and extra-axial structures such as CSF. Brainstem masks were subsequently manually edited to remove any overlapping non-parenchymal structures.

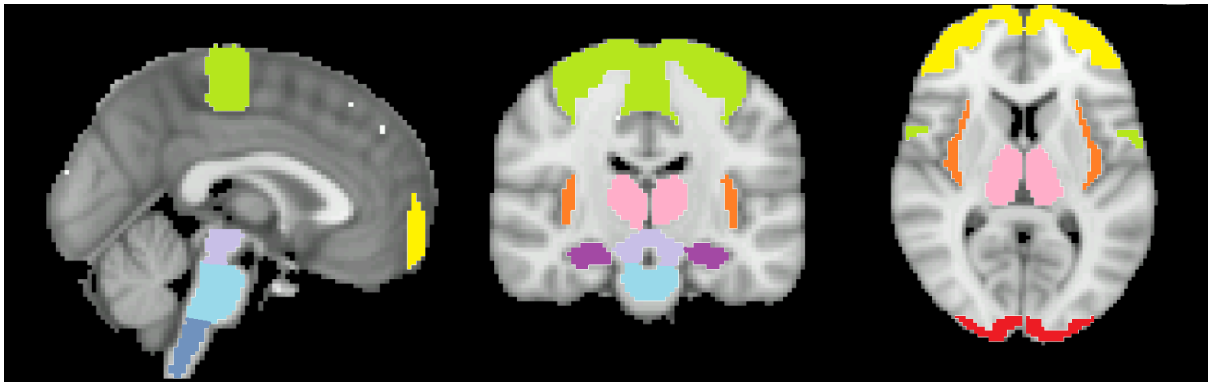

Figure 6.2: 25 regions of interest were considered in total: Midbrain (violet), pons (light blue), medulla (blue), precentral gyrus (green), insula (orange), frontal poles (yellow), occipital poles (red), thalamus (pink), hippocampus (purple), amygdala, hypothalamus, superior parietal lobule, temporal poles, superior frontal gyrus. Bilateral structures were considered individually (e.g. right insula and left insula).

The first three volumes of the BOLD EPI data were discarded prior to data processing to ensure steady state magnetisation was reached. BOLD and ASL data were motion corrected using FSL MCFLIRT. The middle volume of each dataset was set as the reference volume against which motion correction was performed. Furthermore, assessment of participant motion was performed using the FSL utility 'FSL motion outliers'.

Motion parameter assessment revealed that, on average, there were 7 motion outliers (in this chapter, outliers are defined as datapoints greater than the 75th percentile + 1.5 times the interquartile range) per participant, with a maximum of 17. Volume censoring was not performed because the removal of individual volumes could affect the ALFF calculation by disrupting the temporal structure of the data (Bijsterbosch 2017).

The method applied to calculate ASL CVR and BOLD CVR was described in sections 2.2.5 and 2.2.7. Voxelwise ALFF was calculated using the same method described in section 5.5.3. Firstly, the linear trend in the data was removed and the data were de-meaned. This addresses the potential confounding effect on ALFF of low-frequency scanner drift, and of between session differences in baseline BOLD signal intensity. Data were subsequently temporally filtered using 119 unique bandpass filters. As previously discussed, Liu et al. investigated which bandpass frequency range yields rsfMRI-CVR data with the strongest spatial correlation with BOLD CVR maps (Liu 2021). The upper and lower limits of the bandpass filters used in our analysis were based on those used by Liu et al. In summary there are 119 bandpass filters of various widths. 15 low-cutoff frequencies were defined between 0 and $0.01 \times 1.25^{n-1}$ Hz, and 15 high-cut-off frequencies were defined between 0.01 and 0.01×1.25^{n} Hz, where n = 1, 2, 3, etc up to 14. The 119 bandpass frequencies are then defined by combining every possible combination of low- and high-cut-off frequency, as long as the high-cut-off frequency is greater than the low-cut-off frequency. The highest high-cut-off frequency is well below the Nyquist frequency of the rsfMRI data (TR = 1.2 s), which equals 0.42 Hz. The voxelwise bandpass filtered data were transformed to voxelwise power spectra using *fslpspec*. The power of a frequency component is proportional to the square of the amplitude at that frequency. The square root of the voxelwise power spectrum data was obtained, and the mean was calculated to give the ALFF. To calculate fALFF, the mean amplitude of the square root of the power spectra across the entire frequency range (0 to 0.42 Hz) of the rsfMRI signal was calculated, then the voxelwise ALFF maps were divided by these maps (see figure 6.3) (Zou 2008). Representative examples of ALFF and fALFF maps are shown in figure 6.16.

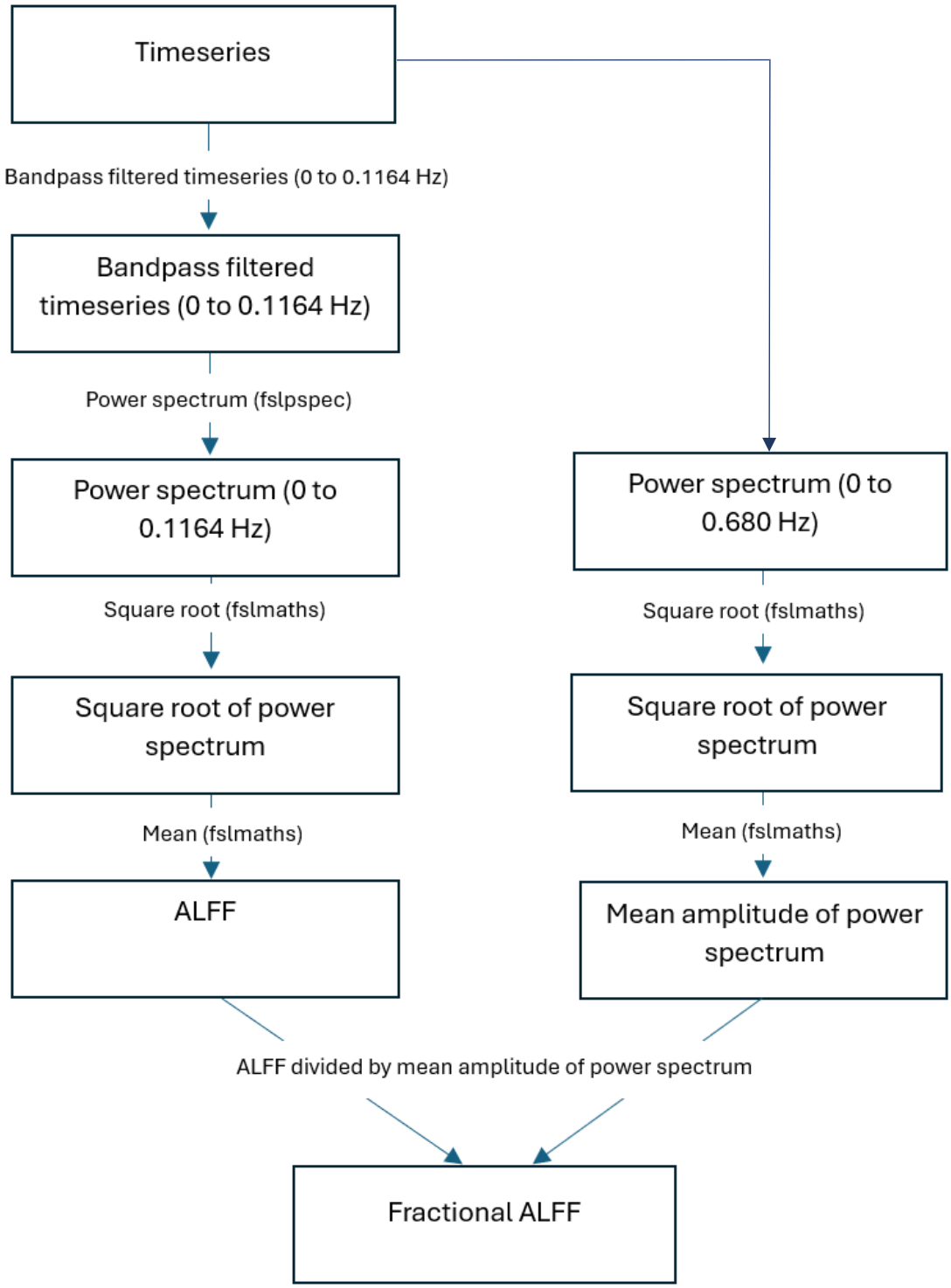

Figure 6.3: Outline of ALFF and fALFF calculation.

6.2.1. Statistical analysis

The voxel-by-voxel distribution of ALFF, fALFF and CVR values within the cortical grey matter and brainstem was evaluated at different bandpass frequencies, and a representative example within the brainstem is shown in figure 6.4 below. In general, the distribution of ALFF and fALFF values in both the brainstem and cortical grey matter are positively skewed with several high-lying outliers. ASL CVR approaches a normal distribution but also contains both low and high-lying outliers. Therefore, when considering regional ALFF, fALFF and CVR values, the regional median was interrogated rather than the regional mean. The median is a better representation of the centre of a skewed dataset than the mean and is robust to the influence of outliers (Penhill 2023), as demonstrated by the difference in position of the median and means in figure 6.4 below.

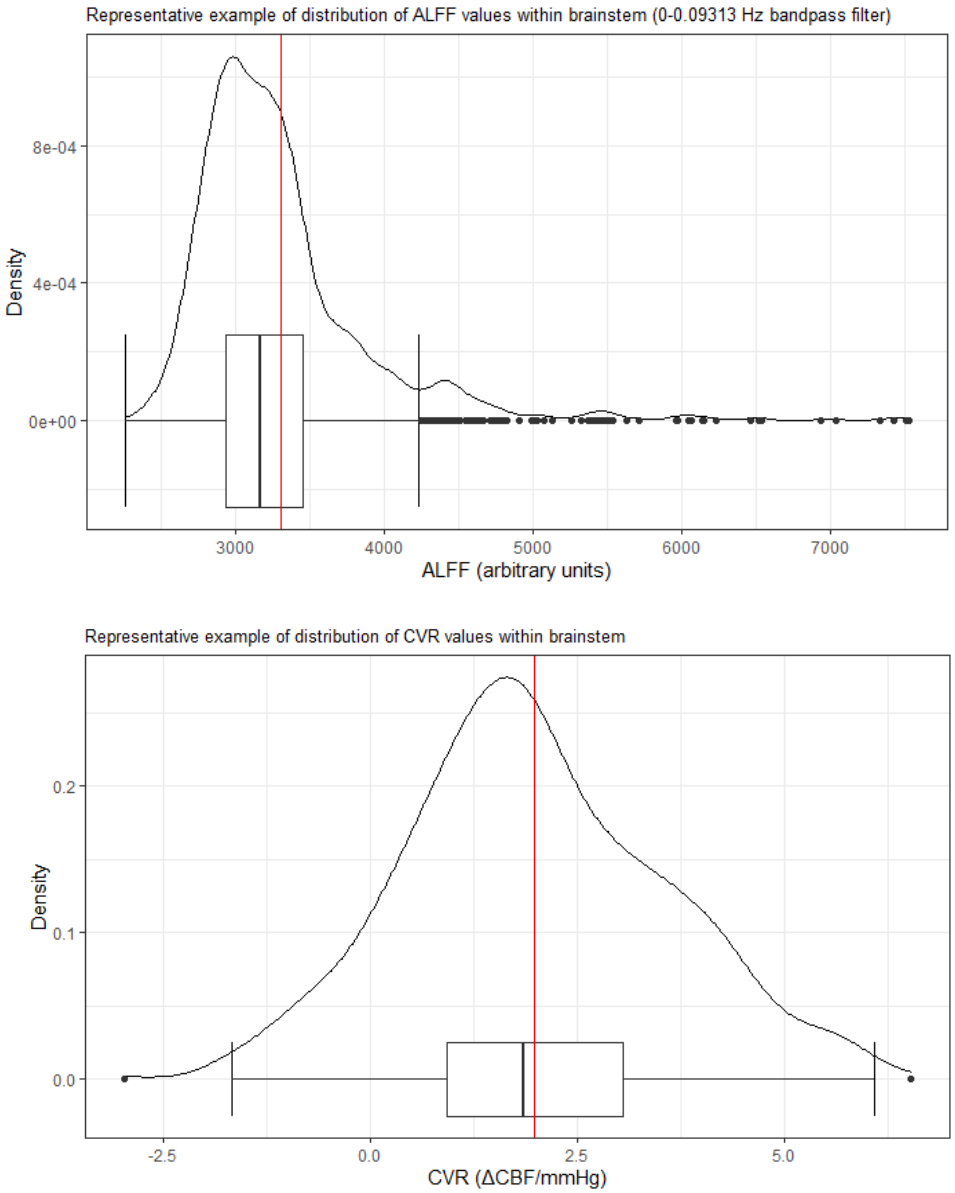

Figure 6.4: Density and boxplots of ALFF and ASL CVR values within the brainstem demonstrating the positive skew of the ALFF data. Red line = mean. Centre-line of boxplot = median.

Next, the regional distribution of fALFF and CVR values was evaluated (figure 6.5). The distribution of regional median fALFF and BOLD CVR are both positively skewed, whilst median ASL CVR values approach a normal distribution. The presence of outliers in the data, as well as the positive skew of the fALFF and BOLD CVR data, means that the data are non-parametric. Therefore, correlation analysis was performed using Spearman's (rather than Pearson's) correlation coefficient, a non-parametric statistic which is robust against violations of the assumptions of parametric testing (Field 2012).

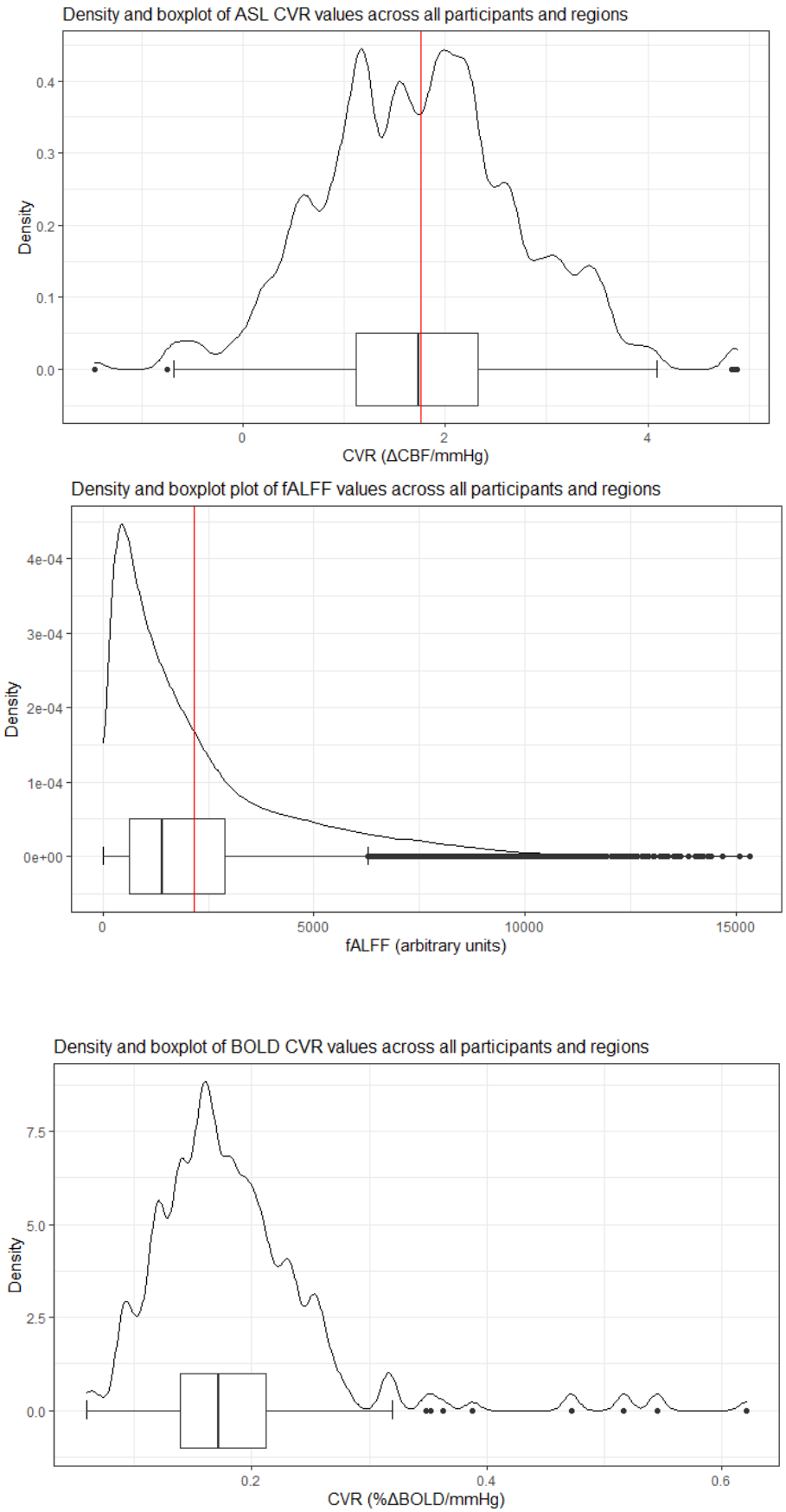

Figure 6.5: Median regional fALFF and BOLD CVR are positively skewed, whilst median regional ASL CVR approaches a normal distribution.

ALFF and fALFF were compared with ASL and BOLD CVR separately within the cortical grey matter and brainstem. The correlation between ASL CVR and BOLD CVR was also assessed to further validate BOLD as a method of measuring CVR.

The results of the above analysis led to a subsequent comparison of regional fALFF and regional ASL and BOLD CVR within each subject (across the 25 regions of interest demonstrated in figure 6.2), in order to investigate whether fALFF maps accurately represent the spatial distribution of CVR within each subject. The frequency range 0.0125 – 0.07450 Hz was selected because, in the absence of evidence of a significant correlation between ALFF or fALFF with CVR at any other bandpass frequency range, this was the closest available frequency range to that of 0.01 – 0.08 Hz that has typically been used in previous studies of ALFF/fALFF.

6.3. Results

6.3.1. ALFF v ASL CVR

The correlation between ALFF and ASL CVR at each bandpass filtering frequency, in both the brainstem and cortical grey matter, is summarised in figures 6.6 and 6.7 below. The y-axis represents the high-cut-off frequency, and the x-axis represents the low-cut-off frequency. The colour of each point reflects the strength of the correlation (green = stronger positive correlation, red = stronger negative correlation).

There is no statistically significant correlation between ALFF and ASL CVR in any of the bandpass frequency ranges, neither in the cortical grey matter nor in the brainstem, after Bonferroni correction for multiple comparisons (see tables 6.1 and 6.2 in appendix 6 for a breakdown of the relationship between ALFF and ASL CVR within each frequency range).

Figure 6.6 suggests that in the cortical grey matter there is a negative (though non-significant) correlation in the majority of bandpass frequencies between ALFF and ASL CVR. This is further illustrated by the mean value of the Spearman correlation coefficient (the mean across all 119 correlation coefficients, one for each bandpass frequency)) of-0.14 ± 0.07 in the cortical grey matter. In the brainstem, Spearman's correlation coefficient appears to be

close to zero in the majority of bandpass frequencies, as illustrated in figure 6.7, and by the mean correlation of 0.01 ± 0.03 in the brainstem.

Cortical grey matter

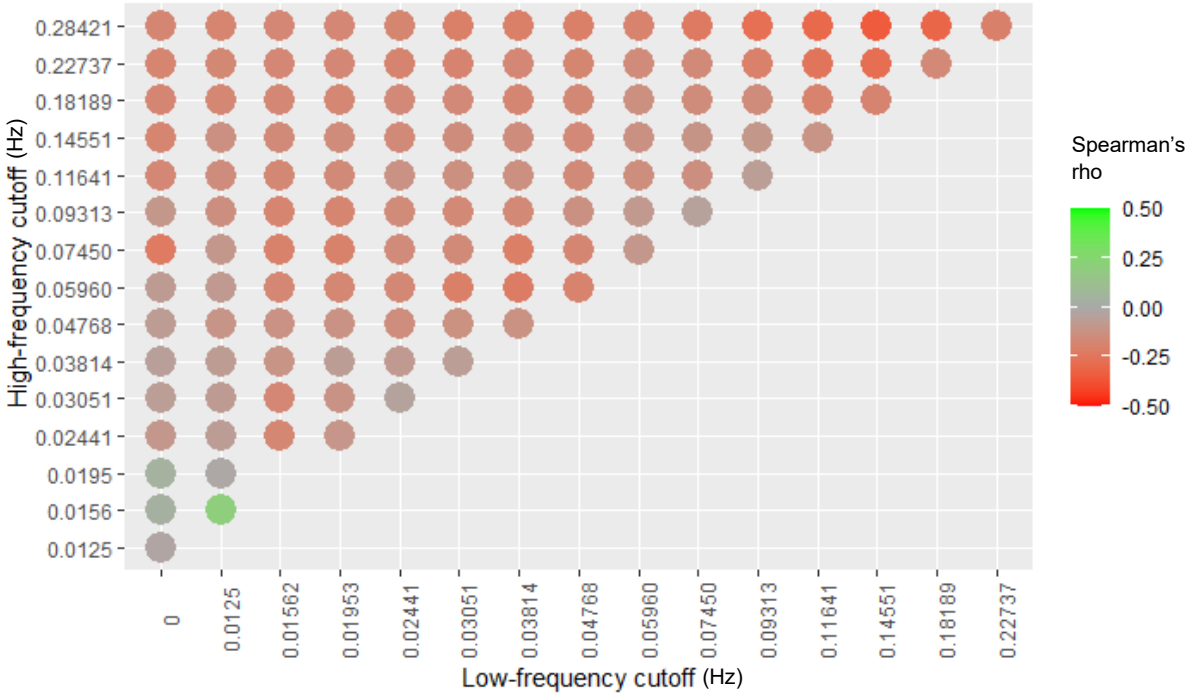

Figure 6.6: Correlation between median cortical grey matter ALFF and median cortical grey matter ASL CVR. No statistically significant correlation was found in any of the filtering frequency ranges.

Brainstem

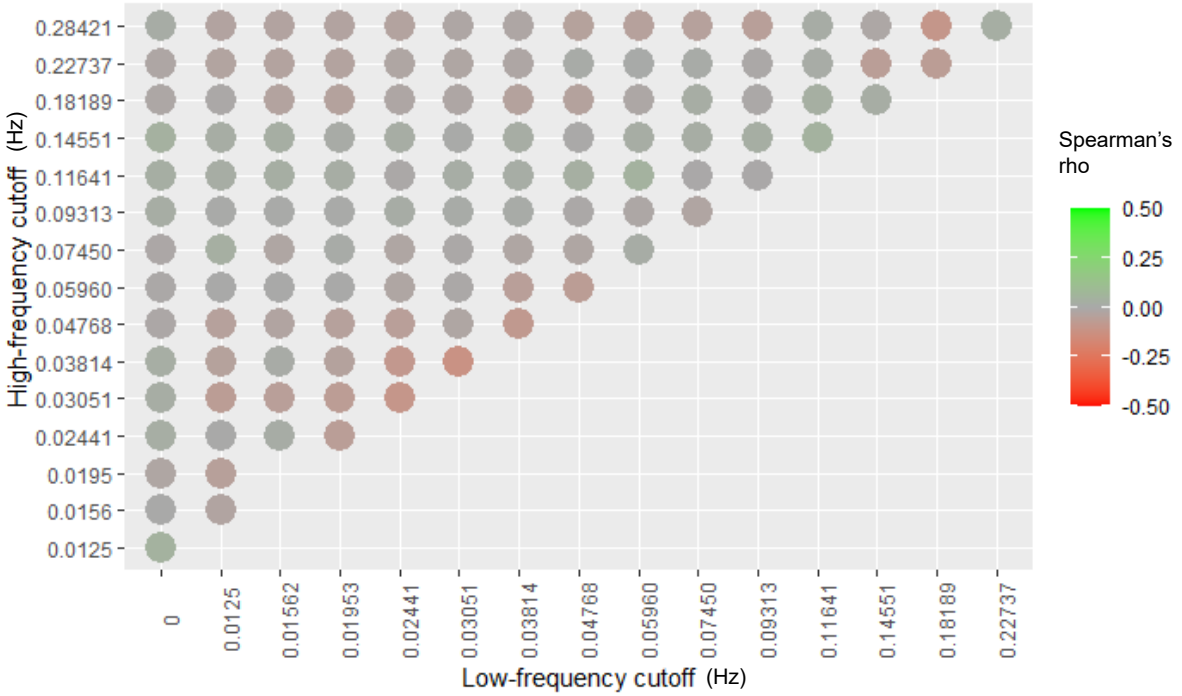

Figure 6.7: Correlation between median brainstem ALFF and median brainstem ASL CVR. No statistically significant correlation was found in any of the filtering frequency ranges.

6.3.2. fALFF v ASL CVR

The correlation between fALFF and ASL CVR at each bandpass filtering frequency, in both the brainstem and cortical grey matter, is summarised in figure 6.8 and 6.9.

There is no statistically significant correlation between fALFF and ASL CVR in any of the bandpass frequency ranges after Bonferroni correction for multiple comparisons (see tables 6.3 and 6.4 in appendix 6 for a breakdown of the relationship between fALFF and ASL CVR within each frequency range).

In the cortical grey matter, the vast majority of bandpass frequencies demonstrate a positive (though non-significant) correlation between fALFF and ASL CVR. This is further illustrated by the mean value of the Spearman correlation coefficient of 0.25 ± 0.05 in the cortical grey matter. In the brainstem, Spearman's correlation coefficient appears to be weakly positive in majority of bandpass frequencies, as illustrated by the mean correlation of 0.07 ± 0.10 in the brainstem.

Cortical grey matter

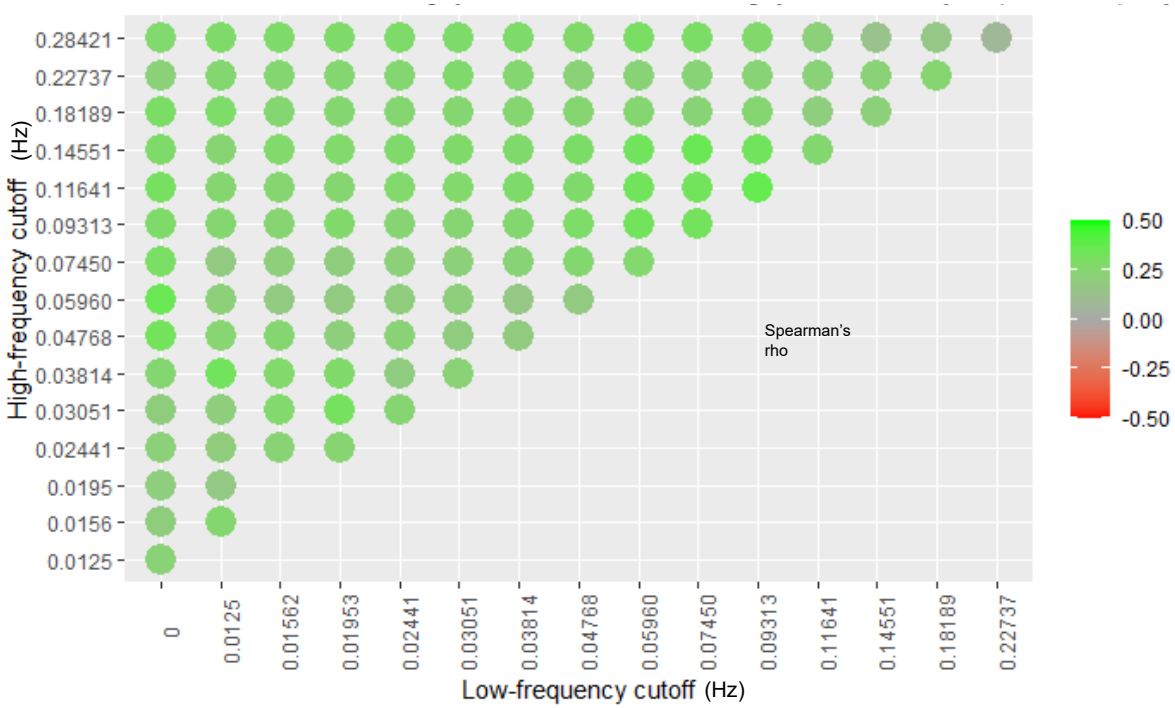

Figure 6.8: Correlation between median cortical grey matter fALFF and median cortical grey matter ASL CVR. There is a positive but non-significant correlation in all the bandpass filtering frequency ranges.

Brainstem

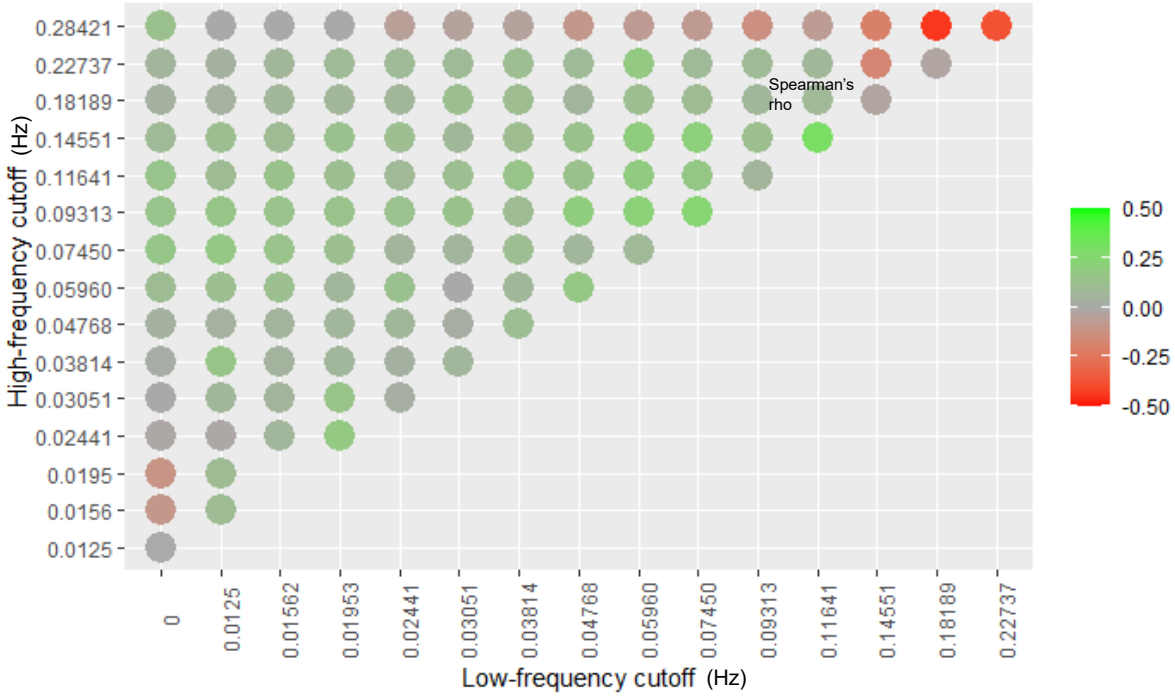

Figure 6.9: Correlation between median brainstem fALFF and median brainstem ASL CVR. There is a weakly positive but non-significant correlation in most of the bandpass filtering frequency ranges.

6.3.3. ASL CVR v BOLD CVR

Figures 6.10 and 6.11 demonstrate that there is a significant positive correlation between ASL CVR and BOLD CVR (Spearman's rho = 0.69, $p < 2.2 \times 10^{-6}$) within the cortical grey matter and the brainstem. This agrees with previous work by Taneja et al., who also demonstrated a positive correlation between ASL CVR and BOLD CVR (Pearson's r = 0.34, p = 0.016) (Taneja 2020).

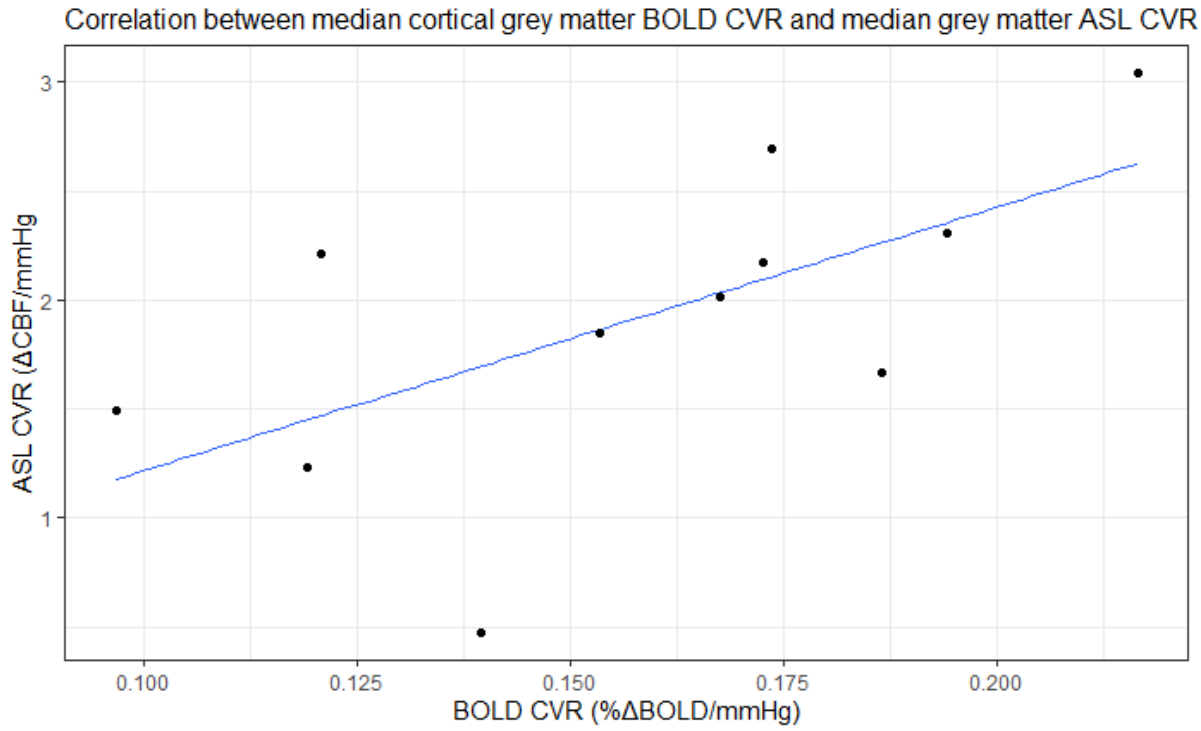

Figure 6.10: Correlation between median cortical grey matter BOLD CVR values and median cortical grey matter ASL CVR values. Each point represents one of the 11 subjects. Spearman's rho = 0.69, $p < 2.2 \times 10^{-6}$. Therefore, there is a significant positive correlation between median regional BOLD CVR and median regional ASL CVR. A linear model has been fit to the data to illustrate the statistically significant positive correlation.

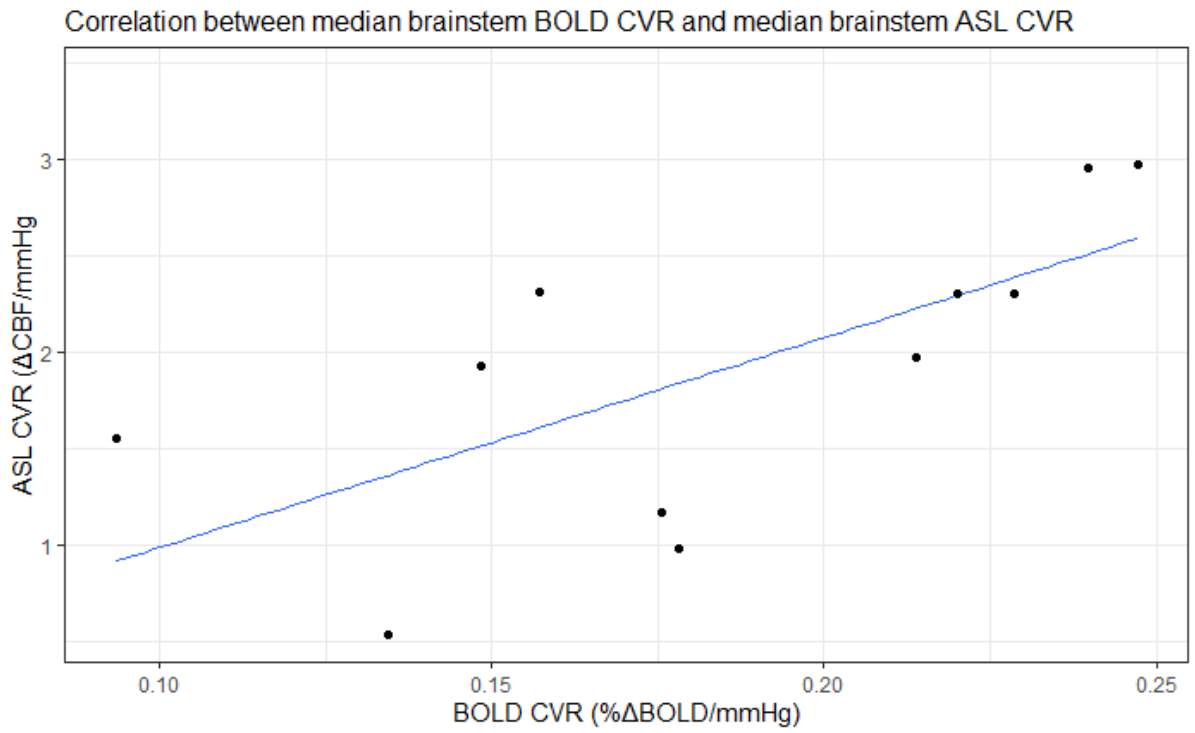

Figure 6.11: Correlation between median brainstem BOLD CVR values and median brainstem ASL CVR values. Spearman's rho = 0.70, $p < 2.2x10^{-6}$.

6.3.4. ALFF v BOLD CVR

The correlation between ALFF and BOLD CVR at each bandpass filtering frequency, in both the brainstem and cortical grey matter, is summarised in figures 6.12 and 6.13.

There is no statistically significant correlation between ALFF and BOLD CVR in any of the bandpass frequency ranges after Bonferroni correction for multiple comparisons (see tables 6.5 and 6.6 in appendix 6 for a breakdown of the relationship between ALFF and ASL CVR within each frequency range).

In the cortical grey matter, there is no consistent pattern to the direction of correlation between ALFF and BOLD CVR across the different bandpass frequencies. In the brainstem, Spearman's correlation coefficient appears to be weakly positive in many of the bandpass frequencies, with a mean of 0.05 ± 0.09.

Cortical grey matter

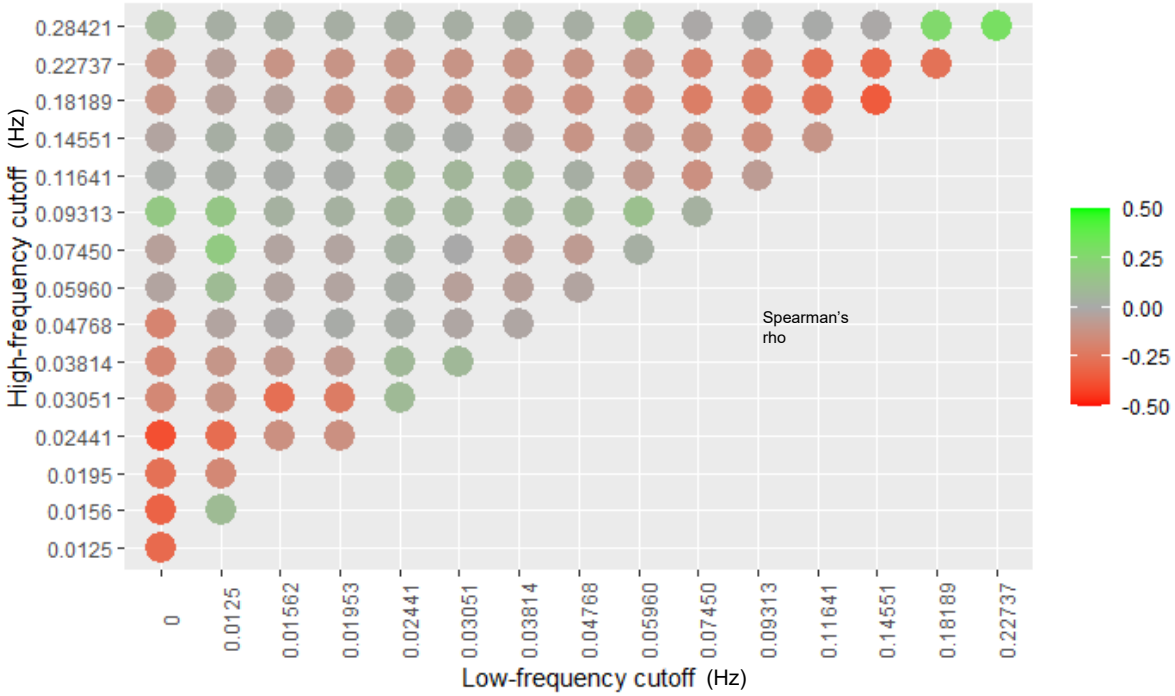

Figure 6.12: Correlation between median cortical grey matter ALFF and median cortical grey matter BOLD CVR. No statistically significant correlation in any of the filtering frequency ranges.

Brainstem

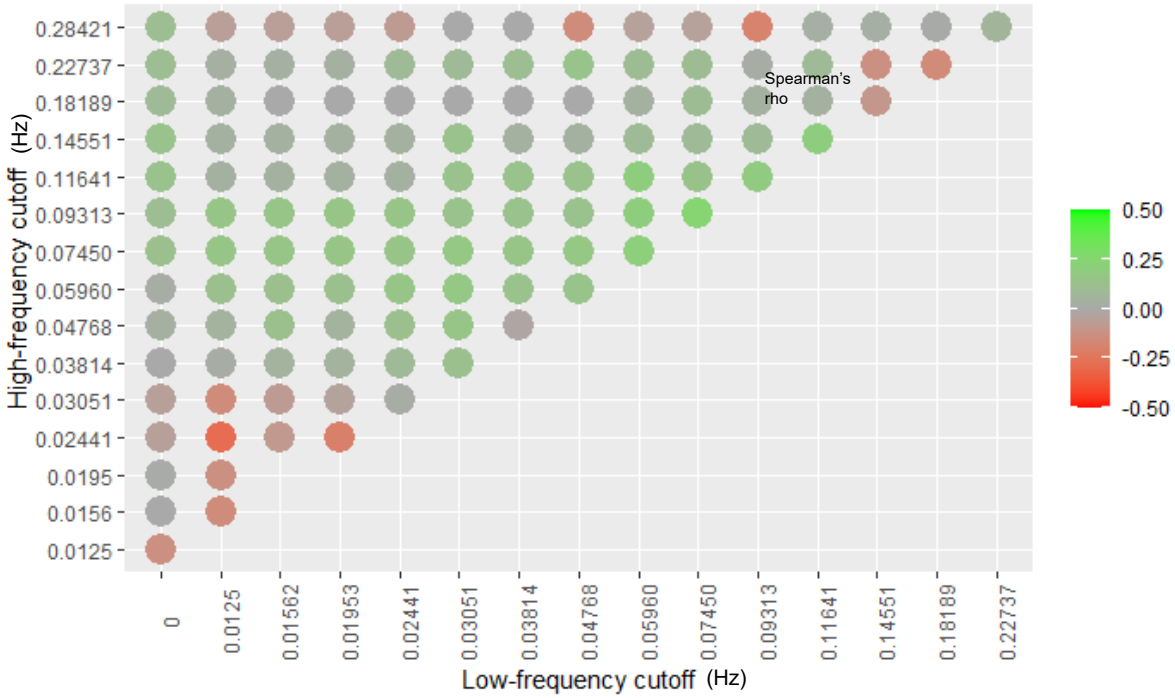

Figure 6.13: Correlation between median brainstem ALFF and median brainstem BOLD CVR. No statistically significant correlation in any of the filtering frequency ranges.

6.3.5. fALFF and BOLD CVR

After the fractional ALFF correction has been applied, the majority of bandpass frequencies demonstrate a non-significant positive correlation between fALFF and BOLD CVR in both the cortical grey matter and the brainstem. In the brainstem, the strongest positive correlation is at a bandpass frequency of 0.03051 – 0.03814 Hz (Spearman's rho = 0.50, p = 0.12).

Cortical grey matter

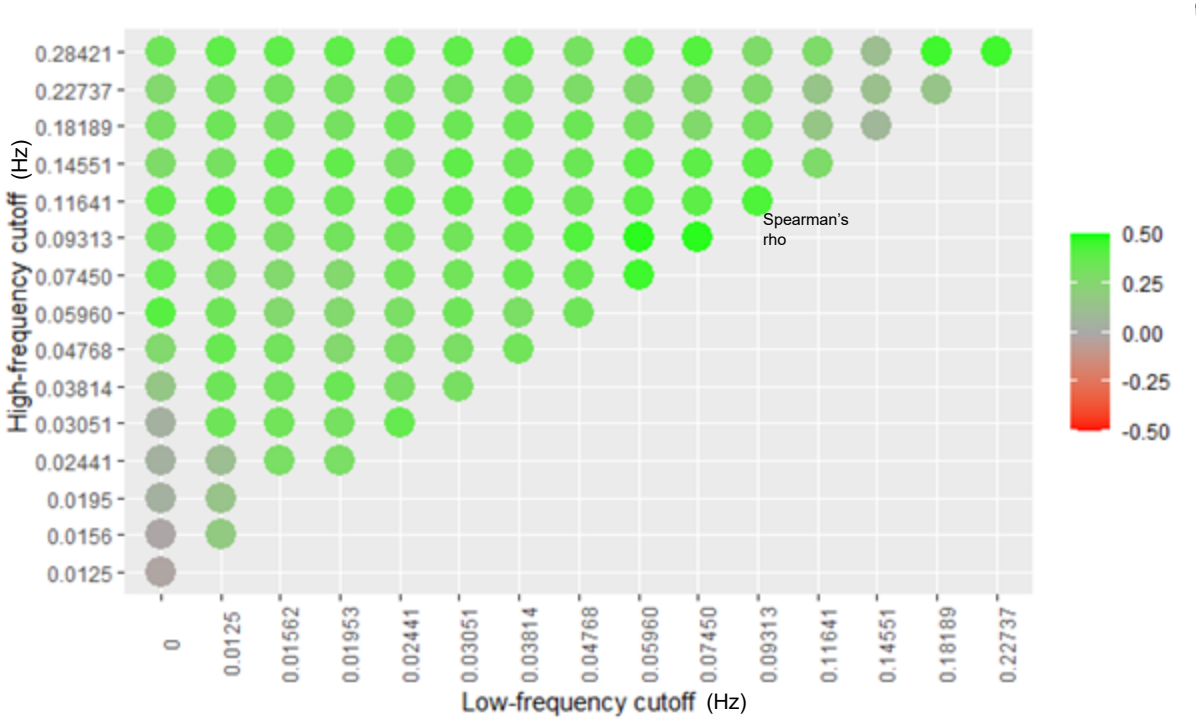

Figure 6.14: Correlation between median cortical grey atter fALFF and median cortical grey matter BOLD CVR. No statistically significant correlation in any of the filtering frequency ranges.

Brainstem

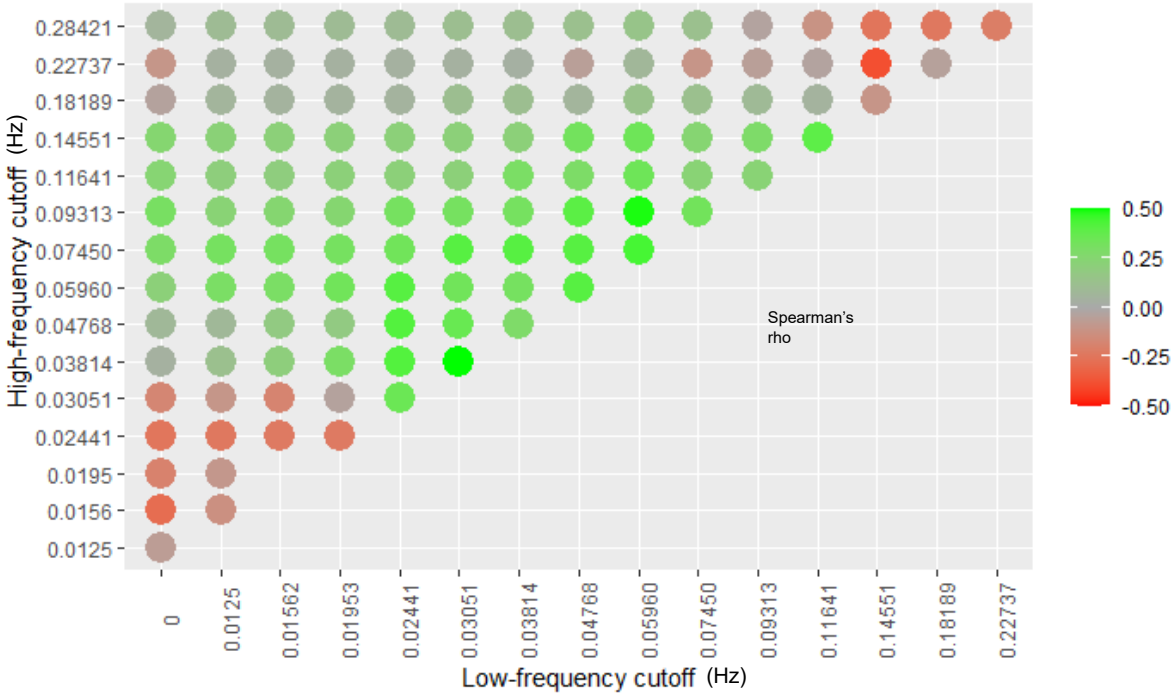

Figure 6.15: Correlation between median brainstem fALFF and median brainstem BOLD CVR. No statistically significant correlation in any of the filtering frequency ranges.

6.3.6. Summary of comparisons between ALFF/fALFF, ASL CVR and BOLD CVR

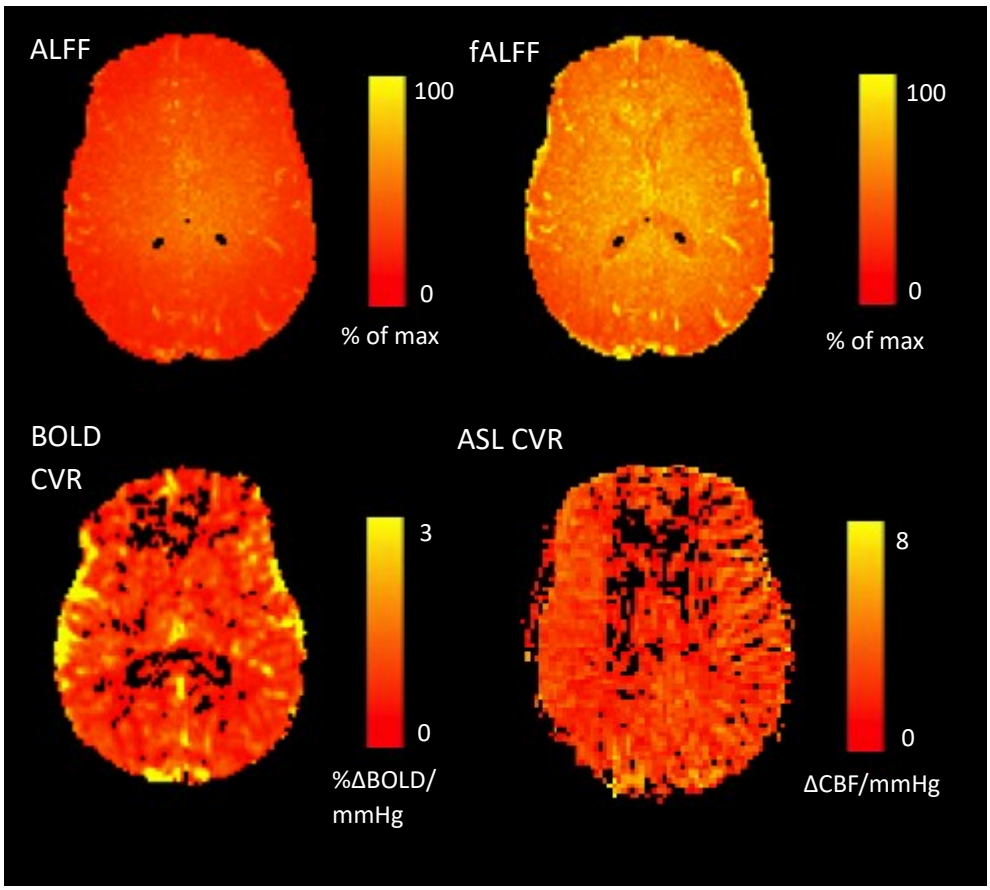

Figure 6.16: Representative examples of ALFF, fALFF, BOLD CVR and ASL CVR maps.

Representative examples of ALFF, fALFF, BOLD CVR and ASL CVR maps are demonstrated in figure 6.16. Figure 6.17 demonstrates a summary of the comparisons between ALFF/fALFF and ASL CVR/BOLD CVR. The mean Spearman correlation coefficient for each comparison is denoted by the red point. In summary:

- There was no statistically significant correlation between ALFF or fALFF with either ASL or BOLD CVR in any of the bandpass frequencies.
- Subjective evaluation of figures 6.6-6.9 and 6.12-6.15 suggest that there may be a positive correlation between fALFF and both ASL and BOLD CVR across a broad range of frequencies. This is stronger in the cortical grey matter, where the correlation coefficients across the vast majority of frequencies were positive (as demonstrated on figures 6.8 and 6.14).

- ALFF does not demonstrate a clear pattern of correlation either in the brainstem or cortical grey matter. In fact, if anything, when comparing ALFF and CVR (both BOLD and ASL) in the cortical grey matter, correlation coefficients are generally weakly negative. Brainstem ALFF v CVR correlation coefficients are clustered around zero.

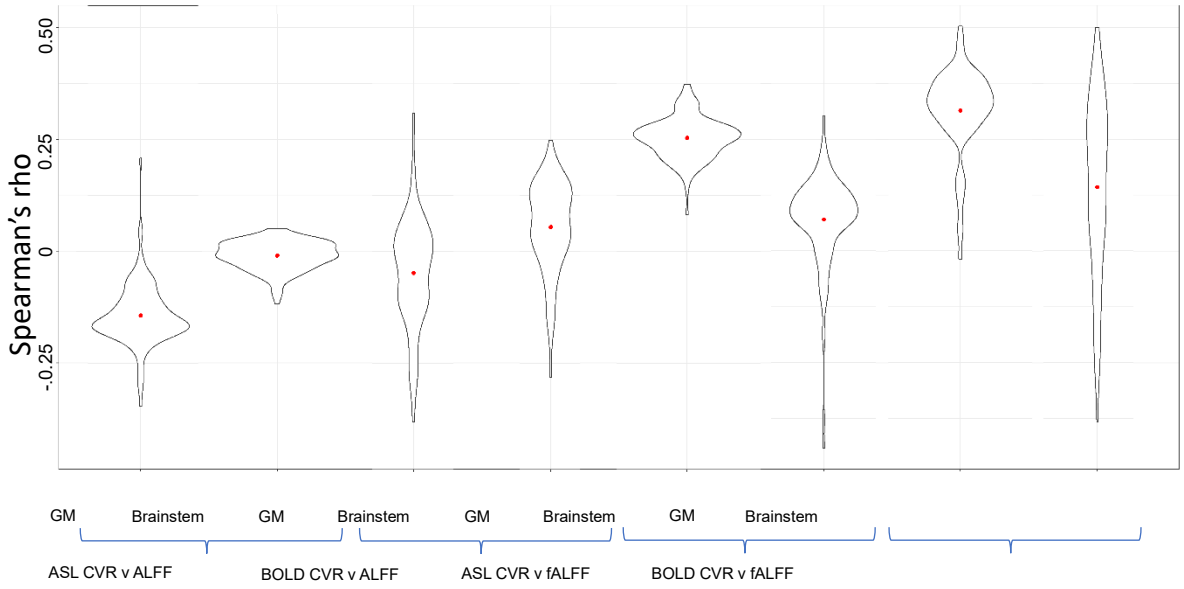

Figure 6.17: Summary of comparisons between ALFF/fALFF and ASL CVR/BOLD CVR. The mean Spearman correlation coefficient for each comparison, across the 119 frequency bands, is denoted by the red point. This illustrates that, when considering all the bandpass frequencies that were evaluated, the possibility is raised of a non-significant positive correlation between fALFF and CVR, which is most apparent in the cortical grey matter.

6.3.7. Within-subject regional comparisons

It has not been possible to isolate a single frequency band within which the correlation between fALFF and CVR is strongest. Instead, the correlation is present across a wide range of frequencies. In the absence of evidence of a significant correlation between fALFF and CVR, the frequency range 0.0125 – 0.07450 Hz was selected for the within-subject regional comparison to facilitate comparison with previous studies of ALFF/fALFF that have used a similar frequency range of 0.01 – 0.08 Hz.

There is no consistent pattern to the within-subject correlation between regional fALFF and regional ASL CVR. The threshold for statistical significance is met in only two of the

seventeen participants (figure 6.18) after a Holm correction for multiple comparisons (see appendix 7 for a breakdown of test statistics), and the correlation was unexpectedly negative in both cases.

By contrast, there is a positive correlation between regional fALFF and regional BOLD CVR across all eleven datasets, and the threshold for statistical significance is reached in eight of these (see appendix 7).

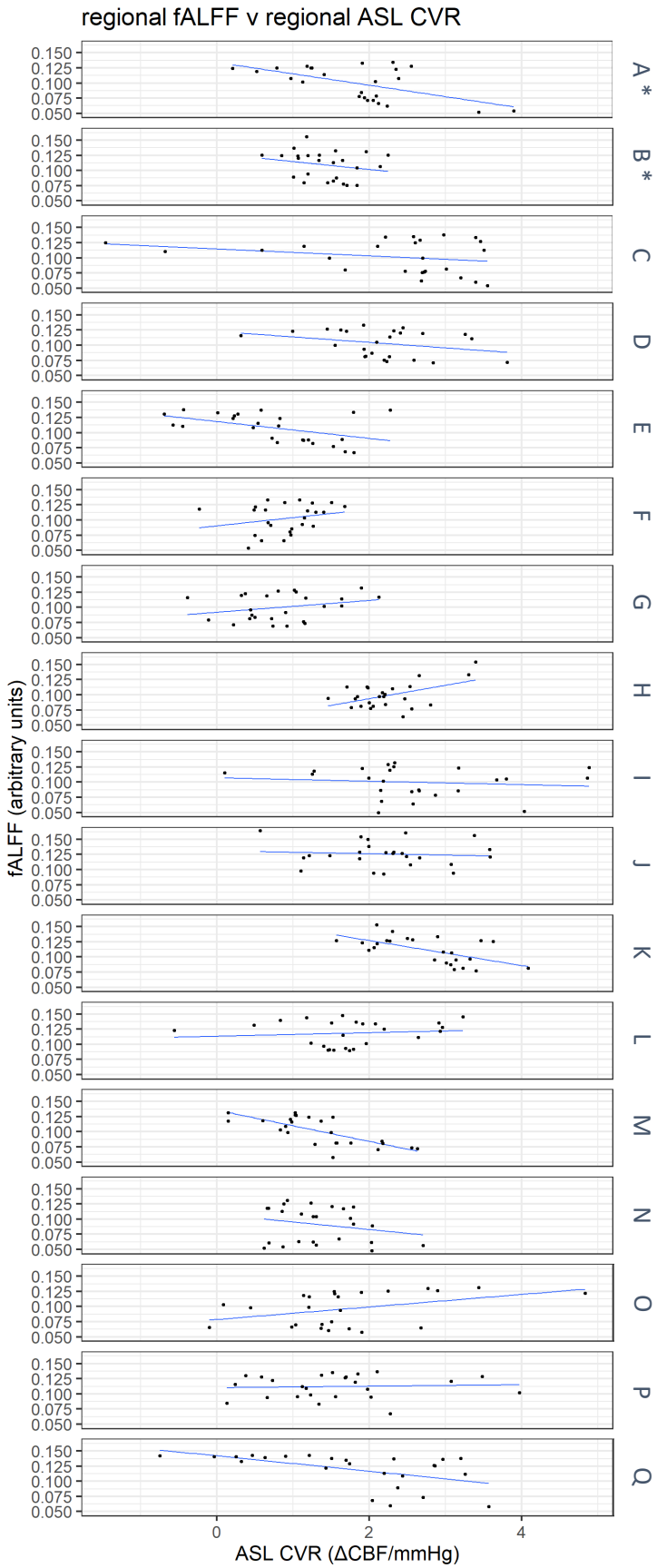

Figure 6.18: Spearman correlation between regional fALFF and regional ASL CVR within each subject (A-Q). The correlation reached significance for two of the seventeen subjects (*) after a Holm correction for multiple comparisons (α = 0.05/17 = 0.0029).

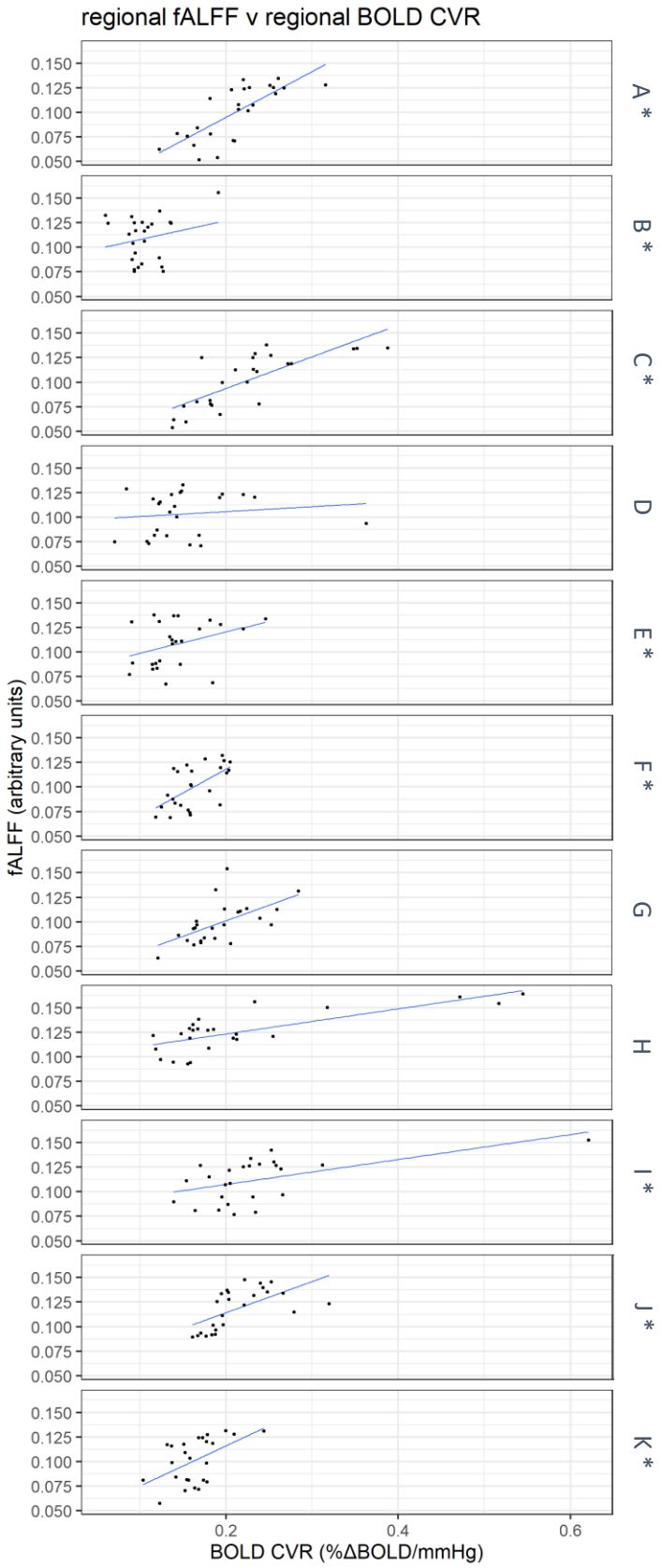

Figure 6.19: Spearman correlation between regional fALFF and regional BOLD CVR within each subject (A-K). There was a statistically significant correlation within eight of the eleven subjects (*) for whom BOLD CVR data was available, after a Holm correction for multiple comparisons ($\alpha = 0.05/11 = 4.5 \times 10^{-3}$).

6.3.8. Impact of head motion on ALFF/fALFF

There is no statistically significant correlation between ALFF or fALFF with the mean framewise displacement (maximum value of Spearman's rho = 0.25, p = 0.32), or the maximum framewise displacement (maximum value of Spearman's rho = 0.59, p = 0.02) at any of the bandpass frequencies, after Bonferroni correction for multiple comparison.

6.3.9. Re-evaluation of UK Biobank data

In chapter 5, fALFF in the bandpass frequency ranges of 0 – 0.1164 Hz and 0.01 – 0.08 Hz was compared between normotensives and hypertensives in the UK Biobank dataset. It has not been possible to isolate a single frequency range that demonstrates a strong correlation between fALFF and CVR, but in the brainstem, fALFF in the frequency range of 0.03051 – 0.03814 Hz has the largest correlation coefficient. The UK Biobank data was therefore re-evaluated in this frequency range. The results were essentially the same as the analysis in the other two frequency ranges. A two-way ANCOVA comparing blood pressure (1724 normotensives v 2054 hypertensives) and brain region (medulla, pons, midbrain, amygdala, hippocampus, hypothalamus, thalamus, insula cortex and visual cortex) on fALFF z-score, with age, BMI and sex included as covariates, found that the mean fALFF z-score across all regions of interest in hypertensives (-0.38 (standard deviation = 0.35, standard error = 0.003)) was higher than in normotensives (-0.41 (standard deviation = 0.34, standard error = 0.003), $F(1) = 55.17$, $p = 1.13 \times 10^{-13}$), although the effect size is again extremely small (partial $\eta^2 = 0.002$). There was a significant regional variation in fALFF z-score ($F(14) = 1049.78$, $p < 2 \times 10^{-16}$, partial $\eta^2 = 0.26$). Age, BMI and sex also significantly predict fALFF z-score. However, there was no statistically significant effect of the interaction between brainstem region and blood pressure group on fALFF z-score ($F(14) = 0.17$, $p = 0.99$, partial $\eta^2 = 7 \times 10^{-5}$).

6.4. Discussion

The aim of this chapter was to further investigate whether ALFF and fractional ALFF are markers of CVR, and which frequency range should be considered when evaluating fluctuations in resting state BOLD data as a surrogate marker of CVR. Previously, ALFF has only been compared to CVR values derived from BOLD data, and only within one frequency range (0.01 – 0.08 Hz) (Golestani 2016). Here, low-frequency fluctuations in the resting-state BOLD signal between a variety of bandpass frequencies were compared with CVR values derived from ASL data, which is a more specific measure of cerebral blood flow than BOLD. Furthermore, fractional ALFF, a potentially more sensitive metric which aims to correct for physiological noise contributions, was also evaluated in addition to ALFF.

There was no statistically significant correlation between ALFF or fALFF and ASL or BOLD CVR in any of the bandpass frequency ranges. Figures 6.8 – 6.9 and 6.14 – 6.15 suggest that there may be a positive correlation between fractional ALFF and both ASL and BOLD CVR across a wide range of frequencies, but that the threshold for statistical significance was not reached. Whilst there is no clear pattern of correlation between ALFF and ASL or BOLD CVR, the results are unexpectedly suggestive of a negative correlation between ALFF and ASL CVR in the cortical grey matter.

A positive correlation between the regional distribution in fALFF and BOLD CVR was seen in all eleven participants, and the threshold for statistical significance was reached in eight of these. fALFF has not been previously compared to BOLD CVR, but Golestani et al.'s previous work, which demonstrated a significant correlation between the within-subject regional distribution in ALFF and BOLD CVR in 8 out of 13 subjects (Golestani 2016), is supportive of the present findings. However, the analysis of the regional distribution of fALFF and ASL CVR within each subject demonstrated a negative correlation between fALFF and ASL CVR in eleven out of seventeen participants. Statistical significance was reached in only two cases, both of which showed negative correlations, casting significant doubt over the validity of fALFF as a tool to study within-subject regional differences in CVR.

As discussed in chapter 5, the amplitude of BOLD signal fluctuations in non-parenchymal regions such as in the convexity cerebrospinal fluid, basal cisterns, ventricles, and in the vicinity of large blood vessels is larger across the entire frequency spectrum than in

parenchymal regions of interest (Zou 2008). The fractional ALFF method suppresses contributions from these extra-axial regions. This might explain why the values of Spearman's rho are larger for fALFF than ALFF – the ALFF signal might be overwhelmed by noise from CSF or vascular pulsations.

Partial volume effects due to fluctuations in the volumes of the extra-axial spaces that occur during the cardiac cycle and in response to hypercapnia (Blockley 2011) might explain the negative correlation between ALFF and ASL CVR. During hypercapnia, there is an overall reduction in CSF volume, and voxels that border CSF spaces will contain an increased proportion of brain tissue, which has a lower BOLD signal than the noisy CSF space. Therefore, in the absence of a fractional correction, which suppresses physiological noise contributions from the extra-axial CSF spaces, the magnitude of ALFF during hypercapnia is potentially lower in voxels that contain both CSF and brain, such as at the boundary between cortical grey matter sulci and gyri. Therefore, whilst the ASL signal increases in response to hypercapnia, the measured ALFF in the cortical grey matter masks might decrease because there is less CSF within these masks during hypercapnia, explaining the negative correlation between ALFF and ASL CVR in the cortical grey matter. Due to the complex anatomy of cortical sulci and gyri, some overlap between cortical grey matter masks and CSF spaces is inevitable. This is less of a problem in the brainstem, which has a less convoluted shape and therefore no encroachment of CSF spaces into brainstem masks. This might explain why a negative correlation between ALFF and ASL CVR is seen in the cortical grey matter, but not in the brainstem.

Resting-state BOLD signal fluctuations that correlate with resting fluctuations in P_aCO_2 are inevitably much smaller than the BOLD signal response to induced hypercapnia. Therefore, whilst the partial volume effect might significantly impact on the relatively small BOLD signal fluctuations that correlate with small resting fluctuations in P_aCO_2, the more robust BOLD signal response to induced hypercapnia might not be significantly impacted, hence the positive correlation between BOLD CVR and ASL CVR is preserved.

Whilst there is not a single narrow fALFF frequency range that stands out as being a candidate metric of CVR, the strongest correlation between fALFF and BOLD CVR in the brainstem was in the frequency range of 0.03051 – 0.03814 Hz. The UK Biobank data from chapter 5 was re-evaluated within this frequency range. There is a significant regional

variation in fALFF, but the pattern of regional variation is no different between hypertensives and normotensives. These results are essentially the same as those previously discussed in chapter 5.

There are numerous confounding factors that might have masked a statistically significant relationship between ALFF/fALFF and CVR. Firstly, SNR might be too low (especially in regions of relatively high noise such as the brainstem) to provide sufficient power to detect a significant correlation between ALFF/fALFF and ASL CVR. Another possible confounding factor is head motion. Although motion correction was performed, there were motion parameter outliers associated with every participant, suggesting that none of the participants were completely still for the entire duration of the BOLD acquisitions. Volume censoring would not have been appropriate because removal of individual volumes would affect the temporal distribution of the data, and therefore ALFF. Another option would have been to apply a GLM to the BOLD data with the motion parameters as regressors. However, the standard ALFF calculation does not typically involve this step, and therefore motion parameter regression was not performed, because the aim was to evaluate ALFF as it is conventionally calculated. Despite the presence of motion outliers, it is reassuring that no statistically significant correlation was found between ALFF/fALFF and the mean or maximum framewise displacement.

For similar reasons physiological noise correction was not performed. If physiological noise correction were necessary to elucidate the relationship between ALFF/fALFF and ASL CVR or BOLD CVR, this would limit the utility of ALFF/fALFF to only datasets that contained physiological monitoring data. Furthermore, it is debatable whether physiological noise correction would have a significant impact on ALFF – Jahanian et al. have previously evaluated the coefficient of variation in the resting-state BOLD fMRI signal both before and after physiological noise correction using RETROICOR, and found no significant difference (Jahanian 2014).

Whilst it is possible that a larger sample size might yield a statistically significant relationship between ALFF/fALFF and CVR, even for the strongest positive correlation (Spearman's rho = 0.50 between fALFF and BOLD CVR in the brainstem with a bandpass frequency of 0.03051 – 0.03814 Hz) the proportion of shared variance between fALFF and CVR is only 25%. There is good evidence that low frequency fluctuations in the BOLD signal

correlate with fluctuations in resting arterial CO_2 concentration (Wise 2004), and this chapter confirms previous evidence of a significant correlation between ASL CVR and BOLD CVR (Zhou 2015). Therefore at least some of the variance in ALFF and fALFF is likely to be related to the cerebrovascular response to fluctuations in P_aCO_2. However, the results of this chapter suggest that there are too many other sources of variance in the resting-state BOLD signal for ALFF/fALFF to serve as specific metrics of CVR.

As previously discussed, the biophysical principles that underpin the BOLD signal are complex. There are several factors which contribute to the BOLD signal, including signal fluctuations that are physiological in origin, such as spontaneous fluctuations in neuronal activity (Biswal 1995), (Lowe 1998), (Cordes 2000), (N. K. Logothetis 2001) and fluctuations in arterial O_2 (Obrig 1996), as well as those that are related to physiological and thermal noise (Bianciardi 2009). Together, spontaneous neural activity and thermal noise are thought to contribute to a substantial proportion of the variance in low-frequency BOLD fluctuations at a voxel level (Bianciardi 2009). Lipp et al. have previously derived CVR maps from resting-state BOLD data by using the $ETCO_2$ trace as a regressor in a GLM, and found that the $ETCO_2$ regressor accounted for less than 20% of the variance in the BOLD signal (Lipp 2015), which is also comparable to previous studies (Wise 2004). Fluctuations in CO_2 are therefore likely to contribute only a small fraction to fluctuations in the resting BOLD signal. The amplitude of resting BOLD fluctuations that are related to resting variations in CBF not associated with changing metabolic demand might be so small that they are overwhelmed by fluctuations due to other components of the BOLD signal.

The maximum possible BOLD signal change is determined by the baseline deoxyhaemoglobin concentration. The BOLD signal response approaches its maximum in an asymptotic manner (Buxton 2013). The BOLD signal response is therefore non-linear (Taneja 2020), and this non-linearity varies across the brain. Therefore, it might not be possible to extrapolate the low amplitude fluctuations in the baseline BOLD signal to predict the magnitude of the BOLD signal response to a relative strong stimulus like inhaled-CO_2. The BOLD signal is also sensitive to changes in CBV as well as CBF, but the relationship between CBF and CBV is also non-linear. Laminar flow is directly proportional to r^4 (r = radius of the blood vessel) (Openstax 2019), whereas the vascular volume, and therefore CBV, is proportional to r^2. Most of the resistance to CBF in the intracranial vasculature is in the

arterioles, therefore whilst a small change in arteriolar diameter can lead to a large change in CBF, the change in CBV is much smaller (Buxton 2013). However, if induced-hypercapnia were also to cause dilation of larger upstream vessels as well as the smaller arterioles, the increase in CBV would be proportionally larger, and a significant proportion of the BOLD signal response might be driven by changes in CBV rather than purely CBF. Therefore, whilst ASL CVR is a function of CBF, a proportion of the variance in the BOLD signal might be driven by changes in CBV rather than CBF. This might partly explain why there isn't a perfect positive correlation between ASL CVR and BOLD CVR (figures 6.10 and 6.11).

There are some limitations associated with ASL as well as BOLD. Although ASL is a more direct measure of CBF than BOLD, the SNR of ASL is inherently lower than BOLD. SNR is not uniform across the brain, therefore ASL CVR values from regions of the brain that are susceptible to a large amount of noise might be disproportionately affected and are potentially less reliable than BOLD CVR measurements in the same location. Additionally, there are confounding factors that affect CVR measurements derived from ASL data acquired with a hypercapnic challenge. Hypercapnia significantly lowers ASL labelling efficiency (Aslan 2010), which might result in a global underestimation of ASL CVR. Hypercapnia also reduces bolus arrival time (Donahue 2014), which might further inflate the ASL signal during hypercapnia. The relationship between ASL signal and arrival time is non-linear, and therefore the effect of a reduced arrival time might vary as a function of distance from the label location, confounding the regional variation in ASL CVR measurements. Ultimately, although ASL is a more specific measure of CBF, and therefore of CVR, than BOLD, it has its limitations, and these might also contribute towards masking the relationship between ALFF and CVR.

$PaCO_2$ is a function of the rate of metabolic production of CO_2 and of the rate of CO_2 clearance via the lungs. Metabolic processes tend not to induce significant hypercapnia unless there is a problem with ventilation (Rawat 2023). $PaCO_2$ is therefore predominantly influenced by fluctuations in respiratory rate and tidal volume, which might vary between individuals, or even within the same individual with time. The frequency at which resting $PaCO_2$ fluctuates therefore probably varies with time and between individuals. Therefore, low frequency fluctuations in the BOLD signal that occur due to fluctuations in vascular tone might be distributed across a broad range of frequencies, and it might be difficult to isolate a narrow frequency band within which ALFF correlates with CVR. This is exemplified by the

results of this chapter, which hint at a positive correlation between fALFF and CVR across a wide range of frequencies.

There is conflicting evidence from previous studies of the utility of resting-state BOLD data in the evaluation of CVR. As previously discussed, Golestani et al. demonstrated a qualitative similarity between whole-brain ALFF maps and CVR maps obtained by modulating the BOLD signal through a sinusoidal variation of the inspired CO_2 (Golestani 2016). They also demonstrated that global grey matter ALFF significantly correlates with standard BOLD CVR measurements. However, Golestani only investigated ALFF in the frequency range 0.01 – 0.08 Hz. Furthermore, whilst the statistical analysis methodology is not described in detail, they appear to have applied a parametric method of evaluating correlation, whereas this chapter has demonstrated that a non-parametric analysis might be more appropriate.

Cerebral autoregulation involves factors other than arterial CO_2 concentration that modulate cerebrovascular tone. These include the myogenic response, governed by cerebrovascular smooth muscle contraction and relaxation in response to changes in pressure (Silverman 2022), fluctuations in response to changes in local concentrations of endothelial factors such as nitric oxide (Silverman 2022), and fluctuations in the concentrations of metabolic by-products, or in O_2 concentration (Willie 2014). During induced-hypercapnia, the magnitude of the vascular response to CO_2 inevitably dominates these other factors. At rest, however, one or more of the other factors could be driving fluctuations in vascular tone at any time. The magnitude of the vascular response to these other factors might not directly correlate with the magnitude of the vascular response to CO_2. The method of measuring CVR using a hypercapnic challenge may not be representative of vascular reactivity to these other factors. Since we have attempted to validate ALFF against a CVR measurement derived from a hypercapnic challenge, the same limitation applies to ALFF.

Various other metrics of CVR derived from resting-state BOLD data have been proposed, with variable success. Jahanian et al. (Jahanian 2016) used the mean resting BOLD signal within CSF as the predictor in a voxel-wise GLM, and used the parameter estimate, β, within each voxel as an indicator of CVR. They found a significant spatial correlation with CVR maps generated using a breath-hold. On the other hand, Golestani et al. attempted a similar method, but did not find a significant correlation between standard CVR maps obtained by modulating the BOLD signal through a sinusoidal variation of the inspired CO_2, and global grey

matter CVR estimates derived from a GLM applied to resting BOLD data (Golestani 2016). Similarly, Liu et al. (Liu 2021) used the global BOLD signal (rather than CSF signal as per Jahanian) as a regressor in a GLM to derive a metric of CVR. rsfMRI-CVR maps based on a frequency range of 0 – 0.1164 Hz yielded the highest spatial correlation (r = 0.74). Jahanian et al. also have also proposed the coefficient of variation (the temporal standard deviation within each voxel divided by the mean signal intensity of the voxel) as a surrogate for CVR by demonstrating a correlation with CVR maps generated using a breath-hold (Jahanian 2016). On the other hand, Lipp et al. found no statistically significant correlation between the coefficient of variation and breath-hold CVR (Lipp 2015).

6.5. Conclusion

In summary, our analysis is not supportive of the utility of ALFF and fALFF as specific surrogate markers of CVR. Based on our analysis of the within-subject correlation between regional fALFF and ASL CVR, it is not possible to validate fALFF as a method of mapping within-subject CVR. There is no statistically significant correlation between ALFF/fALFF and ASL CVR, although the sample size is small. The maximum proportion of shared variance between fALFF and CVR equates to only 25%. Because of the multifactorial nature of the BOLD signal, it is highly unlikely that ALFF or fALFF can serve as a reliable metric of CVR.

7. The effect of dexmedetomidine, an α_2-adrenergic agonist, on brainstem autonomic activity and functional connectivity of the locus coeruleus – a pilot study

7.1. Introduction

As discussed in the introductory chapter, several parts of the central nervous system have an influence on sympathetic output to the cardiovascular system. One of the main physiological centres that influences sympathetic projections to the cardiovascular system is the rostral ventrolateral medulla (RVLM) (Lunblad 2014), which is a believed to be a central component in the generation of basal sympathetic tone (Feldman 2013). It has projections to and from multiple cortical and subcortical sites, including the locus coeruleus (LC), a small nucleus located in the brainstem. The LC has many functions, including regulation of pain processing and forming a key part of the arousal pathway, influencing the sleep-wake cycle. It is the largest group of noradrenergic neurones in the central nervous system, and has extensive projections throughout the CNS, including to parasympathetic and sympathetic centres in the brainstem and spinal cord, as well as throughout the cerebral hemispheres (Sara 2009). Therefore, it also forms an important component of the autonomic network that plays a part in regulating systemic blood pressure (Liu 2017), (Samuels 2008).

The LC is believed to have two modes of activity, a phasic mode involving a brief stimulus-evoked LC activation which facilitates orientation to the current task and a tonic mode which is thought to facilitate exploration for other sources of stimulation or reward (Ashton-Jones 2005). For example, phasic LC activity has been demonstrated in monkeys shortly after presentation of a visual cue prompting the monkey to pull a lever in exchange for a reward. Following a distractor stimulus (one not yielding a reward) LC phasic activity was minimal or absent. This suggests that phasic activity in the LC plays a role in optimising and facilitating behavioural response to tasks as well as increasing vigilance to subsequent similar tasks (Ashton-Jones 2005). On the other hand, the tonic mode involves a persistent elevation in LC neuronal firing which suppresses the phasic response (Yang 2021). This is thought to support disengagement from a current task to facilitate a search for other tasks or sources of

reward. The LC therefore functions to sustain attention to the general surroundings in its tonic mode, whilst focussing attention on a specific task in its phasic mode.

In this chapter we will use a high-resolution structural magnetisation transfer-weighted MRI sequence to image and accurately locate the locus coeruleus. This will enable precise localisation and segmentation of the LC, enabling us to generate an anatomical localiser of the LC within each participant. The feasibility of studying functional activity in the LC will then be investigated. The anatomical localiser, together with a BOLD gradient-echo EPI acquisition, will be used to investigate the amplitude of low-frequency fluctuations (ALFF) in the LC, as well as functional connectivity of the LC with other brainstem, cortical and subcortical regions. We will also test the feasibility of eliciting a measurable change in LC ALFF and functional connectivity following suppression of LC noradrenergic function using a moderate sedative, dexmedetomidine. Finally, we aim to evaluate whether accurate and reproducible measurement of LC contrast and volume is possible at an individual level.

The LC is a very small structure located in the dorsal pons near the pontomesencephalic junction. In humans, on average it measures 14.5 mm in length and 2.5 mm in thickness (K. Y. Liu 2017). Neuromelanin is a metabolite of noradrenaline and is deposited in brainstem catecholaminergic structures, including the locus coeruleus (Schwarz 2016), (Wakamatsu 2016). Previous studies have successfully imaged the LC using magnetisation-transfer weighted MRI sequences which are sensitive to the presence of neuromelanin (Priovoulos 2018), (X. Chen 2014). Autonomic dysfunction has been linked to changes in LC neuromelanin-based MRI contrast (Mather 2017), and several studies have suggested that locus coeruleus contrast and volume loss is linked to neurodegenerative diseases such as Parkinson's and Alzheimer's (K. Y. Liu 2017). Structural MT-weighted MRI of the LC may therefore be useful in assessing long-term noradrenergic activity in the LC as well as serving as an anatomic localiser for this important component of central autonomic regulation. We will explore whether reliable assessment of LC volume and contrast can be made using a MT-weighted acquisition.

The correlation between temporal fluctuations in resting state BOLD activity can be used to delineate functional connectivity between different parts of the brain (Bijsterbosch 2017). Previous studies have reported successfully mapping various functional connectivity networks in the brainstem (Bär 2016) (Singh 2022) (Bianciardi 2016). However, these studies

have relied on a standard-space atlas to identify brainstem nuclei. For example, Bianciardi et al. (Bianciardi 2015) have developed a probabilistic atlas of brainstem nuclei which demonstrated very good overlap across the majority of subjects, especially for the larger brainstem nuclei (16 out of 17 brainstem nuclei with a volume of greater than 100 mm^3 achieved up to 100% overlap across the 12 subjects from which the atlas was developed). However, the smallest brainstem nuclei (the median raphe and raphe magnus, with volumes of 14 and 16 mm, respectively) had a maximum overlap of 92% and 83%, respectively. This calls into question the validity of using generic atlases to perform functional connectivity analyses on very small nuclei such as the locus coeruleus, especially in regions with low SNR and high physiological noise like the brainstem. Even the slightest misregistration between individual participant's data and the coordinate space of the LC atlas could lead to a significant discrepancy in localisation of the LC. Only one (Bär 2016) of the above studies tailored their co-registration method towards the brainstem – others relied on whole-brain co-registration methods which we have previously found to be suboptimal when trying to achieve accurate brainstem co-registration. We will use a localiser tailored to each individual participant, together with tailored brainstem co-registration methods, when interrogating LC functional activation.

The overall effect on the autonomic system of an increase in noradrenergic activity in the LC is an increase in sympathetic activity, and a decrease in parasympathetic activity. The LC sends direct neuronal projections to several sympathetic and parasympathetic nuclei in the brainstem and spinal cord, including the Edinger-Westphal nucleus, dorsal motor nucleus of the vagus nerve (DMV) and the nucleus ambiguus (NA). It also indirectly influences the autonomic nervous system via projections to the paraventricular nucleus of the hypothalamus (PVN), the caudal raphe (CR) and the RVLM. The locus coeruleus has an inhibitory effect on the RVLM, but it sends excitatory projections to preganglionic sympathetic neurones in the intermediolateral nuclei of the spinal cord (IML). The resultant increase in IML sympathetic activity outweighs medullary sympathetic inhibition. The net effect of an increase in locus coeruleus activity is therefore an increase in sympathetic, and a decrease in parasympathetic, supply to the cardiovascular system (Samuels 2008). We will attempt to interrogate the functional connectivity of the LC as part of the central autonomic network using seed-based correlation analysis derived from a LC timeseries.

Whilst the LC is an important component of the autonomic nervous system (Samuels 2008), it also sends and receives extensive neural inputs from other parts of the central nervous system, including to the cerebral cortex, cerebellum, limbic system, thalamus, hypothalamus, and several other nuclei in the brainstem. Therefore, resting-state functional connectivity of the LC is not a specific marker of autonomic activity. To study the behaviour of the LC as part of the central autonomic network, a task designed to induce a functional response in the brainstem and an increase in systemic blood pressure will be used. Static handgrip exercise followed by a period of sustained post-exercise ischaemia (induced by inflating a blood pressure cuff to act as a tourniquet) has previously been shown to cause an increase in both muscle sympathetic nerve activity and blood pressure (Sander, 2010). This task stimulates production of metabolic byproducts which stimulate neuronal afferents that project to the medulla, stimulating activity in the RVLM and increasing central sympathetic output to the cardiovascular system, ultimately leading to an increase in blood pressure (Sander, 2010). Sander et al. have previously found an increase in the BOLD signal intensity in the medulla, thought to be at the site of the NTS and RVLM, in response to this task (Sander, 2010). The RVLM also send excitatory projections to the LC, and as previously discussed the LC has a sympathomimetic effect on the cardiovascular system. We therefore hypothesise an increase in functional activity in the LC in response to this task.

Dexmedetomidine is a specific and selective α_2-receptor agonist (Gerlach 2007). There are three subtypes α_2-receptor ($\alpha_{2A,}$ α_{2B} and α_{2C}-receptors). Blood pressure haemostasis mediated by α_2-receptors predominantly involves α_{2A} and α_{2B}-receptors. The blood pressure response to α_2-receptor activation by intravenous dexmedetomidine is biphasic and involves an initial brief increase in blood pressure which is thought to be mediated by α_{2B}-mediated peripheral vasoconstriction, followed by a more prolonged hypotensive phase driven by the central sympatholytic effect of α_{2A}-receptor activation (Philipp 2002). Low dexmedetomidine plasma concentrations (concentrations less than 1.9 ng/mL) are associated with a reduction in MAP whereas higher concentrations (greater than 1.9 ng/mL) increase MAP (Chamadia, 2020). At the doses utilised in this study the overall effect of dexmedetomidine on the cardiovascular system is expected to be a reduction in blood pressure and heart rate. Dexmedetomidine can also be used to induce a state of moderate sedation with a relatively short duration, whilst the recipient remains easily rousable. For example, it is of use during awake craniotomy procedures, which require the patient to be easily rousable so that

intraoperative functional mapping of the brain can be performed to minimise damage to eloquent areas during tumour resection (Hall 2008). Its main sedative effects are thought to be due to its action on noradrenergic neurones in the LC. Coupled with its pharmacological properties, it is therefore a suitable drug to administer in the MRI environment to investigate the effect of inhibiting neuronal activity in the LC. We hypothesise that, following dexmedetomidine administration, functional connectivity of the LC with other components of the central autonomic network will be reduced, and functional activity in the LC in response to the static handgrip task will be suppressed.

Finally, we will also investigate the amplitude of low frequency fluctuations in the BOLD signal (ALFF) in the LC. As previously discussed in chapters 5 and 6, ALFF is a non-specific marker of brain activity containing signal contributions that are both neuronal and vascular in origin. ALFF in certain regions of the brain has been shown to vary between some pathophysiological conditions and healthy controls, as well as between different physiological states in healthy participants. For example, ALFF in the visual cortex has been shown to be significantly higher during the eyes open condition compared to eyes closed in healthy participants (Yang 2007). We hypothesise that dexmedetomidine administration will lead to a lower ALFF and fractional ALFF in the LC compared to baseline.

From the perspective of the selfish brain mechanism, the ultimate goal will be to translate the outcomes of this pilot study to a larger study investigating how brainstem autonomic functional connectivity differs between hypertensive and normotensive patients. This will enable investigation of whether noradrenergic overactivity in the locus coeruleus is implicated in the aetiology of hypertension, by using the LC contrast and volume measurement techniques developed in this pilot study to investigate the relationship between blood pressure and LC contrast and volume.

7.1.1. Summary of aims

1. Demonstrate the feasibility of using a MT-weighted sequence to generate individual LC localisers for each participant.
2. Evaluate whether accurate and reproducible measurement of LC contrast and volume is possible at an individual level.

3. Demonstrate the feasibility of measuring the amplitude of low-frequency fluctuations (ALFF) of resting-state functional MRI data in the LC.
4. Investigate functional connectivity of the LC with other brainstem, cortical and subcortical regions.
5. Investigate the feasibility of eliciting a functional response in the LC to a task designed to increase systemic blood pressure via an increase in sympathetic output from the CNS.
6. Test the feasibility of eliciting a measurable change in LC ALFF, functional connectivity and functional response to the above task following inhibition of LC neuronal activity using a moderate sedative, dexmedetomidine. Following dexmedetomidine administration we hypothesise:
    a. A reduction in LC ALFF/fALFF.
    b. A reduction in functional connectivity between the LC and other components of the CAN.
    c. A reduction in functional activity in the LC.

7.2. Methods

The study was performed as part of a broader study investigating the role of human brainstem noradrenergic centres in sedation, analgesia and haemodynamic control, which had been reviewed and approved by the School of Psychology Research Ethics Committee. Recruitment was performed via posters placed in Cardiff University buildings and through the existing CUBRIC and School of Psychology subject databases of participants who had agreed to receive information about research studies.

Participants were issued with a study information sheet (appendix 10), medical screening questionnaire, MRI screening questionnaire and consent form (appendix 11) in advance. Participants who expressed an interest in taking part and met the inclusion criteria (appendix 9) were invited to attended CUBRIC before the main study day to be familiarised with the MRI scanner and tasks as well as the risks of sedation, and to undergo detailed medical screening by an anaesthetist. Written informed consent was obtained from all five participants during this visit. On the main study day, informed consent to undergo sedation

was again obtained by a trained anaesthetist (in addition to the consent process performed during the familiarisation visit). This ensured that the participant was fully aware of all potential risks and that they remained suitable to undergo sedation. Following this, intravenous cannulation was performed by an experienced (post-fellowship) anaesthetist. A saline infusion was administered during the first half of the MRI session as a placebo. After the end of the first MRI session (as outlined in figure 7.1) the participant was offered a comfort break. Dexmedetomidine was then administered intravenously by a post-fellowship anaesthetist using a computer controlled targeted infusion pump whilst the participant was supine on the MRI scanner bed (outside the bore). The initial target concentration was 0.1 ng/mL. Once the target dose was achieved it was increased every 5 minutes by 0.1 ng/mL until the desired sedation level (mild-to-moderate sedation measured as level 3-4 on a modified Observer Assessment of Alertness/ Sedation scale (Chernik 1990)) was reached. The infusion was then maintained at the same dose for the duration of the second MRI session (lasting no more than one hour). Four researchers were always present in the MRI control room – two anaesthetists to monitor the participant, an MRI operator and a fourth researcher to administer the experimental stimuli. Physiological monitoring was performed using non-invasive monitoring of heart rate, single channel ECG, blood pressure, blood oxygen saturation levels, $ETCO_2$ and respiratory rate. Resuscitation equipment was available at all times. The participant had access to a call button whilst inside the MRI scanner, enabling them to alert the MRI operator at any time. Dexmedetomidine infusion was immediately stopped if at any time during the study there was evidence of unexpected increased sedation, reduced respiratory rate, desaturation (blood oxygen saturation levels of < 90% whilst breathing air enriched with oxygen at a rate of 2 litres/minute), a reduction in blood pressure or heart rate > 20% below pre-sedation levels, or if any other intolerance of the drug was suspected. Following cessation of the dexmedetomidine infusion, participants were monitored for at least two hours.

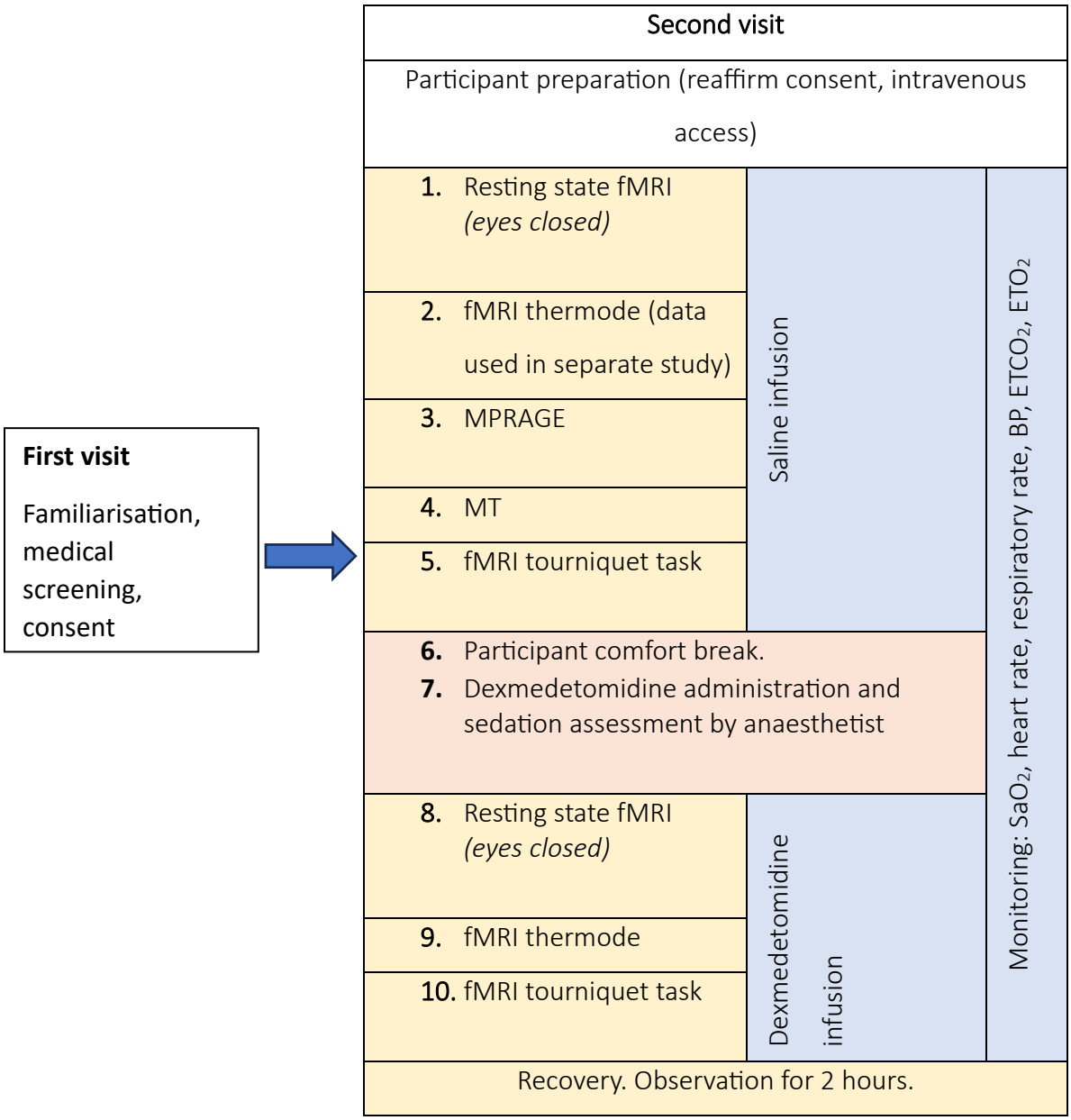

Figure 7.1: Outline of study procedure and experimental design.

7.2.1. MRI sequence parameters

All MRI data were acquired using a 7 Tesla Siemens Magnetom scanner, with a 32-channel receive-only head coil. A BOLD gradient-echo echo planar imaging fMRI sequence with the following parameters was utilised: TR = 2000 ms, TE = 25 ms, 300 volumes, voxel size = 1.5 mm isotropic, multiband factor = 4, GRAPPA = 4 to minimise acquisition time and

susceptibility artefacts. Multiband uses both gradient and coil-encoding to spatially localise signal and enables simultaneous acquisition of multiple slices (Moeller 2010). This reduces acquisition time without a significant reduction in SNR. The multiband slices were oriented such that the brainstem was wholly within one multiband segment, in order to minimise the impact of multiband-related artefacts from adjacent segments on brainstem functional activity.

The MT sequence utilised to image the locus coeruleus consisted of a magnetization transfer-weighted turbo flash (MT-TFL) sequence developed by Priovoulos et al. (Priovoulos 2018) with slice thickness of 0.5 mm, in-plane resolution of 0.43 x 0.43 mm, flip angle = 8°, TE = 4.08 ms, TR = 538 ms. The slice direction was oriented perpendicular to the craniocaudal axis of the brainstem to maximise spatial resolution through the smallest diameter of the LC. A high-resolution structural scan (MPRAGE with 0.7 mm isotropic spatial resolution) was acquired to aid co-registration.

7.2.2. Generic pre-processing methods

Brain extraction was performed using FSL BET, and careful manual evaluation and correction of the images was undertaken to ensure accurate brain extraction, especially around the skull base and brainstem. Motion correction was performed using FSL MCFLIRT with the middle volume as the reference image. Monitoring of respiratory rate and volume and of heart rate was performed using AD instruments photoplethysmogram and respiratory pressure belt. Physiological noise correction was performed using linear regression to remove signal variance related to heart rate, respiratory volume per unit time and fluctuations related to the phase of the respiratory and cardiac cycles (RETROICOR) (Glover 2000). The mean BOLD timeseries from a manually drawn CSF mask was also removed via linear regression. Distortion correction was performed using a pair of phase-encode reversed images and the FSL tool topup. For the resting-state fMRI analysis, BOLD data was high-pass filtered with a cut-off of 100 seconds, to remove scanner drift (except for blood-pressure stimulus acquisition, see below). A mask of the CSF spaces was applied to exclude CSF spaces from the GLM analysis, thus improving sensitivity to detect parenchymal fMRI signal. All data were co-registered to MNI space, via an intermediate co-registration to individual structural space using a high-resolution MPRAGE acquisition. Landmark based co-registration was applied for

both co-registration steps (from function to structural and from structural to MNI space), as described in previous chapters.

We do not necessarily expect a significant difference in the results between the left and right locus coeruleus, but nevertheless they are anatomically separate structures with a separate (but overlapping) vascular supply. Analysing them separately is a useful way of validating the results, especially in an exploratory analysis of whole-brain functional connectivity where the right and left LC connectivity maps should be reasonably symmetrical. This will help avoid any spurious inferences from being drawn from the data.

7.2.3. Resting-state functional connectivity of the locus coeruleus

The locus coeruleus was manually segmented into right and left on the MT image. In general, the LC was found to be poorly defined relative to surrounding brainstem tissue (figure 7.3). The LC atlas developed by Ye et al. (Ye 2021) was therefore transformed into the co-ordinate space of the LC acquisition and used as a guide to identify and segment the LC. The right and left LC masks were then co-registered to the pre-processed functional data via the high-resolution structural data using LBC. Right and left LC timeseries were then extracted from the resting-state fMRI data using the LC masks. Whole-brain subject-level seed-based correlation analysis (SCA) was then performed by using the R and L LC timeseries as regressors in two separate GLM (one for right and one for left). Subsequently, another SCA was performed, this time limited to the brainstem (a brainstem mask generated using Freesurfer, as described in previous chapters, was applied prior to SCA), to try and maximise sensitivity to detect functional activity in the brainstem noradrenergic network.

Following the first-level analysis, FSL Randomise was used to perform a group level analysis. Randomise was chosen in order to avoid potentially erroneous assumptions about the parametric nature of the MRI data. The mean functional activation across all ten datasets (five subjects, pre and post sedation) against baseline was tested using a one-sample t-test with threshold-free cluster enhancement, to investigate whether any significant functional activation is detectable within this small sample. Functional activation before and after sedation was also compared using a paired t-test.

7.2.4. Functional activity in response to blood pressure perturbation

A 12-minute BOLD fMRI sequence was acquired, during which the participant was asked to perform a task designed to elicit a systemic blood pressure response via an increase in sympathetic nerve activity. Intermittent static handgrip, which involves repeatedly squeezing and releasing a handgrip device, followed by forearm ischaemia, induced via inflation of a blood pressure cuff that acts as a tourniquet, has been shown to cause an increase in sympathetic nerve activity which persists even after handgrip exercise has ended (Leuenberger 2003). A version of this task was used in this study. Following a 6-minute period of rest at the start of the scan, the participant was asked to repeatedly squeeze and release a handgrip device every two seconds for 90 seconds in total, using their right hand. After 60 seconds of this activity, a blood pressure cuff, also attached to the right arm, was remotely inflated to 200 mmHg to act as a tourniquet and was left inflated for the duration of the BOLD acquisition (approximately 5 minutes in total). As discussed in section 7.1, the subsequent accumulation of metabolic products in the forearm induces a sympathetic response and an increase in systemic blood pressure. Each participant was familiarised with this task outside the scanner during the familiarisation visit and on the main study day and instructed to repeatedly squeeze the handgrip to approximately 70% of their maximum effort. During the analysis of this data, high-pass filtering of the fMRI data was not performed, because this might remove some of the variance in the data attributable to the blood pressure fluctuations.

During the fMRI acquisition, blood pressure recordings were made every minute, using a sphygmomanometer attached to the left arm. This was attached to a system which transmitted readings via telemetry to a monitoring station in the MRI control room, used as part of the anaesthetic monitoring of the participant. The task can induce an uncomfortable or painful sensation, and at the end of each session (before and after dexmedetomidine),

participants were asked to rate the degree of pain or discomfort experienced, if any, on a scale of 1 to 10.

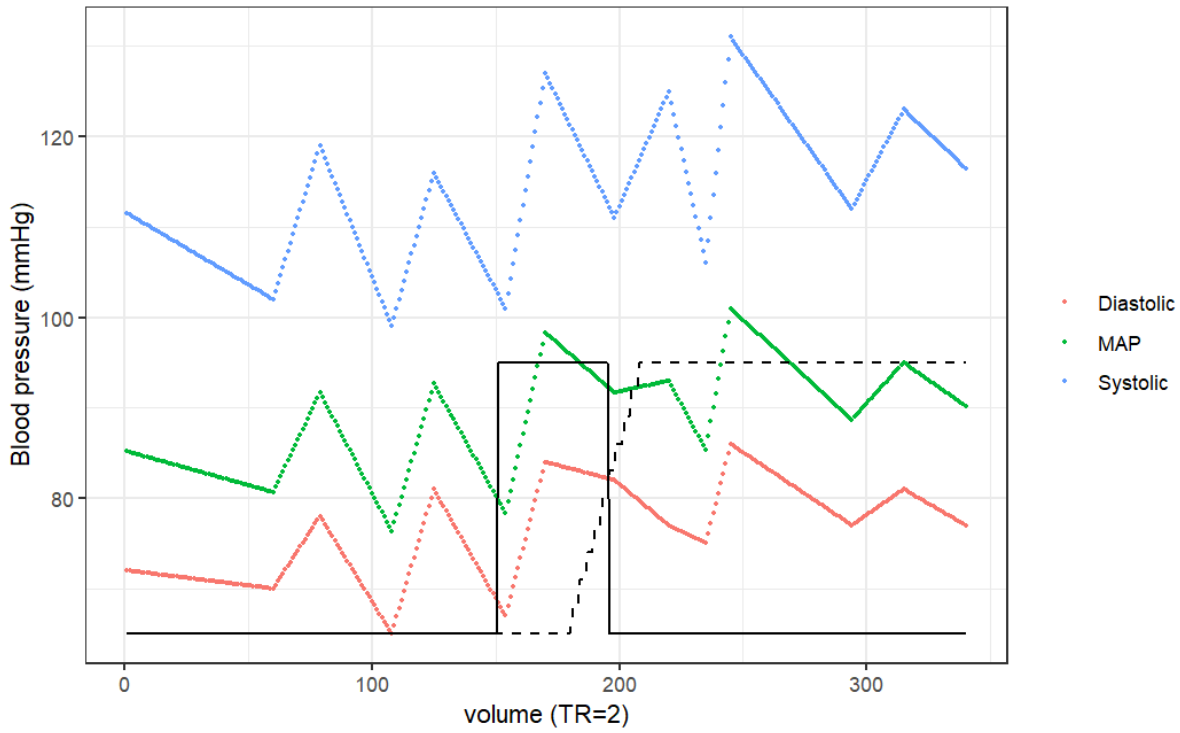

Figure 7.2. Design matrix for the ischaemic handgrip task. The solid black line represents the boxcar function used to model the motor component. The dashed black line represents the model of the sensory component. Linear interpolation between each blood pressure reading was performed, and the MAP, in green, was used in the GLM to represent the blood pressure response.

A GLM was applied using FEAT to evaluate the whole-brain BOLD response to the ischaemic forearm task. The GLM design matrix consisted of three regressors, one to model the mean arterial pressure, one to model the motor component of the hand grip task, and one to model the sensory component of the tourniquet (figure 7.2), with physiological noise parameters included as nuisance regressors. Blood pressure was modelled through linear interpolating of the mean arterial pressure from one-minute intervals to two second intervals (equal to TR of BOLD acquisition) (figure 7.2). The motor component was modelled as a 90 second boxcar function. The sensory component consisted of a linear ramp, to model the gradual inflation of the tourniquet, followed by a constant. Modelling the motor component of the task is useful to validate the presence of a robust functional response in the expected

areas (predominantly the left motor cortex and right cerebellar hemisphere). Similarly, the sensory component can be used to determine whether tourniquet inflation induces a significant sensory or painful response in the left ventral posterolateral nucleus of the thalamus, where second order neurons of the spinothalamic tract synapse with third order neurons projecting to the sensory cortex. Following this subject-level analysis, group-level analysis was performed using FSL Randomise. As per the SCA method described above, this analysis was subsequently repeated exclusively within the brainstem. Three contrasts were evaluated: blood pressure v baseline, motor response v baseline, and sensory response v baseline.

7.2.5. Locus coeruleus contrast-to-noise

The right and left LC contrast-to-noise ratio (LC CNR) was calculated as per equation 7.1:

$$LC\ CNR = \frac{LC_{MT-mean} - BS_{MT-mean}}{BS_{MT-stdev}}. \quad (7.1)$$

$LC_{MT-mean}$ was obtained by outputting the mean signal in a manually labelled LC mask on the MT-weighted sequence, $BS_{MT-mean}$ is the mean signal in an adjacent brainstem region of interest and $BS_{MT-stdev}$ is the standard deviation within the same brainstem region of interest.

7.2.6. Locus coeruleus ALFF

As discussed in section 6.5.1, ALFF and fALFF values are not normally distributed within regions of interest in the brain. Therefore, median LC ALFF/fALFF is reported rather than the mean.

The assumptions of normality were checked. The boxplots in figures 7.6 and 7.7 below demonstrate that there are outlying data points which may bias the statistical analysis. However, QQ plots (which draw a correlation between the data residuals and the normal distribution) reveal that the residuals of the linear model are approximately normally distributed (appendix 8). This is confirmed by a Shapiro-Wilk test, which did not return a

statistically significant result at any of the levels of the model. Furthermore, Levene's test for was non-significant, confirming homogeneity of variance. It was not deemed appropriate to exclude any outlying data because of the small size of the dataset. This is an exploratory analysis of a small dataset, and therefore t-tests were performed for illustrative purposes, and to guide power estimates in a future larger study. A non-parametric Wilcoxon test may be more appropriate when the full study is performed if the larger dataset also deviates from the assumptions of parametric testing.

7.3. Results

Clinical parameters were recorded by the anaesthetist at 10-minute intervals pre-sedation and 5-minute intervals post-sedation. The mean values of these clinical parameters are shown alongside participant characteristics in table 7.1. As expected, heart rate and blood pressure were significantly lower post-sedation.

*Table 7.1: Summary of participant characteristics, including clinical parameters before and after sedation. * $p < 0.05$ v pre-sedated group. Dexmedetomidine dose is the maintenance dose at the desired level of sedation.*

Age	23.3 ± 4.6	
BMI	23.6 ± 3.0	
Sex	Male (100%)	
	Pre-sedation	**Post-sedation**
Heart rate	74.2 ± 11.2	65.7 ± 11.7 *
Systolic BP	123.0 ± 8.0	111.2 ± 4.6 *
Diastolic BP	74.1 ± 2.9	64.3 ± 3.8 *
MAP	90.4 ± 4.6	79.9 ± 4.1 *
SpO_2	98.7 ± 0.4	98.1 ± 1.2
Dexmedetomidine dose	NA	0.22 ± 0.04 ng/mL
Sedation level (Observer Assessment of Alertness/ Sedation scale)	5 ± 0 (not sedated)	4 ± 0 (mildly sedated)
Pain rating	5.0 ± 1.6	4.7 ± 2.5

As previously mentioned in section 7.2.4, blood pressure was recorded every minute during the tourniquet task fMRI scan, both before and after cuff inflation. The mean MAP before and after cuff inflation, both pre- and post-sedation, for each participant is shown in table 7.2. There is an increase in MAP after cuff inflation in every participant bar one, although the threshold for statistical significance was only met in four cases.

Table 7.2: Mean arterial pressure in each participant during the tourniquet task fMRI scan before and after cuff inflation, pre- and post-sedation.

	Pre-sedation		Post-sedation	
	Mean MAP before cuff inflation	Mean MAP after cuff inflation	Mean MAP before cuff inflation	Mean MAP after cuff inflation
Participant 1	91.2 ± 2.0	91.6 ± 3.1	81.2 ± 5.5	82.2 ± 3.3
Participant 2	91.1 ± 1.5	95.2 ± 2.0 *	81.3 ± 4.7	88.2 ± 2.3 *
Participant 3	80.9 ± 3.5	80.4 ± 4.0	68.8 ± 2.9	64.0 ± 3.9
Participant 4	82.0 ± 2.1	88.2 ± 1.7 *	74.1 ± 2.8	72.3 ± 2.1
Participant 5	95.2 ± 4.9	101 ± 7.3	73.6 ± 0.9	78.2 ± 2.9 *
Mean	*88.1 ± 5.6*	*91.3 ± 6.9*	*75.8 ± 4.8*	*77.0 ± 8.3*

7.3.1. Locus coeruleus segmentation and contrast-to-noise

The LC was found to be visible on each of 5 MT acquisitions. However, careful adjustment of the window (contrast and brightness) settings in FSL eyes was required to differentiate it from the adjacent brain parenchyma. There are enough hyperintense voxels within the centre of the LC to enable it to serve as an anatomical localiser for SCA, but because its margins are poorly defined, accurate measurement of its volume is not possible (figure 7.3).

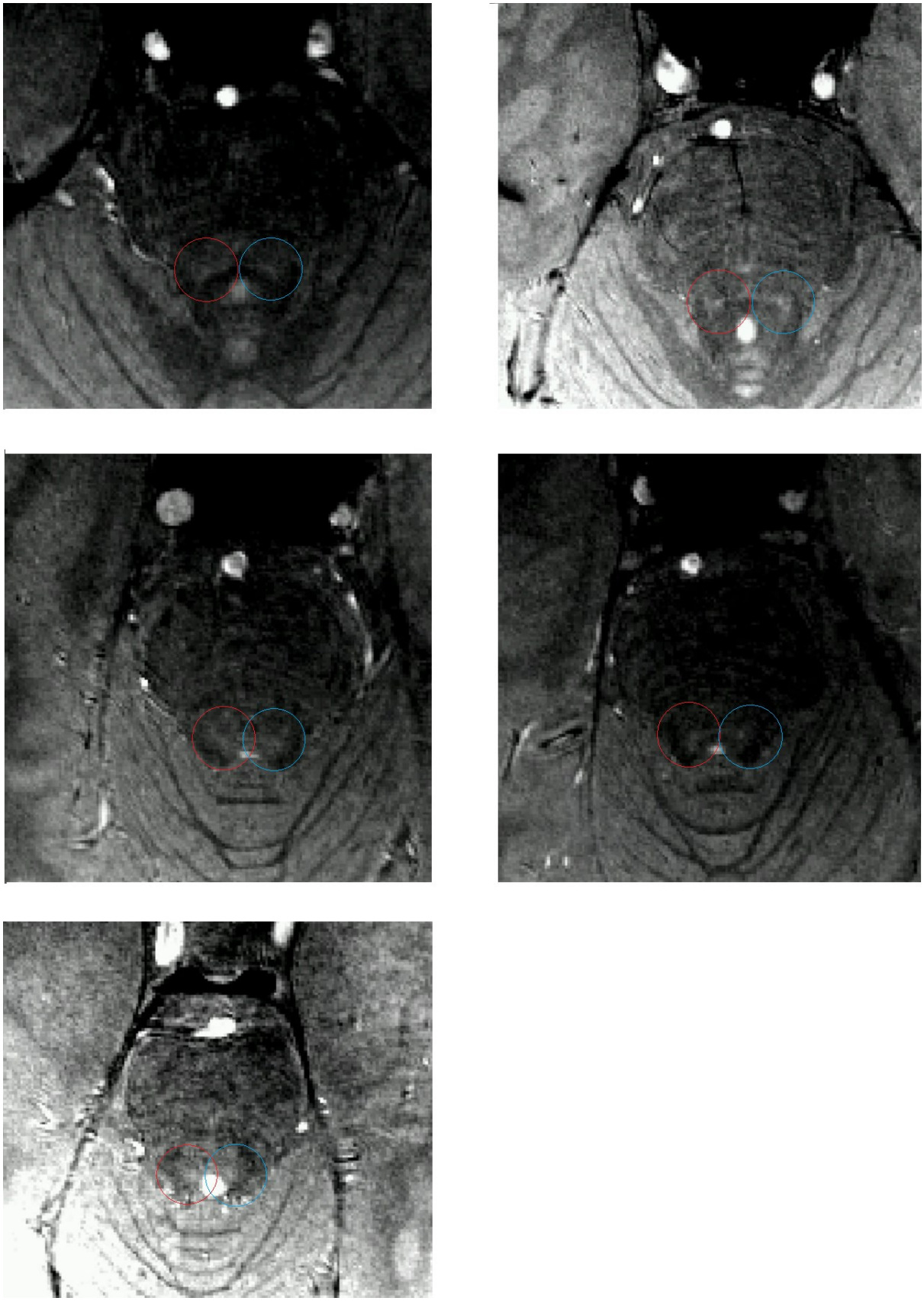

Figure 7.3: Axial views through the pons, MT-weighted acquisition. The right (centre of red circle) and left (centre of blue circle) locus coeruleus is visible as a subtle hyperintense focus on the MT acquisition of each of the 5 participants. The edge of the LC is poorly defined, precluding accurate measurement of its overall volume.

Figure 7.4 shows an example of a resting-state BOLD EPI acquisition from a single participant, co-registered to MNI space, with the location of the LC according to the atlas developed by Ye et al. (Ye 2021) (yellow and green), and the location of the LC according to the result of manual segmentation of the MT-weighted acquisition (red and blue), that has also subsequently been co-registered to MNI space. There is a clear disagreement between the atlas and the MT-segmentation. This reinforces the importance of using within-subject data-driven methods of localising small regions of interest such as the LC, rather than relying on a generic atlas derived from a different set of individuals.

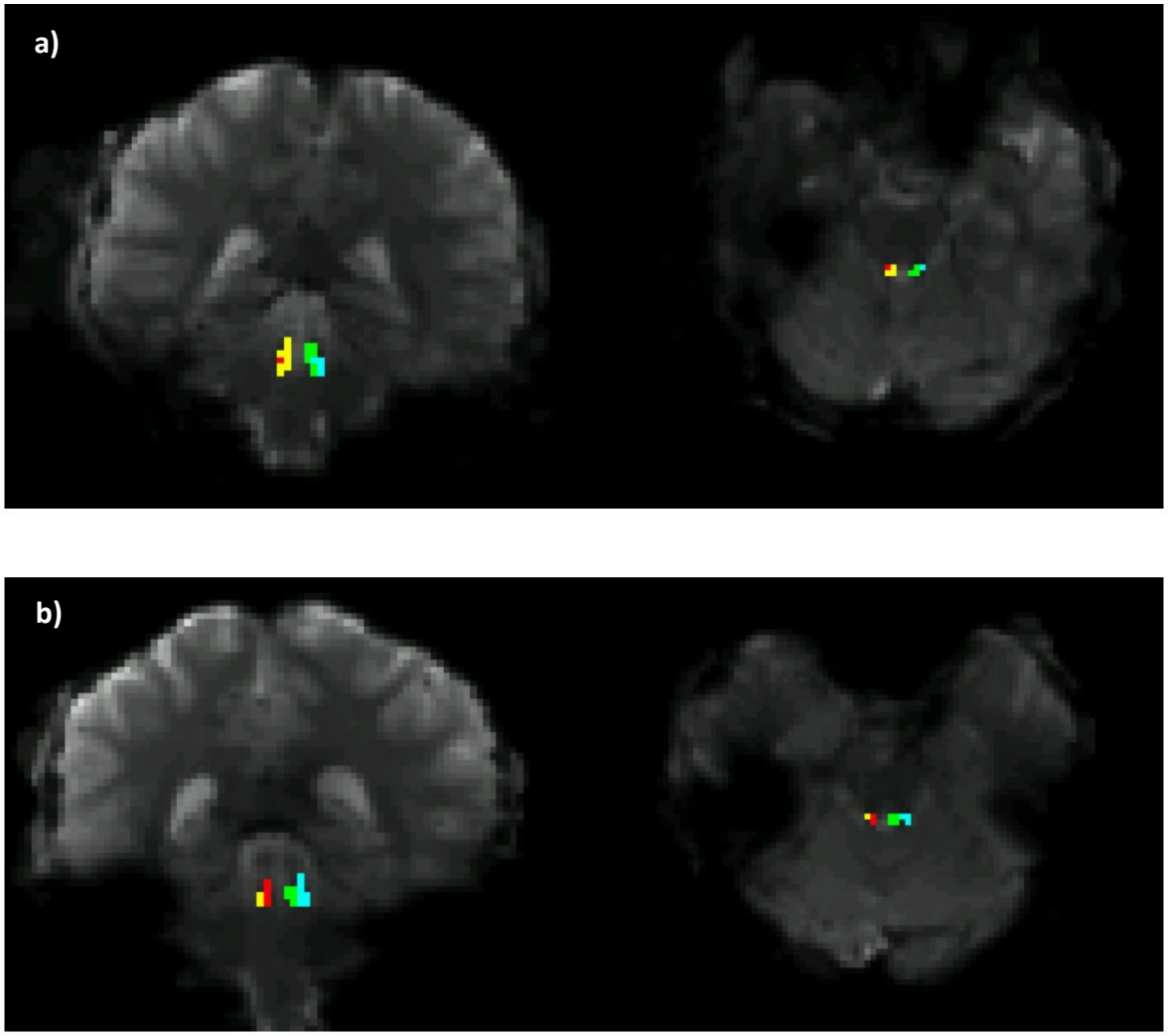

Figure 7.4: Location of the LC according to the LC atlas (yellow and green) and the manually-segmented MT acquisition (red and blue). The mean of each participant's rsfMRI acquisition is displayed for reference. All data have been co-registered to MNI space using the co-registration methods described above. The left LC atlas (green) is too medial and overlies the fourth ventricle in c) and d) (see next page). Manually-segmented LC consistently overlies brain parenchyma.

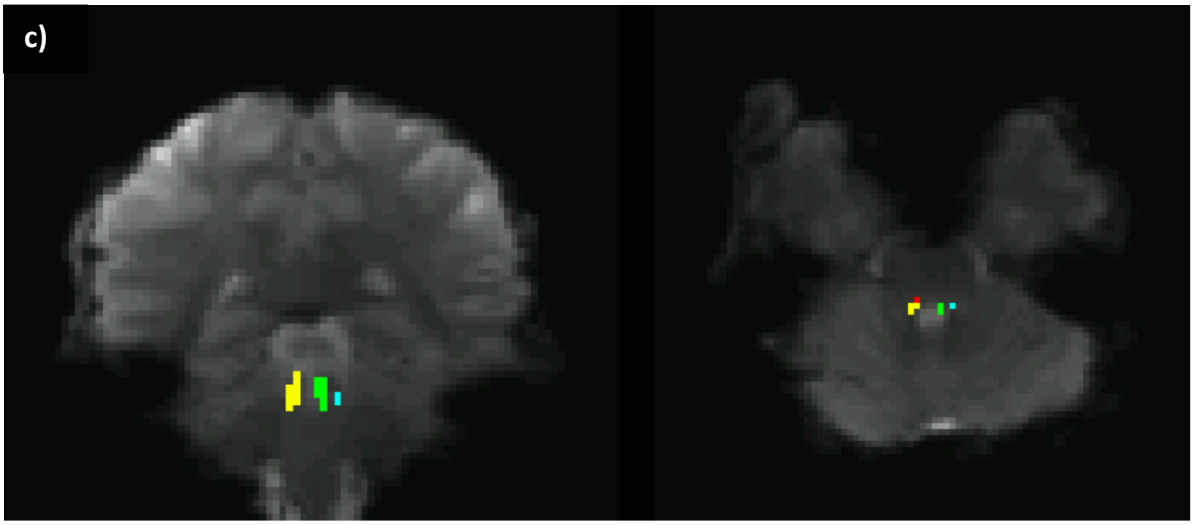

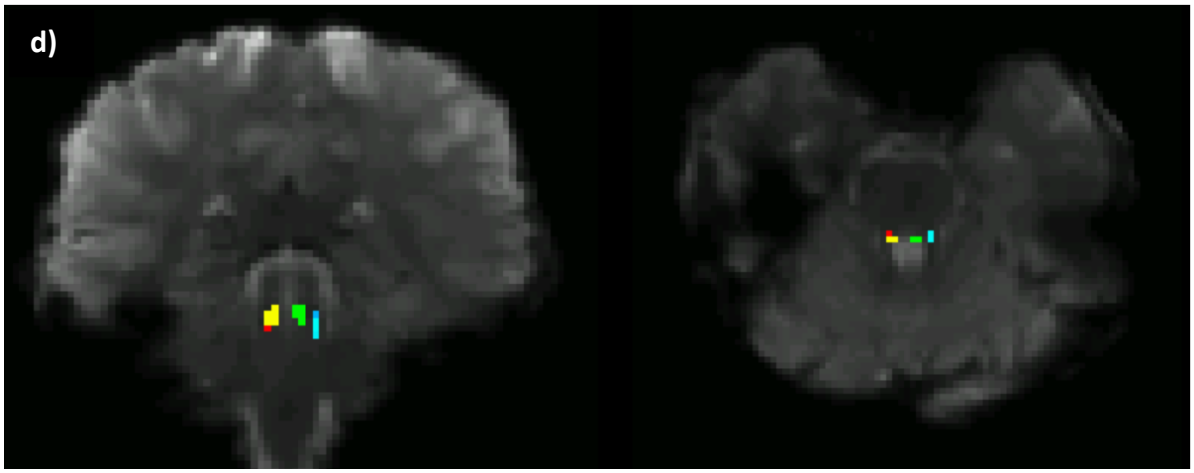

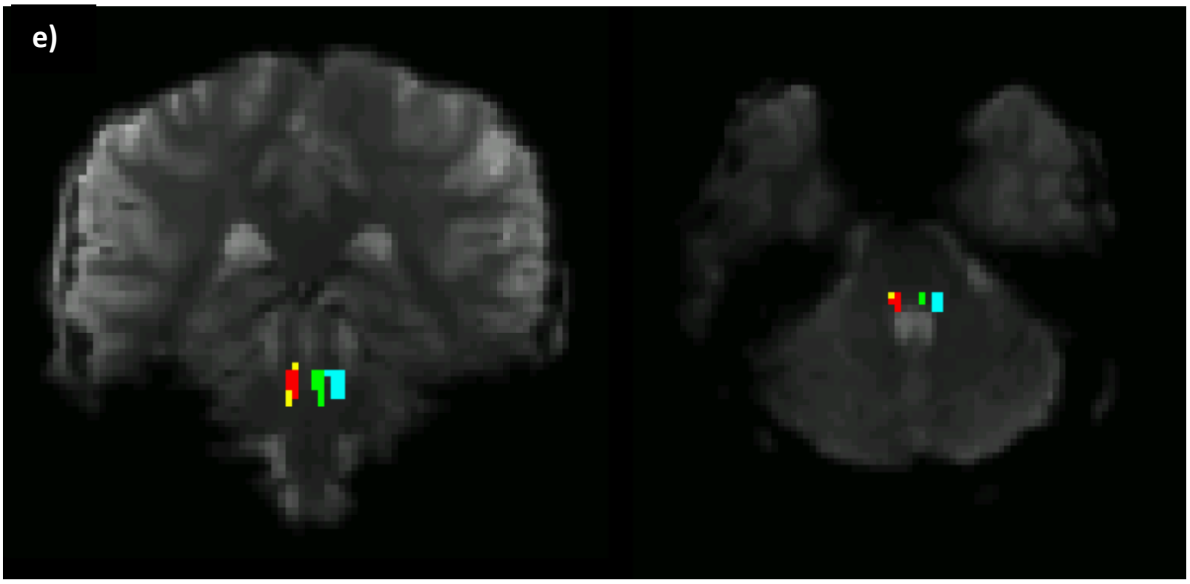

Figure 7.4 continued

The contrast to noise ratio was calculated by measuring the signal intensity in voxels that were of sufficiently high intensity to confidently localise them within the LC. Boundary voxels were not included. The CNRs in figure 7.5 are therefore somewhat overinflated, and do not reflect the technical difficulty in identifying and segmenting the LC.

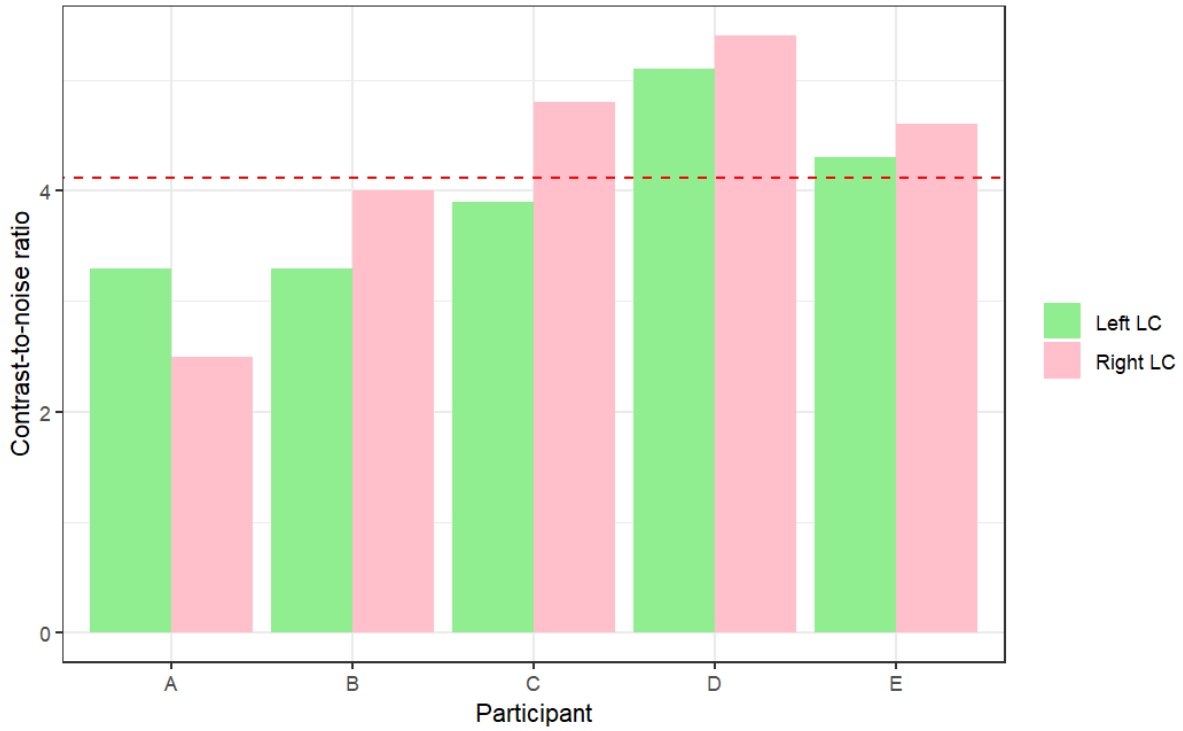

Figure 7.5: Contrast-to-noise ratio in the right and left locus coeruleus on the MT-weighted acquisition. The dashed red line represents the mean CNR across all participants of 4.1 ± 0.9.

7.3.2. Locus coeruleus ALFF and fALFF

Left and right LC ALFF and fALFF were compared separately before and after sedation (figures 7.6 and 7.7), using a paired two-tailed t-test. None of the comparisons reached the threshold of $\alpha < 0.05$ for statistical significance. The results are displayed in tables 7.3 and 7.4.

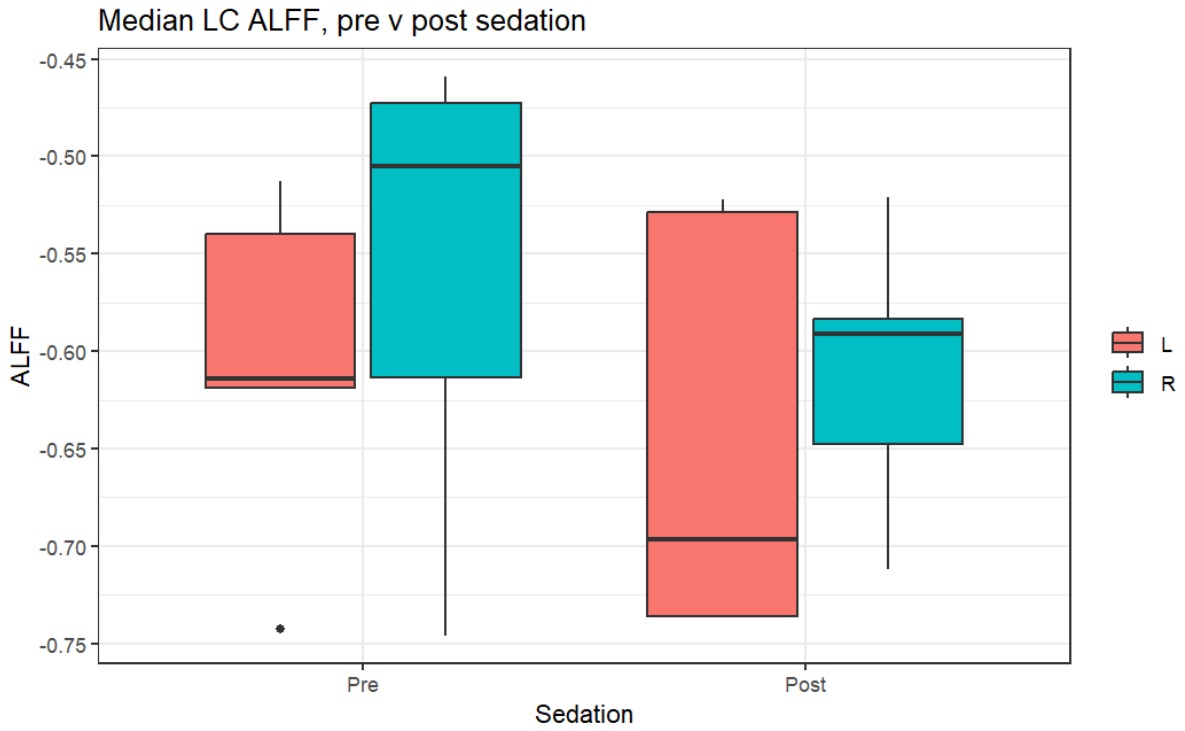

Figure 7.6: Median LC ALFF pre v post sedation.

Table 7.3: Two-tailed t-test comparing ALFF in the left and right LC, pre and post sedation.

ALFF	*mean difference pre v post*	*t-statistic*	*degrees of freedom*	*p-value*	*effect size (Cohen's d)*
L LC	-0.04	0.54	4	0.62	0.24
R LC	-0.05	0.66	4	0.54	0.30

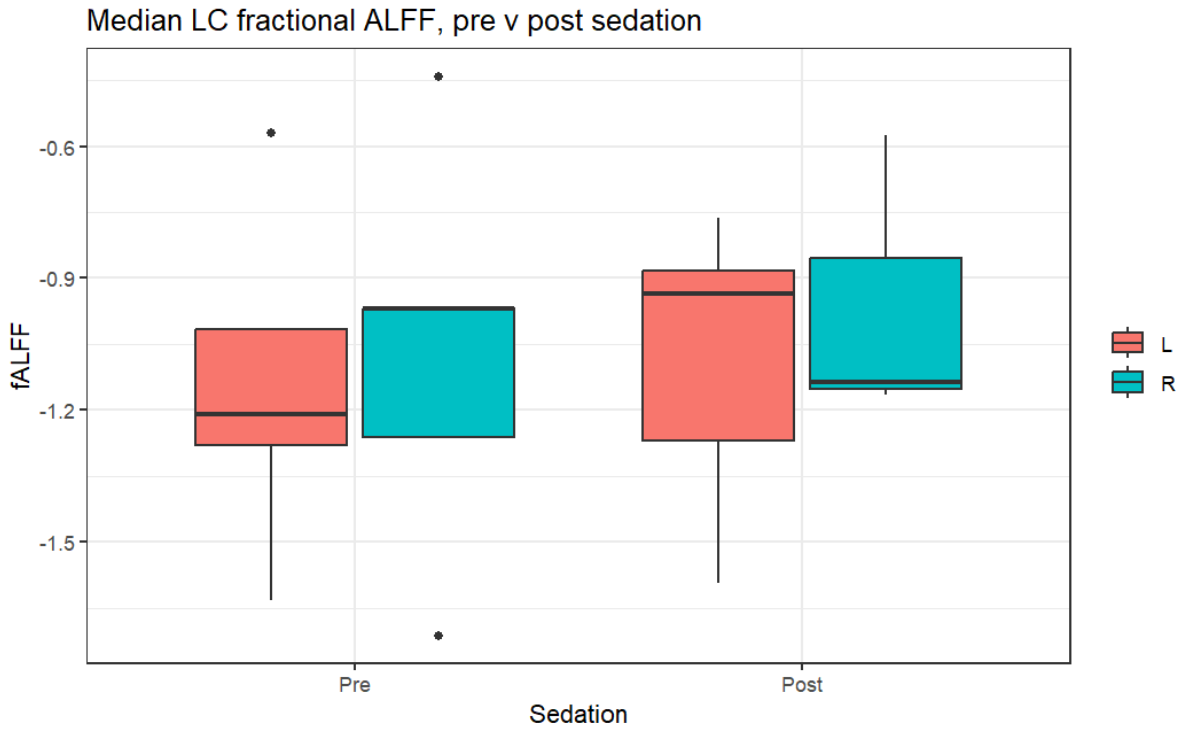

Figure 7.7: Median LC fractional ALFF pre v post sedation.

Table 7.4: Two-tailed t-test comparing fractional ALFF in the left and right LC, pre and post sedation.

fALFF	*mean difference pre v post*	*t-statistic*	*degrees of freedom*	*p-value*	*effect size (Cohen's d)*
L LC	-0.05	-0.31	4	0.77	0.14
R LC	-0.09	-0.43	4	0.69	0.19

7.3.3. Resting-state functional connectivity of the locus coeruleus

Figure 7.8 demonstrates whole-brain SCA maps for the left (top) and right (bottom) LC (p-values with an α-threshold of 0.05). There are significant areas of functional connectivity throughout the brain on both. Figure 7.9 demonstrates the results of SCA limited to the brainstem only. Figure 7.10 compares the functional connectivity map of the right (red) and left (blue) LC, displaying only voxels with p-values above the 99th percentile of the maximum p-values for the right and left LC maps, to limit analysis to the areas of the brain displaying the

most robust response. Other than in the LC themselves, there is no discernible symmetry between the activation maps of the right and left LC, even when the analysis is limited to the brainstem.

A two-tailed paired t-test did not reveal any significant difference in the SCA maps of the left or right LC pre v post sedation, even when the analysis was limited to the brainstem.

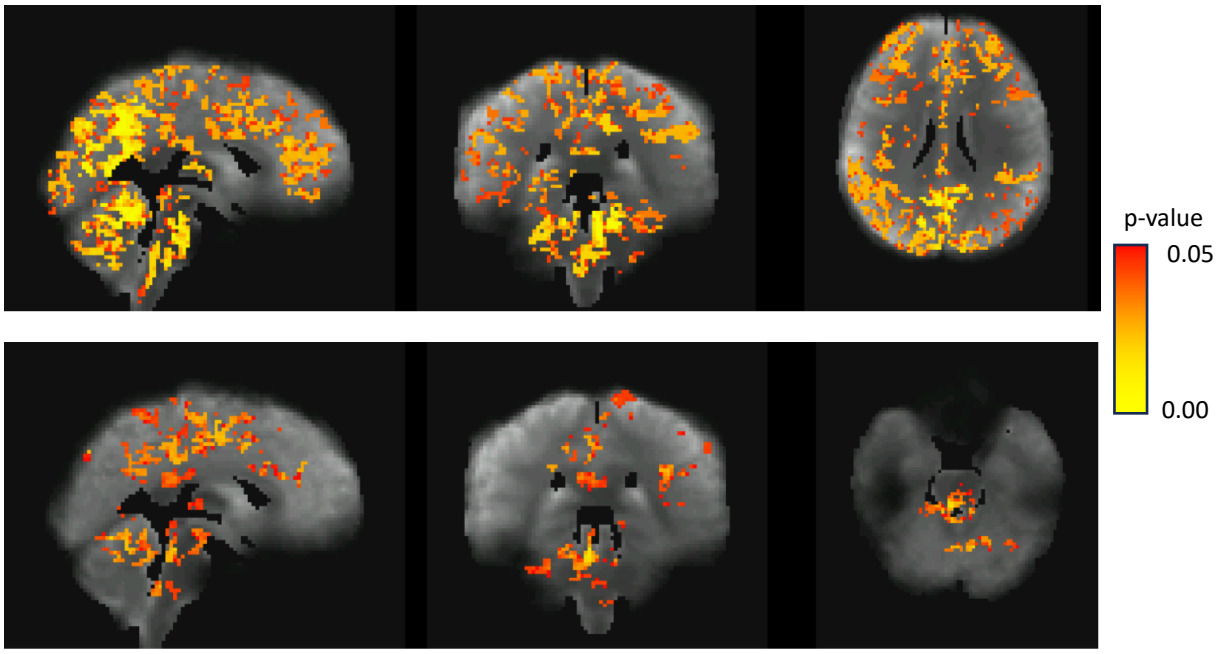

Figure 7.8: Group-level resting-state SCA maps of the left (top) and right (bottom) LC, thresholded at p < 0.05.

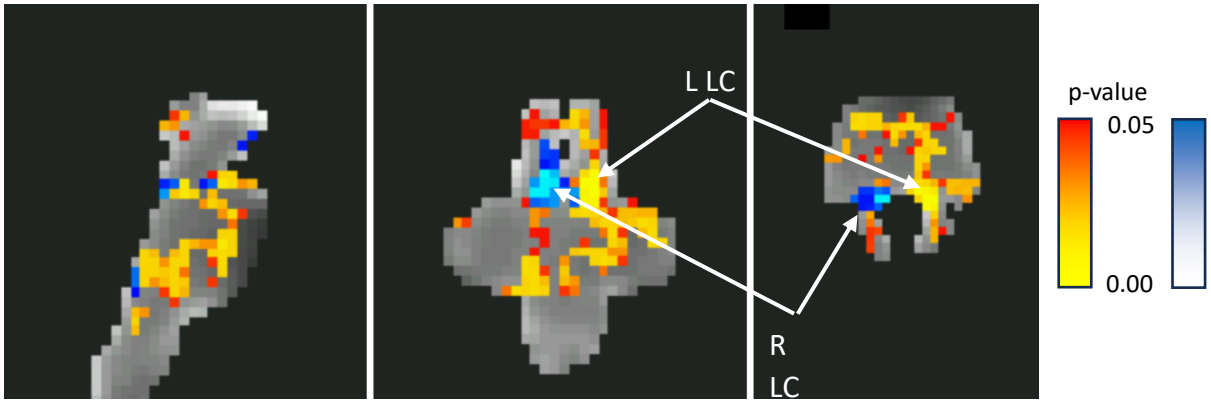

Figure 7.9: Group-level resting-state SCA map of the L (yellow/red) and R (blue) LC, analysis limited to the brainstem only, thresholded at p < 0.05.

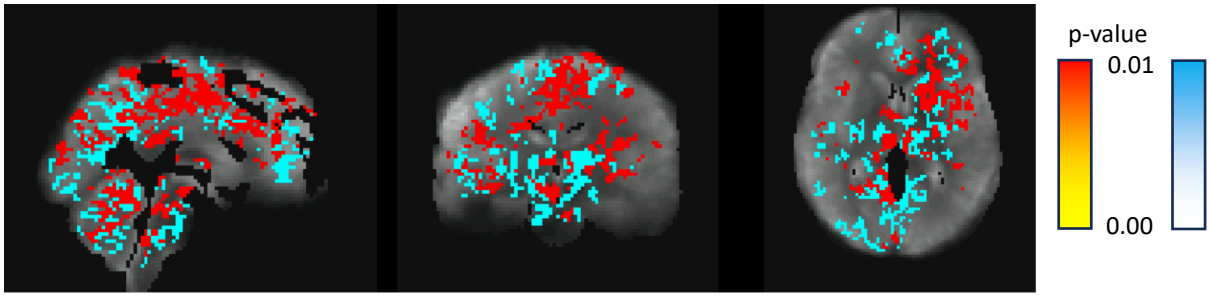

Figure 7.10: Comparison of group-level SCA map of R (red) and L (blue) LC. Only p-values above the 99th percentile are shown (p < 0.01).

7.3.4. Functional activity in response to blood pressure perturbation

When considering the motor component of the ischaemic handgrip task (figure 7.2), there is a single voxel overlying the left central sulcus, and another in the right cerebellar hemisphere (figure 7.11, top) which reach the threshold for statistical significance of < 0.05. The lower part of figure 7.11 demonstrates that when the α-value is increased to 0.15, larger clusters of activation are seen in the right cerebellar hemisphere and left motor cortex, as expected in response to a right-handed motor task. There are also clusters of activation in the left thalamus and left postcentral gyrus, consistent with activation in sensory areas in response to the sensation of performing the handgrip task. The sample size is probably too low for these larger clusters to reach the threshold for statistical significance. The fact that only a few cortical voxels demonstrated statistically significant functional activity in response to this relatively robust motor task tempers any expectations of detecting functional activity in the brainstem in response to the modest blood pressure fluctuation elicited by the ischaemic handgrip task (figure 7.2) in this small sample.

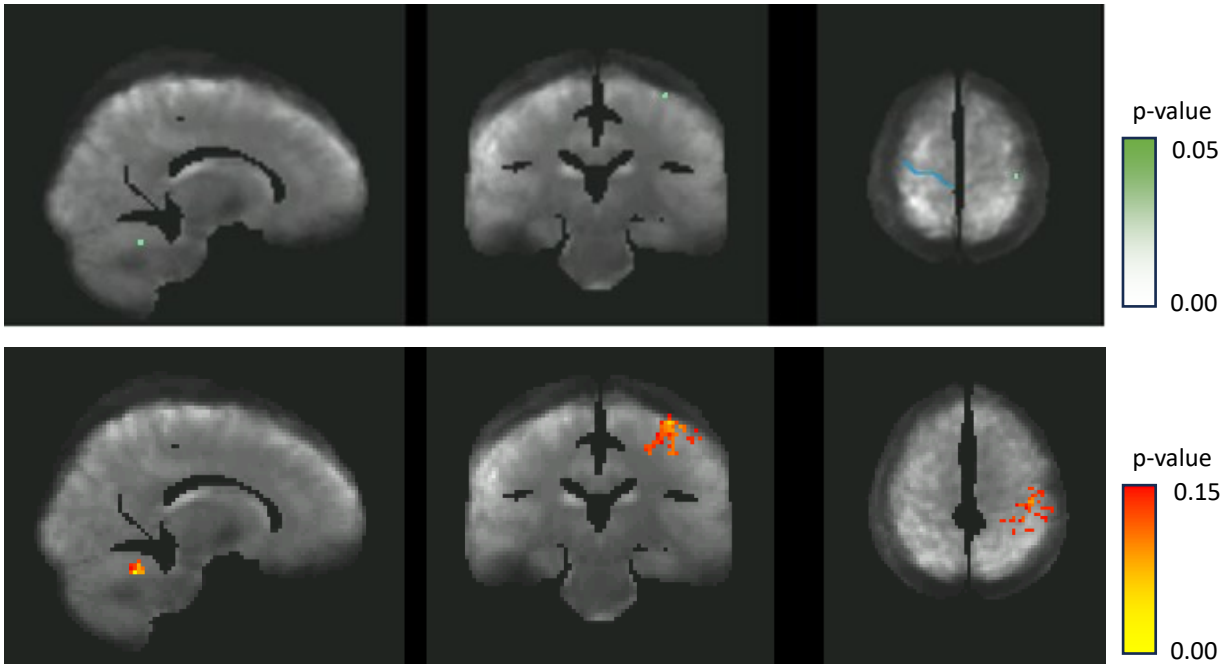

Figure 7.11: Group-level functional activation in response to the motor component of the model, with α < 0.05 (top) and α < 0.15 (bottom). On the axial view in the top right, the right central sulcus is delineated in blue for reference. A single voxel of activation (p < 0.05) is seen overlying the left central sulcus. In the bottom figure, clusters of activation are seen in the left sensorimotor cortex and right cerebellar hemisphere, as expected from a right-handed task.

No statistically significant clusters of activation are demonstrated in the brain for the blood pressure or the sensory contrast. There are two tiny clusters of a few voxels in volume within the left cerebellar hemisphere with a p-value of up to 0.81 for the sensory contrast, but none in the left sensory cortex, which is at least somewhat reassuring that the sensory component of the task is not likely to be a significant confound.

When this same analysis was limited to the brainstem, no statistically significant clusters of activation were demonstrated for any of the three contrasts. Furthermore, there were no statistically significant differences in brain activity pre- and post-sedation in response to any of the three components of the model, even when the analysis was limited to the brainstem.

7.4. Discussion

7.4.1. Locus coeruleus segmentation and contrast-to-noise

The LC was visible on a MT-weighted acquisition in all 5 participants. However, its boundaries are not well defined, and contrast is low compared to surrounding brainstem parenchyma, making reproducible volume measurements impossible. It is unlikely that accurate longitudinal evaluation of LC CNR is possible using the MT-weighted sequence utilised here. However, there is sufficient contrast to enable segmentation of the LC for it to serve as an anatomical localiser for functional connectivity analysis. There are examples from previous structural imaging studies of the LC which subjectively appear to demonstrate higher signal in the LC compared to the results we present in figure 7.3 (Chen 2014), (Mather 2017). The data in this chapter were acquired at a higher magnetic field strength than the majority of previous studies, which mostly used 3T MRI (Liu 2017). We might therefore expect the higher SNR and CNR conferred by 7T to translate into improved visualisation of the LC. However, these previous studies at 3T all used a much larger voxel size than the sequence used in this chapter. Liu et al. reviewed 28 structural MRI studies of the LC (Liu 2017). The minimum reported slice thickness was 2.5 mm and minimum in-plane resolution 0.31 x 0.36 mm, compared with 0.5 x 0.43 x 0.43 mm here. We sacrificed SNR and CNR to increase spatial resolution and maximise the accuracy of the LC anatomical localiser segmented from the MT data. Future studies at 7T might consider increasing slice thickness to improve LC contrast, especially if the aim is to assess LC neuromelanin content. However, this would be at the expense of anatomical accuracy, which might confound functional connectivity assessment.

7.4.2. Locus coeruleus ALFF and fALFF

Median ALFF and fALFF in the left and right LC were compared before and after sedation. As previously discussed, dexmedetomidine suppresses noradrenergic activity in the locus coeruleus. Therefore, following its administration, neuronal, and subsequently haemodynamic, activity in the LC is reduced. We therefore hypothesised a reduction in both ALFF and fALFF after dexmedetomidine administration. There was no significant difference in

ALFF or fALFF pre- and post-sedation, which is not unexpected given the low sample size. Figure 7.6 suggests that ALFF might be (non-significantly) lower post-sedation, but figure 7.7 does not demonstrate a consistent pattern between the right and left LC for fALFF. As discussed in previous chapters, the fractional correction to ALFF suppresses noise contributions. It is possible that in a state of mild-to-moderate sedation, physiological noise in the vicinity of the brainstem is reduced (a lower heart rate will lead to less noise from pulsatility of the vertebrobasilar arteries, and a lower respiratory rate will reduce the magnitude and frequency of fluctuations in the static magnetic field at the skull base). In the absence of the fractional correction, ALFF might be lower after sedation not because of reduced activity in the LC, but because of lower physiological noise contributions. Correlating ALFF with fractionally corrected ALFF is therefore especially important in the subsequent full study, to try and disentangle real differences in LC activity pre- and post-sedation from differences in noise contributions.

Based on the effect size of dexmedetomidine on ALFF and fALFF from tables 7.3 and 7.4, a power calculation was performed using the software package G*power (Faul 2007). Optimistically, the largest effect size of 0.3 was used. Based on the results of this pilot study, the sample size required to achieve a power of 0.8 with a type-II error probability of 0.05 in relation to detecting a significant difference in mean LC ALFF pre- and post-sedation is 90 participants. Whilst it is not certain that dexmedetomidine will have a similarly small effect size on functional connectivity between different parts of the brain, this does reinforce the importance of ensuring that data collection and analysis is optimised as much as possible, to maximise any possibility of detecting statistically significant differences in functional brain activity pre- and post-sedation in any future full study.

7.4.3. Resting-state state functional connectivity of the locus coeruleus

When all 10 datasets were analysed together, widespread clusters of significant functional activity that correlate with the resting-state timeseries of the left and right locus coeruleus were demonstrated throughout the cerebral and cerebellar hemispheres, as well as the brainstem. Clusters of activation are seen that overlap several of the autonomic regions that send and receive projections from the LC, including the DMV, NA, CR, RVLM and

hypothalamus. Because there is such widespread activation, it is very difficult to make any specific inference about connectivity between different autonomic centres from these SCA maps. There is no discernible symmetry between the activation maps for the left and right LC. In fact, unexpectedly, functional connectivity of the right LC is much sparser than the left (figures 7.8 and 7.9). The reason for this is unclear. This was a healthy group of young males, therefore there is no reason to suspect any underlying pathology. The resting-state acquisition was performed at the start of the study session so there should not be any residual confound from task-based fMRI acquisitions. In a full study, careful assessment for patterns of symmetry between the left and right LC functional connectivity maps should be performed, to help validate that connectivity maps are a true representation of a temporal correlation between neuronal activity in different parts of the brain, rather than being driven by noise.

We have demonstrated the feasibility of mapping resting-state functional connectivity of the LC using a within-subject LC localiser. However, there was no significant difference in the whole-brain or brainstem connectivity maps pre- and post-sedation. This is not entirely unexpected given the small sample size in this pilot study. However, the small effect size of dexmedetomidine on LC ALFF and fALFF (magnitude of Cohen's d between 0.14 and 0.3), and the corresponding sample size estimate of 90 participants required to achieve a statistical power of 0.8, raises the possibility that a similarly large sample size is required to detect any meaningful differences in connectivity after sedative administration.

7.4.4. Functional activity in response to blood pressure perturbation

In response to the motor component of the model depicted in figure 7.2, clusters of activity were demonstrated in the left sensorimotor cortex, left thalamus and right cerebellum, but apart from a single voxel overlying the left central sulcus and in the right cerebellar hemisphere, these did not reach the threshold for statistical significance, probably due to the small sample size. The sensorimotor component of the task will serve as useful way of validating that the task has elicited a functional response within each participant. No significant clusters of activation were demonstrated in response to the blood pressure or sensory (cuff-inflation) components of the model in this small sample. Increasing the sample

size in the full study will improve the likelihood of detecting activation in response to systemic blood pressure perturbation, and of detecting differences in functional activity after dexmedetomidine administration, with the same caveats that follow the ALFF power calculation previously discussed.

7.4.5. Limitations

We attempted to define the position of the LC within each subject by manually segmenting the LC on a MT-weighted acquisition. This does improve localisation accuracy of the LC compared to using a generic LC atlas (figure 7.4), but it was not possible to identify the LC with sufficient confidence to accurately measure its volume. Robust longitudinal measurement of MT contrast as a surrogate for LC neuromelanin concentration is unlikely to be possible using the current sequence.

No significant activation in response to the blood pressure model was detected. This could be because this pilot study is underpowered. However, there are potential methodological issues which may also be contributing. The blood pressure model applied might not be accurate enough. Blood pressure variation during the fMRI acquisitions was modelled by interpolating between each 1-minute blood pressure reading. Continuous blood pressure monitoring within the scanner might improve this, and was piloted outside the scanner, but found to be unreliable due to its sensitivity to participant motion, and not in agreement with sphygmomanometer readings. Because of the relatively slow temporal fluctuation of blood pressure, no high-pass temporal filtering of the task-based fMRI data was performed, and therefore scanner drift may confound the results.

The major limitations involved in this study are due to the inherent challenges associated with functional MRI of the brainstem. Achieving sufficient signal-to-noise (SNR) and thus spatial resolution to image the sub-millimetre internal architecture of the brainstem is difficult (Sclocco 2017). Efforts were made to optimise the BOLD-EPI sequence to ensure maximal spatial resolution, for example by using multiband to maximise SNR without sacrificing spatial resolution or prolonging acquisition time. However, the voxel size of 1.5 mm^3 is of the order of the size of the locus coeruleus (Liu 2017). Therefore, partial voluming

of brainstem parenchyma is inevitable at the edges of the LC. Of greater concern, because of the position of the LC close to the dorsal edge of the brainstem, there is a significant risk of partial voluming of CSF into LC masks. The slightest co-registration inaccuracy will further compound this. Inaccurate co-registration of even a single millimetre could result in the LC mask, originally segmented in the space of the MT-weighted acquisition, overlying a CSF space when co-registered to MNI-space (this was found to occur when attempting to co-register the generic LC atlas to MNI-space, as demonstrated in figure 7.4). The use of anatomical atlases or masks is also reliant on accurate co-registration. Subtle variations in brainstem size or internal architecture between participants might mean that anatomical atlases are not aligned with the true location of brainstem nuclei, even with good co-registration to a common anatomical space.

The brainstem's caudal location places it away from the elements of typical MRI receiver head coils, further compromising SNR. Spatial smoothing is a commonly used post-processing technique which can increase SNR. However, care must be taken when applying this to the brainstem to avoid mixing signal from extra-axial structures such as CSF and blood vessels with brainstem signal. Only minimal smoothing was applied in this study, and only after removing CSF spaces around the brainstem. The susceptibility-induced gradient in the static magnetic field of the scanner caused by air-tissue interfaces in the nearby paranasal sinuses causes distortions and signal drop out (Glover 2001). Gradient-echo echo planar imaging (GE-EPI) is almost ubiquitous for BOLD fMRI, but it is especially vulnerable to such artefacts (Brooks 2013). We attempted to minimise such artefacts by using parallel imaging, which reduces image acquisition time and susceptibility-induced distortion (Brooks 2013). However, signal dropout and distortion were still seen at the ventral surface of the pons across most of the GRE-EPI acquisitions and is visible in figures 7.8 – 7.10 above.

The brainstem is especially subject to physiological noise. The change in the volume and position of the lungs during respiration causes fluctuations in the static magnetic field present at the brainstem (Raj 2000). This causes misregistration of MRI signal and subsequent anatomic distortion. This effect decreases with the cube of the distance from the lungs, and therefore the brainstem is more strongly affected than the cerebral hemispheres (Sclocco 2017). Head movement, physiological tissue displacements due to pressure pulsations from the adjacent vertebrobasilar artery or CSF pulsation can cause BOLD artefacts (Sweetman

2010), (Beissner 2015). The brainstem is especially vulnerable to physiological pulsations; motion of structures across the cardiac cycle are of the order of 0.5 mm close to the brainstem compared to 0.05 mm in the cerebral cortex (Harvey 2008), (Enzmann 1992).

Moving towards higher static magnetic fields can increase SNR which can be traded for an increase in spatial resolution which is necessary to better resolve brainstem nuclei. However, the stronger static magnetic field may introduce problems of its own. These include less uniform transmit and receive radiofrequency fields (Ladd 2018), stronger field gradients at air-tissue interfaces exacerbating susceptibility-induced artefacts (Ladd 2018), (Oliveira 2021), and increased soft tissue energy deposition (Oliveira 2021) associated with the higher Larmor frequency. Furthermore, physiological noise is proportional to the square of the magnetic field strength (Brooks 2013). Physiological parameters including heart and respiratory rate, $ETCO_2$ and ETO_2 were recorded using physiological monitoring and a retrospective correction applied (Glover 2000), Alternatively, physiological noise can be addressed prospectively using navigator methods which track brain motion during the MRI acquisition (Hu 1994) or through cardiac gating (Beissner 2015), or via data driven methods based on the spatio-temporal characteristics of physiological noise (Brooks 2013). A brainstem mask was applied to remove areas of high physiological noise such as the surrounding CSF and vascular spaces, and this can also improve sensitivity to detect functional activity (Beissner 2014), but it is impossible to fully correct for variance in the BOLD-EPI signal introduced by non-physiological sources.

Whilst we were able to demonstrate widespread functional connectivity of the LC, it will be difficult to make specific inferences about connectivity with small subcortical and brainstem nuclei. An alternative approach to SCA is node-based connectivity, which studies the correlation between timeseries from predefined nodes. In theory this might enable more specific assessment of connectivity between the components of the central autonomic network that send and receive projections to the LC. However, whilst we can accurately localise the LC using an MT-weighted acquisition, there is no way of precisely localising the other nodes in the network. As demonstrated in figure 7.4, it is not always possible to accurately localise small structures using a generic atlas. In the absence of a robust and accurate method of localising each component of the central autonomic network within each

participant, accurate analysis of node-based connectivity of the central autonomic network is impossible.

Given the challenges involved in brainstem functional imaging, in a full study it might be beneficial to include an additional method of validating that our methodology is capable of detecting task-based functional activity in the brainstem. Faull et al. (Faull 2015) have previously used a finger opposition task to demonstrate functional activation in the cuneate nucleus of the medulla, where ascending dorsal-column axons that carry proprioception and fine-touch sensory information synapse with second-order neurons that decussate and project to the contralateral thalamus. A form of this task could be inserted into the six-minute rest period preceding the ischaemic-handgrip task.

7.5. Conclusion

A MT-weighted sequence was successfully used to produce within-subject anatomical localiser of the locus coeruleus. However, the edges of the LC are not sufficiently well defined to accurately measure its volume, or to enable longitudinal assessment of contrast-to-noise. The within-subject localiser was used to demonstrate widespread areas of resting-state functional connectivity of the LC throughout the brain, but making inferences about connectivity between specific components of the autonomic nervous system difficult given the widespread connectivity with the LC demonstrated on figure 7.8, especially in the absence of any functional response to a task designed to perturb systemic blood pressure. A much larger sample size is required to achieve sufficient power to detect significant differences in ALFF/fALFF in the LC between sedation states. Given the inherent challenges associated with brainstem functional MRI, a much larger sample size may ultimately be required to achieve sufficient sensitivity to study functional activation and connectivity of the LC.

General discussion

8.1. Development of methods

The overall aim of this thesis was to validate, optimise and apply MRI-based methods of quantifying human cerebrovascular function, which may then be used in future studies of brainstem haemodynamics, specifically to further investigate the selfish brain mechanism. Arterial spin labelling can be used to generate whole-brain perfusion maps without the need for an exogenous contrast agent, but the accuracy of CBF values derived from ASL measurements and the sensitivity of those measurements is dependent on careful optimisation of ASL pulse sequence parameters. This is especially true when it comes to the brainstem, as discussed in section 2.1. In chapter 2 using an ASL sequence we demonstrated the feasibility of measuring CBF and CVR within subregions of the brainstem (the midbrain, pons and medulla). The ASL sequence was tailored to maximise brainstem SNR and minimise potentially confounding effects such as inefficient labelling (addressed by using a PC-MRA acquisition to place the labelling plane perpendicular to the vertebral arteries) and arterial transit artefacts (addressed by tailoring the post-label delay according to the brainstem arterial transit time). ASL and BOLD CVR values agreed with values previously quoted in the literature. However, the inherent limitations of ASL are highlighted by the unexpected apparent reduction in brainstem CBF during hypercapnia that was demonstrated in one out of ten participants. The cause of this potentially erroneous measurement is uncertain but is likely related to one of the many challenges associated with brainstem ASL that were discussed in section 2.1. The variation across participants in CVR values is also much higher using ASL than BOLD (figures 2.11 and 2.13). Therefore, whilst it is possible to have confidence in group-level brainstem CVR values using ASL, ASL-CVR may not be robust enough to obtain reliable values within every individual. BOLD-CVR appears to be more robust, the downside being the lack of specificity of the BOLD signal and the inability to obtain quantitative measurements using BOLD. Future studies of brainstem haemodynamics should take every care to tailor ASL sequence parameters and post-processing methods to maximise the likelihood of obtaining reliable brainstem CBF and CVR measurements. The

outcomes of the chapter pave the way for future studies to elucidate the relationship between regional brainstem haemodynamics and systemic hypertension.

Another critical component of applying any functional or structural MRI method to the brainstem is that the data processing pipeline must be thorough and robust. Generic post-processing methods are not always sufficiently accurate when it comes to brainstem MRI. Image co-registration is a critical component of any MRI pre-processing analysis pipeline, but especially important when studying small structures such as the brainstem. In chapter 4, machine learning was successfully applied to facilitate accurate brainstem co-registration. This method could be applied to large datasets with minimal user input, and the convolutional neural network developed could potentially be re-trained to facilitate accurate co-registration of other structures in the brain.

Another challenge inherent to brainstem MRI is the relatively low SNR in the vicinity of the brainstem, and the subsequent impact this has on the statistical power of brainstem ASL methods. To overcome this, efforts were made in chapter 6 to validate ALFF and fALFF, derived from resting-state BOLD data, as metrics of CVR. This might facilitate the use of data from large repositories such as UK Biobank to study the association between variations in CVR and various physiological and pathophysiological parameters, as well as obviating the need for a vasoactive stimulus and physiological monitoring when studying CVR, which would be especially useful in the clinical setting. It was not possible to confirm ALFF or fALFF as a metric of CVR. The variable impact of noise on the ALFF/fALFF measurement across the brain, the multifactorial nature of the BOLD signal, and the relatively small sample size are all potential confounds. ALFF and fractional ALFF are unlikely to be a reliable metrics of CVR. Our analysis of the regional distribution of fALFF within individual participants was also consistent with this, and it seems unlikely that fALFF can be used to map regional CVR with enough accuracy to be clinically useful. Further large-scale studies, as well as detailed investigation of the impact of confounds such as physiological noise, are required.

The outcomes of chapter 7 further underline the low signal to noise regimes inherent in functional MRI when imaging the brainstem at high resolution. The feasibility of mapping functional connectivity of the locus coeruleus using an anatomical localiser derived from a MT-weighted acquisition was successfully demonstrated. However, power calculations based on the effect size of dexmedetomidine on ALFF and fALFF highlighted the importance of a

sample size to achieve sufficient power to detect any significant between-group differences in functional activity.

8.2. Evidence to support the selfish brain mechanism

The thesis also aimed to apply some of the above methods to existing data to study the selfish brain mechanism as a potential cause of hypertension. As discussed in chapter 3, previous work has demonstrated an increased prevalence of VAH in hypertensives compared to normotensives (Warnert 2016), as well as a statistically significant difference in whole-brain CBF between those with and without VAH, but only in the presence of hypertension. There is also some evidence tentatively suggesting that locally impaired cerebrovascular function and CBF in parts of the central autonomic network, such as the medulla, could serve as a trigger for systemic hypertension (Meglic 2001), (Waki 2011), (Waki 2014). In light of this, pre-existing data were revisited to investigate whether there is an association between VAH and regional CBF in the brainstem and other cortical centres involved in autonomic regulation of the cardiovascular system, and to determine whether this association (if any) varies according to blood pressure status. We hypothesised that hypertensives with VAH would demonstrate hypoperfusion in the posterior circulation and brainstem relative to the anterior circulation. Contrary to expectations, mean CBF across the ROIs, which included the brainstem, cortical regions involved in the central autonomic network, and cortical grey matter, is higher in participants with VAH compared to those without VAH, but this relationship is only statistically significant in normotensives. This finding is unexpected and contrary to our hypothesis that VAH negatively affects CBF, but there is some uncertainty in the data and limitations to the analysis, not least the fact that the ASL sequence was not specifically optimised to obtain accurate brainstem CBF measurements. In the presence of VAH, mean CBF is significantly lower in untreated hypertensives compared to normotensives and treated hypertensives. This suggests that treatment of hypertension is beneficial to CBF, which is also somewhat contrary to the selfish brain mechanism (we would expect removal of hypertension as a compensatory mechanism to reduce CBF in treated hypertensives). There is no evidence of a significant difference between posterior and anterior circulation CBF according to VAH or blood pressure status, and therefore we cannot reject the null hypothesis that there is no association between regional CBF, VAH and hypertension. However, because

of the physiological complexity of blood pressure homeostasis there are several possible explanations for this, including the possibility of compensatory CBF to the posterior circulation via the circle of Willis/secondary to the selfish brain mechanism, or vertebral artery narrowing being a result of rather than cause of hypertension. The only way to clarify the relationship (if any) between these three variables of interest is through a longitudinal study using methods tailored to the brainstem, which identifies participants with VAH at a young age and follows them through to adulthood to elucidate the temporal relationship between VAH, CBF and hypertension.

ASL data from the UK Biobank repository was explored in chapter 5 to investigate whether CBF and AAT in the medulla and other parts of the central autonomic network are differentially affected in hypertensives. Resting-state BOLD fMRI data were also used to derive ALFF (with a fractional correction to address physiological noise contributions – fractional ALFF or fALFF). A statistically significant, but extremely small, difference in mean fALFF across all ROIs between hypertensives and normotensives was found. However, the regional variation in fALFF does not vary between hypertensives and normotensives. Mean CBF across all the ROIs under consideration was found to be lower in hypertensives, but there was no significant difference in arrival time between the two groups. Our analysis does not therefore support the hypothesis that the selfish brain mechanism is driven by local haemodynamic impairment to parts of the brain involved in cardiovascular autonomic regulation. The principal limitations attached to this analysis are the relatively small number of available ASL datasets, and once again the lack of MRI sequences specifically tailored towards studying the brainstem. The utility of fALFF as a metric of CVR is also uncertain, as discussed above, and this led to the investigation in chapter 6 of the validity of using fALFF as a surrogate marker of CVR.

8.3. Future prospects

ASL is already widely applied in research as well as in the clinical setting. The outcomes of chapter 2 demonstrate that regional measurement of brainstem CBF is feasible using ASL provided an appropriately tailored ASL pulse sequence and robust data processing methods are used. The convolutional neural network developed in chapter 4 to achieve accurate co-registration of functional and structural data could potentially form part of a data

processing pipeline, in conjunction with the ASL sequence optimised in chapter 2, facilitating further research of brainstem haemodynamics using MRI. CVR is also widely used in research, but less so clinically, possibly due to the additional technical demands associated with administering a vasoactive stimulus and monitoring of physiological parameters required to derive CVR measurements. There is no robust within-participant correlation between regional fALFF and regional ASL CVR, and neither ALFF nor fALFF account for a large enough proportion of the resting-state BOLD signal to facilitate their use as surrogate CVR measurements.

The thesis has not yielded any further evidence supportive of the selfish brain mechanism as a cause of essential hypertension. As discussed in the introductory chapter, the homeostasis of the cardiovascular system is complex, involving several interlinked physiological mechanisms, of which the autonomic nervous system is only one. Isolating the contribution of the autonomic nervous system to the development of hypertension is therefore challenging. Future studies could attempt to assess brainstem perfusion together with measurement of autonomic activity via methods such as peripheral microneurography, which have previously been used in this context (Hart 2016). It remains conceivable that the selfish brain mechanism plays a role in the development of essential hypertension, but that it might be only one of several interlinked factors driving a pathological increase in systemic blood pressure. It is possible that essential hypertension is not due to a single disease process, but rather due to a combination of pathologies related to one or more of the many components that regulate systemic blood pressure. Another hurdle to overcome in studying the selfish brain mechanism, and the cause of many of the challenges in this thesis, is that some of the principal components of the autonomic nervous system that modulate systemic blood pressure are located in an especially difficult part of the brain to study. As demonstrated in this thesis, evaluation of regional brainstem haemodynamics using MRI is possible, but only with careful optimisation of the methods used to acquire and process the data.

8.4. Conclusion

The complexity of homeostatic regulation of systemic blood pressure, and the challenges inherent to brainstem MRI, make the study of the selfish brain mechanism challenging. The assessment of regional brainstem haemodynamics, specifically CBF and CVR, are possible using the functional MRI techniques that were optimised in this thesis. In addition to sequence optimisation, careful post-processing is also essential, and methods such as co-registration facilitated by machine-learning may be beneficial, especially to facilitate efficient data analysis in large studies. The methods developed here might facilitate a larger longitudinal study of a hypertensive population, to further elucidate the relationship between brainstem haemodynamics and systemic blood pressure.

Appendix 1 – Summary of study protocol 'Investigating the control of cerebral blood flow in hypertensives using MRI'.

Purpose of project and its academic rationale

Hypertension is a leading global risk factor for multiple causes of morbidity and mortality including stroke, myocardial infarction, chronic kidney disease, cognitive decline and premature death (NICE 2011). Despite this, in the majority of cases the aetiology is poorly understood (Oparil 2018).

Harvey Cushing's early experimental work with animals suggested that systemic blood pressure increases in response to a reduction in cerebral blood flow (Hart 2016). Since then, further studies have demonstrated that in hypertensives there is an association between vascular anatomical variations in the posterior cerebral circulation and a reduction in cerebral blood flow, as well as an increase in cerebrovascular resistance (Warnert 2016), (Alosoco 2014). The association between elevated sympathetic nerve activity (SNA) and hypertension is established (Hart 2016), (Grassi 2016). The rostral ventrolateral medulla (RVLM) is a physiological control centre situated in the medulla and is an important source of excitatory sympathetic input to the cardiovascular system (Lunblad 2014). It is believed to play a central role in the generation of basal sympathetic tone (Feldman 2013). Cushing's hypothesis therefore proposes that if there is an impairment in blood flow to the brain, a compensatory increase in sympathetic activity in brainstem autonomic centres, including the brainstem, drives an increase in systemic blood pressure, thus restoring cerebral perfusion back towards normal levels. This mechanism may be important in the aetiology of essential hypertension.

Cerebrovascular reactivity (CVR) represents the capacity of cerebral blood vessels to dilate in response to a stimulus. Measurement of CVR provides information on the functional reserve of the vascular system and is an important marker of the health of the cerebrovascular system. Impaired CVR has been associated with many diseases, including stroke and TIA (Markus 2002), and multiple sclerosis (Marshall 2014).

Induced hypercapnia (elevated arterial partial pressure of carbon dioxide) is routinely used as a vasodilator in MRI studies of CVR (Fisher 2016), (Whittaker 2016). When the arterial partial pressure of carbon dioxide ($PaCO_2$) increases, CO_2 diffuses across the blood brain

barrier and reduces the pH of the interstitial compartment (Willie 2014), (Liu 2019). This is thought to cause hyper-polarisation of smooth muscle and endothelial cells, resulting in smooth muscle relaxation and an increase in the release of endothelial factors such as nitric oxide. The end result is vasodilation and an increase in blood flow. The cerebral blood flow (CBF) response to induced hypercapnia can therefore be used as a measure of cerebrovascular reactivity.

Previous work using arterial spin labelling (ASL) to measure cerebral blood flow has found that, after accounting for stroke and white matter hyperintensity volume, hypertensive participants had lower global vasoreactivity (Hajjar 2010). Transcranial Doppler ultrasound studies of the cerebral blood flow response to hypercapnia have also previously demonstrated an impaired CVR in hypertensives compared to normotensives (Ostrovskaya 2015), (Maeda 1994). Only a small number of studies have investigated the effects of antihypertensive medications on CBF and CVR, with equivocal results, and there is a lack of studies that have focused specifically on hypertensive patients (Webb 2019).

With increasing age, there are inevitably an increasing number of confounding factors such as multiple comorbidities and polypharmacy. In addition, there is evidence that β-receptor mediated vasodilation protects premenopausal women from the vasoconstrictor effects of noradrenaline released from sympathetic nerve terminals (Hart 2011). For these reasons, the study will focus on young untreated hypertensive males.

In this study, arterial spin labelling and blood oxygen level dependent MRI will be used to measure regional cerebral blood flow and functional activity. Arterial spin labelling MRI is able to map cerebral blood flow without the use of injected contrast agents. Participants will be asked to breath an increased concentration of carbon dioxide for a period during scanning. The change in CBF and/or BOLD signal compared to normocapnic baseline will be used to measure CVR. Regional CVR and CBF will be compared between a cohort of young hypertensive male patients and a matched healthy control group, in order to investigate whether brainstem vascular reactivity is impaired in young hypertensives. The effect on CVR and CBF of treatment with anti-hypertensive medication will also be investigated in the hypertensive group.

Project Summary

Planned start date	May 2020
Study Design	Cross sectional. structural and functional MRI scanning with administration of a hypercapnic challenge.
Study Participants	Male hypertensive volunteers plus healthy volunteers
Planned Sample Size	Approximately 20 hypertensives and 20 healthy controls
Planned Study Period	12 months
Project Aim	The overall aim of the study is to investigate differences in regional brainstem and cortical CBF and CVR between hypertensives and healthy controls. Furthermore, we will also investigate the effect of a period of treatment with anti-hypertensive medication on CBF and CVR in the hypertensive cohort.
Primary Objectives	Compare regional CVR and CBF between hypertensives and healthy controls. Compare regional CVR and CBF before and after a period of antihypertensive treatment.

Inclusion criteria

1. (Hypertensive cohort) Diagnosed as hypertensive (systolic blood pressure (SBP) > 140 and/or diastolic blood pressure (DBP) > 90 mmHg on office measurement or SBP > 135 and/or DBP > 90 on 24 hour ambulatory blood pressure (ABPM) / home BP monitoring).
2. Secondary causes of hypertension excluded (labelled as idiopathic/essential hypertension).
3. Less than 40 years old.

4. Male.
5. BMI < 30.
6. (Hypertensive cohorot) untreated hypertension (not yet commenced on any anti-hypertensive medication or willing to undergo a period without antihypertensive treatment, provided this is deemed safe)
7. (Hypertensive cohort) planned to commence on antihypertensive treatment in the near future (within a few months of initially being scanned).

Exclusion criteria

1. SBP >180 and/or DBP > 120
2. Any self-reported physical or psychiatric condition that would prohibit the participant from completing the full study (including rest angina, shortness of breath at rest, dizziness, epilepsy and/or any psychiatric condition that affects the ability to comprehend verbal or written instructions)
3. Currently actively involved in any interventional trial (i.e. have begun the intervention) or within four weeks of completing an interventional trial
4. MRI contraindications (e.g. a pacemaker) as established using CUBRIC's standard screening procedures.
5. Any known neurological condition / abnormality relevant to the study
6. Currently experiencing dizziness or fainting on a regular basis.
7. Type 1 or Type 2 Diabetes Mellitus
8. Illicit drug use in the last 4 weeks
9. Any absolute contraindication to hypercapnic stimulus, including:
    i. Obstructive or resistive lung disease with PaCO2 at rest greater than 50mmHg or venous bicarbonate greater than 26 mEq/L.
    ii. Pre-existing respiratory acidosis.
    iii. Requiring portable oxygen at rest or with exercise.
    iv. Chronic heart failure or severe pulmonary disease and unable to climb one flight of stairs due to shortness of breath.

v. Severe heart failure or restrictive lung disease with resting respiratory rate over 15 breaths/min.

Appendix 2 – Inclusion and exclusion criteria - Development of non-invasive measurements of regional brainstem CVR

Inclusion criteria:

- In good health, with no significant cardiovascular or respiratory disease.
- Aged 18-60 years old.
- Able to understand and communicate in spoken English (for consent purposes and behavioural testing).
- Not taking any medications that may alter cerebrovascular function, cerebral blood flow, or central noradrenergic activity, or which may confound the measurement of CVR.
- No respiratory disease (asthma/COPD/obstructive sleep apnoea etc) which may preclude the use of the Respiract Gas Delivery System.

Exclusion criteria:

- Any self-reported physical or psychiatric condition that would prohibit the participant from completing the full study (including rest angina, hypotension or hypertension, shortness of breath at rest, dizziness, epilepsy and/or any psychiatric condition that affects the ability to comprehend verbal or written instructions).
- Currently actively involved in any interventional trial (i.e. have begun the intervention) or within four weeks of completing an interventional trial.
- MRI contraindications (e.g. a pacemaker) as established using CUBRIC's standard screening procedures.
- Any known neurological condition / abnormality.
- Pregnancy or childbirth in the last 6 weeks.
- Current and/or history within the past two years of cardiac (heart), vascular (blood vessel) or respiratory/pulmonary (breathing/lung) conditions, including high blood pressure, asthma.
- Currently experiencing dizziness or fainting on a regular basis.
- Type 1 or Type 2 Diabetes Mellitus.
- Illicit drug use in the last 4 weeks.

Appendix 3 – Inclusion and exclusion criteria - Vertebral artery hypoplasia and brainstem blood flow in patients with hypertension

Inclusion criteria:

- Aged 18 – 75 years old.
- No history of diabetes.

Exclusion criteria:

- Significant cardiovascular/respiratory disease (e.g. heart failure, conduction abnormalities such as atrial fibrillation, emphysema).
- Receiving treatment for cancer.
- Pregnancy.
- Body mass index >30 kg/m^2.
- MRI contraindications such as implanted magnetic devices

Appendix 4

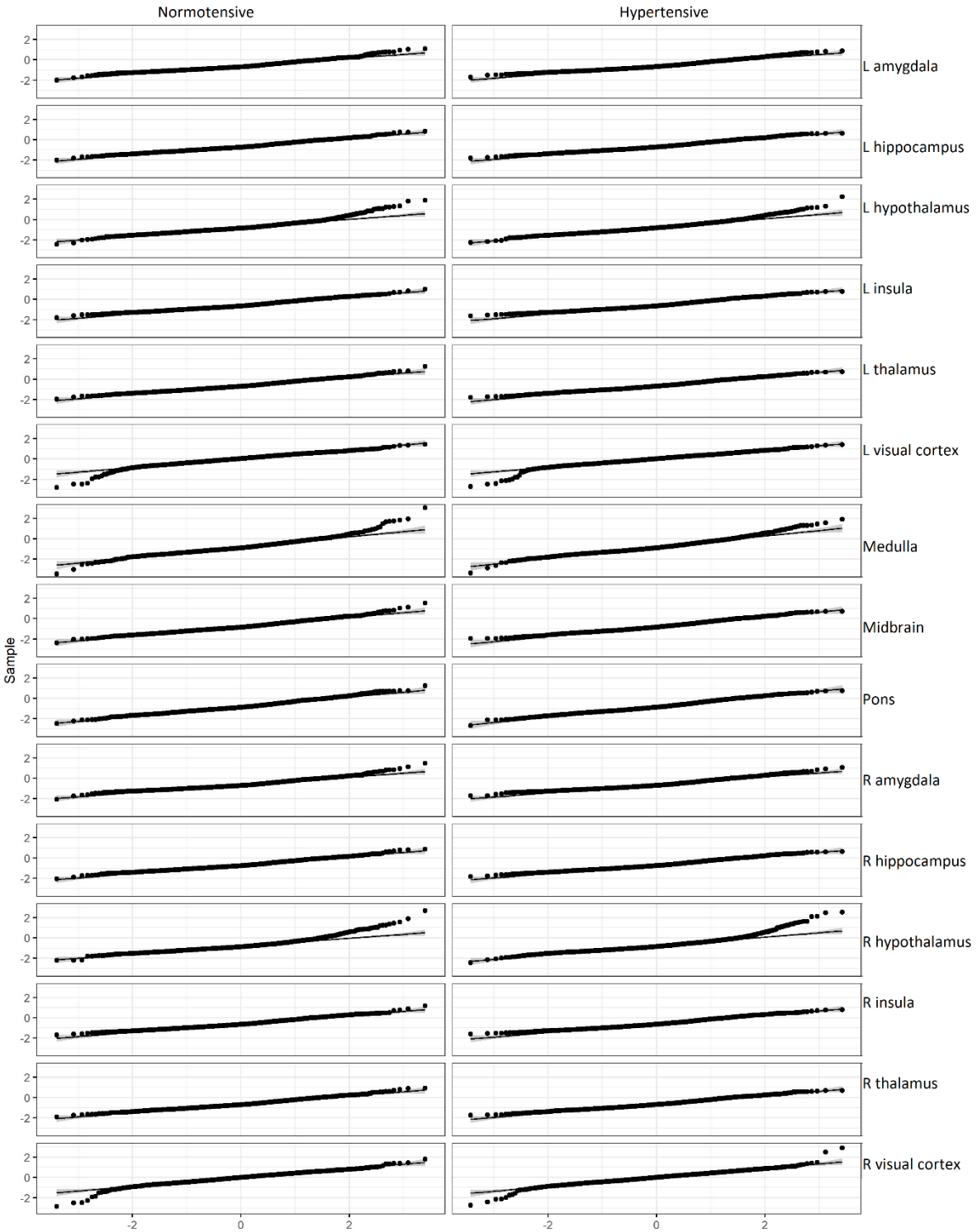

Figure 5.10: Q-Q plots of fALFF grouped by region and blood pressure status reveals that there is some deviation from normality in the distribution of fALFF values in some of the groups. However, the majority of fALFF values conform to a normal distribution. ANCOVA is robust against deviations from normality for large samples (Statology 2023).

Appendix 5

Table 5.5: Summary of mean and standard deviation of fALFF z-scores for all regions in normotensives and hypertensives. The ratio of the largest to smallest standard deviation is 1.46 (Statistics How To 2023). The data is therefore homoscedastic. Regardless, ANCOVA is robust against violations of the assumption of homogeneity of variance as long as group sizes are equal (equal group sizes being defined as: ratio of the largest to smallest group < 1.5 (Statistics Solutions 2023).

BP group	Region	Mean fALFF z-score	SD fALFF z-score
Normotension	L amygdala	-0.622	0.394
Hypertension	L amygdala	-0.607	0.395
Normotension	L hippocampus	-0.687	0.404
Hypertension	L_hippocampus	-0.677	0.409
Normotension	L hypothalamus	-0.787	0.474
Hypertension	L hypothalamus	-0.774	0.478
Normotension	L insula	-0.599	0.404
Hypertension	L insula	-0.589	0.419
Normotension	L thalamus	-0.659	0.419
Hypertension	L thalamus	-0.652	0.422
Normotension	L visual cortex	0.022	0.45
Hypertension	L visual cortex	0.006	0.439
Normotension	Medulla	-0.824	0.573
Hypertension	Medulla	-0.812	0.577
Normotension	Midbrain	-0.788	0.47
Hypertension	Midbrain	-0.785	0.469
Normotension	Pons	-0.813	0.493
Hypertension	Pons	-0.808	0.501
Normotension	R amygdala	-0.643	0.396
Hypertension	R amygdala	-0.632	0.402
Normotension	R hippocampus	-0.691	0.408
Hypertension	R hippocampus	-0.684	0.412
Normotension	R hypothalamus	-0.779	0.501
Hypertension	R hypothalamus	-0.766	0.518
Normotension	R insula	-0.601	0.404
Hypertension	R insula	-0.593	0.415
Normotension	R thalamus	-0.654	0.414
Hypertension	R thalamus	-0.646	0.418
Normotension	R visual cortex	-0.027	0.458
Hypertension	R visual cortex	-0.011	0.461

Appendix 6

Table 6.1: Correlation between brainstem ALFF and brainstem ASL CVR by frequency range

FREQUENCY RANGE	STATISTIC	P VALUE	SPEARMAN'S RHO
0-0.0125	776	0.854	0.049
0-0.0156	814	0.996	0.002
0-0.0195	830	0.951	-0.017
0-0.02441	796	0.928	0.025
0-0.03051	798	0.936	0.022
0-0.03814	796	0.928	0.025
0-0.04768	824	0.974	-0.010
0-0.05960	822	0.981	-0.007
0-0.07450	824	0.974	-0.010
0-0.09313	798	0.936	0.022
0-0.11641	792	0.913	0.029
0-0.14551	782	0.876	0.042
0-0.18189	826	0.966	-0.012
0-0.22737	828	0.959	-0.015
0-0.28421	802	0.951	0.017
0.0125-0.0156	836	0.928	-0.025
0.0125-0.0195	854	0.861	-0.047
0.0125-0.02441	814	0.996	0.002
0.0125-0.03051	866	0.817	-0.061
0.0125-0.03814	848	0.883	-0.039
0.0125-0.04768	850	0.876	-0.042
0.0125-0.05960	814	0.996	0.002
0.0125-0.07450	790	0.906	0.032
0.0125-0.09313	812	0.989	0.005
0.0125-0.11641	798	0.936	0.022
0.0125-0.14551	798	0.936	0.022
0.0125-0.18189	820	0.989	-0.005
0.0125-0.22737	838	0.921	-0.027
0.0125-0.28421	840	0.913	-0.029
0.01562-0.02441	802	0.951	0.017
0.01562-0.03051	858	0.846	-0.051
0.01562-0.03814	806	0.966	0.012
0.01562-0.04768	836	0.928	-0.025
0.01562-0.05960	814	0.996	0.002
0.01562-0.07450	830	0.951	-0.017
0.01562-0.09313	812	0.989	0.005
0.01562-0.11641	794	0.921	0.027
0.01562-0.14551	794	0.921	0.027
0.01562-0.18189	842	0.906	-0.032
0.01562-0.22737	842	0.906	-0.032
0.01562-0.28421	840	0.913	-0.029
0.01953-0.02441	862	0.831	-0.056

0.01953-0.03051	868	0.809	-0.064
0.01953-0.03814	846	0.891	-0.037
0.01953-0.04768	850	0.876	-0.042
0.01953-0.05960	814	0.996	0.002
0.01953-0.07450	808	0.974	0.010
0.01953-0.09313	812	0.989	0.005
0.01953-0.11641	798	0.936	0.022
0.01953-0.14551	806	0.966	0.012
0.01953-0.18189	846	0.891	-0.037
0.01953-0.22737	842	0.906	-0.032
0.01953-0.28421	840	0.913	-0.029
0.02441-0.03051	896	0.708	-0.098
0.02441-0.03814	886	0.744	-0.086
0.02441-0.04768	858	0.846	-0.051
0.02441-0.05960	830	0.951	-0.017
0.02441-0.07450	830	0.951	-0.017
0.02441-0.09313	802	0.951	0.017
0.02441-0.11641	820	0.989	-0.005
0.02441-0.14551	798	0.936	0.022
0.02441-0.18189	828	0.959	-0.015
0.02441-0.22737	830	0.951	-0.017
0.02441-0.28421	842	0.906	-0.032
0.03051-0.03814	912	0.653	-0.118
0.03051-0.04768	830	0.951	-0.017
0.03051-0.05960	822	0.981	-0.007
0.03051-0.07450	822	0.981	-0.007
0.03051-0.09313	808	0.974	0.010
0.03051-0.11641	800	0.943	0.020
0.03051-0.14551	812	0.989	0.005
0.03051-0.18189	828	0.959	-0.015
0.03051-0.22737	830	0.951	-0.017
0.03051-0.28421	828	0.959	-0.015
0.03814-0.04768	882	0.758	-0.081
0.03814-0.05960	858	0.846	-0.051
0.03814-0.07450	830	0.951	-0.017
0.03814-0.09313	808	0.974	0.010
0.03814-0.11641	800	0.943	0.020
0.03814-0.14551	798	0.936	0.022
0.03814-0.18189	846	0.891	-0.037
0.03814-0.22737	828	0.959	-0.015
0.03814-0.28421	828	0.959	-0.015
0.04768-0.05960	866	0.817	-0.061
0.04768-0.07450	830	0.951	-0.017
0.04768-0.09313	820	0.989	-0.005
0.04768-0.11641	790	0.906	0.032
0.04768-0.14551	818	0.996	-0.002

0.04768-0.18189	846	0.891	-0.037
0.04768-0.22737	808	0.974	0.010
0.04768-0.28421	848	0.883	-0.039
0.05960-0.07450	668	0.952	0.018
0.05960-0.09313	688	0.969	-0.012
0.05960-0.11641	646	0.856	0.050
0.05960-0.14551	664	0.935	0.024
0.05960-0.18189	688	0.969	-0.012
0.05960-0.22737	676	0.987	0.006
0.05960-0.28421	708	0.882	-0.041
0.07450-0.09313	694	0.943	-0.021
0.07450-0.11641	682	0.996	-0.003
0.07450-0.14551	664	0.935	0.024
0.07450-0.18189	664	0.935	0.024
0.07450-0.22737	672	0.969	0.012
0.07450-0.28421	708	0.882	-0.041
0.09313-0.11641	682	0.996	-0.003
0.09313-0.14551	660	0.917	0.029
0.09313-0.18189	684	0.987	-0.006
0.09313-0.22737	684	0.987	-0.006
0.09313-0.28421	714	0.856	-0.050
0.11641-0.14551	648	0.865	0.047
0.11641-0.18189	658	0.908	0.032
0.11641-0.22737	670	0.961	0.015
0.11641-0.28421	668	0.952	0.018
0.14551-0.18189	664	0.935	0.024
0.14551-0.22737	718	0.839	-0.056
0.14551-0.28421	688	0.969	-0.012
0.18189-0.22737	722	0.822	-0.062
0.18189-0.28421	746	0.721	-0.097
0.22737-0.28421	660	0.917	0.029

Table 6.2: Correlation between cortical grey matter ALFF and cortical grey matter ASL CVR by frequency range

FREQUENCY RANGE	STATISTIC	P VALUE	SPEARMAN'S RHO
0-0.0125	834	0.936	-0.022
0-0.0156	786	0.891	0.037
0-0.0195	776	0.854	0.049
0-0.02441	890	0.730	-0.091
0-0.03051	864	0.824	-0.059
0-0.03814	858	0.846	-0.051
0-0.04768	870	0.802	-0.066
0-0.05960	874	0.787	-0.071
0-0.07450	1000	0.383	-0.225
0-0.09313	894	0.715	-0.096
0-0.11641	954	0.515	-0.169
0-0.14551	962	0.491	-0.179
0-0.18189	958	0.503	-0.174
0-0.22737	962	0.491	-0.179
0-0.28421	958	0.503	-0.174
0.0125-0.0156	646	0.421	0.208
0.0125-0.0195	826	0.966	-0.012
0.0125-0.02441	868	0.809	-0.064
0.0125-0.03051	876	0.780	-0.074
0.0125-0.03814	870	0.802	-0.066
0.0125-0.04768	900	0.694	-0.103
0.0125-0.05960	880	0.766	-0.078
0.0125-0.07450	892	0.723	-0.093
0.0125-0.09313	924	0.612	-0.132
0.0125-0.11641	932	0.585	-0.142
0.0125-0.14551	920	0.625	-0.127
0.0125-0.18189	956	0.509	-0.172
0.0125-0.22737	952	0.521	-0.167
0.0125-0.28421	964	0.485	-0.181
0.01562-0.02441	956	0.509	-0.172
0.01562-0.03051	954	0.515	-0.169
0.01562-0.03814	906	0.673	-0.110
0.01562-0.04768	912	0.653	-0.118
0.01562-0.05960	956	0.509	-0.172
0.01562-0.07450	974	0.455	-0.194
0.01562-0.09313	964	0.485	-0.181
0.01562-0.11641	952	0.521	-0.167
0.01562-0.14551	942	0.553	-0.154
0.01562-0.18189	954	0.515	-0.169
0.01562-0.22737	954	0.515	-0.169
0.01562-0.28421	954	0.515	-0.169
0.01953-0.02441	898	0.701	-0.100
0.01953-0.03051	908	0.666	-0.113

0.01953-0.03814	868	0.809	-0.064
0.01953-0.04768	912	0.653	-0.118
0.01953-0.05960	956	0.509	-0.172
0.01953-0.07450	974	0.455	-0.194
0.01953-0.09313	964	0.485	-0.181
0.01953-0.11641	944	0.547	-0.157
0.01953-0.14551	936	0.572	-0.147
0.01953-0.18189	956	0.509	-0.172
0.01953-0.22737	954	0.515	-0.169
0.01953-0.28421	954	0.515	-0.169
0.02441-0.03051	846	0.891	-0.037
0.02441-0.03814	880	0.766	-0.078
0.02441-0.04768	930	0.592	-0.140
0.02441-0.05960	950	0.528	-0.164
0.02441-0.07450	938	0.566	-0.150
0.02441-0.09313	940	0.559	-0.152
0.02441-0.11641	912	0.653	-0.118
0.02441-0.14551	942	0.553	-0.154
0.02441-0.18189	946	0.540	-0.159
0.02441-0.22737	966	0.479	-0.184
0.02441-0.28421	960	0.497	-0.176
0.03051-0.03814	864	0.824	-0.059
0.03051-0.04768	918	0.632	-0.125
0.03051-0.05960	982	0.432	-0.203
0.03051-0.07450	942	0.553	-0.154
0.03051-0.09313	948	0.534	-0.162
0.03051-0.11641	922	0.619	-0.130
0.03051-0.14551	932	0.585	-0.142
0.03051-0.18189	946	0.540	-0.159
0.03051-0.22737	966	0.479	-0.184
0.03051-0.28421	982	0.432	-0.203
0.03814-0.04768	914	0.646	-0.120
0.03814-0.05960	996	0.393	-0.221
0.03814-0.07450	986	0.421	-0.208
0.03814-0.09313	948	0.534	-0.162
0.03814-0.11641	922	0.619	-0.130
0.03814-0.14551	932	0.585	-0.142
0.03814-0.18189	958	0.503	-0.174
0.03814-0.22737	954	0.515	-0.169
0.03814-0.28421	982	0.432	-0.203
0.04768-0.05960	970	0.467	-0.189
0.04768-0.07450	958	0.503	-0.174
0.04768-0.09313	916	0.639	-0.123
0.04768-0.11641	942	0.553	-0.154
0.04768-0.14551	946	0.540	-0.159
0.04768-0.18189	950	0.528	-0.164

0.04768-0.22737	960	0.497	-0.176
0.04768-0.28421	982	0.432	-0.203
0.05960-0.07450	742	0.738	-0.091
0.05960-0.09313	738	0.755	-0.085
0.05960-0.11641	772	0.617	-0.135
0.05960-0.14551	762	0.656	-0.121
0.05960-0.18189	768	0.633	-0.129
0.05960-0.22737	782	0.579	-0.150
0.05960-0.28421	808	0.484	-0.188
0.07450-0.09313	710	0.874	-0.044
0.07450-0.11641	770	0.625	-0.132
0.07450-0.14551	752	0.697	-0.106
0.07450-0.18189	780	0.586	-0.147
0.07450-0.22737	786	0.564	-0.156
0.07450-0.28421	836	0.391	-0.229
0.09313-0.11641	720	0.831	-0.059
0.09313-0.14551	744	0.730	-0.094
0.09313-0.18189	780	0.586	-0.147
0.09313-0.22737	814	0.463	-0.197
0.09313-0.28421	864	0.310	-0.271
0.11641-0.14551	754	0.689	-0.109
0.11641-0.18189	808	0.484	-0.188
0.11641-0.22737	848	0.355	-0.247
0.11641-0.28421	882	0.263	-0.297
0.14551-0.18189	804	0.498	-0.182
0.14551-0.22737	868	0.299	-0.276
0.14551-0.28421	916	0.188	-0.347
0.18189-0.22737	790	0.549	-0.162
0.18189-0.28421	890	0.244	-0.309
0.22737-0.28421	816	0.456	-0.200

Table 3.3: Correlation between cortical grey matter fALFF and cortical grey matter ASL CVR by frequency range

FREQUENCY RANGE	STATISTIC	P VALUE	SPEARMAN'S RHO
0-0.0125	630	0.377	0.228
0-0.0156	650	0.432	0.203
0-0.0195	646	0.421	0.208
0-0.02441	638	0.399	0.218
0-0.03051	650	0.432	0.203
0-0.03814	606	0.317	0.257
0-0.04768	544	0.191	0.333
0-0.05960	522	0.156	0.360
0-0.07450	572	0.243	0.299
0-0.09313	584	0.268	0.284
0-0.11641	560	0.220	0.314
0-0.14551	584	0.268	0.284
0-0.18189	574	0.247	0.297
0-0.22737	634	0.388	0.223
0-0.28421	596	0.294	0.270
0.0125-0.0156	604	0.313	0.260
0.0125-0.0195	670	0.491	0.179
0.0125-0.02441	652	0.438	0.201
0.0125-0.03051	646	0.421	0.208
0.0125-0.03814	546	0.194	0.331
0.0125-0.04768	616	0.342	0.245
0.0125-0.05960	638	0.399	0.218
0.0125-0.07450	666	0.479	0.184
0.0125-0.09313	604	0.313	0.260
0.0125-0.11641	608	0.322	0.255
0.0125-0.14551	612	0.332	0.250
0.0125-0.18189	582	0.264	0.287
0.0125-0.22737	606	0.317	0.257
0.0125-0.28421	586	0.272	0.282
0.01562-0.02441	620	0.352	0.240
0.01562-0.03051	596	0.294	0.270
0.01562-0.03814	592	0.285	0.275
0.01562-0.04768	610	0.327	0.252
0.01562-0.05960	664	0.473	0.186
0.01562-0.07450	642	0.410	0.213
0.01562-0.09313	614	0.337	0.248
0.01562-0.11641	608	0.322	0.255
0.01562-0.14551	592	0.285	0.275
0.01562-0.18189	606	0.317	0.257
0.01562-0.22737	606	0.317	0.257
0.01562-0.28421	586	0.272	0.282
0.01953-0.02441	618	0.347	0.243
0.01953-0.03051	554	0.209	0.321

0.01953-0.03814	588	0.276	0.279
0.01953-0.04768	642	0.410	0.213
0.01953-0.05960	664	0.473	0.186
0.01953-0.07450	650	0.432	0.203
0.01953-0.09313	594	0.290	0.272
0.01953-0.11641	608	0.322	0.255
0.01953-0.14551	592	0.285	0.275
0.01953-0.18189	606	0.317	0.257
0.01953-0.22737	606	0.317	0.257
0.01953-0.28421	586	0.272	0.282
0.02441-0.03051	618	0.347	0.243
0.02441-0.03814	656	0.449	0.196
0.02441-0.04768	628	0.372	0.230
0.02441-0.05960	652	0.438	0.201
0.02441-0.07450	638	0.399	0.218
0.02441-0.09313	618	0.347	0.243
0.02441-0.11641	592	0.285	0.275
0.02441-0.14551	590	0.281	0.277
0.02441-0.18189	608	0.322	0.255
0.02441-0.22737	606	0.317	0.257
0.02441-0.28421	586	0.272	0.282
0.03051-0.03814	628	0.372	0.230
0.03051-0.04768	656	0.449	0.196
0.03051-0.05960	644	0.415	0.211
0.03051-0.07450	638	0.399	0.218
0.03051-0.09313	618	0.347	0.243
0.03051-0.11641	592	0.285	0.275
0.03051-0.14551	588	0.276	0.279
0.03051-0.18189	608	0.322	0.255
0.03051-0.22737	590	0.281	0.277
0.03051-0.28421	586	0.272	0.282
0.03814-0.04768	660	0.461	0.191
0.03814-0.05960	680	0.521	0.167
0.03814-0.07450	622	0.357	0.238
0.03814-0.09313	602	0.308	0.262
0.03814-0.11641	586	0.272	0.282
0.03814-0.14551	590	0.281	0.277
0.03814-0.18189	608	0.322	0.255
0.03814-0.22737	606	0.317	0.257
0.03814-0.28421	586	0.272	0.282
0.04768-0.05960	664	0.473	0.186
0.04768-0.07450	602	0.308	0.262
0.04768-0.09313	582	0.264	0.287
0.04768-0.11641	590	0.281	0.277
0.04768-0.14551	576	0.251	0.294
0.04768-0.18189	608	0.322	0.255

0.04768-0.22737	630	0.377	0.228
0.04768-0.28421	594	0.290	0.272
0.05960-0.07450	500	0.321	0.265
0.05960-0.09313	456	0.213	0.329
0.05960-0.11641	452	0.204	0.335
0.05960-0.14551	454	0.208	0.332
0.05960-0.18189	506	0.338	0.256
0.05960-0.22737	518	0.373	0.238
0.05960-0.28421	474	0.253	0.303
0.07450-0.09313	460	0.221	0.324
0.07450-0.11641	452	0.204	0.335
0.07450-0.14551	436	0.173	0.359
0.07450-0.18189	518	0.373	0.238
0.07450-0.22737	518	0.373	0.238
0.07450-0.28421	478	0.263	0.297
0.09313-0.11641	426	0.155	0.374
0.09313-0.14551	454	0.208	0.332
0.09313-0.18189	506	0.338	0.256
0.09313-0.22737	518	0.373	0.238
0.09313-0.28421	494	0.304	0.274
0.11641-0.14551	502	0.326	0.262
0.11641-0.18189	538	0.436	0.209
0.11641-0.22737	528	0.404	0.224
0.11641-0.28421	530	0.410	0.221
0.14551-0.18189	530	0.410	0.221
0.14551-0.22737	522	0.385	0.232
0.14551-0.28421	586	0.609	0.138
0.18189-0.22737	506	0.338	0.256
0.18189-0.28421	568	0.541	0.165
0.22737-0.28421	624	0.763	0.082

Table 6.4: Correlation between brainstem fALFF and brainstem ASL CVR by frequency range

FREQUENCY RANGE	STATISTIC	P VALUE	SPEARMAN'S RHO
0-0.0125	808	0.974	0.010
0-0.0156	894	0.715	-0.096
0-0.0195	906	0.673	-0.110
0-0.02441	826	0.966	-0.012
0-0.03051	810	0.981	0.007
0-0.03814	800	0.943	0.020
0-0.04768	780	0.869	0.044
0-0.05960	732	0.694	0.103
0-0.07450	686	0.540	0.159
0-0.09313	698	0.579	0.145
0-0.11641	698	0.579	0.145
0-0.14551	740	0.723	0.093
0-0.18189	780	0.869	0.044
0-0.22737	764	0.809	0.064
0-0.28421	708	0.612	0.132
0.0125-0.0156	731	0.694	0.103
0.0125-0.0195	734	0.701	0.100
0.0125-0.02441	826	0.966	-0.012
0.0125-0.03051	754	0.773	0.076
0.0125-0.03814	690	0.553	0.154
0.0125-0.04768	776	0.854	0.049
0.0125-0.05960	722	0.660	0.115
0.0125-0.07450	676	0.509	0.172
0.0125-0.09313	690	0.553	0.154
0.0125-0.11641	730	0.687	0.105
0.0125-0.14551	720	0.653	0.118
0.0125-0.18189	776	0.854	0.049
0.0125-0.22737	780	0.869	0.044
0.0125-0.28421	812	0.989	0.005
0.01562-0.02441	760	0.795	0.069
0.01562-0.03051	762	0.802	0.066
0.01562-0.03814	770	0.831	0.056
0.01562-0.04768	768	0.824	0.059
0.01562-0.05960	718	0.646	0.120
0.01562-0.07450	700	0.585	0.142
0.01562-0.09313	700	0.585	0.142
0.01562-0.11641	702	0.592	0.140
0.01562-0.14551	734	0.701	0.100
0.01562-0.18189	758	0.787	0.071
0.01562-0.22737	758	0.787	0.071
0.01562-0.28421	812	0.989	0.005
0.01953-0.02441	670	0.491	0.179
0.01953-0.03051	696	0.572	0.147

0.01953-0.03814	756	0.780	0.074
0.01953-0.04768	760	0.795	0.069
0.01953-0.05960	760	0.795	0.069
0.01953-0.07450	718	0.646	0.120
0.01953-0.09313	700	0.585	0.142
0.01953-0.11641	722	0.660	0.115
0.01953-0.14551	708	0.612	0.132
0.01953-0.18189	758	0.787	0.071
0.01953-0.22737	742	0.730	0.091
0.01953-0.28421	812	0.989	0.005
0.02441-0.03051	790	0.906	0.032
0.02441-0.03814	782	0.876	0.042
0.02441-0.04768	754	0.773	0.076
0.02441-0.05960	714	0.632	0.125
0.02441-0.07450	768	0.824	0.059
0.02441-0.09313	710	0.619	0.130
0.02441-0.11641	746	0.744	0.086
0.02441-0.14551	722	0.660	0.115
0.02441-0.18189	758	0.787	0.071
0.02441-0.22737	742	0.730	0.091
0.02441-0.28421	856	0.854	-0.049
0.03051-0.03814	756	0.780	0.074
0.03051-0.04768	792	0.913	0.029
0.03051-0.05960	810	0.981	0.007
0.03051-0.07450	766	0.817	0.061
0.03051-0.09313	702	0.592	0.140
0.03051-0.11641	726	0.673	0.110
0.03051-0.14551	750	0.758	0.081
0.03051-0.18189	718	0.646	0.120
0.03051-0.22737	742	0.730	0.091
0.03051-0.28421	846	0.891	-0.037
0.03814-0.04768	728	0.680	0.108
0.03814-0.05960	748	0.751	0.083
0.03814-0.07450	726	0.673	0.110
0.03814-0.09313	736	0.708	0.098
0.03814-0.11641	696	0.572	0.147
0.03814-0.14551	724	0.666	0.113
0.03814-0.18189	724	0.666	0.113
0.03814-0.22737	728	0.680	0.108
0.03814-0.28421	846	0.891	-0.037
0.04768-0.05960	680	0.521	0.167
0.04768-0.07450	760	0.795	0.069
0.04768-0.09313	652	0.438	0.201
0.04768-0.11641	706	0.605	0.135
0.04768-0.14551	706	0.605	0.135
0.04768-0.18189	766	0.817	0.061

0.04768-0.22737	740	0.723	0.093
0.04768-0.28421	888	0.737	-0.088
0.05960-0.07450	622	0.755	0.085
0.05960-0.09313	526	0.398	0.226
0.05960-0.11641	552	0.484	0.188
0.05960-0.14551	546	0.463	0.197
0.05960-0.18189	600	0.664	0.118
0.05960-0.22737	558	0.505	0.179
0.05960-0.28421	730	0.788	-0.074
0.07450-0.09313	512	0.355	0.247
0.07450-0.11641	564	0.531	0.169
0.07450-0.14551	534	0.423	0.215
0.07450-0.18189	612	0.713	0.100
0.07450-0.22737	618	0.738	0.091
0.07450-0.28421	732	0.780	-0.076
0.09313-0.11641	634	0.805	0.068
0.09313-0.14551	594	0.641	0.126
0.09313-0.18189	628	0.780	0.076
0.09313-0.22737	614	0.721	0.097
0.09313-0.28421	766	0.641	-0.126
0.11641-0.14551	474	0.253	0.303
0.11641-0.18189	622	0.755	0.085
0.11641-0.22737	624	0.763	0.082
0.11641-0.28421	726	0.805	-0.068
0.14551-0.18189	698	0.926	-0.026
0.14551-0.22737	798	0.519	-0.174
0.14551-0.28421	816	0.456	-0.200
0.18189-0.22737	696	0.935	-0.024
0.18189-0.28421	980	0.089	-0.441
0.22737-0.28421	936	0.151	-0.376

Table 6.5: Correlation between cortical grey matter ALFF and cortical grey matter BOLD CVR by frequency range

FREQUENCY RANGE	STATISTIC	P VALUE	SPEARMAN'S RHO
0-0.0125	284	0.386	-0.291
0-0.0156	290	0.341	-0.318
0-0.0195	278	0.435	-0.264
0-0.02441	304	0.248	-0.382
0-0.03051	256	0.634	-0.164
0-0.03814	258	0.614	-0.173
0-0.04768	260	0.595	-0.182
0-0.05960	226	0.946	-0.027
0-0.07450	230	0.903	-0.045
0-0.09313	182	0.614	0.173
0-0.11641	218	0.989	0.009
0-0.14551	226	0.946	-0.027
0-0.18189	244	0.755	-0.109
0-0.22737	244	0.755	-0.109
0-0.28421	204	0.839	0.073
0.0125-0.0156	198	0.776	0.100
0.0125-0.0195	256	0.634	-0.164
0.0125-0.02441	282	0.402	-0.282
0.0125-0.03051	244	0.755	-0.109
0.0125-0.03814	242	0.776	-0.100
0.0125-0.04768	226	0.946	-0.027
0.0125-0.05960	198	0.776	0.100
0.0125-0.07450	180	0.595	0.182
0.0125-0.09313	184	0.634	0.164
0.0125-0.11641	216	0.968	0.018
0.0125-0.14551	214	0.946	0.027
0.0125-0.18189	230	0.903	-0.045
0.0125-0.22737	230	0.903	-0.045
0.0125-0.28421	214	0.946	0.027
0.01562-0.02441	248	0.714	-0.127
0.01562-0.03051	280	0.418	-0.273
0.01562-0.03814	238	0.818	-0.082
0.01562-0.04768	222	0.989	-0.009
0.01562-0.05960	226	0.946	-0.027
0.01562-0.07450	226	0.946	-0.027
0.01562-0.09313	210	0.903	0.045
0.01562-0.11641	218	0.989	0.009
0.01562-0.14551	214	0.946	0.027
0.01562-0.18189	230	0.903	-0.045
0.01562-0.22737	244	0.755	-0.109
0.01562-0.28421	214	0.946	0.027
0.01953-0.02441	248	0.714	-0.127
0.01953-0.03051	268	0.521	-0.218

0.01953-0.03814	238	0.818	-0.082
0.01953-0.04768	218	0.989	0.009
0.01953-0.05960	226	0.946	-0.027
0.01953-0.07450	226	0.946	-0.027
0.01953-0.09313	210	0.903	0.045
0.01953-0.11641	218	0.989	0.009
0.01953-0.14551	214	0.946	0.027
0.01953-0.18189	244	0.755	-0.109
0.01953-0.22737	244	0.755	-0.109
0.01953-0.28421	214	0.946	0.027
0.02441-0.03051	200	0.797	0.091
0.02441-0.03814	202	0.818	0.082
0.02441-0.04768	216	0.968	0.018
0.02441-0.05960	216	0.968	0.018
0.02441-0.07450	212	0.924	0.036
0.02441-0.09313	206	0.860	0.064
0.02441-0.11641	204	0.839	0.073
0.02441-0.14551	214	0.946	0.027
0.02441-0.18189	244	0.755	-0.109
0.02441-0.22737	244	0.755	-0.109
0.02441-0.28421	214	0.946	0.027
0.03051-0.03814	202	0.818	0.082
0.03051-0.04768	224	0.968	-0.018
0.03051-0.05960	230	0.903	-0.045
0.03051-0.07450	220	1.000	0.000
0.03051-0.09313	206	0.860	0.064
0.03051-0.11641	204	0.839	0.073
0.03051-0.14551	218	0.989	0.009
0.03051-0.18189	244	0.755	-0.109
0.03051-0.22737	244	0.755	-0.109
0.03051-0.28421	214	0.946	0.027
0.03814-0.04768	224	0.968	-0.018
0.03814-0.05960	230	0.903	-0.045
0.03814-0.07450	234	0.860	-0.064
0.03814-0.09313	206	0.860	0.064
0.03814-0.11641	204	0.839	0.073
0.03814-0.14551	228	0.924	-0.036
0.03814-0.18189	244	0.755	-0.109
0.03814-0.22737	244	0.755	-0.109
0.03814-0.28421	214	0.946	0.027
0.04768-0.05960	226	0.946	-0.027
0.04768-0.07450	236	0.839	-0.073
0.04768-0.09313	204	0.839	0.073
0.04768-0.11641	214	0.946	0.027
0.04768-0.14551	244	0.755	-0.109
0.04768-0.18189	248	0.714	-0.127

0.04768-0.22737	244	0.755	-0.109
0.04768-0.28421	214	0.946	0.027
0.05960-0.07450	160	0.946	0.030
0.05960-0.09313	144	0.733	0.127
0.05960-0.11641	178	0.838	-0.079
0.05960-0.14551	178	0.838	-0.079
0.05960-0.18189	188	0.707	-0.139
0.05960-0.22737	182	0.785	-0.103
0.05960-0.28421	152	0.838	0.079
0.07450-0.09313	158	0.919	0.042
0.07450-0.11641	186	0.733	-0.127
0.07450-0.14551	184	0.759	-0.115
0.07450-0.18189	200	0.560	-0.212
0.07450-0.22737	194	0.632	-0.176
0.07450-0.28421	166	1.000	-0.006
0.09313-0.11641	176	0.865	-0.067
0.09313-0.14551	188	0.707	-0.139
0.09313-0.18189	200	0.560	-0.212
0.09313-0.22737	194	0.632	-0.176
0.09313-0.28421	164	1.000	0.006
0.11641-0.14551	182	0.785	-0.103
0.11641-0.18189	206	0.492	-0.248
0.11641-0.22737	206	0.492	-0.248
0.11641-0.28421	164	1.000	0.006
0.14551-0.18189	222	0.331	-0.345
0.14551-0.22737	212	0.427	-0.285
0.14551-0.28421	166	1.000	-0.006
0.18189-0.22737	208	0.470	-0.261
0.18189-0.28421	120	0.448	0.273
0.22737-0.28421	114	0.387	0.309

Table 6.6: Correlation between brainstem ALFF and brainstem BOLD CVR by frequency range

FREQUENCY RANGE	STATISTIC	P VALUE	SPEARMAN'S RHO
0-0.0125	248	0.714	-0.127
0-0.0156	220	1.000	0.000
0-0.0195	218	0.989	0.009
0-0.02441	230	0.903	-0.045
0-0.03051	230	0.903	-0.045
0-0.03814	220	1.000	0.000
0-0.04768	212	0.924	0.036
0-0.05960	216	0.968	0.018
0-0.07450	192	0.714	0.127
0-0.09313	196	0.755	0.109
0-0.11641	190	0.694	0.136
0-0.14551	190	0.694	0.136
0-0.18189	200	0.797	0.091
0-0.22737	196	0.755	0.109
0-0.28421	196	0.755	0.109
0.0125-0.0156	252	0.673	-0.145
0.0125-0.0195	248	0.714	-0.127
0.0125-0.02441	282	0.402	-0.282
0.0125-0.03051	252	0.673	-0.145
0.0125-0.03814	216	0.968	0.018
0.0125-0.04768	208	0.881	0.055
0.0125-0.05960	192	0.714	0.127
0.0125-0.07450	186	0.654	0.155
0.0125-0.09313	186	0.654	0.155
0.0125-0.11641	210	0.903	0.045
0.0125-0.14551	210	0.903	0.045
0.0125-0.18189	210	0.903	0.045
0.0125-0.22737	212	0.924	0.036
0.0125-0.28421	232	0.881	-0.055
0.01562-0.02441	238	0.818	-0.082
0.01562-0.03051	236	0.839	-0.073
0.01562-0.03814	208	0.881	0.055
0.01562-0.04768	192	0.714	0.127
0.01562-0.05960	192	0.714	0.127
0.01562-0.07450	186	0.654	0.155
0.01562-0.09313	186	0.654	0.155
0.01562-0.11641	210	0.903	0.045
0.01562-0.14551	210	0.903	0.045
0.01562-0.18189	220	1.000	0.000
0.01562-0.22737	212	0.924	0.036
0.01562-0.28421	232	0.881	-0.055
0.01953-0.02441	264	0.558	-0.200
0.01953-0.03051	228	0.924	-0.036

0.01953-0.03814	208	0.881	0.055
0.01953-0.04768	208	0.881	0.055
0.01953-0.05960	192	0.714	0.127
0.01953-0.07450	186	0.654	0.155
0.01953-0.09313	186	0.654	0.155
0.01953-0.11641	210	0.903	0.045
0.01953-0.14551	210	0.903	0.045
0.01953-0.18189	220	1.000	0.000
0.01953-0.22737	212	0.924	0.036
0.01953-0.28421	232	0.881	-0.055
0.02441-0.03051	216	0.968	0.018
0.02441-0.03814	200	0.797	0.091
0.02441-0.04768	192	0.714	0.127
0.02441-0.05960	186	0.654	0.155
0.02441-0.07450	186	0.654	0.155
0.02441-0.09313	186	0.654	0.155
0.02441-0.11641	210	0.903	0.045
0.02441-0.14551	210	0.903	0.045
0.02441-0.18189	220	1.000	0.000
0.02441-0.22737	200	0.797	0.091
0.02441-0.28421	236	0.839	-0.073
0.03051-0.03814	192	0.714	0.127
0.03051-0.04768	186	0.654	0.155
0.03051-0.05960	182	0.614	0.173
0.03051-0.07450	182	0.614	0.173
0.03051-0.09313	190	0.694	0.136
0.03051-0.11641	190	0.694	0.136
0.03051-0.14551	190	0.694	0.136
0.03051-0.18189	220	1.000	0.000
0.03051-0.22737	200	0.797	0.091
0.03051-0.28421	220	1.000	0.000
0.03814-0.04768	224	0.968	-0.018
0.03814-0.05960	190	0.694	0.136
0.03814-0.07450	186	0.654	0.155
0.03814-0.09313	190	0.694	0.136
0.03814-0.11641	190	0.694	0.136
0.03814-0.14551	210	0.903	0.045
0.03814-0.18189	220	1.000	0.000
0.03814-0.22737	196	0.755	0.109
0.03814-0.28421	220	1.000	0.000
0.04768-0.05960	188	0.673	0.145
0.04768-0.07450	182	0.614	0.173
0.04768-0.09313	190	0.694	0.136
0.04768-0.11641	190	0.694	0.136
0.04768-0.14551	210	0.903	0.045
0.04768-0.18189	220	1.000	0.000

0.04768-0.22737	188	0.673	0.145
0.04768-0.28421	252	0.673	-0.145
0.05960-0.07450	130	0.560	0.212
0.05960-0.09313	132	0.584	0.200
0.05960-0.11641	132	0.584	0.200
0.05960-0.14551	150	0.811	0.091
0.05960-0.18189	158	0.919	0.042
0.05960-0.22737	148	0.785	0.103
0.05960-0.28421	172	0.919	-0.042
0.07450-0.09313	124	0.492	0.248
0.07450-0.11641	142	0.707	0.139
0.07450-0.14551	150	0.811	0.091
0.07450-0.18189	148	0.785	0.103
0.07450-0.22737	148	0.785	0.103
0.07450-0.28421	172	0.919	-0.042
0.09313-0.11641	134	0.608	0.188
0.09313-0.14551	150	0.811	0.091
0.09313-0.18189	158	0.919	0.042
0.09313-0.22737	162	0.973	0.018
0.09313-0.28421	196	0.608	-0.188
0.11641-0.14551	132	0.584	0.200
0.11641-0.18189	158	0.919	0.042
0.11641-0.22737	150	0.811	0.091
0.11641-0.28421	160	0.946	0.030
0.14551-0.18189	180	0.811	-0.091
0.14551-0.22737	186	0.733	-0.127
0.14551-0.28421	160	0.946	0.030
0.18189-0.22737	190	0.682	-0.152
0.18189-0.28421	164	1.000	0.006
0.22737-0.28421	154	0.865	0.067

Table 6.7: Correlation between brainstem fALFF and brainstem BOLD CVR by frequency range

FREQUENCY RANGE	STATISTIC	P VALUE	SPEARMAN'S RHO
0-0.0125	234	0.860	-0.064
0-0.0156	282	0.402	-0.282
0-0.0195	262	0.576	-0.191
0-0.02441	274	0.468	-0.245
0-0.03051	258	0.614	-0.173
0-0.03814	210	0.903	0.045
0-0.04768	202	0.818	0.082
0-0.05960	172	0.521	0.218
0-0.07450	156	0.386	0.291
0-0.09313	152	0.356	0.309
0-0.11641	166	0.468	0.245
0-0.14551	164	0.451	0.255
0-0.18189	228	0.924	-0.036
0-0.22737	242	0.776	-0.100
0-0.28421	206	0.860	0.064
0.0125-0.0156	248	0.709	-0.128
0.0125-0.0195	240	0.797	-0.091
0.0125-0.02441	272	0.485	-0.236
0.0125-0.03051	242	0.776	-0.100
0.0125-0.03814	192	0.714	0.127
0.0125-0.04768	202	0.818	0.082
0.0125-0.05960	154	0.371	0.300
0.0125-0.07450	150	0.341	0.318
0.0125-0.09313	168	0.485	0.236
0.0125-0.11641	174	0.539	0.209
0.0125-0.14551	170	0.503	0.227
0.0125-0.18189	206	0.860	0.064
0.0125-0.22737	210	0.903	0.045
0.0125-0.28421	198	0.776	0.100
0.01562-0.02441	270	0.503	-0.227
0.01562-0.03051	260	0.595	-0.182
0.01562-0.03814	174	0.539	0.209
0.01562-0.04768	180	0.595	0.182
0.01562-0.05960	154	0.371	0.300
0.01562-0.07450	150	0.341	0.318
0.01562-0.09313	164	0.451	0.255
0.01562-0.11641	176	0.558	0.200
0.01562-0.14551	172	0.521	0.218
0.01562-0.18189	208	0.881	0.055
0.01562-0.22737	210	0.903	0.045
0.01562-0.28421	198	0.776	0.100
0.01953-0.02441	270	0.503	-0.227
0.01953-0.03051	228	0.924	-0.036

0.01953-0.03814	154	0.371	0.300
0.01953-0.04768	180	0.595	0.182
0.01953-0.05960	146	0.313	0.336
0.01953-0.07450	150	0.341	0.318
0.01953-0.09313	164	0.451	0.255
0.01953-0.11641	172	0.521	0.218
0.01953-0.14551	172	0.521	0.218
0.01953-0.18189	208	0.881	0.055
0.01953-0.22737	210	0.903	0.045
0.01953-0.28421	198	0.776	0.100
0.02441-0.03051	142	0.286	0.355
0.02441-0.03814	128	0.203	0.418
0.02441-0.04768	128	0.203	0.418
0.02441-0.05960	130	0.214	0.409
0.02441-0.07450	146	0.313	0.336
0.02441-0.09313	150	0.341	0.318
0.02441-0.11641	172	0.521	0.218
0.02441-0.14551	172	0.521	0.218
0.02441-0.18189	208	0.881	0.055
0.02441-0.22737	210	0.903	0.045
0.02441-0.28421	198	0.776	0.100
0.03051-0.03814	110	0.121	0.500
0.03051-0.04768	140	0.273	0.364
0.03051-0.05960	146	0.313	0.336
0.03051-0.07450	130	0.214	0.409
0.03051-0.09313	150	0.341	0.318
0.03051-0.11641	172	0.521	0.218
0.03051-0.14551	172	0.521	0.218
0.03051-0.18189	194	0.734	0.118
0.03051-0.22737	210	0.903	0.045
0.03051-0.28421	194	0.734	0.118
0.03814-0.04768	158	0.402	0.282
0.03814-0.05960	150	0.341	0.318
0.03814-0.07450	130	0.214	0.409
0.03814-0.09313	150	0.341	0.318
0.03814-0.11641	154	0.371	0.300
0.03814-0.14551	172	0.521	0.218
0.03814-0.18189	194	0.734	0.118
0.03814-0.22737	212	0.924	0.036
0.03814-0.28421	194	0.734	0.118
0.04768-0.05960	130	0.214	0.409
0.04768-0.07450	130	0.214	0.409
0.04768-0.09313	132	0.225	0.400
0.04768-0.11641	156	0.386	0.291
0.04768-0.14551	148	0.327	0.327
0.04768-0.18189	206	0.860	0.064

0.04768-0.22737	232	0.881	-0.055
0.04768-0.28421	192	0.714	0.127
0.05960-0.07450	92	0.204	0.442
0.05960-0.09313	84	0.154	0.491
0.05960-0.11641	108	0.331	0.345
0.05960-0.14551	108	0.331	0.345
0.05960-0.18189	142	0.707	0.139
0.05960-0.22737	152	0.838	0.079
0.05960-0.28421	140	0.682	0.152
0.07450-0.09313	110	0.349	0.333
0.07450-0.11641	125	0.510	0.237
0.07450-0.14551	124	0.492	0.248
0.07450-0.18189	144	0.733	0.127
0.07450-0.22737	182	0.785	-0.103
0.07450-0.28421	144	0.733	0.127
0.09313-0.11641	126	0.514	0.236
0.09313-0.14551	118	0.427	0.285
0.09313-0.18189	150	0.811	0.091
0.09313-0.22737	174	0.892	-0.055
0.09313-0.28421	170	0.946	-0.030
0.11641-0.14551	100	0.263	0.394
0.11641-0.18189	156	0.892	0.055
0.11641-0.22737	170	0.946	-0.030
0.11641-0.28421	184	0.759	-0.115
0.14551-0.18189	182	0.785	-0.103
0.14551-0.22737	228	0.279	-0.382
0.14551-0.28421	206	0.492	-0.248
0.18189-0.22737	172	0.919	-0.042
0.18189-0.28421	204	0.514	-0.236
0.22737-0.28421	200	0.560	-0.212

Table 6.8: Correlation between cortical grey matter fALFF and cortical grey matter BOLD CVR by frequency range

FREQUENCY RANGE	STATISTIC	P VALUE	SPEARMAN'S RHO
0-0.0125	224	0.968	-0.018
0-0.0156	222	0.989	-0.009
0-0.0195	210	0.903	0.045
0-0.02441	210	0.903	0.045
0-0.03051	210	0.903	0.045
0-0.03814	184	0.634	0.164
0-0.04768	162	0.435	0.264
0-0.05960	130	0.214	0.409
0-0.07450	138	0.261	0.373
0-0.09313	144	0.299	0.345
0-0.11641	136	0.248	0.382
0-0.14551	158	0.402	0.282
0-0.18189	152	0.356	0.309
0-0.22737	162	0.435	0.264
0-0.28421	144	0.299	0.345
0.0125-0.0156	180	0.595	0.182
0.0125-0.0195	188	0.673	0.145
0.0125-0.02441	196	0.755	0.109
0.0125-0.03051	144	0.299	0.345
0.0125-0.03814	144	0.299	0.345
0.0125-0.04768	140	0.273	0.364
0.0125-0.05960	144	0.299	0.345
0.0125-0.07450	154	0.371	0.300
0.0125-0.09313	140	0.273	0.364
0.0125-0.11641	132	0.225	0.400
0.0125-0.14551	150	0.341	0.318
0.0125-0.18189	144	0.299	0.345
0.0125-0.22737	150	0.341	0.318
0.0125-0.28421	134	0.237	0.391
0.01562-0.02441	154	0.371	0.300
0.01562-0.03051	146	0.313	0.336
0.01562-0.03814	148	0.327	0.327
0.01562-0.04768	148	0.327	0.327
0.01562-0.05960	162	0.435	0.264
0.01562-0.07450	162	0.435	0.264
0.01562-0.09313	152	0.356	0.309
0.01562-0.11641	142	0.286	0.355
0.01562-0.14551	136	0.248	0.382
0.01562-0.18189	150	0.341	0.318
0.01562-0.22737	150	0.341	0.318
0.01562-0.28421	134	0.237	0.391
0.01953-0.02441	154	0.371	0.300
0.01953-0.03051	150	0.341	0.318

0.01953-0.03814	142	0.286	0.355
0.01953-0.04768	162	0.435	0.264
0.01953-0.05960	162	0.435	0.264
0.01953-0.07450	162	0.435	0.264
0.01953-0.09313	148	0.327	0.327
0.01953-0.11641	142	0.286	0.355
0.01953-0.14551	136	0.248	0.382
0.01953-0.18189	150	0.341	0.318
0.01953-0.22737	150	0.341	0.318
0.01953-0.28421	134	0.237	0.391
0.02441-0.03051	138	0.261	0.373
0.02441-0.03814	154	0.371	0.300
0.02441-0.04768	154	0.371	0.300
0.02441-0.05960	154	0.371	0.300
0.02441-0.07450	146	0.313	0.336
0.02441-0.09313	146	0.313	0.336
0.02441-0.11641	136	0.248	0.382
0.02441-0.14551	150	0.341	0.318
0.02441-0.18189	142	0.286	0.355
0.02441-0.22737	150	0.341	0.318
0.02441-0.28421	134	0.237	0.391
0.03051-0.03814	152	0.356	0.309
0.03051-0.04768	154	0.371	0.300
0.03051-0.05960	144	0.299	0.345
0.03051-0.07450	146	0.313	0.336
0.03051-0.09313	146	0.313	0.336
0.03051-0.11641	136	0.248	0.382
0.03051-0.14551	134	0.237	0.391
0.03051-0.18189	142	0.286	0.355
0.03051-0.22737	150	0.341	0.318
0.03051-0.28421	134	0.237	0.391
0.03814-0.04768	146	0.313	0.336
0.03814-0.05960	154	0.371	0.300
0.03814-0.07450	140	0.273	0.364
0.03814-0.09313	140	0.273	0.364
0.03814-0.11641	134	0.237	0.391
0.03814-0.14551	142	0.286	0.355
0.03814-0.18189	142	0.286	0.355
0.03814-0.22737	150	0.341	0.318
0.03814-0.28421	134	0.237	0.391
0.04768-0.05960	144	0.299	0.345
0.04768-0.07450	140	0.273	0.364
0.04768-0.09313	128	0.203	0.418
0.04768-0.11641	142	0.286	0.355
0.04768-0.14551	142	0.286	0.355
0.04768-0.18189	142	0.286	0.355

0.04768-0.22737	156	0.386	0.291
0.04768-0.28421	150	0.341	0.318
0.05960-0.07450	90	0.191	0.455
0.05960-0.09313	86	0.166	0.479
0.05960-0.11641	100	0.263	0.394
0.05960-0.14551	100	0.263	0.394
0.05960-0.18189	112	0.368	0.321
0.05960-0.22737	120	0.448	0.273
0.05960-0.28421	100	0.263	0.394
0.07450-0.09313	86	0.166	0.479
0.07450-0.11641	100	0.263	0.394
0.07450-0.14551	100	0.263	0.394
0.07450-0.18189	120	0.448	0.273
0.07450-0.22737	120	0.448	0.273
0.07450-0.28421	96	0.232	0.418
0.09313-0.11641	94	0.218	0.430
0.09313-0.14551	100	0.263	0.394
0.09313-0.18189	112	0.368	0.321
0.09313-0.22737	120	0.448	0.273
0.09313-0.28421	118	0.427	0.285
0.11641-0.14551	118	0.427	0.285
0.11641-0.18189	138	0.657	0.164
0.11641-0.22737	140	0.682	0.152
0.11641-0.28421	118	0.427	0.285
0.14551-0.18189	152	0.838	0.079
0.14551-0.22737	144	0.733	0.127
0.14551-0.28421	146	0.759	0.115
0.18189-0.22737	140	0.682	0.152
0.18189-0.28421	90	0.191	0.455
0.22737-0.28421	82	0.143	0.503

Appendix 7

Table 6.9: Spearman correlation between regional fALFF and regional ASL CVR within each subject (frequency range 0.0125 – 0.07450 Hz). There was a statistically significant correlation within only two of the seventeen subjects (highlighted in green) after a Holm correction for multiple comparisons, and these were both negative.

Participant	Statistic	P-Value	Spearman's Rho	α (Holm Corrected)
A	4392	0.0002	-0.69	0.003
B	4282	0.0006	-0.65	0.003
C	3970	0.0076	-0.53	0.003
D	3784	0.0232	-0.46	0.004
E	1516	0.0392	0.42	0.004
F	3566	0.0682	-0.37	0.004
G	3490	0.0944	-0.34	0.005
H	3388	0.1407	-0.30	0.005
I	1956	0.2316	0.25	0.006
J	3216	0.2530	-0.24	0.006
K	2052	0.3104	0.21	0.007
L	2060	0.3176	0.21	0.008
M	3108	0.3477	-0.20	0.010
N	2268	0.5415	0.13	0.013
N	22619	0.5519	-0.09	0.017
O	2920	0.5563	-0.12	0.025
P	2284	0.5613	0.12	0.050

Table 6.10: Spearman correlation between regional fALFF and regional BOLD CVR within each subject (frequency range 0.0125 – 0.07450 Hz. There was a statistically significant correlation within eight of the eleven subjects (highlighted in green) for whom BOLD CVR data was available, after a Holm correction for multiple comparisons.

Participant	Statistic	P-Value	Spearman's Rho	α (Holm Corrected)
J	486	2.51×10^{-06}	0.81	0.0045
N	8698	9.16×10^{-06}	0.58	0.0050
F	608	1.35×10^{-05}	0.77	0.0056
P	736	8.56×10^{-05}	0.72	0.0063
B	852	3.28×10^{-04}	0.67	0.0071
C	1066	2.30×10^{-03}	0.59	0.0083
L	1080	2.57×10^{-03}	0.58	0.0100
A	1238	7.97×10^{-03}	0.52	0.0125
D	1798	1.34×10^{-01}	0.31	0.0167
G	2014	2.77×10^{-01}	0.23	0.0250
H	2528	8.96×10^{-01}	0.03	0.0500

Appendix 8

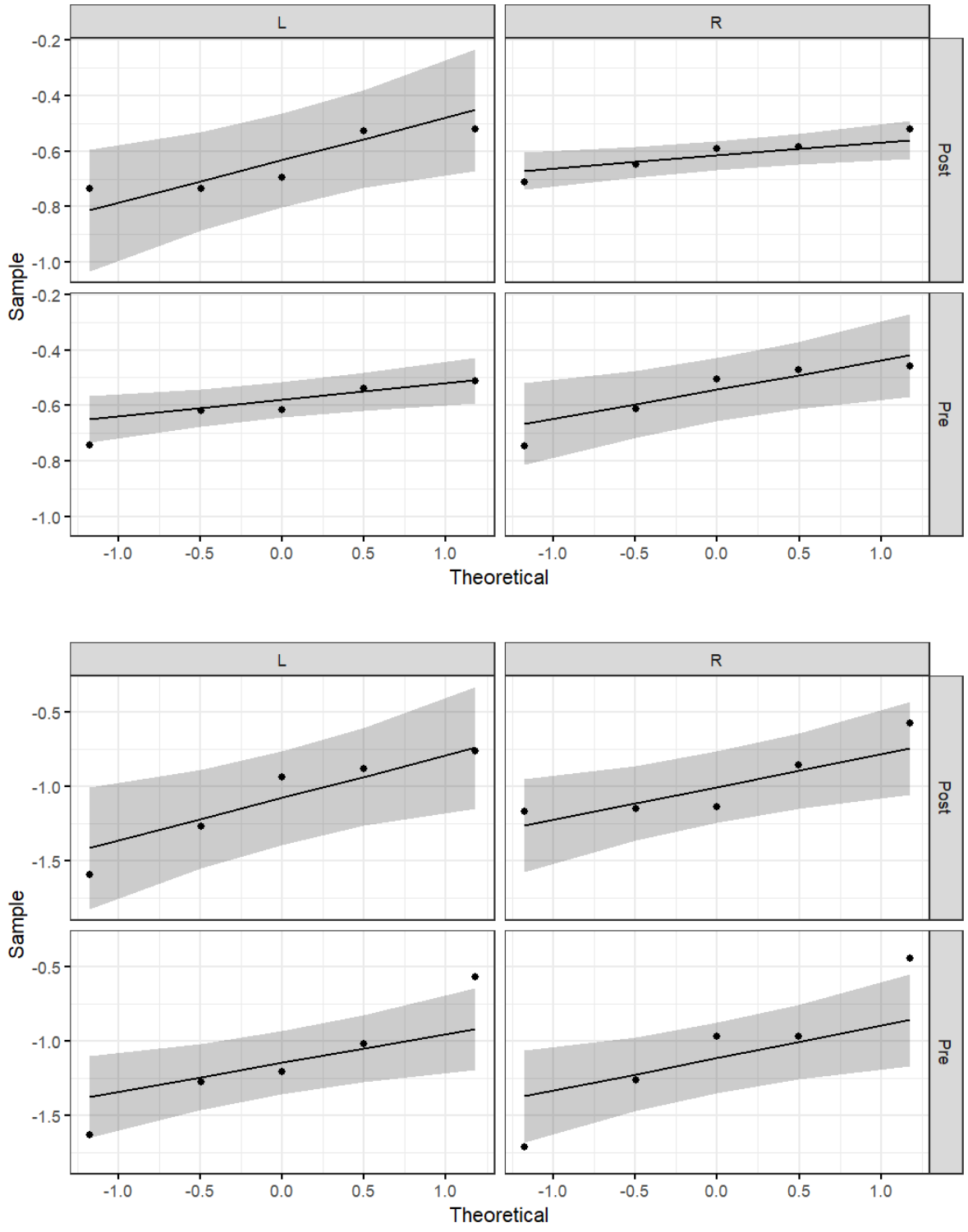

Figure 7.11: QQ plots demonstrating that the residuals of the ALFF (top) and fALFF (bottom) linear models are approximately normally distributed. As demonstrated by the boxplots in figures 7.5 and 7.6 there are some outliers which may bias the data, but otherwise the residuals fall approximately along the reference line for a normal distribution.

Appendix 9 – Inclusion and exclusion criteria - The effect of dexmedetomidine, an α_2-adrenergic agonist, on brainstem autonomic activity and functional connectivity of the locus coeruleus – a pilot study

Inclusion criteria:

- Aged 18-60 years old.
- ASA (American Society of Anaesthesiologists grade 1)- no known medical problems, including no history of gastro-oesophageal reflux.
- No potentially difficult airway (on assessment by an anaesthetist).
- Resting heart rate greater than 60 beats per minute.
- Able to understand and communicate in spoken English (for consent purposes and behavioural testing).
- Not taking any regular medications.
- No allergies/previous adverse reactions to dexmedetomidine, other sedatives/anaesthetic agents or other similar medications.

Exclusion criteria:

- Any self-reported or diagnosed medical or psychiatric condition.
- MRI contraindications (e.g. a pacemaker, metallic implants, claustrophobia) as established using CUBRIC's standard screening procedures.
- Pregnancy or childbirth in the last 6 weeks
- Resting heart rate < 60 beats per minute
- Illicit drug use in the last 4 weeks.
- History of anaphylaxis.

Appendix 10 – Participant information sheet: Investigating the role of human brainstem noradrenergic centres in sedation, analgesia and haemodynamic control.

Professor Neil Harrison
CUBRIC, Maindy Road
Cardiff
CF24 4HQ

Tel: +44 (0)29 2087 0358 0365 (reception)
email harrisonn4@cardiff.ac.uk

MRI Volunteer Information Sheet (Version 1.2 1/12/21)

Approval ref: **EC.19.09.10.5673RA**

Part 1

Study title: Investigating the role of human brainstem noradrenergic centres in sedation, analgesia and haemodynamic control.

You are being invited to take part in a research study. Before you decide it is important for you to understand why the research is being done and what it will involve. Please take time to read the following information carefully and discuss it with others if you wish. Part 1 tells you about the purpose of this study and what will happen to you if you take part. Part 2 gives you more detailed information about the conduct of the study. Ask us if there is anything that is not clear or if you would like more information. Please take time to decide whether or not you wish to take part.

Thank you for reading this.

What is the purpose of the study?

We are performing a study which involves magnetic resonance imaging (MRI) of the human brain to measure brain activity and how this is altered by sedation. We are doing this study on up to 20 volunteers to learn more about how sedation, produced by dexmedetomidine, alters the activity of the brain, especially in the brain areas involved in consciousness, pain perception and blood pressure control. With that in mind, we will measure activity from various parts of your brain while you undergo various sensory, motor and moderately painful tasks. This study is for research purposes only and as a volunteer you would receive no therapeutic benefit for taking part.

Why have I been invited?

As a volunteer you responded to our request for healthy adult subjects to participate in the study.

Do I have to take part?

It is up to you to decide whether to take part. We will describe the study and go through this information sheet. If you do decide to take part, you will be given this information sheet to keep and be asked to sign a consent form. You are free to withdraw at any time and without giving a reason. You must know that there is no pressure for you to take part. In addition, you will be able to withdraw from the study at any time and no explanation is necessary.

Am I able to take part?

We are looking for fit and healthy male volunteers between the ages of 18 and 50 who speak fluent English. You will receive a comprehensive medical screening, conducted by a fully qualified medical doctor, registered with the General Medical Council, prior to your acceptance into the study. Details of the screening process are given below. Should any problems be identified in the screening, you will be informed of them and referred to appropriate medical personnel within the UK NHS system as necessary. This will probably involve a referral to your general practitioner.

What will happen to me if I take part?

You will be asked to visit the Cardiff University Brain Research Imaging Centre on two occasions. You would be supervised by a trained doctor during each visit.

First visit: We would screen you for contraindications for MRI and carry out a health screen. To qualify for the study, you must have no illnesses at all, only the very simplest prescribed and over the counter medication is allowed (what is allowable will be assessed by the doctor), and you must not be overweight for your height. We would take you around the MRI suite to help you familiarize yourself with the scanning equipment. We will also take you through the tasks to be performed for the experiments, to familiarize you with the experiments and determine your suitability. The first visit will last up to 1 hour.

Second visit: On this occasion you will receive dexmedetomidine and must not have, or be recovering from a cough, cold, or the 'flu'. First, your brain will be scanned using MRI. Then, while you are outside the scanner but still on the MRI bed, you will receive dexmedetomidine. The amount of dexmedetomidine you will be given will only make you moderately sleepy. To ensure that that you are completely safe with this small dose of drug, we will give it to you outside the scanner closely monitored by a doctor. You will then have your brain scanned again using MRI while receiving the drug. The brain scans will measure your brain activity while you are doing different tasks such as watching a screen, performing a motor task, or stimulation of your skin (moderately painful). This visit would last up to 5 hours.

What do I have to do before the visits?

For the first visit, no special preparation is necessary.

In preparation for the second visit, to be safe you should have an empty stomach before the drug infusion. You should not eat solid food for at least six hours before the drug infusion. This includes the chewing of gum, which is not allowed. Clear fluid is allowed up to 2 hours before the study session. We would remind you of these times before the scan session. At the end of the scan session, you would be offered food and refreshments.

Expenses and payments

You will receive £20 per hour plus travel expenses. This will amount to about £100 in total.

What are the possible benefits of taking part?

This study involves the recording of typical brain function. Since we are only studying healthy volunteers, there is no intended clinical benefit to you from taking part this study. We hope that the information we get from this study may help us to better understand how the brain works and how its function is altered during sedation, a state of reduced consciousness or arousal.

What happens if you find something unusual on my scan?

The researchers involved do not have expertise in MRI diagnosis, as they are psychologists, imaging scientists and doctors who give anaesthetics during operations, but not radiological experts. The person conducting your scans will not be able to comment on the results of your scans. You should not regard these research scans as a medical screening procedure. Occasionally when we image healthy participants, the researchers may be concerned that a potential abnormality may exist on the scan. In this case, we will ask a neurological consultant, such as a neuroradiologist, with MRI expertise to examine the scans. If the specialist

radiologist feels it to be appropriate, a report can be forwarded to your GP so that he/she may arrange to further investigate any potential abnormality. Early detection may have the benefit of starting treatment early but, in a small number of cases, may have implications for future employment and insurance.

In most cases a neurological consultant will not look at the images of your brain. It is important that you realise that these scans are not intended to provide any information that may help in the diagnosis of any medical condition. If you do have any health concerns, you should contact a qualified medical practitioner in the normal way.

What are the possible disadvantages and risks of taking part?

Some people find that the scanner makes them feel uncomfortable because they have to keep still for a long time. MRI scanning can be loud. You would wear earplugs to reduce the noise of the scanner, and if you should find the experience claustrophobic, you are free to withdraw at any time without explaining why. Otherwise, MRI is thought to be a safe, non-invasive imaging technique. However, it is our policy not to give an MRI scan to someone who is pregnant. If there is a possibility that you are pregnant, therefore, you should not take part in this study. It may not be safe to have a scan if you have metal or a pacemaker in your body. This is because of the strong magnetic field in the scanner room. For your safety you will be asked to fill out a MRI Safety Screening Questionnaire, and to remove any metallic items (e.g. jewellery, coins) before you enter the scanner room.

The drug, dexmedetomidine, would be given to you through a cannula inserted into a vein of your hand or arm using a needle. The insertion of the needle is painful and may result in some bruising for a few days. The cannula would remain in your vein while you are in the scanner but once inserted is not painful. There is a minimal risk of infection associated with having a cannula inserted into your vein.

In order that the drug, dexmedetomidine can be given safely, the environment of the brain scanner has been set up to the highest national standards for the delivery of sedation. Full medical monitoring will be used at all times and two qualified anaesthetists will be in attendance. The possible side effects of receiving dexmedetomidine are reduced breathing, slow or fast heart rate, lowering of blood pressure, and allergic reaction. However, in most volunteers significant unpleasant sensations are not experienced. The main experience is one of sedation. A trained doctor will be present at all times to take care of you during the drug administration. He or she will carefully monitor your heart rate and breathing and if any significant changes occur the doctor may decide to stop the infusion of the drug. The side effects of dexmedetomidine can be reversed, very rapidly, by stopping the infusion. If you have any side effects, which you find distressing, or you feel unwell you can ask for the infusion to be stopped and we will do so immediately. We will give you additional oxygen to breathe while you receive the drug. This will be given by a plastic tube resting lightly near your nostrils.

Breathing the air and oxygen mixture is not harmful or dangerous and should not produce any side effects.

You would be asked to undergo simple tasks such as looking at a screen or resting with eyes closed. In addition, we would apply some heat (moderately painful) level on your forearm, in short bursts. We will also ask you to perform a hand-grip task, by repeatedly squeezing a handheld device, while a tourniquet applied to the upper arm is inflated. This test is designed to slightly increase your blood pressure, and is designed to be moderately painful.

What will happen to the results of the study?

We hope to publish the results of this study in a scientific journal. We may also present the results at a scientific conference or a seminar in a university. We may also publish results on our website. We would be happy to discuss the results of the study with you and to send you a copy of the published results. It will not be possible to identify you or images of your brain in any report or publication.

What if there is a problem?

Any complaint about the way you have been dealt with during the study or any possible harm you might suffer will be addressed. In the unlikely event of anything untoward happening and this being due to someone's negligence, then you may have grounds for a legal action for compensation against Cardiff University for negligent but not non-negligent harm. You may have to pay your own legal costs.

Will my taking part in this study be kept confidential?

All information that is collected about you during the course of the research will be kept strictly confidential under the direction of Prof Neil Harrison We may share the data we collect with researchers at other institutions both commercial and non-commercial and within and outside the European Union. However, any information about you that leaves the Centre will have your name and address removed so that you cannot be recognised from it. Any information about your identity obtained from this research will be kept private. In any sort of report we might publish we will not include information that will make it possible for other people to know your name or identify you in any way. You will be simply referred to by your gender, age and possibly some characteristic such as left or right handedness. If you join the study, some parts of your records and the data collected for the study may be looked at by authorised persons from the University, for the purposes of monitoring and audit.

The information provided will be held in compliance with GDPR regulations. The data controller is Cardiff University and the Data Protection Officer is Matt Cooper CooperM1@cardiff.ac.uk.

What will happen if I don't want to carry on with the study?

You are free to withdraw at any time, without giving a reason. A decision to withdraw at any time, or a decision not to take part, will not affect you in any way.

Who is organising and funding the research?

This research study is organised by Cardiff University and is funded by the Wellcome Trust.

Who has reviewed the study?

This study has been reviewed and approved by the School of Psychology Research Ethics Committee.

What should I do after the study?

The effects of dexmedetomidine should wear off within a few minutes of the end of the study. The doctor involved in the study will have made sure that you are fit to leave the imaging Centre after the study before you go home. You should not drive home after the study. We advise you not to drive or operate dangerous machinery until at least the day after the study. We also advise you not to drink alcohol until at least the day after the study. We advise you also to make sure there is someone at home with you on the night of the study.

What if new information becomes available during the course of the study?

If the new information pertains specifically to the health of the participant, you will be informed, and continued inclusion in the research discussed with the participant.

What will happen if I don't want to carry on with the study?

You are free to withdraw from the study at any time. Any data already collected in you will be retained and used for our research.

Will my General Practitioner be notified of my participation in the research?

Your GP will not be notified of involvement in the study unless considered necessary as a result of an unexpected finding on your scan.

What if I am unhappy about some aspect of the study?

If you have a concern about any aspect of this study, you should ask to speak to the researchers who will do their best to answer your questions (Dr Neeraj Saxena, 02920688802). If you remain unhappy and wish to complain formally, you can do this through the School of Psychology Ethics Committee, Cardiff University (psychethics@cardiff.ac.uk).

Contact for further information about the study

Dr Neeraj Saxena

Cardiff University Brain Research Imaging Centre (CUBRIC)

School of Psychology

Cardiff University

Maindy Road,

Cardiff, CF24 4HQ

Email: waans@cf.ac.uk

Tel: 02920688802

This completes Part 1.

If the information in Part 1 have interested you and you are considering participation, please read the additional information in Part 2 before making any decisions.

Part 2

Study title: Investigating the role of human brainstem noradrenergic centres in sedation, analgesia and haemodynamic control.

The First Visit

A questionnaire checking for contraindications to MRI will be carried out. This makes sure that you do not have any metal in your body and that it is safe for you to enter the scanner. In addition, on this same visit you will undergo a comprehensive medical assessment. You will only be able to go on with the study if you have a healthy heart (cardiovascular), breathing (respiratory), normal airway anatomy and digestive system. Included in this, you must not suffer from indigestion regularly, especially on lying down. In addition, you must not be overweight for your height. Your heart rate and blood pressure will be taken as a routine. You will also be given a chance to lie in the 'mock MRI' scanner to experience what it would feel like in the subsequent visits. We will also take you through the tasks to be performed for the experiments, to familiarize you with the experiments and determine your suitability.

Based upon the results of all of the above, you would either be included or excluded from the study. All data obtained during the study would remain confidential. Access to data would be available to the investigators and doctors attached to the project at CUBRIC.

The Second Visit

When you arrive at the centre you will meet the researcher and doctor who will explain to you what will happen during the scan. The researcher will go through an MRI consent form with you once again and also the MRI Safety Screening Form. The doctor will check that you are still in good health, that you have not developed a recent illness like a cough or cold, that you have starved for food, for six hours and that you are still happy to consent to the procedures involved in the study.

The MRI scanner is a large box with a tube running through the middle. Following the insertion of the cannula for drug injection into a vein in your arm/hand, you would lie on the bed of the MRI scanner. This moves you into the centre of the tube, and a device shaped like a helmet would be put around your head. You would wear earplugs to protect your hearing and so that you can listen to the researcher when spoken to. You will be able to see a screen at the end

of the bed via a mirror on the helmet or via glasses. You would also be given a call button to hold throughout the scan. You can use this to get the attention of the researcher who will be on the other side of a window just outside the scanner room. You can speak to the researcher via a microphone from inside the scanner. It is very important that you keep still during the scans and try not to move your head at all. We would make sure that you were comfortable by providing cushions around the head and under the legs and a blanket if necessary.

We may ask you to perform visual, movement and sensory tasks as well as to lie still without performing any task in particular. These tasks include squeezing a handgrip device while a tourniquet is applied to the arm. Sensory tasks include a thermal stimulus, which involves heat being applied to the forearm to generate moderate pain. These tasks are designed to be moderately painful, but you are free to stop at any point. You may be asked to change your breathing rate in response to cues. You may also be asked to breathe air enriched with oxygen through a tube under your nose. After the first half of the session we will move you out of the tube on the MRI bed. There you will receive dexmedetomidine through the cannula inserted in your vein. Once you have started feeling slightly sleepy you will be moved back into the MRI tube. The second part of the session will then commence and you will be asked to perform the same tasks as before. Once the tasks finish the drug infusion will be stopped and you will be brought out of the MRI tube, assisted.

After we have finished the scanning session you will be given food and drink. We ask you to stay at CUBRIC for an hour so that the doctor may monitor you.

The drug being tested

Dexmedetomidine is a newer anaesthetic drug which has been used around the world for over 15 years and is increasingly being used in the UK. It is commonly used to sedate patients in Intensive Care units and during some operative procedures. It also has pain relieving properties making it suitable in certain situations. In this study dexmedetomidine would be given to you using a pump at low doses to sedate you without sending you to sleep completely. The doctor would be supervising you at all times during the study and your heart rate, breathing, oxygen, breathed gases and other measures would be taken throughout.

Other side-effects described in the British National Formulary include the following:

Common or very common: Agitation, arrhythmias, drymouth, hyperglycaemia, hypertension; hyperthermia, hypoglycaemia, hypotension, myocardial infarction, myocardial ischaemia, nausea, respiratory depression, vomiting

Uncommon: Abdominal distension, apnoea, atrioventricular block, dyspnea, hallucination, hypoalbuminaemia, metabolic acidosis, thirst

In healthy participants, chances of any serious side-effects, especially at the doses we intend to use, are extremely unlikely.

What is MRI?

Magnetic resonance imaging (MRI) is a well-established technique for imaging the body and brain using strong magnetic fields and low energy radio waves to make pictures of the inside of the human body non-invasively. Not only can we generate images of your internal anatomy but we can assess the activity in parts of your brain while you perform some simple task – this is known as functional MRI or fMRI. MRI does NOT use ionizing radiation.

What does MRI involve?

We will need you in the MRI scanner for up to 3 hours with a break to come out mid-way through. Remember that you are free to withdraw from this study at any time, without giving a reason.

In preparation for the MRI scan, you will first be asked a set of safety questions to make sure that you don't have anything in your body that might be affected by the scans, such as a pacemakers and other implanted devices, or metal in your body (e.g. shrapnel from war injuries). You will be asked to remove all metal objects from your person including keys, coins, jewellery and watches and will need to remove credit cards and travel-cards, belts and under-wired bras. Your valuables will then be locked away for security reasons. If you are wearing make-up you may be asked to remove this as well.

Although MRI is not known to affect the unborn child, we exclude subjects who may be pregnant just to be on the safe side.

Wear soft, loose but warm clothing which preferably has no metal fixings.

While the scanner is acquiring images it can be very noisy, so you will be given earplugs and/or ear defenders to wear.

What are the possible disadvantages and risks of taking part in MRI?

MRI involves minimal risk. No serious side effects of being in an MRI scanner have been reported despite millions of scans worldwide. Although the possibility of long-term effects cannot be completely ruled out, the weight of experience and opinion is against this.

A few people have reported minor side effects including dizziness, mild nausea, a metallic taste in the mouth, and the sensation of seeing flashing lights. These side effects, if experienced, go away soon after you leave the magnet. If you experience any of these or others please let us know as soon as possible.

Some people find being inside an MRI scanner claustrophobic although this is less so with the more compact systems like those used in CUBRIC. The scanner also makes quite loud noises for which we provide ear plugs. The radiofrequency waves we use to create the MR scans can cause your head and body to warm up slightly. This is not a problem, and you usually won't notice it, as your blood flow will increase slightly to take the heat away; we also keep the scanner room quite cool so that you always remain comfortable.

If you find the experience in the scanner unpleasant, just let us know straight away and we will stop and take you out of the scanner.

This completes Part 2

Appendix 11

Consent form: Investigating the role of human brainstem noradrenergic centres in sedation, analgesia and haemodynamic control.

Professor Neil Harrison
CUBRIC, Maindy Road
Cardiff
CF24 4HQ

Tel: +44 (0)29 2087 0358 0365 (reception)
email harrisonn4@cardiff.ac.uk

Volunteer Consent Form (Version 1.2 1/12/2021)

Approval ref: EC.19.09.10.5673RA

Study Number: 441

CUBRIC Unique Identifier:

Name of Researcher:

Study title: Investigating the role of human brainstem noradrenergic centres in sedation, analgesia and haemodynamic control.

		Please initial box
1	I confirm that I have read and understand the information sheet dated 1/12/21 (version v1.2) for the above study. I have had the opportunity to consider the information, ask questions and have had these answered satisfactorily.	☐
2	I understand that my participation is voluntary and that I am free to withdraw at any time, without giving any reason, without my medical care or legal rights being affected.	☐
3	I understand and agree that the MRI scan is not a medical screening procedure and that the researchers are not qualified to provide a clinical diagnosis or identify potential abnormalities. However, if the researchers are concerned that there may be a potential abnormality on the scan, I consent to them disclosing the scan to a specialist neuroradiologist to provide a radiological report on the scan. I further consent to the results of this report being disclosed to my General Practitioner, if appropriate.	☐

4	I understand that the research data being collected will include sensitive information. I specifically consent to this information being processed for the purposes of research. Please tick:	☐
5	I understand that the personal data will be processed in accordance with GDPR regulations (see privacy statement below).	☐
6	I agree to take part in the above study	☐

Name of volunteer	Date	Signature
Name of person taking consent (if different from researcher)	Date	Signature
Researcher	Date	Signature

When completed, 1 copy for volunteer; original for researcher.

Privacy Notice:

The information provided will be held in compliance with GDPR regulations. The data controller is Cardiff University and the Data Protection Officer is Matt Cooper CooperM1@cardiff.ac.uk. The lawful basis for the processing of the data you provide is consent**.** This information is being collected by Dr. Bleddyn Woodward.

The information on the consent form will be held securely and separately from the research information. Only the researcher will have access to this form and it will be destroyed after 7 years.

The research information you provide will be used for the purposes of research only and will be stored securely. Only the researchers involved in this study, will have access to this information. After 5 years the data will be anonymised (any identifying elements removed) and this anonymous information may be kept indefinitely or published.

References

Achilles, J P et al. 2013. *Cardiovascular physiology 10th edition.* Elsevier.

ADNI. 2021. *Alzheimer's Disease Neuroimaging Initiative (ADNI).* adni.loni.usc.edu.

Akar, Z et al. 1994. "Microsurgical anatomy of the intracranial part of the vertebral artery." *Neurol Res* 171-80.

Al-Bachari, S et al. 2014. "Arterial spin labelling reveals prolonged arterial arrival time in idiopathic Parkinson's disease." *NeuroImage: Clinical* 1-8.

Alexander, R. Wayne. 1995. "Hypertension and the Pathogenesis of Atherosclerosis. Oxidative Stress and the Mediation of Arterial Inflammatory Response: A New Perspective." *Hypertension* 155–161.

Alfaro-Almagro, F et al. 2018. "Image processing and Quality Control for the first 10,000 brain imaging datasets from UK Biobank." *Neuroimage* 400-424.

Alosoco, M L et al. 2014. "The Impact of Hypertension on Cerebral Perfusion and Cortical Thickness in Older Adults." *Journal of the American Society of Hypertension* 561-570.

Alsop, D et al. 2015. "Recommended Implementation of Arterial Spin-Labeled Perfusion MRI for Clinical Applications: A Consensus of the ISMRM Perfusion Study Group and the European Consortium." *Magnetic Resonance in Medicine* 102-116.

Ashton-Jones, G et al. 2005. "An integrative theory of locus coeruleus-norepinephrine function: adaptive gain and optimal performance." *Annu Rev Neurosci* 403-450.

Aslan, S et al. 2010. "Estimation of labeling efficiency in pseudocontinuous arterial spin labeling." *Magnetic Resonance in Medicine* 765-771.

Awad, I A. 1986. "Incidental subcortical lesions identified on magnetic resonance imaging in the elderly. I. Correlation with age and cerebrovascular risk factors." *Stroke* 1084-89.

Bär, K et al. 2016. "Functional connectivity and network analysis of midbrain and brainstem nuclei." *Neuroimage* 53-63.

Basinger, H et al. 2022. *Neuroanatomy, Brainstem.* https://pubmed.ncbi.nlm.nih.gov/31335017/

Beissner, F et al. 2014. "Advances in functional magnetic resonance imaging of the human brainstem." *Neuroimage* 91-8.

Beissner, F et al. 2015. "Functional MRI of the Brainstem: Common Problems and their Solutions." *Clin Neuroradiology* 251-257.

Beissner, F et al. 2013. "The Autonomic Brain: An Activation Likelihood Estimation Meta-Analysis for Central Processing of Autonomic Function." *Journal of Neuroscience* 10503-10511.

Bhogal, A et al. 2016. “The BOLD cerebrovascular reactivity response to progressive hypercapnia in young and elderly.” *Neuroimage* 94-102.

Bianciardi, M et al. 2016. “In vivo functional connectome of human brainstem nuclei of the ascending arousal, autonomic, and motor systems by high spatial resolution 7-Tesla fMRI.” *MAGMA* 451-62.

Bianciardi, M et al. 2009. “Sources of fMRI signal fluctuations in the human brain at rest: a 7T study.” *Magnetic Resonance Imaging* 1019–1029.

Bianciardi, M et al. 2015. “Toward an In Vivo Neuroimaging Template of Human Brainstem Nuclei of the Ascending Arousal, Autonomic, and Motor Systems.” *Brain Connect* 597-607.

Bijsterbosch, J et al. 2017. *Introduction to Resting state fMRI Functional Connectivity.* Oxford University Press.

Biswal, B. 1995. “Functional Connectivity in the Motor Cortex of Resting Human Brain Using Echo-Planar MRI.” *Magnetic Resonance in Medicine* 537-41.

Block, K T et al. 2014. “Toward routine clinical use of radial stack-of-stars 3D gradient-echo sequences for reducing motion sensitivity.” *J Korean Soc Magn Reson Med* 87-106.

Blockley, N et al. 2011. “An improved method for acquiring cerebrovascular reactivity maps.” *Magnetic Resonance in Medicine* 1278-1286.

Boveiri, H R et al. 2020. “Medical Image Registration Using Deep Neural Networks: A Comprehensive Review.” *Computers & Electrical Engineering.*

Brooks, J C et al. 2013. “Physiological noise in brainstem fMRI.” *Front. Hum. Neurosci.*

Brownlee, J. 2019. *How to Choose Loss Functions When Training Deep Learning Neural Networks.* https://machinelearningmastery.com/how-to-choose-loss-functions-when-training-deep-learning-neural-networks/.

Burt, V L et al. 1995. “Prevalence of hypertension in the US adult population. Results from the Third National Health and Nutrition Examination Survey, 1988–1991.” *Hypertension* 305-313.

Butterbaugh, J et al. 2015. “Cerebrovascular Reactivity in Young Subjects with Sleep Apnea.” *Sleep* 241–250.

Buxton, R B. 2013. *Introduction to Functional Magnetic Resonance Imaging Principles and Techniques.* Cambridge University Press.

Cardenas-Blanco, A et al. 2008. “Noise in Magnitude Magnetic Resonance Images.” *Concepts in Magnetic Resonance Part A* 409-416.

Castillo, R et al. 2020. “Dexmedetomidine improves cardiovascular and ventilatory outcomes in critically ill patients: basic and clinical approaches.” *Frontiers in Pharmacology.*

Chamadia, S et al. 2020. “A pharmacokinetic and pharmacodynamic study of oral dexmedetomidine.” *Anaesthesiology* 1223-1233.

Chang, Yulin V. 2017. “Spiral-in/out BOLD fMRI for increased SNR and reduced susceptibility.” *Magnetic Resonance in Medicine* 1405-1419.

Chappell, M et al. 2017. *Perfusion quantification using arterial spin labelling.* Oxford University Press.

Chappell, M et al. 2017. “Short introduction to MRI physics for neuroimaging.” In *Introduction to Neuroimaging Analysis*, by M et al Chappell. Oxford University Press.

Chappell, M et al. 2009. “Variational Bayesian inference for a non-linear forward model.” *IEEE Transactions on Signal Processing* 223-236.

Chen, Jerry. 2021. *Face landmark detection pytorch version.* https://github.com/jerrychen44/face_landmark_detection_pytorch.

Chen, X. 2014. “Simultaneous imaging of locus coeruleus and substantia nigra with a quantitative neuromelanin MRI approach.” *Magn Resonance Imaging* 1301-6.

Chen, Y. 2012. “Comparison of arterial transit times estimated using arterial spin labeling.” *MAGMA* 135-44.

Cheng, W et al. 2022. “Age-related changes in the risk of high blood pressure.” *Front Cardiovasc Med.*

Chernik, D et al. 1990. “Validity and Reliability of the Observer's Assessment of Alertness/Sedation Scale. Study with IV Midazolam.” *Journal of Clinical Psychopharmacology* 244-251.

Chiong, J R et al. 2008. “Secondary hypertension: Current diagnosis and treatment. .” *In J Cariol* 6-21.

Collaboration, NCD Risk Factor. 2021. “Worldwide trends in hypertension prevalence and progress in treatment and control from 1990 to 2019: a pooled analysis of 1201 population-representative studies with 104 million participants.” *Lancet* 957-980.

Coote, J et al. 2004. *The Hypothalamus and Cardiovascular Regulation.* Springer Link.

Cordes, D. 2000. “Mapping functionally related regions of brain with functional connectivity MR imaging.” *AJNR* 1636-44.

Cox, R W et al. 1996. “AFNI: software for analysis and visualization of functional magnetic resonance neuroimages.” *Comput Biomed Res* 162-173.

Cox, R W et al. 1997. “Software tools for analysis and visualization of FMRI Data.” *NMR in Biomedicine* 171-178.

Dale, A.M., Fischl, B., Sereno, M.I.,. 1999. “Cortical surface-based analysis. I. Segmentation and surface reconstruction.” *Neuroimage* 179-194.

Dampney, R et al. 2002. “Central mechanisms underlying short- and long-term regulation of the cardiovascular system.” *Clin Exp Pharmacol Physiol* 261-268.

Davis, T L et al. 1998. “Calibrated functional MRI: mapping the dynamics of oxidative metabolism.” *Proc Natl Acad Sci U S A* 1834-9.

Demir, A. Gozde, U. and Karaman, K. 2010. “Anatomical Landmark Based Registration of Contrast Enhanced T1-Weighted MR Images.” *Biomedical Image Registration, 4th International Workshop.*

Deshmane, Anagha. 2012. “Parallel MR Imaging.” *J Magn Reson Imaging* 55-72.

Diehl, R R. 1998. “Spontaneous blood pressure oscillations and cerebral autoregulation.” *Clinical Autonomic Research* 7-12.

Dietrich, O et al. 2007. “Measurement of Signal-to-Noise Ratios in MR Images: Influence of Multichannel Coils, Parallel Imaging, and Reconstruction Filters.” *Journal or Magnetic Resonance Imaging* 375-385.

Donahue, M et al. 2014. “Bolus Arrival Time and Cerebral Blood Flow Responses to Hypercarbia.” *Journal of Cerebral Blood Flow & Metabolism.*

Donahue, M et al. 2014. “Routine Clinical Evaluation of Cerebrovascular Reserve Capacity Using Carbogen in Patients With Intracranial Stenosis.” *Stroke.*

Dougherty, P et al. 2020. *Central Control of the Autonomic Nervous System and Thermoregulation.*

Drøyvold, W B et al. 2005. “Change in body mass index and its impact on blood pressure: a prospective population study.” *Int J Obes* 650-5.

Elster, Allen D. 2022. *MRI Questions.* June. http://s.mriquestions.com/why-and-when-to-use.html.

Enzmann, D et al. 1992. “Brain motion: measurement with phase-contrast MR imaging.” *Radiology.*

Esler, M et al. 2010. “The 2009 Carl Ludwig Lecture: Pathophysiology of the human sympathetic nervous system in cardiovascular diseases: the transition from mechanisms to medical management.” *J Applied Physiol* 227-237.

Esler, M et al. 2000. “The sympathetic system and hypertension.” *American Journal of Hypertension.*

Ettehad, D et al. 2016. “. Blood pressure lowering for prevention of cardiovascular disease and death: A systematic review and meta-analysis.” *Lancet* 957-967.

Faul, F., Erdfelder, E., Lang, A.-G., & Buchner, A. 2007. “ G*Power 3: A flexible statistical power analysis program for the social, behavioral, and biomedical sciences.” *Behavior Research Methods* 175-191.

Faull, O et al. 2015. “Functional subdivision of the human periaqueductal grey in respiratory control using 7 Tesla fMRI.” *Neuroimage* 256-264.

Federau, C et al. 2017. “Cerebral blood flow, transit time, and apparent diffusion coefficient in moyamoya disease before and after acetazolamide.” *Neuroradiology* 5-12.

Feldman, J L et al. 2013. *Fundamental Neuroscience 4th edition.* Elsevier.

Ficzere, A et al. 1998. “Cerebrovascular reactivity in hypertensive patients: A transcranial Doppler study.” *Journal of Clinical Ultrasound.*

Field, Andy. 2012. *Discovering Statistics Using R.* Sage Publishing.

Firbank, M J et al. 1999. “A comparison of two methods for measuring the signal to noise ratio on MR images.” *Phys. Med. Biol.*

Fischl, B. 2012. “FreeSurfer.” *NeuroImage* 774-781.

Fisher, J A et al. 2016. “The CO2 stimulus for cerebrovascular reactivity: Fixing inspired concentrations vs. targeting end-tidal partial pressures.” *J Cereb Blood Flow Metab* 1004-11.

Foster, G E et al. 2015. “Changes in cerebral vascular reactivity and structure following prolonged exposure to high altitude in humans.” *Physiol Rep.*

Gerlach, AT et al. 2007. “Dexmedetomidine: an updated review.” *Ann Pharmacother* 245-52.

Glover, G H et al. 2000. “Image-Based Method for Retrospective Correction of Physiological Motion Effects in fMRI: RETROICOR.” *Magnetic Resonance in Medicine* 162-167.

Glover, G H et al. 2001. “Spiral-In/Out BOLD fMRI for Increased SNR and Reduced Susceptibility Artifacts.” *Magnetic Resonance in Medicine* 515-522.

Golanov, E V et al. 2004. “Neurons of a limited subthalamic area mediate elevations in cortical cerebral blood flow evoked by hypoxia and excitation of neurons of the rostral ventrolateral medulla.” *The Journal of Neuroscience* 4032-4041.

Goldstein, D S et al. 1983. “Plasma catecholamines and essential hypertension. An analytical review.” *Hypertension* 86-99.

Golestani, A et al. 2016. “Quantitative Mapping of Cerebrovascular Reactivity using Resting-state BOLD fMRI: Validation in Healthy Adults.” *Neuroimage* 147-163.

Golestani, A et al. 2016. “The association between cerebrovascular reactivity and resting-state fMRI functional connectivity in healthy adults: The influence of basal carbon dioxide.” *Neuroimage* 301-313.

Grassi, G et al. 2016. “Evidence for a critical role of the sympathetic nervous system in hypertension.” *J Am Soc Hypertens* 457-466.

Grassi, G et al. 2016. “The Sympathetic Nervous System Alterations in Human Hypertension.” *Circ Res* 976-990.

Greve, D N et al. 2009. “Accurate and robust brain image alignment using boundary-based registration.” *Neuroimage* 63-72.

Griswold, M A et al. 2002. “Generalized autocalibrating partially parallel acquisitions (GRAPPA).” *Magn Reson Med* 1202-1210.

Hahn, E L. 1950. “Spin echoes.” *Physical Review* 580-594.

Hajjar, I et al. 2010. “Hypertension and Cerebral Vasoreactivity A Continuous Arterial Spin Labeling Magnetic Resonance.” *Hypertension* 859-64.

Halani, S et al. 2015. “Comparing cerebrovascular reactivity measured using BOLD and cerebral blood flow MRI: The effect of basal vascular tension on vasodilatory and vasoconstrictive reactivity.” *Neuroimage* 110–123.

Hall, J A et al. 2008. “Anesthesia for functional neurosurgery: the role of dexmedetomidine.” *Opin Anaesthesiol* 537-43.

Hanson, L G. 2008. “Is Quantum Mechanics necessary for understanding Magnetic Resonance?” *Concepts in Magnetic Resonance Part A* 329-340.

Hart, E C et al. 2016. “Human hypertension, sympathetic activity and the selfish brain.” *Exp Physiolo* 1689-99.

Hart, E C et al. 2011. “Sex and ageing differences in resting arterial pressure regulation: the role of the β-adrenergic receptors.” *J Physiol* 5285-97.

Hart, E C et al. 2009. “Sex differences in sympathetic neural-hemodynamic balance implications for human blood pressure regulation.” *Anesthesiology* 571-576.

Hart, E C et al. 2013. “Translational examination of changes in baroreflex function after renal denervation in hypertensive rats and humans.” *Hypertension* 533-541.

Harvey, A et al. 2008. “Brainstem functional magnetic resonance imaging: disentangling signal from physiological noise.” *J Magn Reson Imaging* 1337-44.

Hemmati, N et al. 2012. “. Correlation between end-tidal and arterial carbon dioxide partial pressure in patients undergoing craniotomy.” *Congr Iran Neurosurgeons.*

Horovitz, S. 2008. “Low frequency BOLD fluctuations during resting wakefulness and light sleep: a simultaneous EEG-fMRI study.” *Human Brain Mapp* 671-682.

Hougard, A et al. 2017. “Increased brainstem perfusion, but no blood-brain barrier disruption, during attacks of migraine with aura.” *Brain* 1633-1642.

Hu, X et al. 1994. “Reduction of signal fluctuation in functional MRI using navigator echoes.” *Magnetic Resonance in Medicine.*

Iglesias, J et al. 2015. “Bayesian segmentation of brainstem structures in MRI.” *Neuroimage* 184-195.

Ivankovic, M et al. 2013. “Influence of hypertension and type 2 diabetes mellitus on cerebrovascular reactivity in diabetics with retinopathy.” *Annals of Saudi Medicine* 130-133.

Jahanian, H et al. 2016. “Measuring vascular reactivity with resting-state blood oxygenation level-dependent (BOLD) signal fluctuations: A potential alternative to the breath-holding challenge?” *Neuroimage* 2526-2538.

Jahanian, H et al. 2014. “Spontaneous BOLD Signal Fluctuations in Young Healthy Subjects and Elderly Patients with Chronic Kidney Disease.” *PLoS One.*

Jenkinson, M et al. 2018. *Introduction to resting state fMRI Functional Connectivity.* Oxford University Press.

Jenkinson, M et al. 2001. “Global Optimisation Method for Robust Affine Registration of Brain Images.” *Neuroimage* 143-156.

Jenkinson, M et al. 2002. “Improved optimisation for the robust and accurate linear registration and motion correction of brain images.” *Neuroimage* 825-841.

Jenkinson, M et al. 2002. “Improved Optimisation for the Robust and Accurate Linear Registration and Motion Correction of Brain Images.” *Neuroimage* 825-841.

Johnston, M E et al. 2015. “Multi-TI Arterial Spin Labeling MRI with Variable TR and Bolus Duration for Cerebral Blood Flow and Arterial Transit Time Mapping.” *IEEE Trans Med Imaging* 1392-1402.

Julien, C. 2006. “The enigma of Mayer waves: Facts and models.” *Cardiovascular research* 12-21.

Kanghan, Oh et al. 2019. “Classification and Visualization of Alzheimer’s Disease using Volumetric Convolutional Neural Network and Transfer Learning.” *Nature.*

Kashour, A et al. 2021. *Physiology, Sinoatrial Node.*

Katura, T. 2006. “Quantitative evaluation of interrelations between spontaneous low-frequency oscillations in cerebral hemodynamics and systemic cardiovascular dynamics.” *NeuroImage* 1592-1600.

Kim, D et al. 2021. “Relationship Between Cerebrovascular Reactivity and Cognition Among People With Risk of Cognitive Decline.” *Front Physiol.*

Klabunde, Richard. 2021. *Cardiovascular Pharmacology Concepts.* Wolters Kluwer.

Kougias, P et al. 2010. “Arterial baroreceptors in the management of systemic hypertension.” *Med Sci Monit.*

Kouvelas, D et al. 2005. “Sinoaortic denervation abolishes blood pressure-induced GABA release in the locus coeruleus of conscious rats.” *Neuroscience Letters.*

Krishnamurthy, V et al. 2021. “The Utility of Cerebrovascular Reactivity MRI in Brain Rehabilitation: A Mechanistic Perspective.” *Frontiers in Physiology.*

Ladd, M et al. 2018. “Pros and cons of ultra-high-field MRI/MRS for human application.” *Progress in Magnetic Resonance Spectroscopy* 1-50.

LeCun, Y., Bottou, L., Bengio, Y., Haffner, P., & others. 1998. “Gradient-based learning applied to document recognition.” *Proceedings of the IEEE* 2278–2324.

Leoni, R F et al. 2017. “Cerebral blood flow and vasoreactivity in aging: an arterial spin labeling study.” *Braz J Med Biol Res.*

Leuenberger, U et al. 2003. “Control of Skin Sympathetic Nerve Activity During Intermittent Static Handgrip Exercise.” *Circulation* 108.

Li, Q. 2018. “Cerebral Small Vessel Disease.” *Cell Transplant* 1711–1722.

Linder, T et al. 2023. “Current state and guidance on arterial spin labeling perfusion MRI in clinical neuroimaging.” *Magn Reson Med* 2024-2047.

Lipp, I et al. 2015. “Agreement and repeatability of vascular reactivity estimates based on a breath-hold task and a resting state scan.” *Neuroimage* 387-396.

Liu, J. 2014. “Alterations in Amplitude of Low Frequency Fluctuation in Treatment-Naive Major Depressive Disorder Measured With Resting-State fMRI.” *Human Brain Mapping* 4979-88.

Liu, K Y et al. 2017. “Magnetic resonance imaging of the human locus coeruleus: A systematic review.” *Neurosci Bibehav Rev* 325-255.

Liu, P. 2021. “Cerebrovascular Reactivity Mapping Using Resting-State BOLD Functional MRI in Healthy Adults and Patients with Moyamoya Disease.” *Radiology* 419-425.

Liu, P et al. 2019. “Cerebrovascular reactivity (CVR) MRI with CO2 challenge: A technical review.” *Neuroimage* 104-115.

Liu, P et al. 2017. “Cerebrovascular reactivity mapping without gas challenge.” *Neuroimage* 320-326.

Liu, Y. 2018. “Hypertension-Induced Cerebral Small Vessel Disease Leading to Cognitive Impairment.” *Chin Med J* 615-619.

Logothetis, K L et al. 2002. “The neural basis of the blood-oxygen-level-dependent functional magnetic resonance imaging signal.” *Philos Trans R Soc Lond B Biol Sci* 1003-1037.

Logothetis, N K. 2001. “Neurophysiological investigation of the basis of the fMRI signal.” *Nature* 150-7.

Lowe, M J. 1998. “Functional connectivity in single andmultislice echo planar imaging using resting-state fluctuations.” *NeuroImage* 119-132.

Luft, A R. 1999. “Patterns of age-related shrinkage in cerebellum and brainstem observed in vivo using three-dimensional MRI volumetry.” *Cerebral Cortex* 712-721.

Lunblad, L C et al. 2014. “Brainstem changes associated with increased muscle sympathetic drive in obstructive sleep apnoea.” *Neuroimage* 258-266.

Lundervold, A et al. 2019. “An overview of deep learning in medical imaging focusing on MRI.” *Z Med Phys* 102-127.

Macintosh, B. 2010. “Assessment of arterial arrival times derived from multiple inversion time pulsed arterial spin labeling MRI.” *Magnetic Resonance in Medicine* 641-7.

MacIntosh, B. 2012. “Hemodynamic Alterations in Vertebrobasilar Large Artery Disease Assessed by Arterial Spin-Labeling MR Imaging.” *AJNR Am J Neuroradiol* 1939-1944.

Maeda, H et al. 1994. “Reactivity of cerebral blood flow to carbon dioxide in hypertensive patients: evaluation by the transcranial Doppler method.” *Journal of Hypertension* 191-197.

Markus, H et al. 2002. “Severely impaired cerebrovascular reactivity predicts stroke and TIA risk in patients with carotid artery stenosis and occlusion.” *Brain* 457-467.

Marquand, AF et al. 2012. “Dissociable effects of methylphenidate, atomoxetine and placebo on regional cerebral blood flow in healthy volunteers at rest: A multi-class pattern recognition approach.” *Neuroimage* 1015-24.

Marshall, O et al. 2014. “Impaired cerebrovascular reactivity in multiple sclerosis.” *JAMA Neurology* 1275-81.

Mather, M. 2017. “Higher locus coeruleus MRI contrast is associated with lower parasympathetic influence over heart rate variability.” *Neuroimage* 329-35.

McDonnell, M N et al. 2013. “. Transcranial Doppler ultrasound to assess cerebrovascular reactivity: reliability, reproducibility and effect of posture.” *Peer J.*

Meglic, B et al. 2001. “ Autonomic Nervous System Function in Patients with Acute Brainstem Stroke.” *Cerebrovascular Disease* 2-8.

Moeller, S et al. 2010. “Multiband multislice GE-EPI at 7 tesla, with 16-fold acceleration using partial parallel imaging with application to high spatial and temporal whole-brain fMRI.” *Magn Reson Med* 1144-1153.

Mohan, G et al. 2019. “Medical imaging with intelligent systems: a review.” In *Deep Learning and Parallel Computing Environment for Bioengineering Systems*, by G et al Mohan, 53-73. Elsevier.

Morilak, D et al. 1987. “Effects of physiological manipulations on locus coeruleus neuronal activity in freely moving cats.” *Brain* 24-31.

Muller, M et al. 2012. “Hypertension and Longitudinal Changes in Cerebral Blood Flow: The SMART-MR Study.” *Ann Neurol* 825-33.

Muscas, G et al. 2022. “Recent Advances and Future Directions: Clinical Applications of Intraoperative BOLD-MRI CVR.” In *Cerebrovascular Reactivity. Neuromethods*, by J et al Chen. New York, NY: Humana.

Naidich, T et al. 2009. *Duvernoy's Atlas of the Human Brain Stem and Cerebellum.* Springer.

Naimish, A. 2017. “Facial Key Points Detection using Deep Convolutional Neural Network - NaimishNet.” *Computer Science.*

Napadow, V et al. 2006. “Automated Brainstem Co-registration (ABC) for MRI.” *Neuroimage* 1113-1119.

Ng, Andrew. 2020. *Deep Learning Specialisation.* https://www.coursera.org/learn/neural-networks-deep-learning.

Ni, L et al. 2022. “The Cerebrovascular Reactivity-Adjusted Spontaneous Brain Activity Abnormalities in White Matter Hyperintensities Related Cognitive Impairment: A Resting-State Functional MRI Study.” *J Alzheimers Dis* 691-701.

NICE. 2011. “Hypertension in adults: diagnosis and managmeent.” *National Institue for Health and Clinical Excellence.* August.

Nobili, F. 1993. “Regional cerebral blood flow in chronic hypertension. A correlative study.” *Stroke* 1148–1153.

Obrig, H. 1996. “Cerebral Oxygenation Changes During Motor and Somatosensory Stimulation in Humans, as Measured by Near-Infrared Spectroscopy.” *Oxygen Transport to Tissue XVII* 219-224.

Oliveira, I et al. 2021. “Can 7T MPRAGE match MP2RAGE for gray-white matter contrast?” *Neuroimage.*

Oparil, S et al. 2018. “Hypertension.” *Nature review.*

Openstax. 2019. *Viscosity and Laminar Flow; Poiseuille’s Law.* https://phys.libretexts.org/Bookshelves/College_Physics/College_Physics_1e_(OpenStax)/12%3A_Fluid_Dynamics_and_Its_Biological_and_Medical_Applications/12.04%3A_Viscosity_and_Laminar_Flow_Poiseuilles_Law

Ostrovskaya, M et al. 2015. “Executive Function and Cerebrovascular Reactivity in Pediatric Hypertension.” *J Child Neurol* 543-546.

Panerai, R B. 2000. “Multivariate Dynamic Analysis of Cerebral Blood Flow Regulation in Humans.” *IEEE TRANSACTIONS ON BIOMEDICAL ENGINEERING* 419-423.

Paton, J F R et al. 2009. “Harvey Cushing and the regulation of blood pressure in giraffe , rat and man : introducing ‘Cushing's mechanism'. .” *Exp Physiol* 11-17.

Pattinson, K et al. 2009. “Determination of the human brainstem respiratory control network and its cortical connections in vivo using functional and structural imaging.” *Neuroimage.*

Pattinson, K et al. 2005. “Determination of the human brainstem respiratory control network and its cortical connections in vivo using functional and structural imaging.” *Neuroimage* 295–305.

Pelizzari, L et al. 2021. “Cerebral blood flow and cerebrovascular reactivity correlate with severity of motor symptoms in Parkinson’s disease.” *Ther Adv Neurol Disord.*

Penhill, B. 2023. *When should I use median instead of mean?* January. https://massinitiative.org/when-should-i-use-median-instead-of-mean/.

Périard, D et al. 2012. “The effect of valsartan versus non-RAAS treatment on autoregulation of cerebral blood flow.” *Cerebrovasc Dis* 78-85.

Philipp, M et al. 2002. “Physiological significance of α2-adrenergic receptor subtype diversity: one receptor is not enough.” *American Journal of Physiology - Regulatory, Inegrative and Comparative Physiology.*

Phillips, A A et al. 2016. “Neurovascular coupling in humans: Physiology, methodological advances and clinical implications.” *J Cereb Blood Flow Metab* 647-664.

Pillai, J et al. 2015. “Cerebrovascular Reactivity Mapping: An Evolving Standard for clinical functional imaging.” *Am J Neuroradiol* 7-13.

Pillai, J et al. 2011. “Clinical utility of cerebrovascular reactivity mapping in patients with low grade gliomas.” *World J Clin Oncol* 397-403.

Pinto, E. 2007. “Blood pressure and ageing.” *Postgrad Med J* 109-114.

Prins, N D et al. 2015. “White matter hyperintensities, cognitive impairment and dementia: an update.” *Nat Rev Neurol* 157-165.

Priovoulos, N et al. 2018. “High-resolution in vivo imaging of human locus coeruleus by magnetization transfer MRI at 3T and 7T.” *Neuroimage* 427-36.

Raininko, R et al. 1994. “The normal brain stem from infancy to old age - A morphometric MRI study.” *Neuroradiology* 364-368.

Raj, D et al. 2000. “A model for susceptibility artefacts from respiration in functional echo-planar magnetic resonance imaging.” *Phys. Med. Biol* 3809–3820.

Raul, L et al. 2003. *Cell. Mol. Neurobiol.* 709-726.

Rawat, D et al. 2023. *Hypercapnea.* Feb. https://www.ncbi.nlm.nih.gov/books/NBK500012/.

Razi, E et al. 2012. “Correlation of End-Tidal Carbon Dioxide with Arterial Carbon Dioxide in Mechanically Ventilated Patients.” *Arch Trauma Res* 58-62.

R-core-team. 2022. *R Core Team (2017). R: A language and environment for statistical computing.*

Rebrova, N et al. 2017. “Effect of lisinopril on cerebrovascular reactivity in hypertensive patients with rheumatoid arthritis.” *The Siberian Journal of Clinical and Experimental Medicine.*

Reckelhoff, J F. 2001. “Gender differences in the regulation of blood pressure.” *Hypertension* 1199-208.

Richiardi, J et al. 2015. “Altered cerebrovascular reactivity velocity in mild cognitive impairment and Alzheimer's disease.” *Neurobiology of Aging* 33-41.

Ritter, J M et al. 2007. *Rang and Dale's Pharmacolohy 6th edition.* Churchill Livingstone.

Rostrup, E et al. 2000. “Regional Differences in the CBF and BOLD Responses to Hypercapnia: A Combined PET and fMRI Study.” *Neuroimage* 87-97.

Samuels, E et al. 2008. “Functional Neuroanatomy of the Noradrenergic Locus Coeruleus: Its Roles in the Regulation of Arousal and Autonomic Function Part I: Principles of Functional Organisation.” *Curr Neuropharmacol* 235-253.

Samuels, E et al. 2008. “Functional neuroanatomy of the noradrenergic locus coeruleus: its roles in the regulation of arousal and autonomic function part II: physiological and pharmacological manipulations and pathological alterations of locus coeruleus activity in humans.” *Curr Neuropharmacol* 254-285.

Sander, M et al. 2010. “Cortical and brain stem changes in neural activity during static handgrip and postexercise ischemia in humans.” *J Appl Physiol.*

Sara, S J et al. 2009. “The locus coeruleus and noradrenergic modulation of cognition.” *Nature Reviews Neuroscience* 211-223.

Schwarz, S et al. 2016. “In Vivo Assessment of Brainstem Depigmentation in Parkinson Disease: Potential as a Severity Marker for Multicenter Studies.” *Radiology* 789-98.

Sclocco, R et al. 2017. “Challenges and opportunities for brainstem neuroimaging with ultrahigh field MRI.” *Neuroimage.*

Seravalle, G et al. 2015. “Sympathetic nerve traffic and baroreflex function in optimal, normal, and high-normal blood pressure states.” *J Hypertens* 1411-1417.

Seravalle, G et al. 2022. “Sympathetic nervous system and hypertension: New evidences.” *Autonomic Neuroscience.*

Settakis, G et al. 2003. “Cerebrovascular reactivity in hypertensive and healthy adolescents: TCD with vasodilatory challenge.” *J Neuroimaging* 106-12.

Shah, A et al. 2019. “Brainstem Anatomy: A Study on the Basis of the Pattern of Fiber Organization.” *World Neurosurgery* 826-846.

Shmueli, K. 2007. “Low-frequency fluctuations in the cardiac rate as a source of variance in the resting-state fMRI BOLD signal.” *NeuroImage* 306-320.

Silverman, A et al. 2022. *Physiology, Cerebral Autoregulation.*

Singh, K et al. 2022. “Functional connectome of arousal and motor brainstem nuclei in living humans by 7 Tesla resting-state fMRI.” *Neuroimage.*

Smith, P A et al. 2004. “Relationship Between Central Sympathetic Activity and Stages of Human Hypertension.” *American Journal of Hypertension* 217-222.

Solberg, L A et al. 1983. “Risk factors and atherosclerotic lesions. A review of autopsy studies.” *Arteriosclerosis* 187-98.

Statistics How To. 2023. https://www.statisticshowto.com/homoscedasticity.

Statistics Solutions. 2023. https://www.statisticssolutions.com/the-assumption-of-homogeneity-of-variance/.

Statology. 2023. https://www.statology.org/anova-assumptions/.

STHDA. 2023. *Compare Multiple Sample Variances in R.* February. http://www.sthda.com/english/wiki/compare-multiple-sample-variances-in-r.

Strika, Luciano. 2019. *Why do Neural Networks Need an Activation Function?* https://towardsdatascience.com/why-do-neural-networks-need-an-activation-function-3a5f6a5f00a.

Sweetman, B et al. 2010. “Cerebrospinal fluid flow dynamics in the central nervous system.” *Ann Biomed Eng* 484-496.

Tajbakhsh, N et al. 2016. “Convolutional Neural Networks for Medical Image Analysis: Full Training or Fine Tuning?” *IEEE Trans Med Imaging* 1299-1312.

Tancredi, F B et al. 2012. “Comparison of Pulsed and Pseudocontinuous Arterial Spin-Labeling for Measuring CO2-InducedCerebrovascular Reactivity.” *J Magn Reson Imaging* 312-321.

Taneja, K et al. 2020. “Quantitative Cerebrovascular Reactivity in Normal Aging: Comparison Between Phase-Contrast and Arterial Spin Labeling MRI.” *Front Neurol.*

Textor, S C et al. 2012. “Association of filtered sodium load with medullary volumes and medullary hypoxia in hypertensive African Americans as compared with whites.” *Am J Kidney Dis* 229-37.

Thierfelder, K M et al. 2014. “Vertebral artery hypoplasia: frequency and effect on cerebellar blood flow characteristics.” *Stroke* 1363-8.

Thomas, B P et al. 2014. “Cerebrovascular reactivity in the brain white matter: magnitude, temporal characteristics, and age effects.” *J Cereb Blood Flow Metab* 242-247.

Thomas, D L et al. 2006. “Regional variation of cerebral blood flow and arterial transit time in the normal and hypoperfused rat brain measured using continuous arterial spin labeling MRI.” *J Cereb Blood Flow Metab* 274-282.

Thrivikraman, K et al. 1988. “Locus coeruleus monoaminergic activity and plasma corticotropin after hemorrhage in cats.” *Am J Physiol.*

Triantafyllou, C et al. 2005. “Comparison of physiological noise at 1.5 T, 3 T and 7 T and optimization of fMRI acquisition parameters.” *Neuroimage* 243-250.

Vidorreta, M et al. 2017. “Whole-brain background-suppressed pCASL MRI with 1D-accelerated 3D RARE Stack-Of-Spirals readout.” *PLOS one.*

Viviani, R et al. 2012. “Effect of paroxetine and bupropion on human resting brain perfusion: An arterial spin labelling study.” *Neuroimage* 773-9.

Wakamatsu, K et al. 2016. “Norepinephrine and its metabolites are involved in the synthesis of neuromelanin derived from the locus coeruleus.” *J Neurochem* 768-76.

Waki, H et al. 2011. “Acute reductions in blood flow restricted to the dorsomedial medulla induce a pressor response in rats.” *Journal of Hypertension* 1536-1545.

Waki, H et al. 2010. “Evidence of specific inflammatory condition in nucleus tractus solitarii of neurogenic hypertension.” *Exp Physiol* 595-600.

Waki, H et al. 2014. “Excessive Leukotriene B4 in Nucleus Tractus Solitarii Is Prohypertensive in Spontaneously Hypertensive Rats.” *Hypertension* 194-201.

Wang, J-J. 2016. “Amplitude of low-frequency fluctuation (ALFF) and fractional ALFF in migraine patients: a resting-state functional MRI study.” *Clinical Radiology* 558-64.

Warnert, E et al. 2014. “In vivo Assessment of Human Brainstem Cerebrovascular Function: A Multi-Inversion Time Pulsed Arterial Spin Labelling Study.” *J Cereb Blood Flow Metab* 956-63.

Warnert, E et al. 2016. “Is High Blood Pressure Self-Protection for the Brain?” *Circulation Research.*

Webb, A J S. 2019. “Effects of vasodilating medications on cerebral haemodynamics in health and disease: systematic review and meta-analysis.” *J Hypertension* 1119-1125.

Wei, W et al. 2019. “Influence of collateral circulation on cerebral blood flow and frontal lobe cognitive function in patients with severe internal carotid artery stenosis.” *BMC Neurology.*

Weir, M R et al. 1999. “The renin-angiotensin-aldosterone system: a specific target for hypertension management.” *Am J Hypertension* 205-213.

Whittaker, J R et al. 2016. “The absolute CBF response to activation is preserved during elevated perfusion: Implications for neurovascular coupling measures.” *Neuroimage* 198-207.

Willie, C K et al. 2014. “Integrative regulation of human brain blood flow.” *J Physiol* 841-59.

Wise, R. 2004. “Resting fluctuations in arterial carbon dioxide induce significant low frequency variations in BOLD signal.” *NeuroImage* 1652-1664.

Wong, L et al. 2011. “Hypertension Impairs Vascular Reactivity in the Pediatric Brain.” *Stroke* 1834-8.

Woolrich, M W et al. 2009. “Bayesian analysis of neuroimaging data in FSL.” *Neuroimage* 173-86.

Yang, H et al. 2007. “Amplitude of low frequency fluctuation within visual areas revealed by resting-state functional MRI.” *Neuroimage* 144-152.

Yang, H et al. 2022. “Coupling between cerebrovascular oscillations and CSF flow fluctuations during wakefulness: An fMRI study.” *J Cereb Blood Flow Metab.*

Yang, L et al. 2018. “Gradual Disturbances of the Amplitude of Low-Frequency Fluctuations (ALFF) and Fractional ALFF in Alzheimer Spectrum.” *Front Neurosci.*

Yang, M et al. 2021. “Phasic activation of the locus coeruleus attenuates the acoustic startle response by increasing cortical arousal.” *Scientific Reports.*

Ye, R et al. 2021. “An in vivo Probabilistic Atlas of the Human Locus Coeruleus at Ultra-high Field.” *Neuroimage.*

Yezhuvath, U et al. 2009. “On the assessment of cerebrovascular reactivity using hypercapnia BOLD MRI.” *NMR Biomed.*

Zhan, J et al. 2016. “Amplitude of Low-Frequency Fluctuations in Multiple-Frequency Bands in Acute Mild Traumatic Brain Injury.” *Front. Hum. Neurosci.*

Zhan, Z et al. 2014. “The contribution of different frequency bands of fMRI data to the correlation with EEG alpha rhythm.” *Brain Res* 235-243.

Zhang, R et al. 2000. “Spontaneous fluctuations in cerebral blood flow: insights from extended-duration recordings in humans.” *Am. J. Physiol.: Heart Circ. Physiol.* 1848-1855.

Zhang, Y et al. 2001. “Segmentation of brain MR images through a hidden Markov random field model and the expectation-maximization algorithm.” *IEEE Trans Med Imaging* 45-57.

Zhang, Z et al. 2010. “FMRI Study of Mesial Temporal Lobe Epilepsy Using Amplitude of Low-Frequency Fluctuation Analysis.” *Human Brain Mapping* 1851-61.

Zhou, Q et al. 2010. “Effects of permissive hypercapnia on transient global cerebral ischemia-reperfusion injury in rats.” *Anesthesiology* 288-297.

Zhou, Y et al. 2015. “Cerebrovascular Reactivity Measured with Arterial Spin Labeling and Blood Oxygen Level Dependent Techniques.” *Magn Resonance Imaging* 566-576.

Zou, Q et al. 2008. “An improved approach to detection of amplitude of low-frequency fluctuation (ALFF) for resting-state fMRI: Fractional ALFF.” *Journal of Neuroscience Methods* 137-141.